UNIVERSIDAD DE CHILE
FACULTAD DE CIENCIAS FÍSICAS Y MATEMÁTICAS
DEPARTAMENTO DE INGENIERÍA MATEMÁTICA

EFFECTS OF RADIATION FEEDBACK ON SMBH INSPIRAL PROPERTIES

TESIS PARA OPTAR AL GRADO DE
MAGÍSTER EN CIENCIAS DE LA INGENIERÍA, MENCIÓN MATEMÁTICAS APLICADAS

MEMORIA PARA OPTAR AL TÍTULO DE INGENIERO CIVIL MATEMÁTICO

JUAN JOSÉ D'ETIGNY SUSAETA

PROFESOR GUÍA:
ANDRÉS ESCALA ASTORQUIZA

MIEMBROS DE LA COMISIÓN:
DOMINIK SCHLEICHER
AXEL OSSES ALVARADO

Este trabajo ha sido financiado parcialmente por CMM ANID BASAL FB210005
SANTIAGO DE CHILE
2022

RESUMEN DE LA TESIS PARA OPTAR AL GRADO DE
MAGÍSTER EN CIENCIAS DE LA INGENIERÍA, MENCIÓN MATEMÁTICAS APLICADAS
POR: JUAN JOSÉ D'ETIGNY SUSAETA
FECHA: 2022
PROF. GUÍA: ANDRÉS ESCALA ASTORQUIZA

EFECTOS DEL FEEDBACK DE RADIACIÓN EN LAS PROPIEDADES DE BINARIAS DE AGUJEROS NEGROS SUPERMASIVOS

Dado el paradigma de formación jerárquica de estructuras, las colisiones son eventos que conforman la historia evolutiva de las galaxias. En estas colisiones se espera que las zonas nucleares de las respectivas galaxias se fusionen en un núcleo virializado común que va ahora a albergar los respectivos agujeros negros supermasivos (SMBH) de cada galaxia. Eventualmete se espera que por fricción dinámica, estos agujeros negros sigan migrando y conformen un sistema binario ligado gravitacionalmente. Esta regimen intermedio de separación entre post-emparejamiento y pre-ondas gravitacionales es donde se lleva a cabo nuestra investigación, donde estudiamos el comportamiento de sistemas binarios de agujeros negros y como este interactúa con el feedback de tipo AGN que aparece como resultado de acreción.

En este contexto se efectuaron tanto simulaciones puramente hidrodinámicas/gravitacionales con el código de grilla adaptativa RAMSES, y también simulaciones en la versión del código RAMSES-RT que acopla la evolución de radiación en forma de fotones dentro de los procesos dinámicos que avanzan en el tiempo al material del sistema. De esta manera se aislaron los efectos del feedback de AGN, con especial énfasis en el feedback de modo radiativo (que será el modo en que los agujeros negros afectan más el ambiente para casos con suficiente acreción). Con esta inclusión de la radiación como una variable de modelo implementamos una receta detallada de feedback, para luego explorar el impacto que se ve en la evolución orbital de la binaria, la estructura del disco, las propiedades de estabilidad, y la evolución del spin de los agujeros negros. La exploración anterior se hizo para sistemas en los que se forma una cavidad por efectos hidrodinámicos y sistemas en los que esto no ocurre, en efecto separando nuestro análisis entre sistemas de migración rápida y de migración lenta respectivamente.

Nuestras simulaciones muestran que la inclusión de feedback no afecta la evolución orbital de sistemas que forman un gap hidrodinámico pero afectan la estructura del disco ejerciendo fotoevaporación a través de radiación incidente en el borde interno de la zona de baja incidencia. Por otra parte las simulaciones de migración rápida inicialmente muestran la formación de una zona de baja densidad, pero el disco gradualmente se estabiliza a través de difusión, mientras gradualmente la radiación pierde eficiencia de acoplaje energético por la ionización del gas.

RESUMEN DE LA TESIS PARA OPTAR AL GRADO DE
MAGÍSTER EN CIENCIAS DE LA INGENIERÍA, MENCIÓN MATEMÁTICAS APLICADAS
POR: JUAN JOSÉ D'ETIGNY SUSAETA
FECHA: 2022
PROF. GUÍA: ANDRÉS ESCALA ASTORQUIZA

EFFECTS OF RADIATION FEEDBACK ON SMBH INSPIRAL PROPERTIES

In the paradigm of hierarchical structure formation, mergers are major players in the evolution history of galaxies. For galactic mergers, the respective nuclear regions are expected to stabilize as a new virialized common nucleus that will now host both of the original nuclear supermassive black holes (SMBHs). Eventually it is expected that the dynamical friction enforced by the common host's stellar and gaseous background will bring the black holes together until they are gravitationally bound conforming a new binary system. This intermediate regime of separation (sometimes referred as the hardening phase) that occurs after the black holes pair, and before gravitational wave emission becomes important, is where our investigation takes place, where we study the behaviour of SMBH binary systems and how these are affected the AGN-mode feedback that will appear as a byproduct of accretion.

It is in this context where we ran both purely hydrodynamical+gravitational simulations on the AMR code RAMSES, and radiation coupled hydrodynamical+gravitational simulations on the RAMSES-RT version of the code, where photons are now included as a new variable that affects the dynamical evolution of the system. In this way we isolated the effects of AGN feedback, with special emphasis on radiative mode feedback (which will be the energetically dominant feedback process when accretion is high enough to sustain it). With this inclusion of radiation as a model variable we implemented a detailed feedback recipe through which we explored its impact on the binary's orbital evolution, on disk structure, on disk stability properties, and the evolution of SMBH spin. This mentioned exploration was done for systems in which a tidal cavity will form purely by hydrodynamical effects, and systems in which a cavity will not form, thus effectively partitioning our analysis between systems that show fast migration and systems that exhibit slow migration respectively.

Our simulations show how the inclusion of our feedback model do not strongly affect the orbital evolution for systems that already formed tidal gaps, although the environment structure is affected in the form of disk photoevaporation through strong radiation that collides with the inner boundary of the cleared low density regions. On the other hand for fast migration simulations, initial orbital decay is stalled as a low density bubble is cleared by feedback, but this is not a permanent feature as the disk is stabilized by diffusion wins out against a coupling efficiency of radiated energy that will lower in inverse proportion of the gas's raising ionization fraction.

a quaint and curious volume of forgotten lore

Agradecimientos

Hay mucho que poner acá y muy poco espacio para hacerlo. Primero tengo que partir dándole las gracias a mi mamá y papá, que me han mostrado lo choro que es mantenerse propio y original, siempre dándome las oportunidades para seguir mi propio camino, la verdad cualquier cosa que yo escriba no va a reflejar todo lo que me han dado, su apoyo incondicional siempre ha sido simplemente increíble. A Santiago, Enrique y a la Javi, les debo mucho crédito también, porque como buen concho, mis aprendizajes y críanza se vieron moldeados por ellos, y cualquier éxito que yo tenga o cosa que construya, pertenece en parte a mis hermanos. No puedo no mencionar a mis 7 bellísimos sobrinos, cada uno con sus personalidades y locuras hacen que me olvide del mundo de los cuadernos.

Tengo la maravillosa suerte de tener tanta gente apoyándome, que por honor al espacio no los puedo a mencionar a todos uno por uno. Parto por mi familia extendida: Le doy las gracias a mis abuelos, mis tíos, mis primos (sobre todo al gordis y mención honrosa a los Murray) y la Milita. También está la familia que uno elige: los cabros de LW (AB, RC, DG, TH, CM, NM, BM, FR, JS, VT, MT) que son mi cable a tierra y siempre una presencia constante, los chiquillos del 22 (MA, FF, FG, GG, HGY, AL, PL, DS, PU, EV) que son todos unos genios que me ayudaron a capear la locura de estos últimos años, y todos los amigos que me he hecho en la universidad, la sección, el DIM, el colegio, el deporte y en la vida en general (acá caen por ejemplo, AA, ARB, ARV, PA, DA, MT, RZ, DP, FV, NB, CG, FH, ER, JM, MF, CR, AG, FL, entre varios más que seguramente se me están pasando).

Quiero agradecer también a todos los geniales docentes que me formaron (y a veces toleraron) a lo largo de los años y a los maravillosos funcionarios y trabajadores que han marcado mi paso por cada institución. Agradezco especialmente la labor de Andrés, quien ha sido mi guía en los pasos de este trabajo, me ha dado una ideal mezcla de independencia y apoyo, de paso mostrándome lo que significa realmente dejar de ser estudiante e intentar ser científico.

A cualquier persona que efectivamente esté leyendo estos agradecimientos pero no encuentra su nombre ni se identifica con algún grupo de arriba: Probablemente eres alguna parte de esto, así que muchas gracias jefe.

La astronomía, las matemáticas, el universo y los agujeros negros son bacanes y todo eso, pero todos ustedes son *obviamente* más importantes!

Table of Content

List of Tables

List of Figures

Introduction

Since the introduction of black holes as a prediction of Einstein's framework of general relativity (GR), they have captured the interest of the scientific community, and as of today they comprehend a necessity when trying to explain several astrophysical behaviours. Black holes are regions in space where densities are extremely high, giving rise to gravitational fields so strong, that it establishes an "event horizon" where light cannot escape.

Black holes (BHs) are found in two mass regimes: Stellar mass BHs which range from $\sim 2-5\,M_\odot$ to $\sim 40-65\,M_\odot$ (the upper limit is not well constrained, as it depends on the onset of pair instability, which is still an active discussion subject, see Woosley, 2017). The other mass regime we have significant observational evidence of, is the one of supermassive BHs (SMBHs), which are usually quoted as black holes in the broad mass range of $\sim 10^6-10^9\,M_\odot$. Between this two classes, there is an observational gap (as of today, only one strong candidate has been detected, via gravitational waves in Abbott et al., 2020) of what is referred to as intermediate mass BHs (IMBHs), which are presently considered one of the main missing links for understanding the history black hole evolution, and the evolution of galactic structure (see eg: Volonteri, 2010).

Super massive black holes gained strong astrophysical relevance when they were introduced as main candidates for explaining the luminosity observed in active galactic nuclei (AGNs) by authors like Salpeter, 1964 and Zel'dovich and Novikov, 1967, who introduced the idea of AGNs being powered by big amounts of accretion onto this dense compact objects. As of today it is accepted that this compact objects are found in the overwhelming majority of galaxies (Richstone et al., 1998, Gültekin et al., 2009), and a pairing of this SMBHs is predicted to occur when galaxies merge (many studies point to this result initially suggested by Begelman et al., 1980, see eg: Chapon et al., 2013 for a more updated exploration). The main topic of this thesis is the modelling of SMBH binaries embedded in the gas-rich nuclear regions that are expected to form when galaxies coalesce. The main aspect we are aiming to tackle inside this topic, is the capacity for merging this binary systems have and how feedback mechanisms affect this process and their environment as a whole.

SMBHs, AGNs and mergers

An active galactic nucleus is what we call abnormally bright galaxy nuclei, these can show bolometric luminosity in the excess of $L_{\text{bol}} = 10^{47}\,\frac{\text{erg}}{s}$, with a broad spectrum that may cover from x-rays to radio frequencies (Sazonov et al., 2004). The high lumonisities AGNs exhibit, together with the fact that they show very broad emission lines (which are consistent with Doppler broadening, predicting very high velocities) and the short variability that is seen in some systems, are the main arguments that made the case for highly massive central black holes as the only possible culprits.

After achieving a general consensus in that the majority galaxies host SMBHs in their cores, it became apparent that this is not a necessarily passive feature, as tight correlations between the black hole and larger-scale galactic properties have been found. Two particularly important examples of this, are how BH mass appears to grow proportionally to the nuclear stellar bulge mass M_b, in the form of

$$M_{\text{BH}} \sim 10^{-3} M_b \tag{1}$$

Häring and Rix, 2004. One other remarkable scaling property is the "$M - \sigma$" relation (presented originally in Ferrarese and Merritt, 2000, see Kormendy and Ho, 2013 for a more recent review), which can be written in the following way

$$M_{\text{BH}} \simeq 3 \times 10^{8} M_{\odot} \sigma_{200}^{\alpha} \tag{2}$$

Linking the central black hole's mass to the host galaxy's central bulge velocity dispersion $\sigma = 200\sigma_{200}\,\text{km}\,\text{s}^{-1}$, where $\alpha \simeq 4.4 \pm 0.3$ an empirically fitted factor.

If we consider the dynamical sphere of influence of a BH (interchangeably named Hill's radius) embedded on a stellar system as

$$R_{\text{inf}} = \frac{G M_{\text{BH}}}{\sigma^2} \tag{3}$$

The resulting radius is always too small to explain the large-scale influence that could be inferred from relations like 1-2. By Soltan's argument (Soltan, 1982) we may establish that present day black holes grew largely as a result of luminous accretion of gas (although not exclusively!), meaning that the feedback from this accretion should be intimately linked with the large scale influence seen from the BHs. A review on how AGN feedback and how it links with the galactic nucleus' environment can be found in King and Pounds, 2015.

When thinking about galaxy evolution as a whole, galactic mergers have to be considered, as in today's understanding of the hierarchical Λ Cold Dark Matter (ΛCDM) paradigm, these are considered as naturally occurring events (White and Rees, 1978, White and Frenk, 1991). This merger events trigger several effects, such as AGN activity (eg Treister et al., 2012), the pairing of central BHs (eg Begelman et al., 1980) and redistribution of gas to the resulting central regions (eg Barnes and Hernquist, 1991). In this context, it is that understanding how the central SMBHs that reside in the original isolated galaxies, may come to coalesce, specially if the presence of nuclear gas is assumed, and the feedback from AGNs is considered.

The road towards SMBH coalescence

Begelman et al., 1980 set a framework that traces the possible SMBH coalescence of merging galaxies to three different stages, and even though this analysis is set in the context of binaries embedded in stellar environments, and before going into the case where the presence and influence of gas is relevant, it is instructional to begin by understanding this first case.

In this three stage paradigm, the first step would be the pairing phase, where after the merger system is settling, the nuclear region of this system relaxes and places both SMBHs coexisting in a nuclear bulge. This nuclear bulge provides a stellar background that brings both black holes towards the center through dynamical friction Binney and Tremaine, 2008. The dynamical friction exerted from stars is approximated by the analytic formula from Chandrasekhar, 1943

$$F^{*}_{\rm DF} = -4\pi\rho\left(\frac{GM_{\rm BH}}{c_s}\right)^2 \times f_s(\mathcal{M}) \tag{4}$$

Where $\mathcal{M} = v_{\rm BH}/c_s$ and $f_s(\mathcal{M})$ is a dimensionless analytical expression stemming from the integration of the maxwellian distribution of the velocity field from the background, taking the form

$$f_s(\mathcal{M}) = \ln(\Lambda)\mathcal{M}^{-2}\left[\mathrm{erf}\left(\frac{\mathcal{M}}{\sqrt{2}}\right) - \sqrt{\frac{2}{\pi}}\mathcal{M}\mathrm{e}^{-\mathcal{M}^2/2}\right] \tag{5}$$

Intuitively this star-induced dynamical friction operates by dragging a perturbing object (the BHs) through the enhanced density of the wake created by the deflection of stars. This analytical formula produces a drag that is nearly proportional to $v_{\rm BH}$ at low $\mathcal{M}$ values, which falls to a proportionality of $\propto v_{\rm BH}^{-2}$ at higher velocities, meaning that the dynamical friction mechanism will become progressively less effective at removing energy from the pair, and thus will lose importance as a shrinking mechanism as the binary approaches (and reaches) a Keplerian regime. This stage has a characteristic 'dynamical friction' timescale (sometimes referred as Chandrasekhar timescale) of

$$\tau_{\rm df} \sim \frac{4\times10^6}{\ln(N)}\left(\frac{\sigma_c}{200\,\mathrm{km\ s^{-1}}}\right)\left(\frac{r_c}{100\,\mathrm{pc}}\right)^2\left(\frac{10^8 M_\odot}{m_{\rm i}}\right)\ \mathrm{yr}\ ;\quad (\mathrm{i}=1,2) \tag{6}$$

Where the formula assumes our core of stars has a one dimensional velocity dispersion σ_c, a radius r_c and N particles Yu, 2002 (this timescale may be found with other equivalent definitions depending on literature). The removal of orbital energy by dynamic friction is efficient even after we say the system may be identified as a Keplerian binary which happens approximately when the mass enclosed in their orbit falls below twice the black hole pair mass, and for a singular isothermal sphere, when their hill spheres intersect (getting to separations comparable to $a_b \sim \frac{GM_{\rm bin}}{2\sigma^2}$). This regime is maintained down to what we define as the hardening length scale a_h.

This hardening length is defined as the point at which the specific kinetic energy of the binary equals the specific kinetic energy of the stars, or equivalently, when the binding energy per unit of mass of the binary exceeds $\frac{3}{2}\sigma^2$ (the average kinetic energy of a star in the stellar system). a_h is characterized by

$$a_h = a_b \frac{\mu}{3M_{\rm bin}} \sim \frac{G\mu}{3\sigma^2} \sim 0.1 \frac{q}{(q+1)^2} \left(\frac{M_{\rm bin}}{10^6 M_\odot}\right) \left(\frac{100\,{\rm km\ s^{-1}}}{\sigma}\right) \tag{7}$$

Where $\mu = \frac{m_1 m_2}{m_1+m_2}$ is the reduced mass and $q = \frac{m_1}{m_2}$ (we can write $\mu = M_{\rm bin}\frac{q}{(q+1)^2}$, which leaves at times a cleaner notation). This second phase, often called the hardening phase (Quinlan, 1996, Merritt and Milosavljević, 2005), sees the angular momentum of the binary reduced by the scattering of stars which have close encounters with the binary, most of which will be expelled with an energy gain after one or more encounters with it. Independently of the binary's binding energy E, the average relative energy change by stellar encounter $\delta E/E = \delta a/a \propto m_*/M_{\rm bin}$. The stellar mass that is needed to be ejected in order to reduce the orbital separation of the system importantly is big, of the order of $M_{\rm bin}/m_*$. If the binary has a cross section for collisions with stars of $A \sim \pi a G M_{\rm bin}/\sigma^2$ and we assume a steady flux of stars $F \sim \sigma n_*$ (n_* being the stellar number density and $\rho_* = n_* m_*$), we could calculate the orbital separation decrease rate $\delta a/a \sim (m_*/M_{\rm bin}) F_* A \delta t$, which may be integrated to define the hardening timescale:

$$\tau_{\rm hard} \sim \frac{\sigma}{\pi G n_* m_* a} \sim 70 \left(\frac{\sigma}{100\ {\rm km\ s^{-1}}}\right) \left(\frac{10^4 M_\odot {\rm pc}^{-3}}{\rho_*}\right) \left(\frac{10^{-3}\ {\rm pc}}{a}\right)\ {\rm Myr} \tag{8}$$

With this naive estimation, we get that the hardening timescale, in opposite to the dynamical friction timescale, is inversely proportional to binary separation, and as such, hardening becomes more difficult as orbital decay advances. We say this is a naive calculation because the assumption of a steady energy-reducing stellar flux is too strong, and it may severely underestimate the hardening decaying timescale, in the sense that the centrophilic star budget (the stars that will interact with our binary) decays as the shrinking of the binary advances. The region of the phase space of the system that contains such low angular momentum ($J^2 \lesssim 2GM_{\rm bin}a$) budget is called the loss cone. In order to reach an orbital separation of $\overline{a}$, the amount of ejected stellar mass may be expressed as

$$M_{\rm eject}(\overline{a}) \sim \mu \ln\left(\frac{a_h}{\overline{a}}\right) \tag{9}$$

In practice if we set $\overline{a} = a_{GW}$ as the separation at which orbital decay from gravitational waves becomes efficient, the amount of ejected mass $M_{\rm eject}(a_{GW})$ cannot be reached if loss cone depletion is considered, causing in principle a stalling of the binary if no further physical considerations are made (this is sometimes called the "last parsec problem" Merritt and Milosavljević, 2005). The refilling of the loss cone by two-body relaxation may sometimes solve this stalling in sensible timescales, and as of today mechanisms such as non axisymmetric potentials or three body perturbations (from a third BH for instance), have been proposed as ways to cope with the last parsec problem, but no definite solution has been found to surmount this major bottleneck in the theory of SMBH binaries embedded in stellar environments.

As it was hinted, when BHs become close enough, we enter the third stage of coalescence, where gravitational radiation becomes quite efficient at extracting angular momentum and thus driving the later stages of the merger. Gravitational radiation comes from the time-space excitation derived from the changing gravitational multipole structure the binary exhibits (the ideal case being only quadrupole induced radiation from a circular orbit, but further multipole radiation may be induced by eccentricity in the binary's orbit). The gravitational radiation timescale that comes from this context is commonly quoted from Peters, 1964, and takes the form of

$$\tau_{GW} = \left(\frac{\dot{a}}{a}\right) \sim \frac{5}{64}\frac{c^5 a^4}{G^3 M_{\rm bin}^3}\frac{(1+q)^2}{q}F(e) \tag{10}$$

With F(e) a dimensionless analytic function that quantifies the effect of eccentricity e in the gravitational radiation regime:

$$F(e) = \frac{(1-e^2)^{7/2}}{1+(73/24)e^2+(37/96)e^4} \tag{11}$$

We can readily appreciate that the timescale for gravitational wave emission is strongly proportional to binary separation, in opposite to the hardening timescale, and we define the the length at which the phase or regime transition occurs, as the point a_{GW} at which $\tau_{GW}(a_{GW}) = \tau_{\rm hard}(a_{GW})$ (Colpi, 2014),

$$a_{GW} = \left(\frac{G^2}{c^5}\frac{256}{5\pi}\right)^{1/5}\left(\frac{\sigma}{\rho_*}\right)^{1/5} F(\mathrm{e})^{-1/5}\left(\frac{q}{(1+q)^2}\right)^{1/5} M_{\rm bin}^{3/5} \tag{12}$$

Sometimes $\overline{a}_{GW}$ is set as the length in which $\tau_{GW} < \tau_{\rm hubble}$ (which would reduce to $\overline{a}_{GW} = 1.4\times10^4(M_{\rm bin}/10^6\,M_\odot)^{-1/4} r_S$, with $r_S = 2GM_{\rm bin}/c^2$ the Schwartzschild radius). If $a_{GW} < \overline{a}_{GW}$ coalescence will happen if the binary surpasses the hardening phase, as our system will reach a point in which gravitational waves will remove angular momentum efficiently enough for the merger to shrink rapidly enough.

Withing the paradigm set by Begelman et al., 1980, the presence and influence of gas as a factor that could affect binary shrinking, was barely considered (gas was only proposed to affect the merger process indirectly through the feeding of the SMBHs). This is a problem, as the coalescence of SMBHs is relevant in the environment resulting from galactic mergers, which are predicted to host highly gas-enriched central regions both from simulations (see eg: the already already mentioned Barnes and Hernquist, 1991 or Barnes and Hernquist, 1996) and in observations (Sanders and Mirabel, 1996, Ueda et al., 2014). This expected gas rich environment is predicted even in relatively dry mergers, and as such it is relevant to consider a gaseous medium's influence over the dynamical evolution of the binary. At first approximation, if a stable gas rich environment (a non trivial assumption which we will further expand on) can be maintained, the first and second phases of coalescence we explored in the stellar case, may be accelerated by a factor $\sim 10^2 - 10^3$ (eg: Escala et al., 2005, Dotti et al., 2007, Cuadra et al., 2009).

When the black holes are still in their pairing phase, the role of stellar induced dynamical friction will be aided by the friction exerted by the gas background (Escala et al., 2004), and just as how equation 4 operated, the couple induced by the gaseous dynamical friction retains the same form, but with a different dimensionless function:

$$F^g_{\rm DF} = -4\pi\rho\left(\frac{GM_{\rm BH}}{c_s}\right)^2 \times f_g(\mathcal{M}) \tag{13}$$

Where the dimensionless factor f_g was determined by Ostriker, 1999 by integrating the contribution from the surrounding fluid elements of the density enhanced wake, separating the cases of subsonic/supersonic perturbers:

$$f_g(\mathcal{M}) = \begin{cases} \frac{1}{2\mathcal{M}^2} \ln\left(\frac{1+\mathcal{M}}{1-\mathcal{M}}\right) - \frac{1}{\mathcal{M}}\,, & \mathcal{M} < 1 \\ \frac{1}{2\mathcal{M}^2} \left[\ln\left(\frac{\mathcal{M}+1}{\mathcal{M}-1}\right) - 2\ln(\Lambda)\right], & \mathcal{M} > 1 \end{cases} \tag{14}$$

Where Coulomb's logarithm is actually corrected by Escala et al., 2004 in order to correct for an overestimation found in Ostriker's formula to

$$\ln(\Lambda) \rightarrow g(\mathcal{M}) = \begin{cases} 4.7\,, & \mathcal{M} \geq 0.8 \\ 1.5\,, & \mathcal{M} < 0.8 \end{cases} \tag{15}$$

This gas induced friction has an influence comparable with that of the stellar background, and further facilitates angular momentum removal at the first stages of binary pairing up to the point where the BHs dominate the dynamics of their immediate environment.

After the pairing phase, instead of three body scattering as the main proposed mechanism for removing angular momentum, when the black holes pair up and there is an important gaseous reservoir, the setup will usually take the form of a binary embedded in a gas disk (circumnuclear disk), and the binary's dynamics will be dominated by the interactions between said binary+disk system. If the system is able to maintain the binary+disk structure robustly, besides mechanisms like Lindblad and corotation resonances, Escala et al., 2004 and Escala et al., 2005 showed that the system naturally forms an ellipsoidal density enhancement that lags behind the binary's gravitational potential, this axis misalignment creates strong torques that remove orbital momentum very efficiently. The relatively self-similar evolution of this configuration means that this torque production can be maintained for long enough to bring the SMBHs close enough for the gravitational radiation regime to begin.

We have mentioned that the preceding analysis depends on the disk being able to preserve healthy amounts of available gas surrounding the binary, which is not always the case. To first approximation, cases like the ones explored in Escala et al., 2004 where the disk mass is very high in proportion to the binary, the coupling of the dynamics does not perturb the disk too strongly and allows this smooth binary migration, which is sometimes referred as *Type I* migration. When the binary-disk mass ratio is on the other end, by being extremely low, the binary is too strong of a perturber for the disk to be able to maintain its structure (this is common in other binary+disks astrophysical contexts, such as in the evolution of stellar binaries). This perturbation manifests as a low density gap is carved outwards from the central pair, by the deposition of angular momentum through the coupling of the binary with the medium. This gap formation reduces the gas budget that could extract angular momentum from the SMBHs, and thus the problem evolves much slowly and is known as *Type II* migration. Beyond the $M_{\rm bin}/M_{\rm disk}$, things such as the binary mass ratio or the orbit's eccentricity could affect the propensity that the system has of forming this tidal cavities, which does play a role in our work, specially when consideration the setups from our problem, the gap-forming criterion from del Valle and Escala, 2012, del Valle and Escala, 2013 (hereafter VE12) will be used as a tool for predicting how our initial conditions will evolve in this matter.

Our work

Already having established that SMBH binaries may not be unexpected to be found in large gas reservoirs at the center of our merging (post merger) system, it is possible that this massive BHs which are embedded in such gas-rich environments may have the capacity to accrete at high-rates and therefore feed a lot of quasar-mode energy back to the system. The interplay between this AGN feedback, the structure of the surrounding circumnuclear disk, and the rate of orbital shrinking, are what motivates the need to explore adhoc simulations that have the capacity to address this questions.

This work was originally motivated by the analysis done in del Valle and Volonteri, 2018 (hereafter VV18), where they simulated by the use of the SPH code GADGET Springel, 2005, different binary+disk setups both with and without the energetic feedback that the BHs may impart in their environments, and tried to isolate the effects the inclusion of this phenomenon has. This feedback was modelled by an implementation of a direct heating method to emulate radiative output and a depositing of material by vertical ejection to emulate jets. They find, in broad terms, that in setups where no tidal cavity opens naturally by the dynamics of the system, AGN feedback is able to quickly open what they denominate as "feedback cavity" which stalls the orbital evolution.

In this thesis we will perform simulations that start from the same initial conditions from VV18, but this time they will be done with the AMR code RAMSES (Teyssier, 2002). The main improvement over the original simulation runs, will be the fact that we will employ a radiation coupled hydrodynamical code that follows the interaction between photons in a multi wave band capacity, and the medium, allowing for a more consistent and better resolved radiative feedback from the central binary. With this result we want to be able to measure more accurately the impact that AGN-mode feedback potentially has as a facilitator/inhibitor for BH coalescence, and the overall effect that this feedback may have on the surrounding medium.

Additionally, beyond doing analysis of the simulation state by looking only at outputted information, we do a post processed approximation of the behaviour we would see in terms of the BH's spin evolution in our context and how it relates to AGN feedback. Specifically we translate the accreted angular momentum and mass, to their actual impact in the spin of our BHs by modelling the Bardeen-Peterson effect (through artificially generated inner accretion disks) and its effect in angular momentum alignment and magnitude.

Projecting towards the future, the general understanding of binary coalescence ties in directly with the expectations the scientific community may have towards missions like the Laser Interferometer Space Antenna project (LISA, see eg: Amaro-Seoane et al., 2012) or future upgrades to the LIGO/Virgo collaboration, where improving theoretical constraints of mergers will work in concert with the understanding of gravitational wave emission sources, and viceversa.

Thesis outline

After this relatively brief introduction to the context of our work, the overall document is organized as follows:

In **Chapter 1**, as the core work of this document is focused in the running and analysis of simulations, we start off giving an in-depth overview of all the main numerical algorithms used in the course of this work. The chapter is mostly focused on understanding the core components of the RAMSES code and the methods used to couple the main hydrodynamical code with radiation. Furthermore we give an additional recounting of the sink particle formalism used in RAMSES, of the DICE galaxy code and of the methods we employ in order to generate the emission spectra of the SMBHs.

Next, in **Chapter 2**, we account for all the specific details of the ingredients that come into play when setting up our simulation suite. Specifically we give the motivation for our physical initial conditions, we specify the subgrid recipes employed, and the actual numerical values and parameters that define our systems. The motivation for this chapter is that an interested reader would have all the necessary information to reproduce our simulations on their own.

Having already laid all the groundwork for the setting up of our experiments, **Chapter 3** details all the analysis and results we obtained. We first perform a preliminary analysis of the radiative and non-radiative feedback runs separately, and we then combine them both in a comparative effort. We top off the analysis of our simulations at 4 with the post processing of our simulations and doing the analysis of how the spin of our BHs evolve in relation with the accretion flow.

In order to tie up the work done, we formally end this thesis with **conclusions** section, where we sum up our findings, discuss their possible implications and mention possible improvements and/or future avenues for work.

Finally we include the appendix **A** where the spectrum grid values are showcased, presenting the 10×10 different grid geometries along with their associated values for energy deposition fractions and weighted ionizing cross sections. At **B**, we link to repositories where some of the codes and routines used for our work are located.

Chapter 1

Numerical methods

The fact that most processes in astronomy are observed statically or partially, leads to the use of numerical simulations to fill in the gaps of our understanding of astrophysics in general, allowing researchers to observe the dynamical evolution of astronomical processes in time. Observations and simulations usually work hand in hand, with the latter used in general as the testing grounds of different theories that arise from observations, where model constraints and testing is harder and far more limited.

The approaches for detailed numerical simulations have historically been split between two competing methods, namely Adaptive Mesh refinement or AMR (Berger and Colella, 1989, and for more recent developments Plewa et al., 2005) and Smoothed Particle Hydrodynamics or SPH (Lucy, 1977; Gingold and Monaghan, 1977, and Springel, 2010 for a more updated review on the subject). It is generally accepted that both have their advantages and fallings depending on the context: In one hand SPH-type codes have Galilean invariance (which AMR methods do not have), their spatial resolution is not fixed by minimum grid lengths, and are well equipped for problems with big dynamic range or when the objects are rapidly traversing across the computational volume (Tasker et al., 2008). On the other side grid-based codes can resolve low-density field regions as accurately as high density regions (at a computational cost, which ties with the last advantage of SPH methods mentioned), physical pehonema that can be specified as hyperbolic systems (integral conservation laws) can be implemented seamlessly and are a much better option for problems where the interesting processes are in places of rapidly changing density (rather than in high-density regions) such as shocks.

More recently, a new class of codes have gained importance, these are based in moving mesh methods (eg: GIZMO Hopkins, 2015; AREPO Weinberger et al., 2019), where the spirit lies in trying to combine AMR and SPH methods by using finite element discretization of space through Voronoi tesselation and particle-tree gravitational interaction, this would eliminate problems such as the artificial dealing of shocks and viscosity for SPH, and grid alignment noise or lack of physical invariances for AMR methods. Of course nothing is perfect, and the moving mesh philosphy has its fallings, such as the lack of clear selection of scales for CFL condition fulfillment, or the potential appearance of strong stiff expressions for numerical integration (points mentioned in Tang, 2005) .

1.1 RAMSES

For the work in this thesis we will work with an AMR-based, N-body and hydrodynamical code: specifically we will be using RAMSES[1] (Teyssier, 2002). RAMSES was originally created as a code that implemented a tree-based data structure adaptive mesh refinement (Khokhlov, 1998) with a second-order Godunov hydrodynamical solver, coupled to a N-body solver heavily inspired by the ART code (Kravtsov et al., 1997).

In its purest form, the original framework of the code can be divided into the routines that deal with the grid construction and modification (AMR service routines), the particle mesh routines, the gravity solver routines, and the routines that deal with solving the overall hydrodynamics of the system. All this, as mentioned, is in the spirit of simplifying the codes' overall functioning, omitting details of additional physics, cosmology and new features that deal with more specific routines (which will be eventually addressed as necessary in the course of this work). For an idea of the general flow diagram of RAMSES execution you can see (1.1), where details are ignored, but the task order is consistent with the code

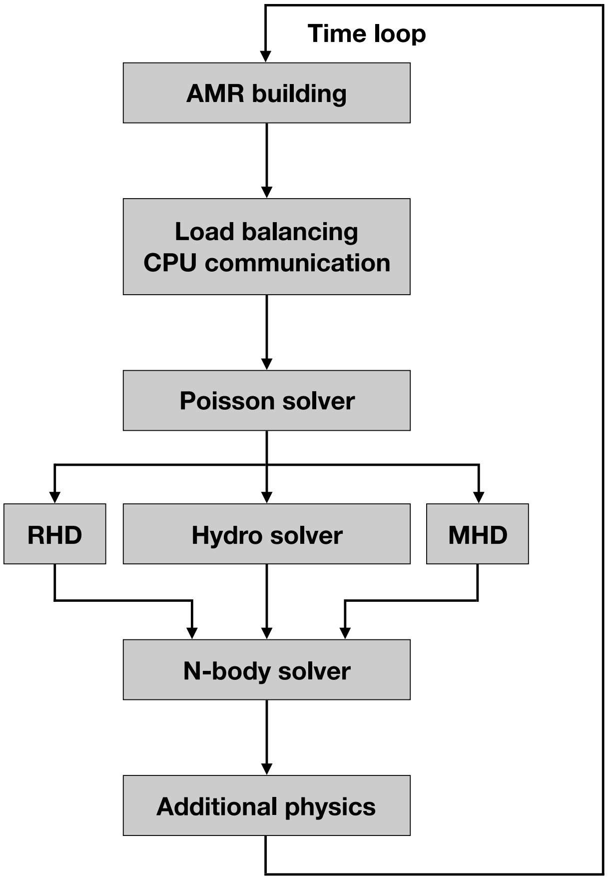

Figure 1.1: General flowchart for the RAMSES code execution

---

[1] https://www.ics.uzh.ch/~teyssier/ramses/RAMSES.html

1.1.1 Adaptive Mesh Refinement

The already mentioned adaptive mesh refinement method was originally described by Berger and Oliger, 1984 and Berger and Colella, 1989. The original method referred to an Eulerian hydrdynamical scheme with a structure made of a hierarchical nested grid that has different levels of coarseness, adjusting its resolution in a user defined ways that make it easier to resolve certain phenomena in simulations. This is opposed to what one is used to when integrating equations numerically, which is usually done in a grid which is fixed in time (and most of the time it has homogeneous geometry). In this original form, the grid was comprised of rectangular blocks, whose positions and aspect ratios are meant to optimize and follow the flow geometry, values, speed and memory constraints (this kind of data structuring is used in other AMR codes such as ENZO Bryan et al., 2014).

In opposition to this original form which had this mentioned rectangular blocks as the data structure, in RAMSES the fundamental structure of the grid comes in the form of a 'Fully Threaded Tree' (FTT) (Khokhlov, 1998). The basic element are groups of 2^{d} sibling cells called *octs* (with $\mathrm{d} \in \{1, 2, 3\}$, standing for the spatial dimensions of the problem), each and any of these octs belong to a corresponding level of grid refinement l (see image 1.2[2]).

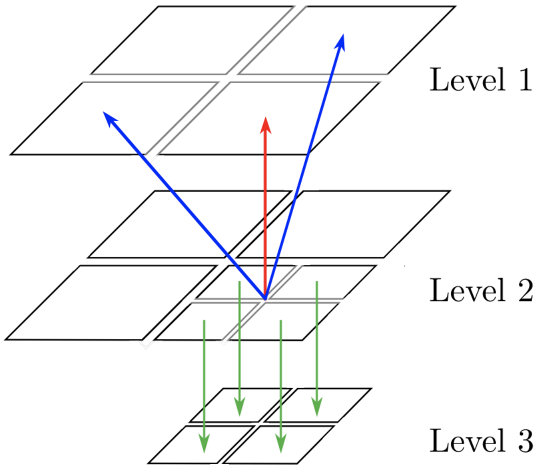

Figure 1.2: 2D representation of the oct-tree structure of ramses. Each oct (here on Level 2) points to it's mother cell (red arrow) and the neighbouring mother cells (blue arrows), and to its children octs (green arrows).

For any given simulation one starts with a regular cartesian grid that defines the base level of refinement, it is called the coarse grid, it sets the first level of the tree structure at $l = 0$ and its resolution. At a refinement level, each oct is assigned a place in a linked list, with every such oct pointing to the next and previous one in the list. Additionally every oct has a pointer to its parent and its 2d neighboring cells at level $l-1$ and to the 2^{d} child octs that would appear at refinement level $l+1$ (when an oct has children, its called a *split* cell, and if not, a *leaf* cell).

On the practical side, if the coarse grid at $l = 0$ is set at a base refinement level of i, for a simulation box of side length L, an oct at level l would then be related to a resolution (cell size) of $\frac{L}{2^{(\mathrm{i}+l)}}$. Now, the fact that one deals with an structured mesh gives the opportunity

---

[2] credit for image `https://tel.archives-ouvertes.fr/tel-01496864/document`

to work with different time-step resolutions for different spatial resolution regions, and hence making it easier to evolve in a detailed way regions that bear more physical significance. The adaptive time step algorithm implemented in RAMSES goes back and forth different refinement levels in a way akin to a W cycle.

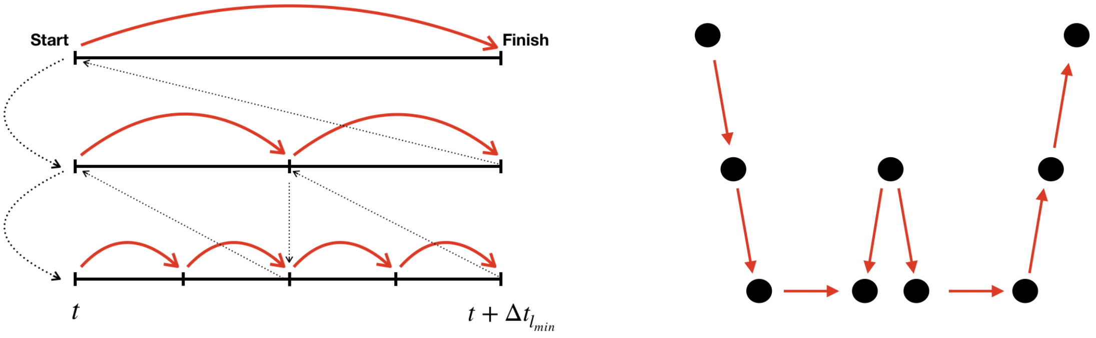

Figure 1.3: Time-stepping order for three refinement level system. Red arrows represent actual time-step execution

The time-step for evolution is estimated recursively through refinement levels with their associated CFL restrictions and then used in the mentioned W cycle, with the additional condition of simultaneity set by finer levels through coarser ones when the instant of time advancing comes (the necessary condition of $\Delta t_\mathrm{i} = \Delta t^2_{\mathrm{i+1}} + \Delta t^2_{\mathrm{i+1}}$, with i the refinement level). If one abuses notation a little and calls l_{min}, l_{max} the respective minimum and maximum levels of refinement, then the sequence of instructions for time multi-stepping would be the following:

- The coarse time-step length $\Delta t_{l_{min}}$ is calculated through its Courant-Friedrichs-Levy conditions in all cells (this will be further explained later)
- Before time integration is executed, the next level at $l_{min} + 1$ makes its own time-step estimation, in two substeps (as the CFL condition should scale linearly with spatial resolution)
- This in turn makes a recursion of nested estimations going down to the finest level which only contains leaf cells
- Here the first two timesteps are finally executed with a length restricted both by the CFL condition and $\Delta t_{l_{max}} \leq \Delta t_{l_{min}}/2^{l_{max}-l_{min}}$
- After this advancement the algorithm goes back a level, and after synchronizing the time step to the sum of the two finer ones already executed, it is executed.
- This is a recursion that starts going up and end the hierarchical advancement once it reaches the coarsest level cells

1.1.1.1 Mapping of cell refinement and modification of the tree

The process of refinement in the code depends on the marking of certain cells as they meet criteria defined by the user and the problems context. This basically proceeds for every level l in the following steps:

- If a split cell contains a children cell that is marked or already refined, then mark it for refinement
- Mark the $3^{\mathrm{d}} - 1$ neighbouring cells
- If any cell satisfies the user-defined refinement criteria, then mark it for refinement

The second instruction is given for the purpose of making the transition of refined to coarse regions, more smooth. Another smoothing procedure is used to reduce the 'noise' that can appear over refinement maps in areas where flows fluctuate over thresholds that define the refinement criteria. This mentioned additional procedure consists of defining a cubic buffer volume around marked cells for a smoother transition, which is basically an expansion of the area of refinement.

After the refinement selection is ready, for every level l, the next step is to create a child oct for every leaf cell that has been marked for refinement, and destroying the child oct for any split cell that was not marked. Even though this process is not necessarily fast (as it involves modifying the linked list structure of the FFT), it is not very time consuming, due to the operations being done only on a reduced number of octs at a time for every time step.

1.1.2 N-body solver

As already mentioned, RAMSES deal with the collisionless portion of simulations through an N-body solver, this is modeled as a system of $p-$particles that obey the Vlasov-Poisson equations:

$$\frac{\mathrm{d}x_p}{\mathrm{d}t} = v_p, \quad \frac{\mathrm{d}v_p}{\mathrm{d}t} = -\nabla_x \phi \,; \quad \Delta_x \phi = 4\pi G \rho \tag{1.1}$$

The scheme can be decomposed in a series of steps:

- Compute the density ρ on the mesh using a Cloud-In-Cell (CIC) interpolation scheme
- Solving for the potential ϕ from the Poisson equation
- Compute the acceleration through a numerical approximation for the gradient of ϕ
- Determining the acceleration for each particle after using an inverse CIC interpolation scheme
- Update the velocity of each particle using the acceleration, and then the position using said velocity.

1.1.2.1 The density field

In order to compute the gravity, one needs the density field across all the simulation, and where the gas density field is easily taken account for thanks to the fact that the grid stores the gas mass deposited in every cell, the particle portion of the density field does not have such a direct treatment. The density field for the particles in a simulation is computed using the CIC interpolation scheme (Hockney and Eastwood, 1981)

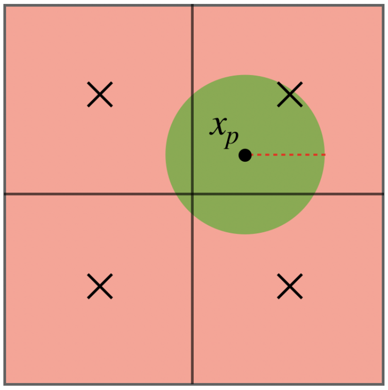

Figure 1.4: Graphic representation of how Cloud-In-Cell deposit particle fields onto the grid

This method defines relies in defining a ”cloud” attached to every particle in the simulation (see 2.7), which distributes its mass across the cells it overlaps with. Formally this spreading out of the particle density, if for instance we consider a cell of volume V_c with N_p particles inside its boundaries, would give a description of the field like this:

$$\rho(x) = \frac{1}{V_c} \sum_{p=1}^{N_p} m_{\mathrm{i}} W(|x - x_{\mathrm{i}}|)$$

Where $W(\cdot)$ is the interpolation function or smoothing kernel defining the cloud geometry that distributes the weight, and m_{i} is the individual particle mass. The information of which octs (and at which level) a particle cloud is overlapping, is contained in a hierarchical linked list which stores and links particles that share similar oct boundaries.

1.1.2.2 Solving for ϕ

The Poisson equation is solved using a one directional scheme that passes information from the coarse grid to the finer levels (Jessop et al., 1994; Kravtsov et al., 1997), which means that the lower resolution levels will not see any effective improvement of the gravity field determination in contrast to if it was solved as an isolated grid, and errors will be propagated through finer levels. In order to start the general method, the Poisson equation is solved for the coarse level using the standard Fast Fourier Transform (FFT) technique (Hockney and Eastwood, 1981) with a green function defined to solve the fourier transform from the central finite approximation of the Laplacian. This transformation in 1D, in continuous form, would transform the problem like:

$$\int_{\infty}^{\infty} \frac{\partial^2 \phi}{\partial x^2} \mathrm{e}^{\mathrm{i}kx} \mathrm{d}x = \int_{\infty}^{\infty} A\rho(x) \mathrm{e}^{\mathrm{i}kx} \mathrm{d}x = A\tilde{\rho}(k) \Rightarrow \tilde{\phi}(k) = A\frac{\tilde{\rho}(k)}{k^2}$$

After the first estimation of the Poisson solution, the finite difference method used here, relies in a central approximation of the Laplacian for 2dim+1 points, with boundary conditions which are passed down to finer levels using linear interpolation and are defined in ghost regions surrounding the involved computation domain. With these conditions the algorithm for determining the potential is a form of the Gauss-Seidel (GS) method with Red/Black ordering and Successive over relaxation (SOR, Press et al., 1992), in which for dim$=2$, the GS iteration writes as (with the initial guess ϕ^0 is defined through a linear reconstruction of the potential from the coarser level $l-1$):

$$\phi^{n+1}_{\mathrm{i},j} = \frac{1}{4}\left(\phi^n_{\mathrm{i}+1,j} + \phi^n_{\mathrm{i}-1,j} + \phi^n_{\mathrm{i},j+1} + \phi^n_{\mathrm{i},j-1}\right) - \frac{h^2}{4}\rho_{\mathrm{i},j}$$

The converge of the Gauss-Seidel algorithm can be improved by different methods, like performing differentiated sequencial updating of indexes (Red/Black ordering) and the freedom to "over-correct" with previous estimates using parameter $\omega \in (1,2)$:

$$\phi^{n+1}_{\mathrm{i},j} = \omega\phi^n_{\mathrm{i},j} + (1-\omega)\phi^{n+1}_{\mathrm{i},j} \Rightarrow \phi^{n+1}_{\mathrm{i},j} = \frac{1-\omega}{4}\left(\phi^n_{\mathrm{i}+1,j} + \phi^n_{\mathrm{i}-1,j} + \phi^n_{\mathrm{i},j+1} + \phi^n_{\mathrm{i},j-1}\right) - \frac{(1-\omega)h^2}{4}\rho_{\mathrm{i},j} + \omega\phi^n_{\mathrm{i},j}$$

Where the choice of the parameter ω makes it so iterations lose estimation power as they advance by making them weight less in proportion to the grid resolution, *ie:* with bad resolution power, the relaxation parameter ω will be closer to 1, as we want low resolution to mean that GS iterations will be less valuable. The explicit form of the optimal parameter selection for a regular $N \times N$ grid is known to be (Press et al., 1992):

$$\omega \simeq \frac{2}{1+\alpha\frac{\pi}{N}}$$

Where α being a parameter set by the boundary condition type (eg: $\alpha = 1$ for Dirichlet conditions). For an irregular grid, the value of w does not have an analytic expression, but in practice the use of the average mesh patch size $\langle L\rangle$ (in number of cells) works very well in replacement of N. In order to test the methods convergence, residuals are defined:

$$R^n_{\mathrm{i},j} = \frac{1}{h^2}\left(\phi^n_{\mathrm{i}+1,j} + \phi^n_{\mathrm{i}-1,j} + \phi^n_{\mathrm{i},j+1} + \phi^n_{\mathrm{i},j-1} - 4\phi^n_{\mathrm{i},j}\right) - \rho_{\mathrm{i},j}$$

Convergence of the estimation for a given level is then decided based on a comparison between the residuals with the scales that come from CIC induced errors, which are the dominant source of error in the force calculation.

1.1.2.3 Acceleration Computation

The acceleration is computed using the potential through a $5-$point finite difference approximation of the gradient. The particles on the simulation recieve their acceleration through an inverse CIC scheme for mass deposition, and they are only passed their acceleration through an interpolation of the mesh if their cloud is completely contained in the cell considered (in other words, if a particle cloud is contained in different cells for level l, then level $l-1$ is considered for the acceleration computation, and so on). This implementation is the same for the ART code (Kravtsov et al., 1997).

1.1.3 Hydrodrynamical solver

The base hydrodynamical set of equations that are to be solved by the code are in their conservative form:

$$\frac{\partial \rho}{\partial t} + \nabla \cdot (\rho u) = 0 \tag{1.2}$$

$$\frac{\partial}{\partial t}(\rho u) + \nabla \cdot (\rho u \otimes u) + \nabla p = -\rho \nabla \phi \tag{1.3}$$

$$\frac{\partial}{\partial t}(\rho \mathrm{e}) + \nabla \cdot [\rho u(\mathrm{e} + p/\rho)] = -\rho u \cdot \nabla \phi \tag{1.4}$$

Where $\otimes$ is the outer vector product, u is the fluid velocity, e is the specific total energy, and p is the thermal pressure given by (at least without RHD):

$$p = (\gamma - 1)\rho \left(\mathrm{e} - \frac{u^2}{2} \right)$$

The energy equation 1.4 is not explicitly conservative due to the non-stiff source term that arises from gravity, and the total energy level is conserved at percent level. If U_{i}^n is the the cell averaged value of the vector $(\rho, \rho u, \rho \mathrm{e})$ at time t^n for cell i, and if $F_{\mathrm{i}+1/2}^{n+1}$ ($F_{\mathrm{i}-1/2}^{n-1}$ respectively) refers to the time centered fluxes across cell interfaces, then the numerical discretization of the Euler equation with gravitational source terms is:

$$\frac{U_{\mathrm{i}}^{n+1} - U_{\mathrm{i}}^n}{\Delta t} + \frac{F_{\mathrm{i}+1/2}^{n+1} - F_{\mathrm{i}-1/2}^{n-1}}{\Delta x} = S_{\mathrm{i}}^{n+1} \tag{1.5}$$

Where the gravitational source terms are included using a time centered, fractional step approach, and get the form:

$$S_{\mathrm{i}}^{n+1/2} = \left(0, \, \frac{\rho_{\mathrm{i}}^n \nabla \phi_{\mathrm{i}}^n + \rho_{\mathrm{i}}^{n+1} \nabla \phi_{\mathrm{i}}^{n+1}}{2}, \, \frac{(\rho u)_{\mathrm{i}}^n \nabla \phi_{\mathrm{i}}^n + (\rho u)_{\mathrm{i}}^{n+1} \nabla \phi_{\mathrm{i}}^{n+1}}{2} \right)$$

As is usual for the numerical solving of hyperbolic PDE systems, the problem is advanced using a second-order Godunov scheme where the intercell fluxes will be approximated through a Riemann solver (the native RAMSES implementation is based on the work of Colella, 1990 and Saltzman, 1994). A general overview of Godunov methods can be found in Toro, 2001. As briefly mentioned before, in order to integrate Euler's equations, we need to compute the time-centered fluxes at cell interfaces, which is done with a Riemann solver, and in practice we choose to use RAMSES implementation of the HLLC solver. Instead of going in depth with the workings of such solver, we reference Toro, 2019 for an updated review on the subject. The HLLC (Harten–Lax–van Leer contact) solver is chosen over other approximate Riemann solvers that have been implemented in the RAMSES framework, as its known to have good capabilites in capturing contact discontinuities (in contrast to LLF, roe,the original HLL, etc.) and is therefore better equiped for modelling shocks. Even though one would expect a strong trade-off in simulation time attached to this improved capabilites, the HLLC solver performance has been positively tested in Lu et al., 2010, where the slight increase in simulation time is validated by the difference in numerical viscosity with the comparable methods. In practice, for our simulations, even without RHD, the simulation time taken up by the Godunov solver falls below 10%.

1.1.4 Time integration and step control

1.1.4.1 Time integration

For a coupled N-body and hydrodynamical AMR code one needs to deal with the possibility of variable time-steps. The solvers' stability with respect on time-step length is given by a (variable in time) CFL condition. We need to establish how we integrate the hydrodynamics of the system and the dynamics from particles. For particles RAMSES has an implementation of a second-order midpoint scheme. We know the acceleration $-\nabla\phi^n$ at time t^n from particle positions x_p^n, positions and velocities are first updated by a predictor step:

$$v_p^{n+1/2} = v_p^n - \nabla\phi^n \Delta t^n/2\,; \quad x_p^{n+1} = x_p^n + v_p^{n+1/2}\Delta t^n \tag{1.6}$$

This is then updated through a corrector step that is updated using the acceleration at t^{n+1}, which means the operation is done in the next time step:

$$v_p^{n+1} = v_p^{n+1/2} - \nabla\phi^{n+1}\Delta t^n/2 \tag{1.7}$$

When a particle exits level l with time step Δt_l, the corrector step is applied at level $l-1$ with Δt_l instead of Δ_{l-1}. This means that "past history" of all particles has to be known to apply this procedure.

In the case of time integration for Hydrodynamics, we now present the steps (which are recursive by the second step) for level l in the involved AMR methodology:

1. Generate refinements at level $l+1$ through interpolation of level l variables and compute Δt_l length
2. Advance the solution in time for level $l+1$
3. Compute boundary conditions in a temporary buffer by conservative interpolation of level $l-1$ variables
4. Compute fluxes using the single grid Godunov solver
5. Replace the fluxes at the coarse-fine interface by averaging the fluxes computed at level $l+1$
6. For leaf cells, update variables using these fluxes
7. For split cells, update variables by averaging down the updated variables of level $l+1$
8. Build the new refinement map

1.1.4.2 Time step restriction

In order to integrate the numerical methods in RAMSES, the time step length has to be determined for each level independently (as is was somewhat implicitly mentioned at 1.3) and we now enumerate all the criteria for this determination (outside of any RHD imposed criteria that would be mentioned in the next section). The firs constraint come from the gravitational evolution of the system, where we want to impose that Δt^l should be smaller than a fraction $C_1 < 1$ of the minimum free-fall time:

$$\Delta t_1^l = C_1 \times \min_l(t_{\rm ff})$$

The second time step restriction comes from particle dynamics in the grid, where we impose that they should move in fractions $C_2 < 1$ of the local cell size. This is a standard measure set in order to correctly follow kinematics along a grid:

$$\Delta t_2^l = C_2 \times \Delta x^l / \max_l(v_p)$$

Since our simulations will not be cosmological, no time restrictions regarding the expansion factor a_{exp} are needed, leaving only the Courant-Friedrichs-Lewy (CFL) condition:

$$\Delta t_3^l = \tilde{C} \times \Delta x^l / \max_l(|u_x| + c,\ |u_y| + c,\ |u_y| + c)$$

Just as the second condition, the CFL condition uses the Courant factor $\tilde{C}$ to put a restriction on how characteristic simulation speeds should not travel faster than how physical information can travel through the grid. With all this in hand the actual time step will be restricted to be

$$\Delta t_l = \min(\Delta t_1^l,\ \Delta t_2^l,\ \Delta t_3^l)$$

1.2 RAMSES-RT: Radiation hydrodynamics (RHD)

The spirit of our work is ultimately explore consistently the effects of radiation in black hole mergers, and the belief that this will be done correctly then relies strongly on the methods used to model such processes in a simulation. Luckily, RAMSES has a very sophisticated state of the art package written for the modelling of non-equilibrium thermochemistry, ionization and radiation hydrodynamics as a whole, namely RAMSES-RT. This deep radiative transfer model was introduced in Rosdahl et al., 2013 and was then finished and coupled to hydrodynamics in Rosdahl and Teyssier, 2015, which methods are of such relevance to this work that we now give an accounting for.

Radiation hydrodynamics have usually been treated as second-order processes in many astrophysical contexts, and if studied altogether, they are frequently relegated to being modelled in a post-processing fashion where radiation is decoupled to the dynamics and structure formation of the system or they strongly rely on subgrid recipes. This stems from fact that the inclusion of coupled radiative transfer is hard because of the big constraints in computation time and memory that the high dimensionality and physical complexities put in simulations, alongside with the inherent difference of timescales between radiative processes with dynamical ones. It is worth mentioning here that the efforts in modelling radiation here, are focused on capturing continuum radiative transfer in opposition to line-driven radiative transfer.

Just how hydrodynamical codes are traditionally split between SPH and AMR, RT schemes also present a dichotomy between ray-tracing codes and moment-based codes. Comparisons between both methods have been carried out (eg Iliev et al., 2006; Petkova and Springel, 2011; Wise and Abel, 2011), and while each of them has its own advantages and disadvantages, we are going to deal with a moment method in RAMSES. It is to be noted that the quoted comparative studies, do not deal with coupled RHD codes, but with pure RT codes.

1.2.1 Moment-Based Radiative Transfer with the M1 Closure

The idea behind moment based methods for treating radiation is to reduce the angular component of the radiative transfer equations taking its angular moments and then closing the equations by adding information with a proposed form of the physical behaviour of the system (in our case it falls into proposing a form for the radiative pressure tensor $\mathbb{P}_\nu$). In the end this reduces to replacing beam direction of radiation, with bulk directions that represent their average behaviour. If we call $I_\nu(\mathbf{x}, \mathbf{n}, t)$ the specific radiation intensity at coordinate $\mathbf{x}$ and time t, such that

$$E_\nu = I_\nu \, \mathrm{d}\nu \, \mathrm{d}\Omega \, \mathrm{d}A \, \mathrm{d}t \tag{1.8}$$

is the energy of radiation with frequency in $[\nu, \, \nu + \mathrm{d}\nu]$ propagating through the area $\mathrm{d}A$ in a solid angle $\mathrm{d}\Omega$ around the direction $\mathbf{n}$. The equation of radiative transfer describes the local change in specific intensity in relation to photon propagation, absorption and emission

$$\frac{1}{c}\frac{\partial I_\nu}{\partial t} + \mathbf{n} \cdot \nabla I_\nu = -\kappa_\nu I_\nu + \eta_\nu \tag{1.9}$$

With c being the speed of light, $\kappa_\nu(\mathbf{x}, \mathbf{n}, t)$ the absorption coefficient and $\eta_\nu(\mathbf{x}, \mathbf{n}, t)$ a function that models sources of radiation. When one takes the first two moments of equation 1.9 and defining the species $S = \{\mathrm{H_I}, \mathrm{He_I}, \mathrm{He_{II}}\}$ (these are used as they are the main contributors on radiative transfer for most regimes, potentially other species could be added), we recover the evolution of the photon number density N_ν and the flux F_ν:

$$\frac{\partial N_\nu}{\partial t} + \nabla \cdot F_\nu = \dot{N}_\nu^* + \dot{N}_\nu^{rec} - \sum_{j \in S} n_j \sigma_{\nu j} c N_\nu \tag{1.10}$$

$$\frac{\partial F_\nu}{\partial t} + c^2 \nabla \cdot \mathbb{P}_\nu = - \sum_{j \in S} n_j \sigma_{\nu j} c F_\nu \tag{1.11}$$

Where as we mentioned $\mathbb{P}_\nu$ is the pressure tensor that remains to be determined in order to close the equations. Absorption has been split into $n_j \sigma_{\nu j}$, with n_j is the number density of one of the given photo-absorbing species we are working with in S, and $\sigma_{\nu j}$ is the corresponding ionization cross-section for photons at frequency ν. Emission sources now have also been split into injection sources $\dot{N}_\nu^*$ (e.g. in our case these will correspond to quasar radiation emission), and also recombination radiation from gas $\dot{N}_\nu^{rec}$. It is worth noting here that in Rosdahl and Teyssier, 2015, this system of equations is expanded to include explicitly the isolated handling of dust absorption and rescattering of radiation into the infrared band (see section 1.2.2.4 for more details, albeit not all, as it is not necessarily a main feature in our context).

The first necessary simplification that arises at this point, is the need to reduce the load from assuming a continuous dependency on ν for the RT equations 1.10-1.11, which leads to a discretization of frequencies into bins that makes it so groups of photons roughly approximate relevant quantities for frequency ranges. This multifrequency approach defines quantities through averages:

$$N_\mathrm{i} = \int_{\nu_{\mathrm{i}0}}^{\nu_{\mathrm{i}1}} N_\nu \, \mathrm{d}\nu \,, \qquad F_\mathrm{i} = \int_{\nu_{\mathrm{i}0}}^{\nu_{\mathrm{i}1}} F_\nu \, \nu$$

Where for $\mathrm{i} \in \{1, ..., M\}$ the frequency groups are defined so that every interval is $(\nu_{\mathrm{i}0},\ \nu_{\mathrm{i}1})$, they are mutually exclusive and cover the whole H-ionizing range (meaning that $[\nu_{00}, \nu_{01} : \nu_{10}, \nu_{11} : ... : \nu_{M0}, \nu_{M1}] = [\nu_{H_I}, \infty[$). With this definition in hand, when integrating the RT equations we get:

$$\frac{\partial N_\mathrm{i}}{\partial t} + \nabla \cdot F_\mathrm{i} = \dot{N}_\mathrm{i}^* + \dot{N}_\mathrm{i}^{rec} - \sum_{j \in S} n_j \sigma_{\mathrm{i}j}^N c N_\mathrm{i} \tag{1.12}$$

$$\frac{\partial F_\mathrm{i}}{\partial t} + c^2 \nabla \cdot \mathbb{P}_\mathrm{i} = - \sum_{j \in S} n_j \sigma_{\mathrm{i}j}^N c F_\mathrm{i} \tag{1.13}$$

Thus yielding a set of $4 \times M$ equations, where we define the average cross sections $\sigma_{\mathrm{i}j}^N$ between group i and species j, as:

$$\sigma_{\mathrm{i}j}^N = \frac{\int_{\nu_{\mathrm{i}0}}^{\nu_{\mathrm{i}1}} \sigma_{\nu j} N_\nu \, \mathrm{d}\nu}{\int_{\nu_{\mathrm{i}0}}^{\nu_{\mathrm{i}1}} N_\nu \, \mathrm{d}\nu}$$

The model is simplified by defining group cross sections as global quantities, assuming a given spectral distribution of energy $J(\nu) = N_\nu \cdot h\nu$ (this is a user given parameter, and in our case is of great importance for depositing radiation energy in the simulation from the AGN feedback, see 2.3.2). The cross sections are then evaluated by using the expression from Verner et al., 1996 for $\sigma_{\nu \mathrm{H_I}}$, $\sigma_{\nu \mathrm{He_I}}$ and $\sigma_{\nu \mathrm{He_{II}}}$ and then doing

$$\sigma^N_{\mathrm{i}j} = \frac{\int_{\nu_{\mathrm{i}0}}^{\nu_{\mathrm{i}1}} \sigma_{\nu j} J(\nu)/h\nu \,\mathrm{d}\nu}{\int_{\nu_{\mathrm{i}0}}^{\nu_{\mathrm{i}1}} J(\nu)/h\nu \,\mathrm{d}\nu} \tag{1.14}$$

At the same time average photon energies within each group are of course evaluated as

$$\bar{\varepsilon}_{\mathrm{i}} = \frac{\int_{\nu_{\mathrm{i}0}}^{\nu_{\mathrm{i}1}} J(\nu) \,\mathrm{d}\nu}{\int_{\nu_{\mathrm{i}0}}^{\nu_{\mathrm{i}1}} J(\nu)/h\nu \,\mathrm{d}\nu} \tag{1.15}$$

As of now, equations 1.12 and 1.13 are to be closed with an adopted expression for the radiative pressure tensor. This is usually done by calling $\mathbb{P}_{\mathrm{i}} = \mathbb{D}_{\mathrm{i}} N_{\mathrm{i}}$, with $\mathbb{D}_{\mathrm{i}}$ the Eddington tensor, through which one will try to capture the most meaningful physical behaviours. Different expressions have been proposed for $\mathbb{D}_{\mathrm{i}}$, such as the original Eddington approximation $\mathbb{D}_{\mathrm{i}} = (1/3)\mathbf{I}$ which would correspond to a model for isotropic intensity, or the optically thin Eddington tensor formalism OTVET (see eg: Gnedin and Abel, 2001). The choice of tensor expression in the case of our work, as we previously mentioned, is the M1 closure relation (Levermore, 1984).

The M1 closure relation is derived by doing analytic approximations on radiative transfer moment equations assuming rotational invariance of intensity sources, the work can get quite technical, and we now give a very brief intuition of where the formulas come from. To understand the intuition of the adopted relation, we first remember that from taking the angular moments of 1.9, the actual expressions we got were:

$$cN_\nu = \int_{4\pi} I_\nu(\mathbf{x}, \mathbf{n}(\Omega), t) \,\mathrm{d}\Omega \,, \qquad F_\nu = \int_{4\pi} \mathbf{n}(\Omega) \cdot I_\nu(\mathbf{x}, \mathbf{n}(\Omega), t) \,\mathrm{d}\Omega \tag{1.16}$$

$$\mathbb{P}_\nu = \int_{4\pi} \mathbf{n}(\Omega)\mathbf{n}(\Omega)^T \cdot I_\nu(\mathbf{x}, \mathbf{n}(\Omega), t) \,\mathrm{d}\Omega \tag{1.17}$$

As is clear from the definition of F_ν in 1.16, we have $|F_\nu| \leq cN_\nu$, and thus define the reduced flux $f_\nu = \frac{|F_\nu|}{cN_\nu}$, which in practice serves as an index of directionality for the radiation flow in each point (low values point to predominantly isotropic flows, and conversely, values nearing unity means that flow is mainly one-directional). Intensity can also be normalized by expressing it through the field Φ so that $I_\nu = cN_\nu \Phi$. One can further prove that the pressure tensor is to have positive matrix trace and that the operator $\mathbb{D} - f \otimes f$ is semi-positive definite. By lastly making the assumption of Φ having a symmetry axis around the flux direction $\overline{\mathbf{n}}_\nu := \frac{F_\nu}{|F_\nu|}$, it can be proven that this direction is an eigenvector with an associated eigenvalue χ_ν typically referred to as the Eddington factor. After some linear algebra (Levermore, 1984) one arrives at the closing expressions for the pressure tensor:

$$\mathbb{D}_\nu = \frac{1 - \chi_\nu}{2}\mathbf{I} + \frac{3\chi_\nu - 1}{2}\overline{\mathbf{n}}_\nu \otimes \overline{\mathbf{n}}_\nu \;; \qquad \chi_\nu = \frac{3 + 4f_{\mathrm{i}}^2}{5 + 2\sqrt{4 - 3f_{\mathrm{i}}^2}} \tag{1.18}$$

This effectively closes the radiation transfer equations by defining bulk flux directionality in a consistent way that can be calculated locally for each grid.

1.2.2 Numerical implementation of radiative transfer

To understand the radiation-hydrodynamics as done in RAMSES, it is best to first understand the radiative transfer implementation without its coupling to the hydrodynamics of the system. For the basic hydrodynamical variable vector $(\rho, \rho\mathbf{u}, E, Z)$ we will first need to add $4 \times M$ variables that describe the photon densities N_{i} and fluxes F_{i} for $\mathrm{i} \in [M]$, and secondly we will track the evolution of hydrogen and helium ionization through ion density fractions:

$$x_{\mathrm{H_{II}}} = \frac{n_{\mathrm{H_{II}}}}{n_{\mathrm{H}}}, \qquad x_{\mathrm{He_{II}}} = \frac{n_{\mathrm{He_{II}}}}{n_{\mathrm{He}}}, \qquad x_{\mathrm{He_{III}}} = \frac{n_{\mathrm{He_{III}}}}{n_{\mathrm{He}}}$$

In order to solve the system 1.12-1.13 numerically, instead of trying to discretize the whole set of equations simultaneously, the code splits the equations in sequentially solvable systems, that are treated over the same time-step Δt. This is called the operator splitting strategy, and it consists of three steps, the photon injection, the photon transport and the thermochemistry step (the step scheme can be seen in 1.5).

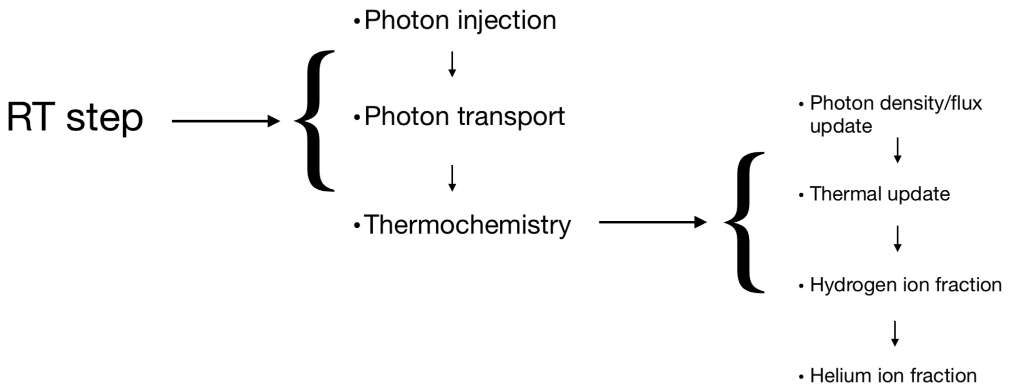

Figure 1.5: Overall operator splitting strategy for the RT formalism, with its different steps

1.2.2.1 The injection step

This is a simple step where energy from radiative sources is introduced in the grid, which means the equations to solve are of the form:

$$\frac{\partial N_{\mathrm{i}}}{\partial t} = \dot{N}_{\mathrm{i}}^{*} \tag{1.19}$$

Where as we have already mentioned, $\dot{N}_{\mathrm{i}}^{*}$ is the rate of injection for photons from group i in a given cell (the way this value is determined is explained in depth at sections 1.4.3 and 2.3). The numerical solution of this equation is done by a straightfoward numerical approximation of the time derivative

$$N_{\mathrm{i}}^{n+1} = N_{\mathrm{i}}^{n} + \Delta t \dot{N}_{\mathrm{i}}^{*}$$

1.2.2.2 The transport step

This part of the operator splitting strategy refers to the propagation of free-flowing photons through the physical system. This means we want to look at the RT equations with the assumption that there is no absorption, recombination radiation or emission from radiative forces, all of which reduces to solving 1.12-1.13 with the RHS set to $= 0$:

$$\frac{\partial N}{\partial t} + \nabla \cdot F = 0 \tag{1.20}$$

$$\frac{\partial F}{\partial t} + c^2 \nabla \cdot \mathbb{P} = 0 \tag{1.21}$$

If one introduces $\mathcal{U} = [N,\ F]$, $\mathcal{F}(\mathcal{U}) = [F,\ c^2\mathbb{P}]$, as in the case of the hydrodynamical equations, the system can be written in conservative form:

$$\frac{\partial \mathcal{U}}{\partial t} + \nabla \mathcal{F}(\mathcal{U}) = 0$$

And if we now consider the problem in one dimension (as to make the notation simpler reducing the number of subindices), and using n as the time index and l as the spatial index, we can define $\mathcal{U}_l^n$ and

$$\mathcal{F}_{l\pm 1/2}^n$$

just as we did in the past for the Godunov scheme philosophy, meaning that the time advancing scheme will equate to solving

$$\mathcal{U}_l^{n+1} = \mathcal{U}_l^n + \frac{\Delta t}{\Delta x}(\mathcal{F}_{l-1/2}^n - \mathcal{F}_{l+1/2}^n) \tag{1.22}$$

The Riemann solver used in this case for the intercell flux expressions is the GLF (Global Lax Friedrich):

$$(\mathcal{F}_{GLF})_{l+1/2}^n = \frac{\mathcal{F}_l^n + \mathcal{F}_{l+1}^n}{2} - \frac{c}{2}(\mathcal{U}_{l+1}^n - \mathcal{U}_l^n)$$

This is usually the preferred option over a HLL-type solution, as in practice it captures isotropic sources better and suffers less of grid-alignment radiation errors (it does have the downfall of being a bit overly diffusive, which would present a problem in contexts where radiation beaming and shadows are actually something of interest).

1.2.2.3 Thermochemistry step

This phase of the RT loop deals with the interaction that photons have with gas. Absorption and emission of photons, heats and cools gas, which means that the thermal energy density fluctuates, and the abundances of the species we consider in the model have to be tracked, which is done through the three ionization fractions $x_{\mathrm{H_{II}}}$, $x_{\mathrm{He_{II}}}$ and $x_{\mathrm{He_{III}}}$. The set of the non-equilibrium thermochemistry equations to be evolved is big, and it is done sequentially, first starting with the photon density and flux equations:

$$\frac{\partial N_{\mathrm{i}}}{\partial t} = -\sum_{j\in S} n_j c \sigma_{\mathrm{ij}}^N N_{\mathrm{i}} + \sum_{j\in S} b_{\mathrm{ij}}^{rec}[\alpha_j^A - \alpha_j^B] n_j n_{\mathrm{e}} \tag{1.23}$$

$$\frac{\partial F_{\mathrm{i}}}{\partial t} = -\sum_{j\in S} n_j c \sigma_{\mathrm{ij}}^N F_{\mathrm{i}} \tag{1.24}$$

Where the $\dot{N}_{\mathrm{i}}^{rec}$ in the original equations is replaced by the full expression of recombinative emissions. In this expression $\alpha_j^A(T)$, $\alpha_j^B(T)$ reperesent case A and case B rates of recombination between electrons and the species in S, $b_{\mathrm{i}j}^{rec}$ is a boolean matrix that determines into which photon group the species j emits into, and as for the rest of this work n_{e} is the electron number density. This two equations are the first solved, and it is done with a purely explicit numerical scheme, using the backwards in time values of the variables in the RHS.

The next equation we have on the step is for the thermal evolution:

$$\frac{\partial \varepsilon}{\partial t} = \mathcal{H} - \mathcal{L} \tag{1.25}$$

Where in the RHS we have the photoheating rate, which is a sum of all the heating contribution that photoionization makes

$$\mathcal{H} = \sum_{j\in S} n_j \sum_{\mathrm{i}=1}^{M} c_r N_{\mathrm{i}}(\overline{\varepsilon}_{\mathrm{i}}\sigma_{\mathrm{i}j}^{E} - \varepsilon_j \sigma_{\mathrm{i}j}^{N}) \tag{1.26}$$

And the primordial cooling rate $\mathcal{L}$,

$$\begin{aligned}\mathcal{L} = {} & \left[\zeta_{\mathrm{H}_I}(T) + \psi_{\mathrm{H}_I}(T)\right] n_{\mathrm{e}} n_{\mathrm{H}_I} + \zeta_{\mathrm{He}_I}(T) n_{\mathrm{e}} n_{\mathrm{He}_I} + \left[\zeta_{\mathrm{He}_{\mathrm{II}}}(T) + \psi_{\mathrm{He}_{\mathrm{II}}}(T) + \eta^A_{\mathrm{He}_{\mathrm{II}}}(T) + \omega_{\mathrm{He}_{\mathrm{II}}}(T)\right] n_{\mathrm{e}} n_{\mathrm{He}_{\mathrm{II}}} \\ & + \eta^A_{\mathrm{H}_{\mathrm{II}}}(T) n_{\mathrm{e}} n_{\mathrm{H}_{\mathrm{II}}} + \eta^A_{\mathrm{He}_{\mathrm{III}}}(T) n_{\mathrm{e}} n_{\mathrm{He}_{\mathrm{III}}} + \theta(T) n_{\mathrm{e}}(n_{\mathrm{H}_{\mathrm{II}}} + n_{\mathrm{He}_{\mathrm{II}}} + 4 n_{\mathrm{He}_{\mathrm{III}}}) + \varpi(T) n_{\mathrm{e}}\end{aligned} \tag{1.27}$$

Where the cooling processes are collisional ionizations ζ, collisional excitations ψ, recombinations η, dieletronic recombinations ω, bremsstrahlung θ and compton cooling ϖ. These are all functions of temperature as defined in Rosdahl et al., 2013 appendix E (we will expand and state these functions in section 1.3). In practice the actual values that is updated is temperature, and it is done semi-implicitly with forward values of the N_{i} and F_{i}, and backwards values for abundancies.

The final set of equations that are to be evolved in this thermochemical step, are the ion abundancy balance equations:

$$n_{\mathrm{H}}\frac{\partial x_{\mathrm{H_{II}}}}{\partial t} = n_{\mathrm{H_I}}\left(\beta_{\mathrm{H_I}} n_{\mathrm{e}} + \sum_{\mathrm{i}=1}^{M} \sigma^{N}_{\mathrm{iH_I}} c N_{\mathrm{i}}\right) - n_{\mathrm{H_{II}}}\alpha^{A}_{\mathrm{H_{II}}} n_{\mathrm{e}} \tag{1.28}$$

$$n_{\mathrm{He}}\frac{\partial x_{\mathrm{He_{II}}}}{\partial t} = n_{\mathrm{He_I}}\left(\beta_{\mathrm{He_I}} n_{\mathrm{e}} + \sum_{\mathrm{i}=1}^{M} \sigma^{N}_{\mathrm{iHe_I}} c N_{\mathrm{i}}\right) + n_{\mathrm{He_{II}}}\alpha^{A}_{\mathrm{He_{III}}} n_{\mathrm{e}} - n_{\mathrm{He_{II}}}\left(\beta_{\mathrm{He_{II}}} n_{\mathrm{e}} + \alpha^{A}_{\mathrm{He_{II}}} n_{\mathrm{e}} + \sum_{\mathrm{i}=1}^{M} \sigma^{N}_{\mathrm{iHe_{II}}} c N_{\mathrm{i}}\right) \tag{1.29}$$

$$n_{\mathrm{He}}\frac{\partial x_{\mathrm{He_{III}}}}{\partial t} = n_{\mathrm{He_{II}}}\left(\beta_{\mathrm{He_{II}}} n_{\mathrm{e}} + \sum_{\mathrm{i}=1}^{M} \sigma^{N}_{\mathrm{iHe_{II}}} c N_{\mathrm{i}}\right) - n_{\mathrm{He_{III}}}\alpha^{A}_{\mathrm{H_{III}}} n_{\mathrm{e}} \tag{1.30}$$

These equations are solved by doing numerical discretization sequentally, using available forward in time values, and the rest set as backwards. This means that the first equations will once again be done semi-implicitly, and the final abundancy equation will be completely implicit.

A final detail worth mentioning on this stage of the RT step, is the fact that thermochemistry is only allowed to be advanced in time if the update of thermal variables does not exceed a 10% change. This is done by subcycling the thermochemical equations inside the RT loop until the change for all relevant variables is bound to a $5\% - 10\%$ change. This is relevant because we want equations being solved sequentially to not introduce too big of a underestimation/overestimation caused as an effect of using backwards/forward in time values in the semi-implicit scheme.

1.2.2.4 The addition of IR multiscattering

One last detail we have not mentioned, and in which we will not go into excessive detail is how the RT equations 1.12-1.13, are actually going to be modified when the i−photon group represents infra-red (IR) radiation. Dust particles can absorb photons from all over the radiation spectrum, but only emit IR photons, which are assumed to be in local thermodynamic equilibrium with the dust particles. This gives IR radiation its status as 'multiscattered' radiation (instead of 'single-scattered'), which at the end means that recombination has to work so that the density for photon groups of higher frequencies diminishes as they get absorbed, and the IR-photon group density gets proportionally bigger.

As a first approximation, this means that for this radiation band, the $\frac{\partial N_{\mathrm{IR}}}{\partial t}$ value needs to have an added factor of

$$\sum_{\mathrm{i}\neq\mathrm{IR}}\sum_{j\in S} b^{\mathrm{rec}}_{\mathrm{i}j}\alpha^{B}_{j} n_{j} n_{\mathrm{e}}$$

The other important fact, is the need to add a coupling between IR radiation density and the gas (dust) temperature, which means substracting a factor proportional to N_{IR} in 1.12. This addition is far from trivial at the time of solving for the evolution, and it adds a further thing to be solved in the thermochemistry step as a last stage which is also solved semi-implicitly.

It is also important to consider that when the optical depth of the local thermodynamic equilibrium becomes unresolved (known as the *diffusion limit*), the numerical diffusion introduced by the M1 solver may be bigger than the true radiation diffusion, and the numerical result becomes inaccurate. The technique that is employed to correct this problem, is to split the energy in IR photon groups between trapped and streaming radiation, where the former is strictly isotropic in angular momentum and corresponds to radiation with vanishing mean free paths (and thus flux is null). the splitting of radiation obeys the simple set of equations

$$E_s = \frac{2}{2+3\tau_c}E, \quad F_s = F$$

$$E_t = \frac{3\tau_c}{2+3\tau_c}E, \quad F_t = 0$$

With which, the Godunov solver can be readily employed with the necessary modifications to the radiation transfer equations in the two photon regimes (see Rosdahl and Teyssier, 2015). Of course this is an extremely basic review, but all of this content is in the forementioned work, and is not too relevant to our work, as IR radiation and dust is not central to our astrophysical context.

1.2.3 Reduced speed of light formalism

Before the RT step is executed, the size of its timestep Δt_{RT} must be determined. Since the method for solving of the equations from 1.2.2 is explicit, the size of such step is constrained by the CFL condition, which states

$$\Delta t_{RT} < \frac{\Delta x}{3c} \tag{1.31}$$

This condition gives timesteps that may typically be over two orders of magnitude shorter than those found in a non-relativistic hydrodynamical simulation. Instead of trying to implement an implicit numerical scheme (which presents problems which are equally or harder to deal with), the approach taken in Rosdahl et al., 2013, is to relax the Courant condition by lowering the speed of light in 1.31 to a value $c_r \ll c$. This c_r is justified in the sense that radiation propagates in a speed limited by the capacity that the ionizing front has (which is of course, much slower in practice), given a specific context, which is what the grid must be able to respond to.

In order to ascertain that the speed c_r is kept faster than the speed of the ionizing front, or more relevant, that changing its value will not affect the evolution of the system by lagging the effects of radiation too much in comparison to the natural dynamics of the setup, the authors from Rosdahl et al., 2013 decide that the speed of light may be reduced by a factor f_c (in the sense that $c_r = f_c c$), which is defined as

$$f_c = \min(1;\, 10 \times t_{cross}/\tau_{sim}) \tag{1.32}$$

Here, the crossing time refers to the time that light takes in order to travel the equivalent distance of the Strömgren radius r_s estimated with values consistent to the setup. The time τ_{sim} is a free parameter that represents the timescales in which the simulation's relevant processes occur. The actual numerical calculation of these parameters is done in 2.4.1

1.2.4 Coupling radiation to hydrodynamics

In order to consistently intertwine the inherent hydrodynamical behaviour of the system, with radiation's capacity to impact it, we have to include the heating, absorption and overall propagation of radiation in our basic hydrodynamical set of equations (1.2,1.3,1.4) throughout our grid. Naturally, this only affects directly the momentum equation 1.3 and the energy equation 1.4, but not the mass continuity equation (the presence of radiation of course does not affect mass continuity in the, making the physically accurate assumption that photons have negligible mass). First the energy conservation equation has to now include the RHS of equation 1.13 (counting the contribution of all photon groups) and and additional factor Λ that represents the cooling and heating via thermochemical processes:

$$\frac{\partial}{\partial t}(\rho \mathrm{e}) + \nabla \cdot [\rho u(\mathrm{e} + p/\rho)] = -\rho u \cdot \nabla\phi + \Lambda(\rho, \mathrm{e}) + \sum_{\mathrm{i}=1}^{M} \sum_{j \in S} n_j \sigma_{\mathrm{i}j}^{N} c F_{\mathrm{i}} \tag{1.33}$$

The factor Λ is just another name for the already mentioned photoheating rate (introduced in 1.25). Having already discussed the numerical solving of these additional terms, the broad strategy to link these, is to solve with an operator splitting strategy, solving in a decoupled manner the radiative terms first, and then directly plugging it as part of the source term S_{n+1}.

In order to accurately model momentum with RHD, equation 1.3 becomes

$$\frac{\partial}{\partial t}(\rho u) + \nabla \cdot (\rho u \otimes u) + \nabla p = -\rho\nabla\phi + \dot{p}_\gamma \tag{1.34}$$

This is the same as the classical one, but with the additional term $\dot{p}_\gamma$, which describes the total local momentum absorbed by gas from all photon groups via all radiation interactions:

$$\dot{p}_\gamma = \sum_{\mathrm{i}=1}^{M} \frac{F_{\mathrm{i}}}{c} \left(\kappa_{\mathrm{i}}\rho + \sum_{j \in S} \sigma_{\mathrm{i}j} n_j \right) \tag{1.35}$$

Once again, momentum transfer is applied with an operator split approach, adding to the gas momentum in each RHD step after the thermochemistry calculation (this is done in every $\sum_k \Delta t_k = \Delta t_{\mathrm{RHD}}$ subcycling, as photon fluxes and densities may change too much over a complete Δt_{RHD} timestep).

1.3 Radiative Cooling

Although RAMSES-RT's cooling method was somewhat described with equations 1.26-1.27, it is a physical process which is both complex and central enough in the following work, for us not to expand a little more on what has already been said. It is relevant to understand the expected loss of thermal energy that stems from radiative processes as it directly affects the disk tendency to fragment, where comparing the cooling timescale with respect to timescales that relate to fluctuations of Toomre's parameter value of the simulation. If ε refers to thermal energy and $\frac{\partial \varepsilon}{\partial t} = \Lambda$ refers to cooling/heating, then the cooling timescale takes the value of:

$$\frac{\varepsilon}{\dot{\varepsilon}} = \frac{\rho k_B T}{m_H(\gamma - 1)\mu} \cdot \frac{1}{\Lambda} \tag{1.36}$$

Taking the usual value of $\gamma = \frac{5}{3}$, we need to determine the values of the mean molecular mass μ and the cooling function Λ. Assuming a primordial gas composition, we may simply calculate the mean molecular mass from

$$\mu = [X(1 + x_{\mathrm{H_{II}}}) + \frac{Y}{4}(1 + x_{\mathrm{He_{II}}} + 2x_{\mathrm{He_{III}}})]^{-1} \tag{1.37}$$

Which in the RAMSES-RT formalism is straightforward, as ion abundances are explicitly calculated in the code. This only leaves the calculation of $\Lambda = \mathcal{H} - \mathcal{L}$ remaining, which from 1.26-1.27 is clear to see that has many different components to take into account. Assuming our gas is well approximated by primordial plasma, we have that the different processes that cool the gas are:

- Collisional excitation, where free electrons when they approach a nucleon with bound electrons, may move these to an excited state, which after decaying, emits a photon.
- Collisional ionization, which happens when free electrons, with an impact, ionize formerly bound electrons, where energy from the free electrons is lost.
- Free electron recombination with ions: the binding energy and the free electron's kinetic energy are radiated away.
- Bremsstrahlung or also called free-free emission. Where free electron when accelerated by ions, emit photons to compensate the energy expense.
- Compton cooling from the microwave background.

As RAMSES-RT gives the abundances of ion species $n_{\mathrm{H_I}}$, $n_{\mathrm{H_{II}}}$, $n_{\mathrm{He_I}}$, $n_{\mathrm{He_{II}}}$, $n_{\mathrm{He_{III}}}$ (and, of course n_{e}), we can use this information in addition to cooling rate recipes that correspond to the processes mentioned (all of which only depend only on temperature). These rates are taken from Cen, 1992 for collisional excitation/ionization, from Hui and Gnedin, 1997, Black, 1981 for recombination rates, Osterbrock and Ferland, 2006 for free-free processes and from Haiman et al., 1996 for Compton cooling. All these cooling rates are summarized in table 1.1:

Process	Species	Cooling rate [erg·s^{-1}·cm^{-3}]
Collisional Ionization	$\mathrm{H_I}$	$1.27\times10^{-21}\ \sqrt{T}\ \left(1+\sqrt{T_5}\right)^{-1}\ \mathrm{e}^{-157\,809.1/T}\cdot n_\mathrm{e}\, n_{\mathrm{H_I}}$
	$\mathrm{He_I}$	$9.38\ \times10^{-22}\ \sqrt{T}\ \left(1+\sqrt{T_5}\right)^{-1}\ \mathrm{e}^{-285\,335.4/T}\cdot n_\mathrm{e}\, n_{\mathrm{He_I}}$
	$\mathrm{He_{II}}$	$4.95\ \times10^{-22}\ \sqrt{T}\ \left(1+\sqrt{T_5}\right)^{-1}\ \mathrm{e}^{-631\,515/T}\cdot n_\mathrm{e}\, n_{\mathrm{He_{II}}}$
Collisional Excitation	$\mathrm{H_I}$	$7.5\times10^{-19}\ \left(1+\sqrt{T_5}\right)^{-1}\ \mathrm{e}^{-118\,348/T}\cdot n_\mathrm{e}\, n_{\mathrm{H_I}}$
	$\mathrm{He_{II}}$	$5.54\times10^{-17}\ T^{-0.397}\left(1+\sqrt{T_5}\right)^{-1}\mathrm{e}^{-473\,638/T}\cdot n_\mathrm{e}\, n_{\mathrm{He_{II}}}$
Recombination	$\mathrm{H_{II}}$	$1.778\times10^{-29}\ T\ \lambda_{\mathrm{H_I}}^{1.965}[1+(\lambda_{\mathrm{H_I}}/0.541)^{0.502}]^{-2.697}\cdot n_\mathrm{e}\, n_{\mathrm{H_{II}}}$
	$\mathrm{He_{II}}$	$3\times10^{-14}\ k_\mathrm{B}\ T\lambda_{\mathrm{He_I}}^{0.654}\cdot n_\mathrm{e}\, n_{\mathrm{He_{II}}}$
	$\mathrm{He_{III}}$	$8\times1.778\times10^{-29}\ T\ \lambda_{\mathrm{He_{II}}}^{1.965}[1+(\lambda_{\mathrm{He_{II}}}/0.541)^{0.502}]^{-2.697}\cdot n_\mathrm{e}\, n_{\mathrm{He_{III}}}$
Dielectric recombination	$\mathrm{He_{II}}$	$1.24\times10^{-13}T^{-1.5}\mathrm{e}^{-470\,000/T}\left(1+0.3\mathrm{e}^{-94\,000/T}\right)\cdot n_\mathrm{e}\, n_{\mathrm{He_{II}}}$
Bremsstrahlung	All	$1.42\times10^{-27}\sqrt{T}\cdot(n_{\mathrm{H_{II}}}+n_{\mathrm{He_{II}}}+4n_{\mathrm{He_{III}}})n_\mathrm{e}$
Compton	None	$5,53\times10^{-36}\ (T-2.727)\cdot n_\mathrm{e}$

Table 1.1: Cooling functions used in RAMSES-RT including all phenomenons the involve ion and electron abundances, which can be traced explicitly in our outputs.

In table 1.1[3], recombination cooling implicitly depends on recombination rate coefficients, which themselves depend on unitless functions:

$$\lambda_{\mathrm{H_I}}(T)=\frac{315\,614\,\mathrm{K}}{T}\ ,\quad \lambda_{\mathrm{He_I}}(T)=\frac{570\,670\,\mathrm{K}}{T}\ ,\quad \lambda_{\mathrm{He_{II}}}(T)=\frac{1263\,030\,\mathrm{K}}{T}$$

Also, the Compton cooling rate from the table, assumes we are working in local universe and redshift is $z=0$. Now, half of our simulations are not done with radiation coupling to hydrodynamics, where ion abundancies are not modelled and other cooling approach is taken. The main cooling module from RAMSES uses the methods described in Katz et al., 1996, which employs the same recipes from 1.1, with a modification for (non-dielectric) recombination cooling, free-free cooling and compton cooling:

---

[3] We employ notation $\mathrm{T}_n = \mathrm{T}/10^n\ K$

Process	Species	Cooling rate [erg·s^{-1}·cm^{-3}]
Recombination	$\mathrm{H_{II}}$	$8.7 \times 10^{-27}\sqrt{T} \cdot T_3^{-0.2}(1 + T_6^{0.7})^{-1} \cdot n_\mathrm{e} n_{\mathrm{H_I}}$
	$\mathrm{He_{II}}$	$1.55 \times 10^{-26} T^{0.3647} \cdot n_\mathrm{e} n_{\mathrm{He_{II}}}$
	$\mathrm{He_{III}}$	$3.48 \times 10^{-26}\sqrt{T} \cdot T_3^{-0.2}(1 + T_6^{0.7})^{-1} \cdot n_\mathrm{e} n_{\mathrm{He_{III}}}$
Bremsstrahlung	All	$1.42 \times 10^{-27} g_\mathrm{ff}\sqrt{T} \cdot (n_{\mathrm{H_{II}}} + n_{\mathrm{He_{II}}} + 4n_{\mathrm{He_{III}}})n_\mathrm{e}$
Compton	None	$5.41 \times 10^{-36} T \cdot n_\mathrm{e}$

Table 1.2: Cooling functions used in RAMSES that differ on the specifications from RT at table 1.1).

While we see some significant changes in recombination cooling rates, free-free emission differs only by a gaunt factor given by $g_\mathrm{ff} = 1.1 + 0.34\exp[-(5.5 - \log T)^2/3.0]$ (which is nearly ≈ 1.1 for temperatures over $10^3\,K$) and Compton cooling (which comes from Ostriker and Ikeuchi, 1983) in our case of $z = 0$, is nearly equivalent as well. The major differences come in the fact that this runs on the hydrodynamics-only version of the code, and since there is no consistent following of ionization states or radiation flux, these have to be taken account for artificially. For this, Katz et al., 1996 cast the following system of equations for the different ionic abundances assuming ionization equilibrium and a specific background of ionizing radiation:

$$
\begin{aligned}
n_{\mathrm{H_I}} &= n_\mathrm{H}\alpha_{\mathrm{H_{II}}}/(\alpha_{\mathrm{H_{II}}} + \Gamma_{\mathrm{eH_I}} + \Gamma_{\gamma\mathrm{H_I}}/n_\mathrm{e}) && (1.38)\\
n_{\mathrm{H_{II}}} &= n_\mathrm{H} - n_{\mathrm{H_I}} && (1.39)\\
n_{\mathrm{He_{II}}} &= y n_\mathrm{H}/[1 + (\alpha_{\mathrm{He_{II}}} + \alpha_\mathrm{d})/(\Gamma_{\mathrm{eHe_I}} + \Gamma_{\gamma\mathrm{He_I}}/n_\mathrm{e}) + (\Gamma_{\mathrm{eHe_{II}}} + \Gamma_{\gamma\mathrm{He_{II}}}/n_\mathrm{e})/\alpha_{\mathrm{He_{III}}}] && (1.40)\\
n_{\mathrm{He_I}} &= n_{\mathrm{He_{II}}}(\alpha_{\mathrm{He_{II}}} + \alpha_\mathrm{d})/(\Gamma_{\mathrm{eHe_I}} + \Gamma_{\gamma\mathrm{He_I}}/n_\mathrm{e}) && (1.41)\\
n_{\mathrm{He_{III}}} &= n_{\mathrm{He_{II}}}(\Gamma_{\mathrm{eHe_{II}}} + \Gamma_{\gamma\mathrm{He_{II}}}/n_\mathrm{e})/\alpha_{\mathrm{He_{III}}} && (1.42)\\
n_\mathrm{e} &= n_{\mathrm{H_{II}}} + n_{\mathrm{He_{II}}} + 2n_{\mathrm{He_{III}}} && (1.43)
\end{aligned}
$$

Having $y = Y/(4-4Y)$ (usually simply taken from the assumed values of $X = 0.76$, $Y = 0.24$ as no precise methods such as equation 1.37 are available) and $\Gamma_{\gamma\bullet}$ as the photoionization rate, in this paradigm $\alpha_\bullet$ which are the recombination rates and $\Gamma_{\mathrm{e}\bullet}$ which are the collisional ionization rates, take the form of functions of temperature, listed from Katz et al., 1996 as:

Parameter	Value
$\alpha_{\mathrm{H_{II}}}$	$8.4\times10^{-11}T^{-1/2}T_3^{-0.2}(1+T_6^{0.7})^{-1}$
$\alpha_{\mathrm{He_{II}}}$	$1.5\times10^{-10}T^{-0.6353}$
$\alpha_{\mathrm{He_{III}}}$	$3.36\times10^{-10}T^{-1/2}T_3^{-0.2}(1+T_6^{0.7})^{-1}$
α_{d}	$1.9\times10^{-3}T^{-1.5}\mathrm{e}^{-470000/T}(1+0.3\mathrm{e}^{-94000/T})$
$\Gamma_{\mathrm{eH_I}}$	$5.85\times10^{-11}T^{1/2}\mathrm{e}^{-157809/T}(1+T_5^{1/2})^{-1}$
$\Gamma_{\mathrm{eHe_I}}$	$2.38\times10^{-11}T^{1/2}\mathrm{e}^{-285335/T}(1+T_5^{1/2})^{-1}$
$\Gamma_{\mathrm{eHe_{II}}}$	$5.68\times10^{-12}T^{1/2}\mathrm{e}^{-631515/T}(1+T_5^{1/2})^{-1}$

Table 1.3: Recombination and Collisional Ionization Rates.

The photoionization rate, is as usual defined by equation

$$\Gamma_{\gamma\mathrm{i}} \equiv \int_{\nu_\mathrm{i}}^{\infty} \frac{4\pi J(\nu)}{h\nu}\sigma_\mathrm{i}(\nu)\,\mathrm{d}\nu\, s^{-1} \tag{1.44}$$

Where $J(\nu)$ is the intensity of the ionizing radiation for frequency ν, and ν_i, $\sigma_\mathrm{i}(\nu)$ are the threshold frequency and cross section for species i. If we assume there is no strong source of photoionizing radiation near our environment (ie: $\Gamma_{\gamma\mathrm{i}} = 0$, $\forall$i), for a fixed temperature and density in the grid, equations 1.38-1.43 take the form of

$$\begin{aligned} n_{\mathrm{H_I}} &= n_H \cdot a_1, & n_{\mathrm{H_{II}}} &= n_H - n_{\mathrm{H_I}} \\ n_{\mathrm{He_{II}}} &= y n_H \cdot a_2, & n_{\mathrm{He_I}} &= n_{\mathrm{He_{II}}} \cdot a_3 \\ n_{\mathrm{He_{III}}} &= n_{\mathrm{He_{II}}} \cdot a_4, & n_\mathrm{e} &= n_{\mathrm{H_{II}}} + n_{\mathrm{He_{II}}} + 2n_{\mathrm{H_{III}}} \end{aligned}$$

Where a_1, a_2, a_3, a_4 are constants found using expressions from table 1.3 that allow us to solve for our six variables sequentially replacing in our six equations (starting with $n_H = \frac{\rho X}{m_H}$). This is true for our simulations without AGN feedback, as there are no ionizing sources/background and cooling on a simulation level should be well approximated by the rates and methods we mentioned.

Now, if we wanted predict the amount of cooling with the methods from Katz et al., 1996 for simulations that include AGN feedback, $J(\nu)$ becomes relevant as the AGN introduces a strong source of ionizing radiation. This is a potentially useful thing to do, but it is not easy, as not only photoheating has to be included and equations 1.38-1.43 become harder to solve with the presence of $J(\nu) \neq 0$, but one also has to make considerations on how the ionizing flux of photons is not constant through the grid and $J(\nu)$ has to be well parametrized to approximate the effect that the binary's radiation has on ionizing the whole disk environment and photoheating. This problem is further discussed in **??**.

1.4 Additional tools

1.4.1 DICE

For the setting up of our simulations we import the initial setups from runs originally made to be run with GADGET. For this we use the initial conditions code package DICE Perret et al., 2014. DICE was originally conceived as a dedicated library for the initialization of astrophysical disk conditions, which are first generated with Lagrangian particles. As the code in its original philosophy already had to convert particles from the Lagrangian framework to the AMR grid, the code was also built so it can read conditions which are originally setup for SPH codes (specifically GADGET) and translate them to the RAMSES grid.

In practice the downside of this ”translation”, is that initialization is far from memory efficient, as the allocation of the Lagrangian components is not as well optimized as initializing our runs from scratch. This means that if a subset of runs are already expected to be memory consuming, measures such as evolving the initial disk without a binary component, and then initializing a run in the form of a RAMSES restart will be more efficient if possible (to do this though, one has to make sure that the disk relaxation does not perturb the outcome of the problem). This is specially relevant when turning the RT module on, as the memory constraints become much bigger.

1.4.2 Sink particle formalism

The sharp contrast of density and spatial scales around a black hole (or in general, regions of gravitational collapse), means that special measures have to be taken in order to deal with the huge dynamic range self-consistently within simulations. For this, RAMSES allows for an approximation small-scale evolution of withing this collapsing regions, treating them as a mixture between an isolated point mass (sink) and a cloud of interacting particles, which are now going to be disconnected to the hydrodynamics of the overall simulation. The first introductions of sink particles were done for SPH codes and it was Bate et al., 1995 who implemented the original version of the algorithms upon which subsequent methods were developed. For AMR, the first implementation came from Krumholz et al., 2004, which was then adapted to codes like ENZO and RAMSES.

The methods RAMSES uses nowadays were refined/developed at Bleuler and Teyssier, 2014. Since we do not create new sinks, the most important features in our treatment of black holes as sink particles, are how trajectories are calculated and how accretion is dealt with. The accretion recipe we are going to use is not native to the code, and it is described in 2.2.

As seen in Lupi et al., 2014, the trajectories of SMBHs are greatly affected by the the resolution and methods in treatment for the sinks. We deal with this issue always choosing the highest level of refinement over the surrounding region at the sink, and using the direct force summation scheme mentioned in Bleuler and Teyssier, 2014. This involves calculating the acceleration due to all possible pairwise interactions between sinks and gas, doing CIC interpolation to locate grid density values that surround the black holes, and applying a Plummer softening of the form

$$F(\vec{r}) = -\vec{r}\frac{GM}{(|r|^2 + R_{\text{soft}}^2)^{3/2}} \tag{1.45}$$

Setting the softening radius to half the accretion radius (with accretion radius we talk about the material eligible to accretion by usual sink-particle standards, not the accretion radius defined by the thresholds we define at 2.2), this implies that sink forces have a resolution of the order of grid spacing (which in this region is set to the maximum level of refining, as already mentioned).

1.4.3 XSPEC and the X-ray spectrum subgrid model generation

As already mentioned, in the RAMSES-RT formalism, for radiation sources, one needs to input an emission SED so that the decision on how to partition the emitted photon energy fractions in different groups can be made in order to solve the binned RT equations. In our case our energy sources are the two black holes we are studying, and the emission spectra has to be consistent with an AGN-type SED in the resolution regime we are working at, and hopefully in good measure, consistent with the systems conditions.

Despite the huge difference in mass, Galactic black holes in binary systems and supermassive black holes in active galactic nuclei have similarly explained emission behaviours, where as being highly massive compact objects, they affect their surrounding material with vast gravitational forces, leading to accretion of large quantities of gas and consequently to the release of large amounts of radiation, mostly in the X-ray band. In particular this X-ray features, in many sources, stem from an emission component, which is generated by high-energy coronal photons that are then reprocessed in an optically thick accretion disk, so that the observer mainly sees reflected hard X-ray emission together with soft X-rays from thermal emission by the disk. Codes that generate spectra by mainly modelling this process (with a lot of additional, quite important factors coming into place), are usually referred as 'disk reflection models' (see eg:Pounds et al., 1990, Ross and Fabian, 1993), models we will be employing in our work.

XPSEC (Arnaud, 1996; we will specifically work through its port to python, PyXspec) is a software designed for spectral-fitting, specifically in the context of X-ray spectrum generation. It acts as a platform in which one can implement, mix and interact with different models for specific X-ray spectrum generation. Between all the models ported to XSPEC we choose to use a mixture between `xillver` (García et al., 2013) as the main tool for modelling the disk reflection spectra, `relconv` (Dauser et al., 2010) to take into account relativistic components and `xstar` (Kallman and Bautista, 2001) to better capture the expected photoionization features.

As we anticipated, we mainly employ the `xillver` when deciding the shape of the spectrum for the energy deposits of the AGN in the different photon bands, we now recount the main ingredients in its functioning. In AGNs the illuminating X-ray continuum is believed to originate through Compton upscattering of thermal photons by electrons in a hot corona or a jet (Haardt and Maraschi, 1993), and is usually characterized by a power-law spectrum of the form

$$F(E) = AE^{\Gamma+1}\exp(-E/E_c) \tag{1.46}$$

Where the photon index values are typically observed to lie in $1.8 \lesssim \Gamma \lesssim 2.2$ (although this can be either closer to 1 or larger than 3 in some extreme cases). The energy cutoff is usually set in the $100 - 300$KeV interval and the amplitude A is chosen as to be consistent with the value of the ionization parameter. This canonical definition of the power law spectrum is slightly modified in `xillver`, where they adopt a broken power law that breaks at lower energies to better account for potential unphysical concentration of photons that occur at steeper spectra ($\Gamma > 2$). The reflection code has to accurately calculate the spectra and features that arise from the irradiation of an optically thick accretion disk that is illuminated by the aforementioned power-law continuum. We recount the main aspects of this calculation, which are fully described in Garcia and Kallman, 2010. If $u(\mu, E, \tau)$ is the energy density of the radiation field (with respect to the normal μ, energy E, and position of the slab which is specified in term of the total optical depth), the we start off with the equation that describes the interaction of radiation with gas in the illuminated atmosphere:

$$\mu^2 \frac{\partial^2 u(\mu, E, \tau)}{\tau^2} = u(\mu, E, \tau) - S(E, \tau) \tag{1.47}$$

The total optical depth is specified using the total opacity χ which includes both scattering and absorption:

$$\mathrm{d}\tau = \chi(E)\mathrm{d}z\,; \quad \chi(E) = \alpha_{\mathrm{kn}}(E) +_a (E) \tag{1.48}$$

The source term $S(E, \tau)$ is given by the ratio of the total emissivity to the total opacity, which can be written as

$$S(E, \tau) = \frac{\alpha_{\mathrm{kn}}(E)}{\chi(E, \tau)} J_c(E, \tau) + \frac{j(E, \tau)}{\chi(E, \tau)} \tag{1.49}$$

where $j(E, \tau)$ is the continuum plus lines emissivity, and $J_c(E, \tau)$ is the Comptonized mean intensity of the radiation field resulting from the convolution,

$$J_c(E, \tau) = \frac{1}{\sigma_{\mathrm{kn}}(E)} \int \mathrm{d}E'\, J(E', \tau)\sigma_{\mathrm{kn}}(E')P(E', E) \tag{1.50}$$

Where $J(E, \tau)$ is the unscatterred mean intensity of the radiation field. The quantity $P(E', E)$ is the probability of a photon with energy E to be Compton scattered to an energy E'. In order to solve for $u(\mu, E, \tau)$, $J_c(E, \tau)$ and $S(E, \tau)$, boundary conditions are needed which are defined at the top of the slab ($\tau = 0$) and at the inner boundary ($\tau = \tau_{\mathrm{max}}$), getting

$$\mu \left[\frac{\partial u(\tau, \mu, E)}{\partial \tau}\right]_0 - u(0, \mu, E) = -\frac{2F_x}{\mu_0}\delta(\mu - \mu_0) \tag{1.51}$$

.

$$\mu \left[\frac{\partial u(\tau, \mu, E)}{\partial \tau}\right]_{\tau_{\mathrm{max}}} + u(\tau_{\mathrm{max}}, \mu, E) = B(T_{\mathrm{disk}}) \tag{1.52}$$

Where F_x is the net flux of the illuminating radiation integrated in the whole energy band. B(T) is the blackbody radiation function which is set to $B(T) = 0$ as it is sufficiently weak compared to the power law incident to the surface. To characterize this models the assumption of constant density allows for the use of the typcal ionization parameter (Tarter et al., 1969) which will be

$$\xi = \frac{4\pi F_x}{n_{\mathrm{e}}} \tag{1.53}$$

The structure of the gas is determined by solving the ionization balance equations for a given gas density and for a particular solution of the radiation field. With this in hand, it is left to the photoionization code `xstar` to solve for temperature, opacity χ and the emissivity $j(E, \tau)$, taking into account emission lines from metals in its calculations. It is important to note that although in our model we are not generating spectra with an angular dependence (as this is used for reproducing the effects of observation of AGNs at an angle), the spectrum has to consider relativistic effects. We specifically explore the effects of the resulting spectrum when varying the BH spin parameter in 2.3.

There are many other factors beyond what we have mentioned, involved in the calculations, but for the sake of brevity we point the reader towards the already mentioned references. The specific list and setting of the model's parameters are specified

Chapter 2

Simulation Setups

2.1 Initial Conditions and Setup

2.1.1 Physical setting-up of the circumbinary disks

As it has been mentioned, the initial conditions used for this work are the same as in VV18, both because they were originally selected as a good sampling to test the effects of radiative feedback in binary evolution, and because it allows for direct comparison with a work done in the same regime but with a different treatment of radiation.

Initially the circumbinary disks are described by a mestel-type density distribution:

$$\rho(R,z) = \begin{cases} \frac{\Sigma_0}{2\,H}\,\frac{1}{R_\mathrm{c}}\cosh^{-2}\left(\frac{z}{H}\right)\ , & R \leq R_\mathrm{c} \\ \frac{\Sigma_0}{2\,H}\,\frac{R_\mathrm{c}}{R^2}\cosh^{-2}\left(\frac{z}{H}\frac{R_\mathrm{c}}{R}\right)\ , & R_\mathrm{c} \leq R \leq R_\mathrm{disk} \end{cases} \tag{2.1}$$

Where we say Mestel-like, in the sense that the superficial density for $R \in [R_c,\ R_{\mathrm{disk}]}$ gets to be $\Sigma(R) \propto R^{-1}$ when integrating the vertical component out (although in the inner region $R \leq R_c$, the profile is defined in such a way that the superficial density is set to be constant).

This disks are embedded in a potential field that imitates the presence of a central stellar bulge, which serves both to stabilize the gaseous disk and potentially to better understand the dynamics of gas outflows from the disk. This is done by adding a fixed additional analytic density source term to the Poisson equation 1.1 that takes the form of an usual Plummer density profile (Plummer, 1911):

$$\rho(r)_\mathrm{bulge} = \frac{3M_\mathrm{bulge}}{4a^3}\left(1+\frac{r^2}{a^2}\right)^{-5/2} \tag{2.2}$$

The actual numerical values of the parameters in these profiles are specified in 2.4. Even though we define a strictly analytic recipe for disk initialization, the potential field of the system including the bulge-disk-binary is strongly non-axisymmetric, which means there is no good a-priori definition for the circular velocity of the binary-disk system. To cope with this, the binary is first approximated with a spherical mass distribution (of a radius equal to the initial binary separation a_{bin} that is going to be used), and the system is relaxed for about ~ 30 orbits. Additional information about the selection of a homogeneous spherical potential can be seen in VE12. After this relaxation the circular velocity is taken from the gas average square velocity of the gas inside a cylinder of radius $a_{\text{bin}}/2$ and height $a_{\text{bin}}/50$. This relaxation process was done previously with GADGET, and is ported to RAMSES through DICE from the work in VV18, as to follow the initial conditions as consistently as possible. It has to be noted that while the initial disk state is that of an analytic profile, after the relaxation process that has been described, the memory of said profile is lost.

Before we go into the more specific details of the initial physical conditions/constraints of our problem, it is worth mentioning that in order to isolate the influence of radiation, there are some simplifications done, that are not going to be mentioned in the following section. The mass ratio for the binaries will always be $q = 1$, the initial velocities of the binary will not try to take into account any eccentricity, and its rotation will be prograde and coplanar to the gas it is embedded on.

2.1.2 Selection of the binary-disk configurations

The idea behind the selection of the disk+binary setup selections, is to contrast simulations where tidal cavities are formed by purely hydrodynamical effects and simulations where a tidal gap is not expected to emerge naturally, and afterwards test how in this two different regimes, the appearance of quasar feedback suppresses or facilitates orbit decay.

When asking about the tidal cavity opening tendencies of the setup, we refer to the gap opening criterion from VE12, which is basically a parametrization of the ratio between the timescale for opening a cavity by the angular momentum exchange between the binary and the circumbinary disk, and the timescale in which viscous diffusion operates when filling such gap:

$$\frac{\Delta t_{\text{open}}}{\Delta t_{\text{close}}} = \frac{1}{0.33}\left(\frac{v}{v_{\text{bin}}}\right)^2\left(\frac{c_s}{v}\right)\left(\frac{h}{a_{\text{bin}}}\right) \tag{2.3}$$

Here v and v_{bin} are the binary-disk and the binary's keplerian velocity respectively, c_s is the sound speed of the gas, a_{bin} is the binary separation and h is the scale height of the disk. The idea is that when 2.3 has a value ≤ 1, the tendency that diffusion has of filling space overtakes the gap opening strength that the system has, this means that in practice, the selection process for gap generating setups will be done by seeing setups that fall in the phase space

$$\frac{1}{0.33}\left(\frac{c_s}{v}\right)\left(\frac{h}{a_{\text{bin}}}\right) \leq \left(\frac{v_{\text{bin}}}{v}\right)^2 \tag{2.4}$$

Another consideration taken, is to set systems which are stable to self gravity, as the disk clumpyness could have effects on the binary dynamics which could be hard to distinguish with the radiative feedback effects. To cope with this uncertainty we recall Toomre's stability parameter Q for self gravitating rotating disks Toomre, 1964

$$Q = \frac{c_s \kappa}{\pi \Sigma G} \tag{2.5}$$

Using the usual dispersion relation for the epicyclic frequency $\kappa^2 = 4\Omega^2 + \Omega r(\mathrm{d}\Omega/\mathrm{d}r)$ at $r = a_{bin}$, VV18 showed that

$$\kappa^2 = \frac{v^2}{a_{\mathrm{bin}}^2 \pi^2}(8\pi + [5f - 3] - 6)\,; \quad f = 1 + \frac{M_{bulge}(< a_{\mathrm{bin}})}{M_{\mathrm{bin}}} \approx 1.1 \tag{2.6}$$

And with this in hand the Toomre criterion at $Q = 1$ can be approximated (using estimates for Σ and $M_{bulge}(< a_{bin})$) in parameter space $\left((v_{\mathrm{bin}}/v)^2, (c_s/v)\,(h/a_{\mathrm{bin}})\right) =: (x, y)$, through the functional form

$$y \approx \frac{2\pi^2 a_{bin}}{h} \frac{(1 - 1.1x)^2}{(4\pi - 3) + 1.25x} \tag{2.7}$$

This parametric form of the Toomre parameter is useful for defining the analytic curve used to somewhat-coarsely separate stable setups, but in practice when we want to profile Q for our simulations we will evaluate directly the values for Σ and c_s, and for the epicyclic frequency we will use equation 2.6 (but evaluating f instead of using the ≈ 1.1 approximation). We note that as the bulge follows a Plummer profile, $M_{bulge}(< a_{bin})$, has an analytic expression:

$$M_{bulge}(< a_{\mathrm{bin}}) = 4\pi \int_0^{a_{\mathrm{bin}}} r^2 \rho_{plum}(r)\,\mathrm{d}r = M_{bulge} \frac{a_{\mathrm{bin}}^3}{(a_{\mathrm{bin}}^2 + a^2)^{3/2}} \tag{2.8}$$

The simultaneous parametrization of the gap opening and stability criterion is summarized in the following graph from VV18:

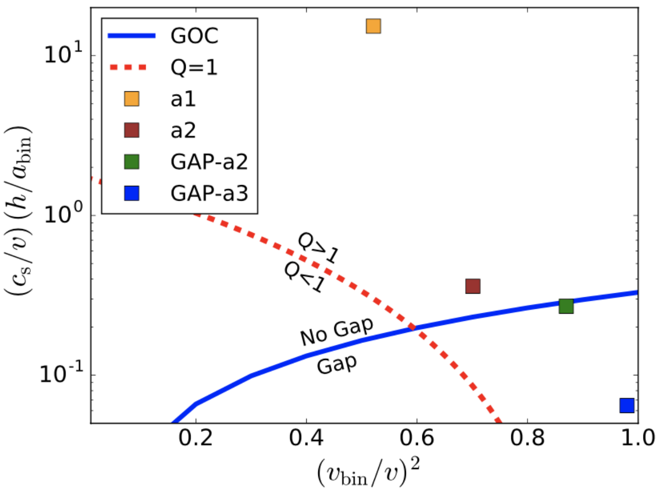

Figure 2.1: Initial conditions and where they figure in terms of their cavity-opening tendency and the gas stability against gravity

The thresholds are overlaid with the four actual setups we use, where we see two conditions which will not form gaps naturally and two that will not. Beyond these constraints, we will elaborate more on some of the actual values (disk mass, binary mass, etc.) these conditions take, at section 2.4.

2.2 Accretion

The most commonly used sub-grid recipe for accretion is the Bondi-Hoyle model (Bondi and Hoyle, 1944, Bondi, 1952). This is proper when dealing with larger-scale dynamics or generally in simulations where spherically-symmetric accretion is not a bad approximation and the resolution near the sink is big compared to the Bondi radius that characterizes the model scale.

Now going beyond the fact that in our problem disk structure is of course resolved (and therefore a spherical flow into the sink stops being a good approximation), the quoted value for the characteristic radius scale is given by $r_{acc} = \frac{2GM}{c_s(\infty)} \simeq 3\times 10^{14}\left(\frac{M}{M_\odot}\right)\left(\frac{10^4 K}{T(\infty)}\right)$. If we use a Mestel distribution temperature of $T = 2\times 10^4 K$, and consider the range of masses for the binaries that appear in our simulations, we would get values up to $r_{acc} \sim 50pc$, which would be above the size of the binary + disk system, and of course way over the resolution of the simulation.

To cope with this, we define a version of threshold accretion similar to the one originally implemented in Bleuler and Teyssier, 2014, but with additional checks that are consistent with the relatively resolved thin-disk accretion regime we are dealing with. The gas inside the threshold defined by the sink particle cloud will be accreted if its specific angular momentum falls below the value that characterizes a circular orbit for the biggest Shakura Sunyaev disk that is stable against self-gravity. This specific angular momentum threshold is set by the value $l_{thr} = \sqrt{GMR_\mathrm{d}}$, where R_d is the size of disk we use for said threshold, where we quote the formula from Kolykhalov and Syunyaev, 1980:

$$R_\mathrm{d} = 3R_g r_\mathrm{d} \approx 2.64R_g(\alpha\dot{m}^2 r_0^{1/2} ct/R_g)^{1/4}$$

With $R_g = \frac{2GM}{c^2}$ being the Schwarzschild radius. For $\dot{m}$ we assume (at least initially) an upper limit set by the Eddington accretion rate $\dot{m} = \theta\dot{m}_\mathrm{edd}$ (with $\theta \in [0, 1]$ set depending on how conservative one wants to be with this bound), where $\dot{m}_\mathrm{edd}$ is given by

$$\dot{m}_\mathrm{edd} = \frac{L_\mathrm{edd}}{\varepsilon_r c^2} = \frac{4\pi GMm_p}{\varepsilon_r c\sigma_T} = \frac{M}{t_s}$$

Where the Salpeter time would take a value of $t_s \simeq 45\varepsilon_{0.1}$ Myr $= 45$ Myr for a radiative efficiency of $\varepsilon_r = 0.1$ (Shakura and Sunyaev, 1973), which is a commonly assumed nominal value, but our simulations have lower radiative efficiency (which is more consistent with our BH masses, see 2.3.2), bringing the Salpeter timescale down and the Eddington accretion upwards. If we quote the values of $\alpha = 1$, $r_0 = 9$, $t = 10^7$ yr from Kolykhalov and Syunyaev, 1980, we can readily calculate R_d.

For a $M_{sink} = 5 \cdot 10^3\ M_\odot$ the radius comes out as $R_\mathrm{d} = 1.57 \times 10^{-7}$ pc, which in turn makes for a threshold specific angular momentum value of $l_{thr} = 2.507 \times 10^{20}\ \frac{\mathrm{cm}^2}{\mathrm{s}}$. At the same time, for a $M_{sink} = 5 \times 10^5 M_\odot$, we get $R_\mathrm{d} = 9.7 \times 10^{-3}$pc and its associated threshold is $l_{thr} = 1.41 \times 10^{24}\ \frac{\mathrm{cm}^2}{\mathrm{s}}$. All the pertinent values for accretions are tabulated at table 2.3.

Now in order to get more consistency along the simulation, the rate that is used inside the calculation for R_d, can be set to be actual accretion previously outputted by the simulation (after the initial estimation, where no $\dot{m}$ candidate has been determined). This means that $m^\mathrm{i+1}_{sink} = m^\mathrm{i}_{sink} + \Delta t\dot{m}^\mathrm{i}_{thr}$, where m^i_{thr} depends on l^i_{thr}, where the threshold instead of being a fixed value, it will depend on

$$R^\mathrm{i}_\mathrm{d} = 2.64R^\mathrm{i}_g(\alpha\dot{m}_\mathrm{i}{}^2 r_0^{1/2} ct/R^\mathrm{i}_g)^{1/4}\ ;\ \ \dot{m}_\mathrm{i} = \begin{cases} \theta\dot{m}_\mathrm{edd} & \mathit{if}\ \mathrm{i} = 0 \\ \dot{m}^{\mathrm{i}-1}_{thr} & \mathit{if}\ \mathrm{i} > 0 \end{cases} \tag{2.9}$$

Notice here the distinction: $\dot{m}_\mathrm{i}$ is the rate used in 2.9 to estimate the threshold value used for determining $\dot{m}^\mathrm{i}_{thr}$, which is the resulting accretion rate at snapshot i.

2.3 Radiation Sources

2.3.1 Shape of the AGN spectrum

We already mentioned how RAMSES-RT deposits radiation on different photon energy bins depending on an adopted spectrum for radiation sources. Now, in the main implementation of the code, stellar radiation sources can have varying SEDs that will allow for a more consistent modelling of evolving stellar populations (in practice the different SEDs are binned in age groups and metallicity contents). Otherwise, in the main version of the code, the energy binning of radiation is assumed to be fixed for sources that are not stars. We modified the code in order to be able to use an AGN-type radiation source for the SMBH feedback, but with an evolving SED as in the case of star sources of radiation. in 1.4.3 we mentioned how we use the `xillver, relconv` and `xstar` models in conjunction to generate the relevant spectra, and how the model templates generated by these codes depend in several parameters, which means we have the opportunity to adjust the generation of said SEDs, binning them for different relevant values we can track in the actual simulation state. We should first begin by specifying which parameters will be fixed for the SED template generation.

- The first fixed parameter will be the emissivity index (see equation 1.49) in the coronal model, which is set as $= 3$ (for both indices), as to be consistent with a classical $\alpha-$disk model.

- Secondly we specify the inner and outer radius of the disk, the reflection model takes. The inner radius, as is usual, is taken as the ISCO value for the given simulation, and the outer radius is taken as R_{d}^{0} from 2.9. This could be set up in such a way that the outer radius follow the $R_{\mathrm{d}}^{\mathrm{i}}$ evolution in time, but in practice the changes for the size of the disk are not big enough to be worth the trouble that generating this new axis of spectrum variation would entail, as the energy deposition will change very little.

- Next we adopt a black hole spin parameter of $a = 0.25$ or $a = -0.25$ for counter-rotating black hole (notice here the slight abuse of notation, a in this context is not the binary separation, and is momentarily employed as to be consistent with the nomenclature at `xillver`, whereas in chapter 4, χ will be used instead), as per the results from King et al., 2008. Even though in practice we will use said values, we show results of how varying the spin parameter affect the SEDs in figure 2.2, and see how only for very high values, the changes become really relevant, as the deposition in low energy photons becomes quite more prominent in the spectrum, for a parameters nearing 1. The value for spin magnitude of our black holes and how it evolves will be a major point of discussion at chapter **??**

- The metal abundancy is set to low values $A_{Fe} = 0.5 - 1$, as to be conservative (this is consistent with the initial set state of metallicity in the simulations variables, which is equal to $Z = 1\,Z_{\odot}$ across the CMD's). Modifying this value strengthens/weakens metal lines from the subgrid recipe and is not a primary factor of change in the spectra. Another "second-order" effecting parameter would be the energy cutoff E_{cut} for the power-law component of the spectrum, which is set to be $E_{cut} = 300$[Kev], value consistent with models such as the ones from Ross and Fabian, 2005 for quasar spectrum fittings.

- As these are models used for modelling the predicted **observed** spectra, there are parameters that can be skipped, such as the redshift and angle parameters. Other parameters like the column density for the `xstar` opacity calculations the limb darkening setting and the reflection fraction, are also defaulted accordingly or have negligible effects on the overall distribution of energy.

This would leave only the ionization parameter $\log(\xi)$ and the Γ factor, as to be parameters to be evolved through the simulation state.

Before moving on to see how the template spectra would look like after moving such values, we see how the spin parameter affects the spectrum for typical values on the spectrum calculation: Here we see indeed how only for values that near $a > 0.9$, relativistic effects from broadening of the spectrum become relevant. This reinforces the idea that adopting the conservative fixed spin values already mentioned would be the correct decision, specially considering that such high spin parameter values for our black holes would be unlikely, and the fact that our simulation is not meant to capture relativistic effects, would mean that trying to capture changes in the spin-parameter through, for example, the accreted angular momentum of the SMBHs, would not be really consistent. One last detail to be addressed would be the distinction of adopting a spectrum for a rotating/counter-rotating SMBH, which we will now see does not really make a big difference when already assuming $a \sim 0.25$

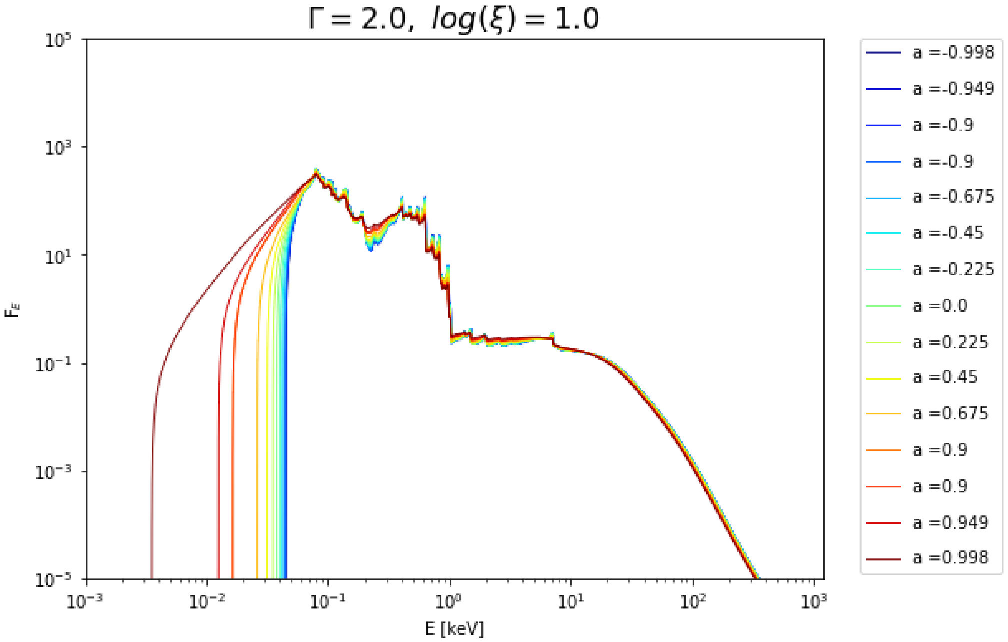

Figure 2.2: Electromagnetic emission spectrum for BHs with power law index $\Gamma = 2.0$, ionization parameter $\log(\xi) = 1.0$ and varying spin parameters in $a \in [-0.998, 0.998]$

We now consider the variation of the Γ parameter for the spectrum generation. We advocate following the evolution of the Γ parameter through asking the total x-ray luminosity L_X from the source (scaled Eddington luminosity units), which in turn is estimated through the measured accretion from the simulation (assuming a fixed radiative efficiency $\varepsilon_r = 0.1$, which for relatively medium-high accretion is a good approximation). For this we use the empirical relationship from Yang et al., 2015, which reads:

$$\Gamma = (0.31 \pm 0.01)\log_{10}(L_x/L_{\text{Edd}}) + (2.48 \pm 0.02), \quad \forall \left(\frac{L_x}{L_{\text{Edd}}}\right) \geq 1\% \tag{2.10}$$

$$\Gamma = (-0.1 \pm 0.02)\log_{10}(L_x/L_{\text{Edd}}) + (1.27 \pm 0.03) \qquad \sim \tag{2.11}$$

With this relation in hand, we tabulated the binned spectra for 10 different luminosity fractions, for both a rotating and a counter-rotating SMBH, first in energy scaled form

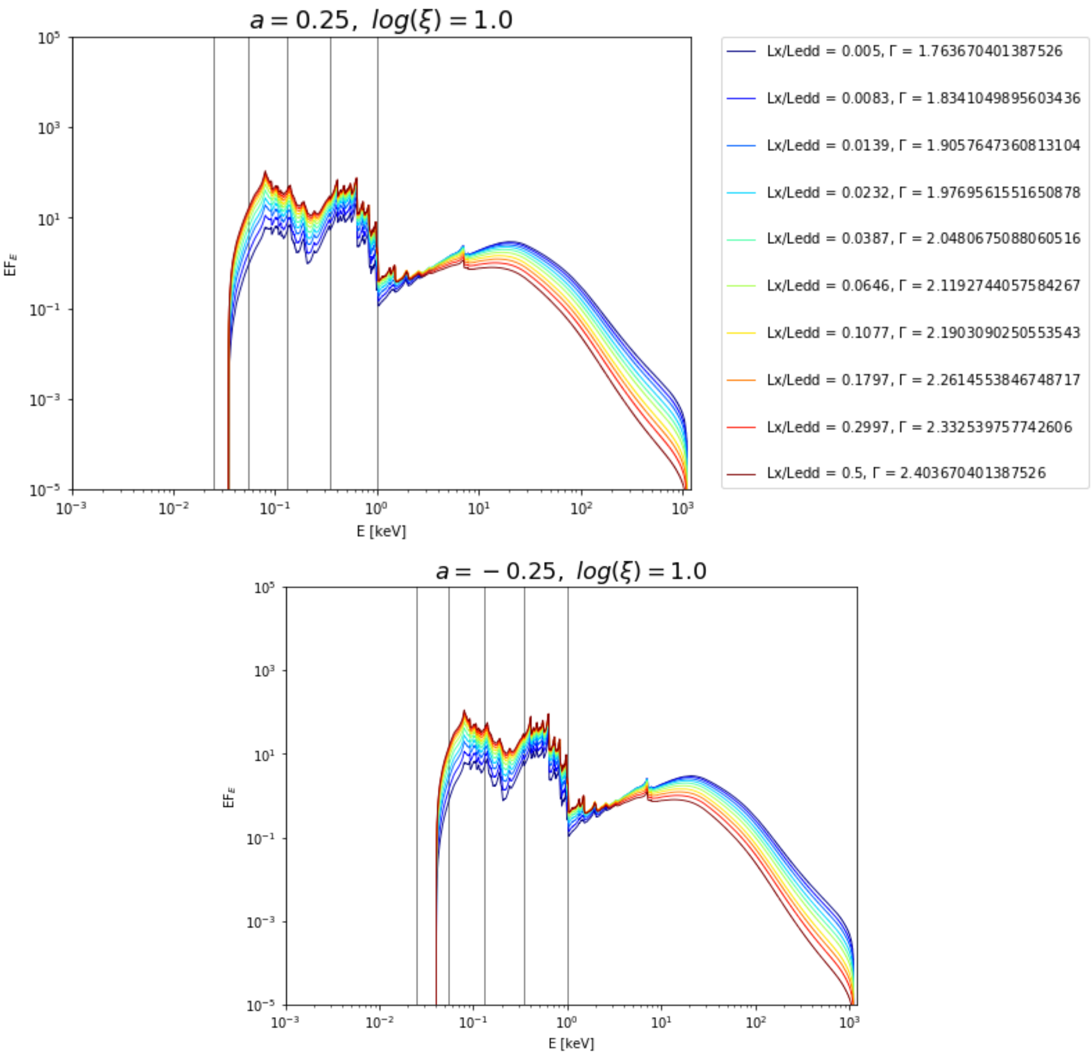

Figure 2.3: Spectra in $E \cdot F(E)$ form. for $\Gamma \in [1.76,\ 2.4]$

And the pure spectra:

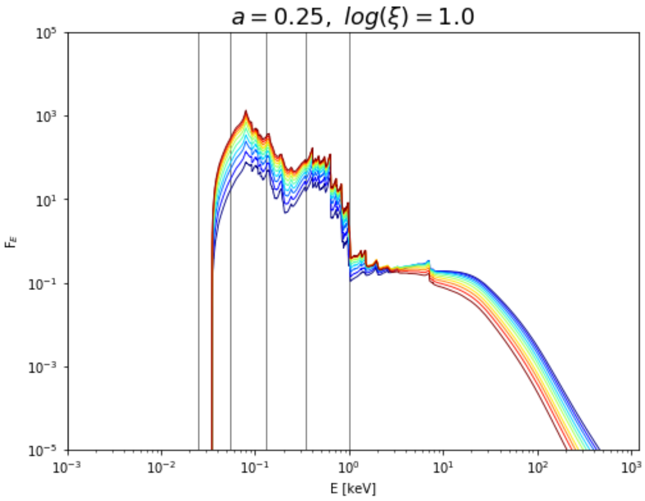

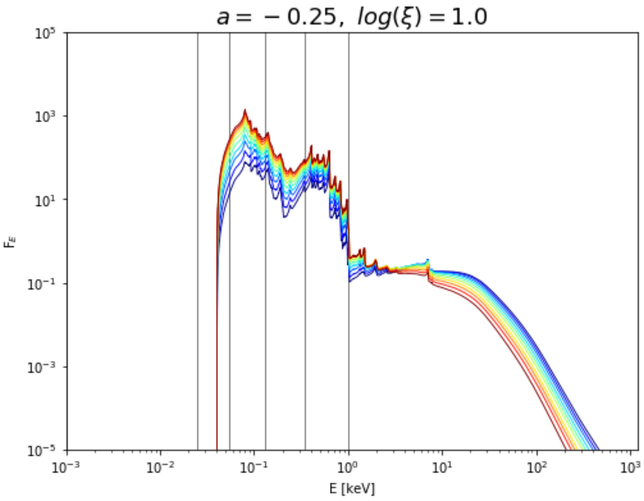

Before anything, the first takeaway is how choosing between $a = \pm 0.25$ is not relevant, as the spectra look basically similar (independently of the variable parameter), so from hereafter, we will assume the SMBHs corrotate with the accreting flow. Looking at $EF(E)$ the spectra (which are good for visualizing the actual energy distribution, as more energetic photons will have a heavier weight when deciding the energy percentages when distributing) we notice how for lower accretion, after the Compton bump (at around and above $2-10$Kev) there is a bigger fraction of energy in the hard x-ray band compared to the higher fraction of energy in the soft x-rays for the higher accretion rates. Whilst is not the aim of the model to capture spectral features that stem from jet geometry that would arise at lower accretion rates, a higher rate of emission from hard x-rays is at least partially consistent with this regime (see for instance Markoff et al., 2005). For effective measures the graphs can be taken to be tabulated in semi-arbitrary units, as the flux geometry is what ultimately matters for the code. The overlaid vertical lines indicate where the energy groups from 2.3.2 would be.

We next see how for a fixed Γ power-law index parameter (see section see section 1.4.3, equation 1.46), the spectral distributions change with a varying $\log(\xi)$ (equation 1.53):

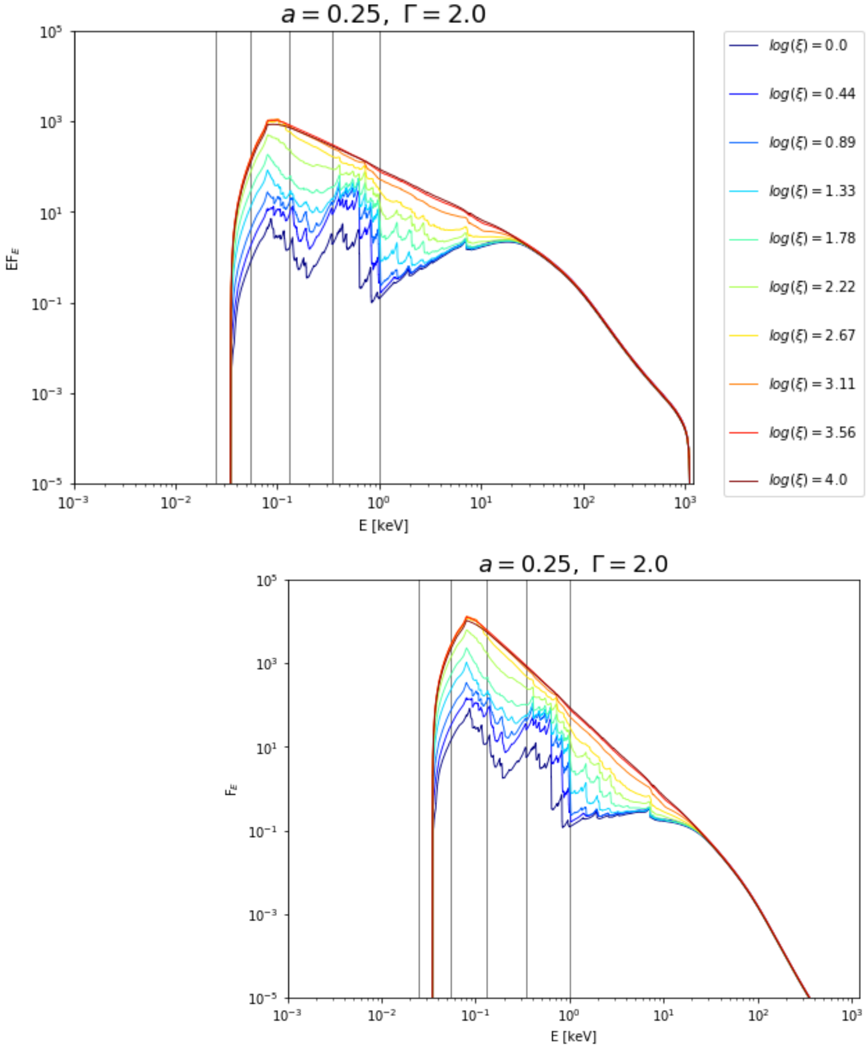

Figure 2.5: Both $E \cdot F$ and pure spectra for spin parameter of $a = 0.25$, power-law index $\Gamma = 2.0$ and variable ionization parameter $\log(\xi) \in [0,\ 4]$

We see a big impact with the variation of this parameter in the overall shape of the spectrum. Line features are more prominent with lower values of $\log(\xi)$, getting up to the point of getting a very smooth distribution for values nearing the upper model limit of 4. To determine the ionization index from the simulation state, we use the fact that RT-enabled simulations track the electron number density, and as such, we only need the X-ray flux from the AGN to recover the needed value from equation 1.53, which we do by modifying the formula to:

$$\xi = \frac{4\pi F_x}{n_\mathrm{e}} = \frac{4\pi}{n_\mathrm{e}} \frac{L_x}{4\pi r_\mathrm{sink}^2} = \frac{L_x}{n_\mathrm{e} r_\mathrm{sink}^2}$$

Since the cross-correlation of Γ and $\log(\xi)$ is big, we create the varying SED grid from binning at the $\Gamma \in [1.5, 2.5]$ and $\xi \in [0, 4]$ intervals. Note that for both of these, we get the energy fraction of the X-ray photons L_x directly from the spectrum emission we are assuming implicitly, meaning that when going from t_{nn+1}, we need a spectrum shape depending on Γ_n, ξ_n to estimate Γ_{n+1}, ξ_{n+1}). Generally for quick calculations, assuming the x-ray fraction is 50% of the total emitted feedback flux is a good approximation. We display all the graphs for our binned template spectra at appendix 5.2, and we also (painstakingly) list all the energy fractions for the different photon groups excluding IR (which is always 0) along with the energy-weighted cross sections to ionization by $\mathrm{H_I}$, $\mathrm{He_I}$, and $\mathrm{He_I}$I.

Before we mention how the simulation-relevant values in terms of 'which' and 'how-many' photons will be introduced from the simulation from feedback, we mention how in past implementations of AGN sources in the RAMSES code, the fixed adopted SED has been taken from the Sazonov et al., 2004 analytic description of a statistically determined quasar characteristic spectrum (see eg: Bieri et al., 2017; Cielo et al., 2018; Trebitsch et al., 2018). This models has its merits but is suitable for setups that do not resolve the inner parsec scales we are dealing with (the setups have to resolve up to scales comparable to those of the instruments used for determining the quasar sample used originally), and as such, the spectrum has to possess the relevant features for the reprocessed radiation from the gas that surrounds the quasar in question. Plus the statistical determination means there will be an overestimation of spectral features from active nuclei with lower accretion setups, which would introduce inconsistencies with our model.

2.3.2 Deposition of energy from the AGN feedback

As we already have mentioned, the sink particles used to model our black-holes will also be used as the sources of radiation, acting as isotropic emitters that radiate in proportion to the expected luminosity that arises from the accretion. The feedback model also incorporates a mechanical feedback fraction characteristic from jet generation after a certain lower threshold of accretion is violated (with a proportion of energy going to the jet generation and a proportion going to luminosity and radiative feedback). This threshold is usually set at accretion rates characteristic for ADAF-type regimes at $\sim 1\% - 0.1\%$ the Eddington rate (see for example Yuan and Narayan, 2014)

Usually the selection of energy groups is done as to capture the spectrum in a well rounded manner depending on the context, and to follow the S ion cross-sections correctly. For instance let us look at the binning scheme of works done with Sazonovs' template spectra (we refer again to eg: Bieri et al., 2017):

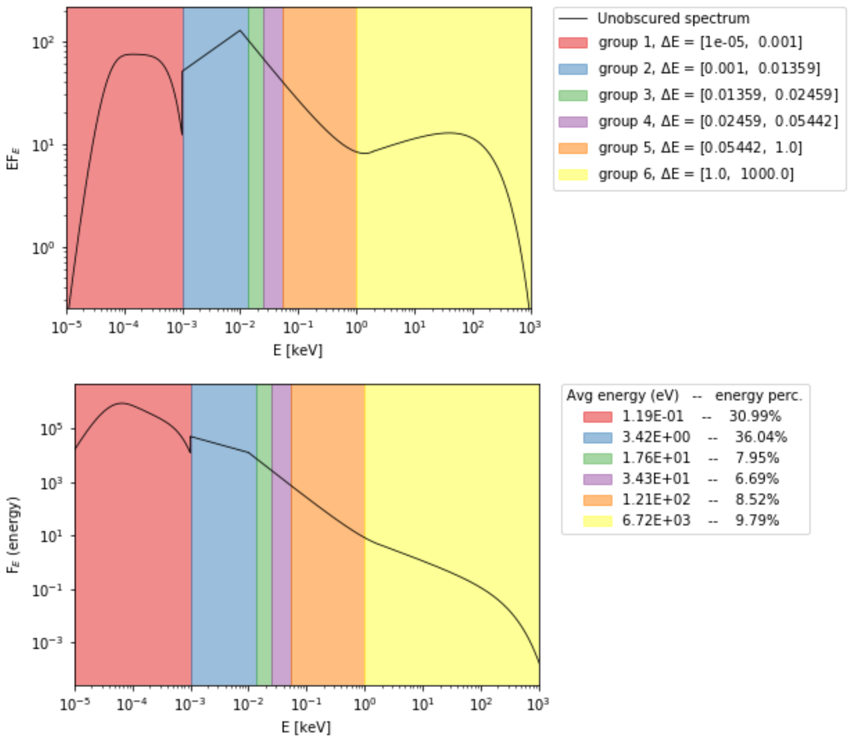

Figure 2.6: Sazonov's AGN template emission spectrum separated in 5 different photon bands

As a contrast to our presented SEDs, these spectra as we advanced in the beginning of this section, have a big optical/IR presence, which makes it more pressing to make photon groups that capture the dynamics of that part of the spectrum radiation, and less pressing to capture and trace the x-rays that come from the sources' emission (even though we list here the properties of a bin for $E > 10^3$KeV, the hard x-ray photons were not modelled in the original work). At the same time the energy groups boundaries align with the cross-section functions as used in the RT calculations (see equation 1.15):

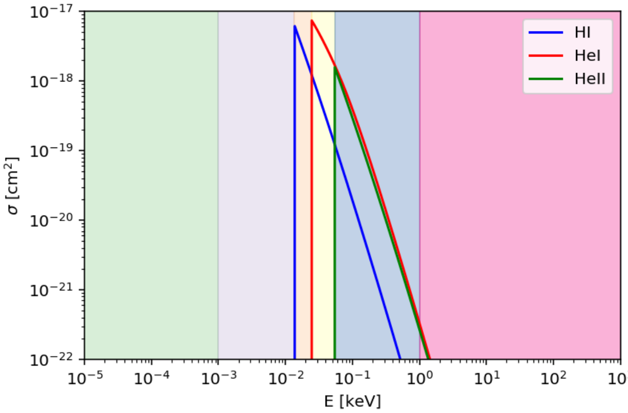

Figure 2.7: Cross-sections for Hydrogen/Helium species following the formulae from Verner et al., 1996

Now, as expected, the spectra we are going to be using are much less broad and have no presence in lower frequency bins, this makes it so that modelling lower frequency photon groups has less importance, as it would only serve to capture reprocessed energy that emerges in time from the gas interacting with the actual radiation sources. The high intensity of the x-ray flux also makes it relevant to have a higher partition for high-energy groups. An example of spectrum taken with typical Γ and $\log(\xi)$ parameters will look like (the complete set of spectrums is at appendix 5.2):

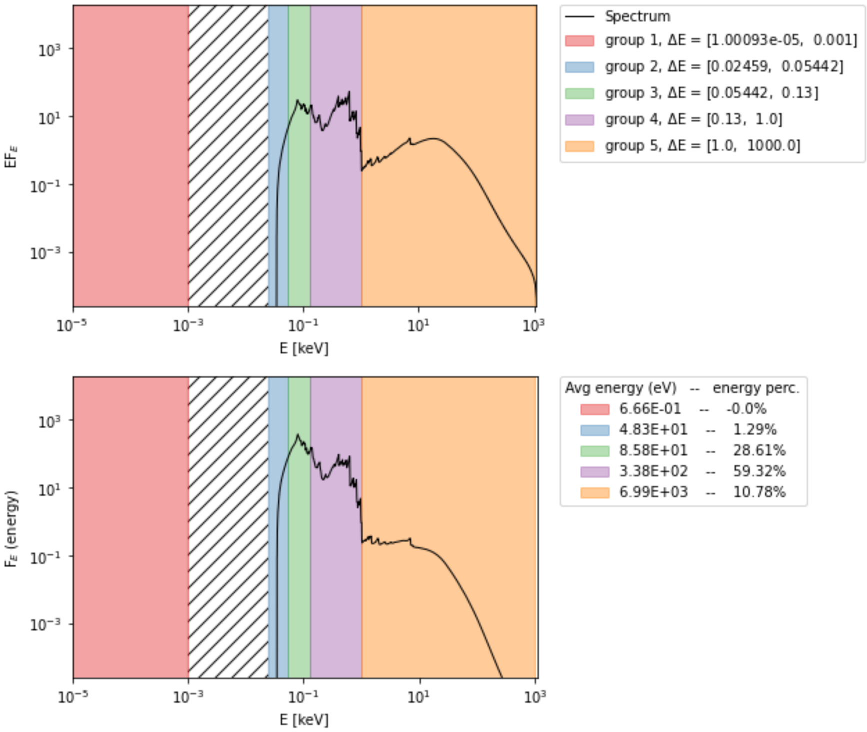

Figure 2.8: Example spectrum generated with $\Gamma = 2 \wedge \log(\xi) = 1$, where we delineate explicitly the different groups and how the energy is allocated between them

Where the overlaid energy groups were chosen as a compromise between capturing the species' cross sections, and balancing the energy fractions through the spectral features observed in our distribution. Even though the AGN does not release energy in the lower frequency bands, we choose to have one IR energy bin in order to capture the energy released by reprocessed radiation, and to skip the optical band of photons (if the low energy bin was to be prolonged to the optical portion, we would have unrealistically energetic reprocessed radiation). Beyond this IR bin, we have two UV groups that align with the peak of the cross-section functions of our Helium species, one energy bin that models soft x-ray radiation ($E \sim 0.28 - 0.53$ KeV) and one energy bin corresponding to the hard x-ray radiation Compton hump ($E > 5 - 10$ KeV). It is worth noting that the decision of using 5 groups, is motivated by memory/computational restrictions. To summarize, the physical parameters that characterize our frequency bands (and are independent of the spectrum's shape), are the following:

Photon group	E_{min} (eV)	E_{max} (eV)	$\overline{\kappa}$ (cm^2g^{-1})	κ_{sc} (cm^2g^{-1})
IR	0.01	1	0	1
UV_1	24.6	54.4	10^3	0
UV_2	54.4	130	10^3	0
Soft X-ray	130	10^3	10^3	0
Hard X-ray	10^3	10^6	10^3	0

Table 2.1: Properties of the photon groups used in the simulations. Columns are name; minimum and maximum energies; dust absorption opacity (Planck); dust scattering opacity (Rosseland)

As already mentioned, the spectrum-dependant values that apply for our different photon groups, which include the fraction of energy of the AGN that is outputted at said group, and the ionization cross-sections for our three atomic species, are tabulated at 5.2.

Having the spectral distributions of the AGN energy deposition established, the code first asks how much luminosity is generated by the usual conversion

$$L_{\text{bol}} = \varepsilon_f \eta \dot{M} c^2 \tag{2.12}$$

Where we use the classical value of radiative efficiency $\eta = 0.1$ and an energy coupling efficiency of $\varepsilon_f = 1$. We choose this values as the resolution of the accretion flow is good enough to merit using an uncorrected value of radiative efficiency, and we assume that the coupling efficiency should be in principle taken into account for, by the RT-framework (as the coupling of the feedback to the gas is done through the photons which are consistently evolved in the simulation). At this point, the code injects photons from each established group at the location of the sink particle's cloud using the group's energy δE_{i} and the deposited percentage from the spectrum χ_{i}, giving a photon injection at each subcycling timestep of

$$\Delta N_{\text{i}} = 0.1 c^2 \Delta M \cdot \frac{\chi_{\text{i}}}{\delta E_{\text{i}}} \tag{2.13}$$

In many cases the selection of these values is not clear cut, as it has shown inconsistencies at worse resolutions. Models that implement direct thermal energy injection as a form of AGN feedback, do not have an universal set value for $\varepsilon_f \cdot \eta$, and suffer when trying to reproduce scaling relations depending on the context of the simulation (see eg: Thacker et al., 2014). Different values have been set and tried for simulations, for instance: Prieto et al., 2021 used the same adjustable prescription as us for a galactic merger simulation and found that the effects of feedback were overestimated. In Volonteri et al., 2015 they set $\varepsilon_f = 0.001$ and $\eta = 0.1$ also for galactic merger simulations, but the value was calibrated manually to reproduce the $M - \sigma$ relation. In cosmological simulations Teyssier et al., 2011 used $\varepsilon_f = 0.15$, which was also $M - \sigma$ calibrated. As uses of RAMSES-RT to model AGN feedback have been limited, there is not a broad testing on how scaling relationships are fulfilled depending on $\varepsilon_f \cdot \eta$, and to the author's knowledge, only galactic-scale simulations have been done (Bieri et al., 2017, Cielo et al., 2018), using the canonical $\eta = 0.1$ and ignoring any coupling efficiency parameter ($\varepsilon_f = 1$).

2.4 Simulation parameter Specifications

All of our circumnuclear disks are initialized having a $R_{disk} = 45\text{pc}$ radius, $H = 5\text{pc}$ and a homogeneous distribution temperature of 2×10^4 K. The external potential contribution by the stellar bulge is modeled by the potential that arises from 2.2, with a Plummer length scale of $a = 65\text{pc}$ and a M_{bulge} consistent with the SMBH-bulge mass relation from equation 1 mentioned at the beginning of this document (Häring and Rix, 2004).

The simulation box domain for all our runs, has a 260pc length, which is chosen to be big enough (four times the Plummer radius) to better capture the dynamics of the material that could end up being launched from the disks. The AMR refinement is set to go from a minimum level of $l_{\text{min}} = 7$ up to $l_{\text{max}} = 16$, which gives a minimum resolution of $\sim$ 4pc and a maximum attainable resolution of $\sim$ 0.008pc on the highest grid partition levels.

The first grid refinement criteria we use, is the typical semi-lagrangian refinement scheme of setting density thresholds for each level, where we focus on getting the disk in its initial stage, at least at $l = 9 - 10$ in its outskirts. The following refinement criteria, is to always maintain the sinks and their immediate environments (modelled by the sink cloud particles) at a maximum resolution independent of gas density, as to avoid problems that may arise when resolving the BH dynamics and gravitational influence (Lupi et al., 2014), and for our accretion computation (this maximally resolved sink idea is already implemented from Bleuler and Teyssier, 2014). The usual requirement from Truelove et al., 1997, of resolving the Jeans thermal scale in order to address artificial fragmentation, is added as a safe-guard, albeit in practice it is not too important, as our simulations always resolve such scale-length.

Our simulation suite includes 16 different physical setups, with 4 different initial conditions which are run with or without radiative feedback, and different feedback settings. This physical setups separate into 2 systems which are inside the dynamical cavity forming regime from VE12, and 2 systems which are not (see figure 2.1). The initial mass and separation of the binaries in this setups is $(a_{\text{bin}},\, M_{\text{bin}}) = (3\,\text{pc},\, 10^6\, M_\odot), (2\,\text{pc},\, 10^6\, M_\odot), (7\,\text{pc},\, 10^5\, M_\odot), (1\,\text{pc}\,,\, 10^4\, M_\odot)$. The mas of the circumbinary disk is $10^6\, M_\odot$ for all setups except for one of the cavity forming conditions. All this values are summarized below in table 2.2.

Name	M_{bin}	$M_{\rm disk}/M_{bin}$	a_{bin}	Tidal Gap	AGN
GAP-a3	1	0.01	3	yes	no
GAP-a3-AGN	1	0.01	3	yes	yes
GAP-a2	1	1	2	yes	no
GAP-a2-AGN	1	1	2	yes	yes
a2	0.1	10	7	no	no
a2-AGN	0.1	10	7	no	yes
a1	0.01	100	1	no	no
a1-AGN	0.01	100	1	no	yes

Table 2.2: Summary of main setup parameters. Masses are in $10^6 M_\odot$ units and lengths are in pc units.

Next we have at table 2.3, physical quantities that are derived from these setups, which will set the inner physical scales of each system. We list then the threshold radius $R_{\rm d}^0$, the Schwarzschild radius R_g, the momentum threshold $l_{\rm d}^0$, the orbital time t_{orb} and the pure orbital speed v_{bin} (which is used for the calculation of things like the real initial circular velocity of the binary or the Toomre parameter).

Name	$R_{\rm d}^0$ [pc]	R_g [pc]	$l_{\rm d}^0$ [cm^2/s]	$v_{\rm bin}$ [cm/s]	t_{orb} [kyr]
GAP-a3	4.96×10^{-5}	4.787×10^{-8}	1.008×10^{23}	5.356×10^{6}	54.78
GAP-a2	4.96×10^{-5}	4.787×10^{-8}	3.187×10^{23}	6.559×10^{6}	29.82
a2	2.79×10^{-3}	4.787×10^{-9}	7.558×10^{22}	1.109×10^{6}	617.4
a1	1.57×10^{-7}	4.787×10^{-10}	5.667×10^{20}	9.276×10^{5}	105.4

Table 2.3: Tabulated values necessary for the accretion rate and physical scales

The orbital speed for a Keplerian binary with no eccentricity was calculated as

$$v_{\rm bin}^2 = \frac{2GM_{\rm bin}}{a_{bin}} \tag{2.14}$$

We also use as our orbital timescale, the value

$$t_{orb} = \sqrt{\frac{a_{\rm bin}^3}{2GM_{\rm bin}}} \tag{2.15}$$

2.4.1 Setting the speed of light fraction

In a work where timescales are as a central as this one, the reduction of the speed of light mentioned in section 1.2.3 might be a concern, as this reduction affects the timescales for photon propagation, affecting the efficiency of radiation propagation, and therefore indirectly affecting the effects over merging timescales. This is all true, but in practice, the timescales at which radiation travels through the simulation and the dynamical timescales that are relevant for our context work in such different regimes, that it does not affect too much the evolution of the system.

If we define the light-crossing-time as the time that it takes at lightspeed to cross the strömgren radius defined with the physical parameters of our system. The formula for this ionization front bubble radius for an ionizing-photon emitting source onto a homogeneous hydrogen medium is

$$r_S = \left(\frac{3\dot{N}}{4\pi\alpha^B n_{\mathrm{H}}^2} \right)^{1/3} \tag{2.16}$$

When considering our circumbinary disks, $\alpha_B \sim 2.6 \times 10^{-13}$ [cm$^3/s$] is a good approximation for B type recombinations at $T \sim 10^4$K (which is nearly the our Mestel equilibrium temperature), we also see typical midplane densities of $\sim 10^{-20}$ [gr/cm^3], which crudely translates to $n_H \sim 5 \times 10^3$ [1/cm^3]. If we take typical values for AGNs (take again, for instance an energy output from Sazonov et al., 2004), we would get a photon number production of around $\dot{N} \sim 10^{50}$ [$1/s$]. With all this we get an Strömgren radius of $r_S = 0.5$ [pc] from 2.16, which itself gives a crossing timescale of $t_{\text{cross}} \approx 1.63$ [yr]. For most of our analysis, the relevant timescale τ_{sim} we measure our simulation in, is the orbital time of the binaries, which in its lower case scenario can be of ≈ 40 [kyr]. In Rosdahl et al., 2013 the quoted lightspeed fraction used is of $f_c = \min\{1, 10t_{\text{cross}}/\tau_{\text{sim}}\}$ (see equation 1.32, which in our case amounts to $f_c = 4 \times 10^{-4}$. In practice, the gain in computational load for such a low fraction is not really necessary and because we want to minimize any possibility of having delays on the radiation effects over coalescence, we raise our actual lights speed approximation to a factor of $f_c = 5 \times 10^{-3}$, which is way above the usual requirements set for the validity of this formalism.

Chapter 3

Results and analysis

3.1 Runs without Radiative Feedback

We first begin analyzing our runs done without radiation, where we will check for consistency with VV18 in order to validate the subsequent comparison of the AGN radiative feedback models. For this posterior analysis we will still need to have extracted certain amount of information from the binary+disk dynamics/interaction in order to ascertain and quanitify the impact that RT has.

As it has already been mentioned, the setup suite we are working with, consists of 2 systems which are expected to open a tidal gap and 2 which are not. In VV18 the systems binary separation evolutions were plotted against their time evolution in t_{orb} units:

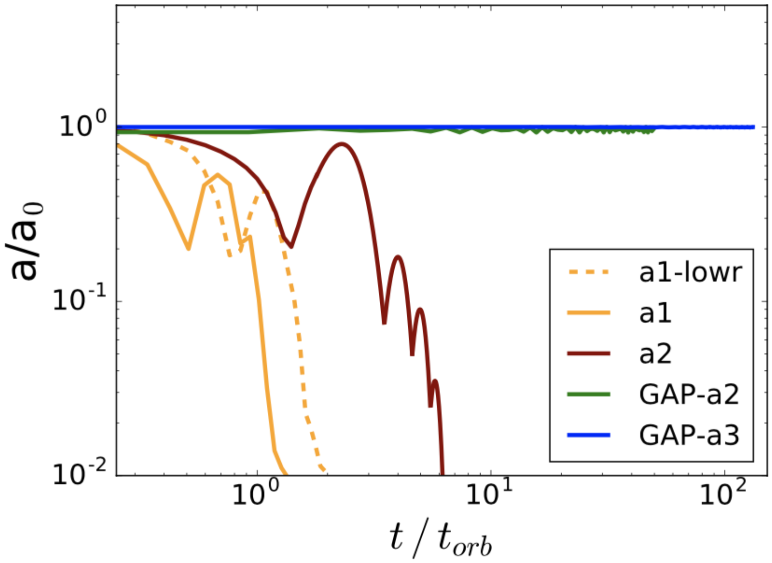

Figure 3.1: Result of simulations from VV18. Normalized binary separation a/a_0 plotted against normalized time units t/t_0.

This plots exhibit how green/blue systems are stuck in a slow migration regime characteristic of how the binary shrinking mechanisms will not be dominated by extraction of angular momentum through interaction with the disk gas content (as the cavity has been excavated and the available gas around the SMBHs has migrated away), and how orange/brown systems have a rapid coalescence evolution, as the binary+disk couple is maintained by viscous diffusion.

3.1.1 No gap opening setups without radiation coupling

Continuing now with the setups we expect no tidal gap to form, we check the results for systems a1 and a2 specified in figure 2.1. The setup parameters can be found at table 2.2, with corresponding values of $M_{\text{bin}} = 10^5 M_\odot$, $M_{\text{disk}} = 10^6 M_\odot$ and an initial SMBH separation of $a_0 = 7$pc for a2 and $M_{\text{bin}} = 10^4 M_\odot$, $M_{\text{disk}} = 10^6 M_\odot$ and an initial SMBH separation of $a_0 = 1$pc.

On the long run we predict no important tidal cavity formation on these setups, but there are some contrasts: For a2, its place on the parameter space partition seen in the graph 2.1, indicates that the expected perturbation of the disk is non-trivial as it is close to the regime-partitioning line. In contrast to a2, a1 is expected too show much less signs of disk perturbation from the binary, as viscous diffusion will be very efficient with respect to angular momentum distribution in the circumbinary disk. For both of this setups we expect to see fast orbital migration, this is specially true as a1 starts out with a much lower initial separation for the binary and a smaller fraction between the BHs and the disk. Let us look at density maps for both setups, beginning with a2:

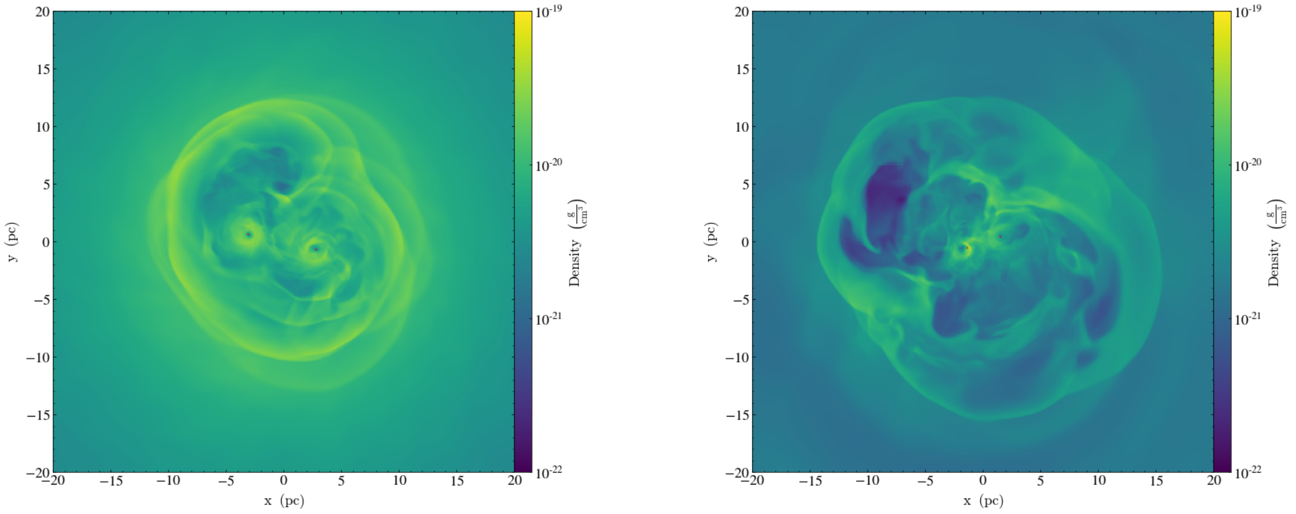

Figure 3.2: Density slice $\rho(x, y, z = 0)$ map for no-gap a2 simulation at times $t = 1t_{orb}$, and $2t_{orb}$

Indeed in the density slices we see a perturbed disk (we see the wake of our black holes leaving a spiral wave perturbation), but the BHs are not effectively excavating a hydrodynamical cavity. Now, the same maps for a1 look like this:

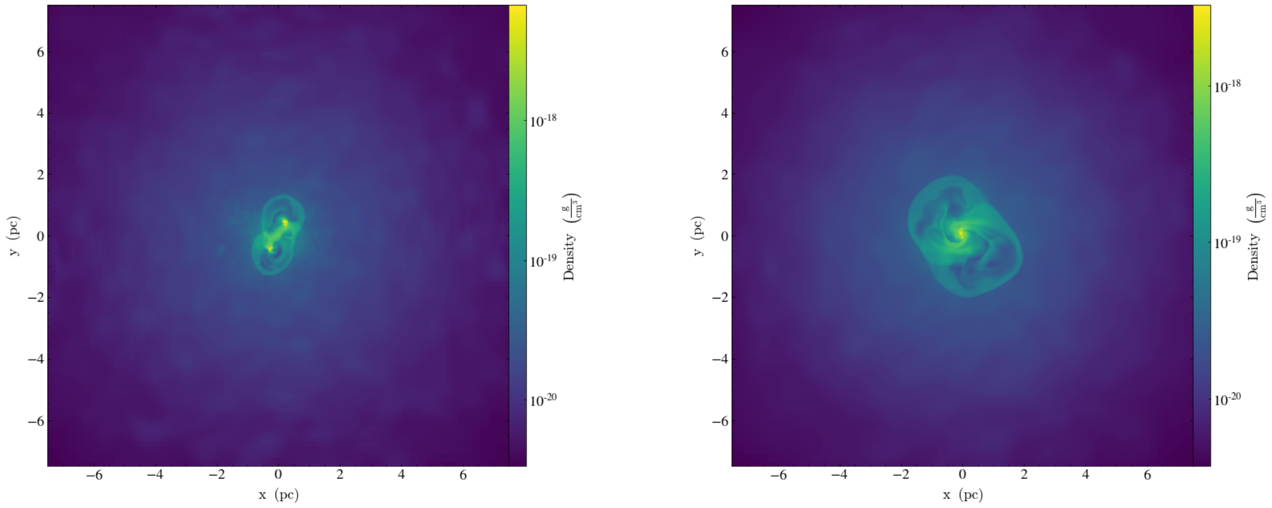

Figure 3.3: Density slice $\rho(x, y, z = 0)$ map for no-gap a1 simulation at times $t = 1t_{orb}$, and $2t_{orb}$. Notice that in difference from the slices for a2, the disk is zoomed to $xy \in (-7.5,\ 7.5)^2$ pc

Now if we see the binary separation graphs, it is apparent that the BHs in these setups are indeed coalescing in timescales that are comparable to how much we are running our simulations. Showing how indeed the low binary to disk mass ratio and the short initial separations affect the disk's structure in a low enough degree such that gas will provide enough influence to make the black holes to merge on a short timescale:

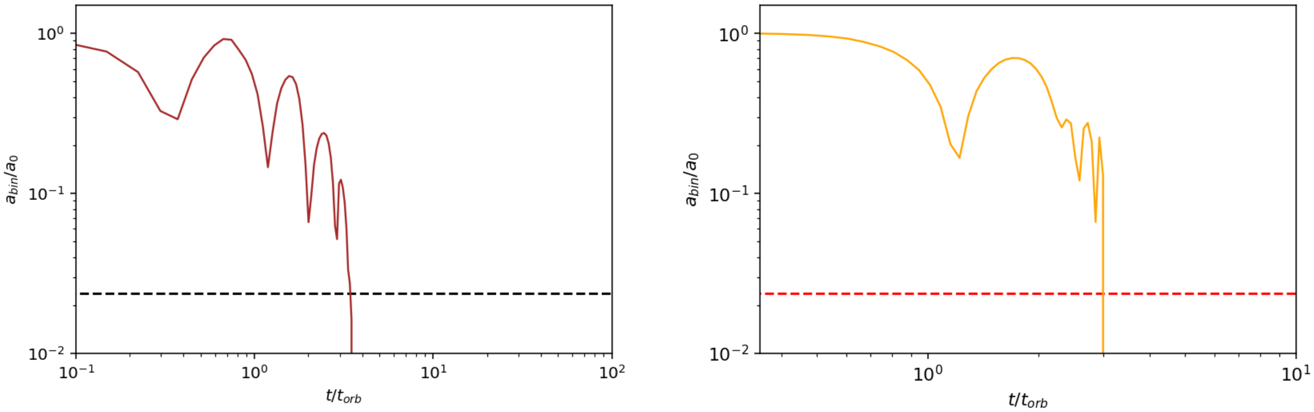

Figure 3.4: Orbital evolution for cases a2 (left) and a1 (right). Both show an evolution where the binary separation steadily decreases after every orbital passage

This is in general good accordance to the results seen with the runs from GADGET at 3.1. but with a less pronounced coalescence, seeing less difference in the peak separations between black hole passages. We see in Orbital evolution for case a2 a gradual lowering of the distances in closeby passages, but in a1 we see a faster and abrupt merge (requiring only two binary passes), before which we see that if the we overlay the influence radius of our BHs in the snapshot right before the merge, it is the only time in which they intercept, which happens at separations that go down to values of $\sim 1.5 \times 10^{-2}$pc:

We expect both setups with fast shrinking regimes, to be the ones most affected by the potential impact that quasar feedback can have. This is both because we would expect more accreting fuel surrounding SMBHs from non-gap-opening systems, and because the this feedback would naturally have more effects at delaying than accelerating orbital decay, which is of course more relevant towards fast shrinking binaries. Another idea supporting this, is how accretion (and proportionally so, radiative feedback) in binaries which are coalescing has episodic enhancements that depend on orbital passes, we see this for both no-gap-opening systems (considering a1 only up to before the time of merging):

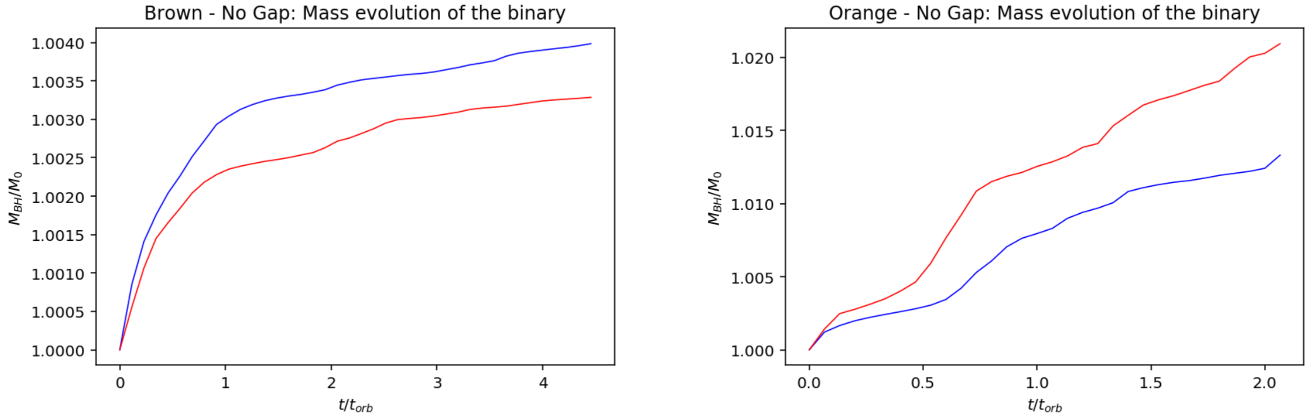

Figure 3.5: Mass evolution of BH pairs for setup a2 (left), and setup a1. Each separate line on the figure represents an individual BH in its respective setup

Differences in the evolution of mass throughout the respective simulations is to be expected. The a2 setup shows a steep initial mass accretion due to how the binary is more massive in proportion to the disk (compared to a1), whilst the subsequent gradual decrease is due to how the BHs perturb the disk somewhat strongly, but without forming a noticeable tidal gap (see how it is placed near the gap forming threshold region of phase space at figure 3.1). As mentioned, a1 does not show such a big, steady decrease in accretion, due to how little of an impact the binary has on its medium, and at the same time shows a strong correlation of accretion enhancement and orbital passes. It is worth mentioning that accretion rates at all simulation times, fall comfortably over the ADAF regime and therefore radiative-mode feedback is predicted to be a relevant mechanism (although since it is a self-regulated mechanism, this has to be seen).

3.1.2 Tidal gap opening setups without radiation coupling

We begin the results analysis for our setups where the initial conditions are primed for tidal gap formation.

As expected these setups **do** in fact form tidal gaps in a few orbital times, and show slow migration times, both for GAP-a3 (which has $M_{\text{bin}} = 10^6 M_\odot$, $M_{\text{disk}} = 10^4 M_\odot$ and an initial SMBH separation of $a_0 = 3$pc, see 2.2) and for GAP-a2 ($M_{\text{bin}} = 10^6 M_\odot$, $M_{\text{disk}} = 10^6 M_\odot$ and an initial SMBH separation of $a_0 = 2$pc). By the way the parameter space is partitioned, we expect a slower gap clearing in GAP-a2 than the one seen in GAP-a3 (this is intuitive: the disk's structure is more affected for setups in which the mass of the BHs is higher relative to the medium), as it is closer to the phase-space partitioning line from 2.1, but it may be more noticeable as the density contrasts are bigger with the more massive disk present here.

If we now observe a density projection of these simulations on the XY axis, we see the following for GAP-a3:

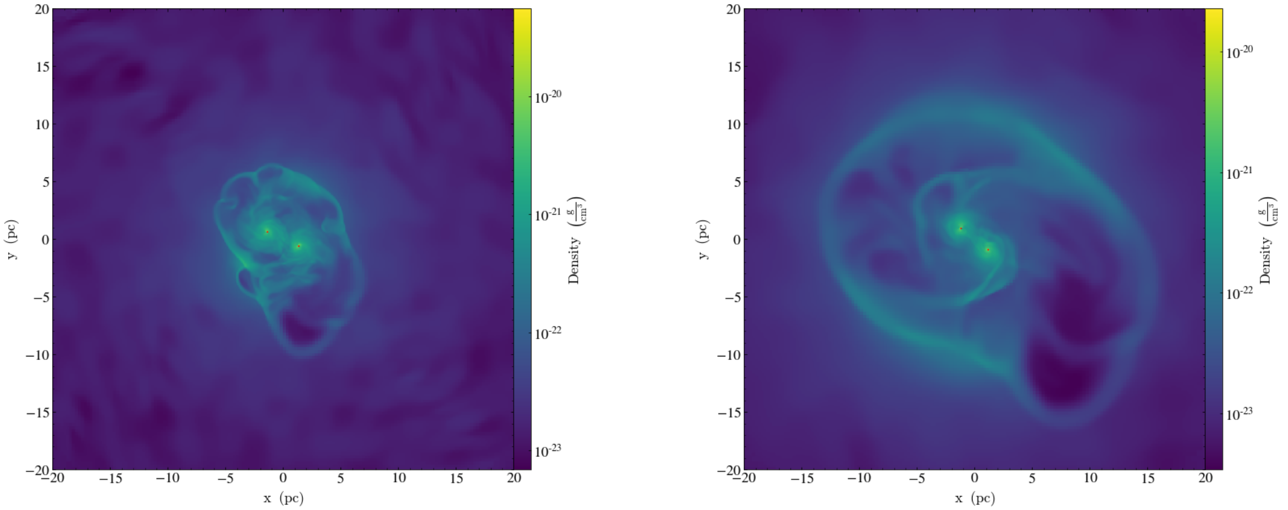

Figure 3.6: Density slices for simulation GAP-a3 at times $t = 0.5t_{orb}$, $1.5t_{orb}$

If we plot the same density slices for GAP-a2 we see at the same evolution time (in units of orbital timescales):

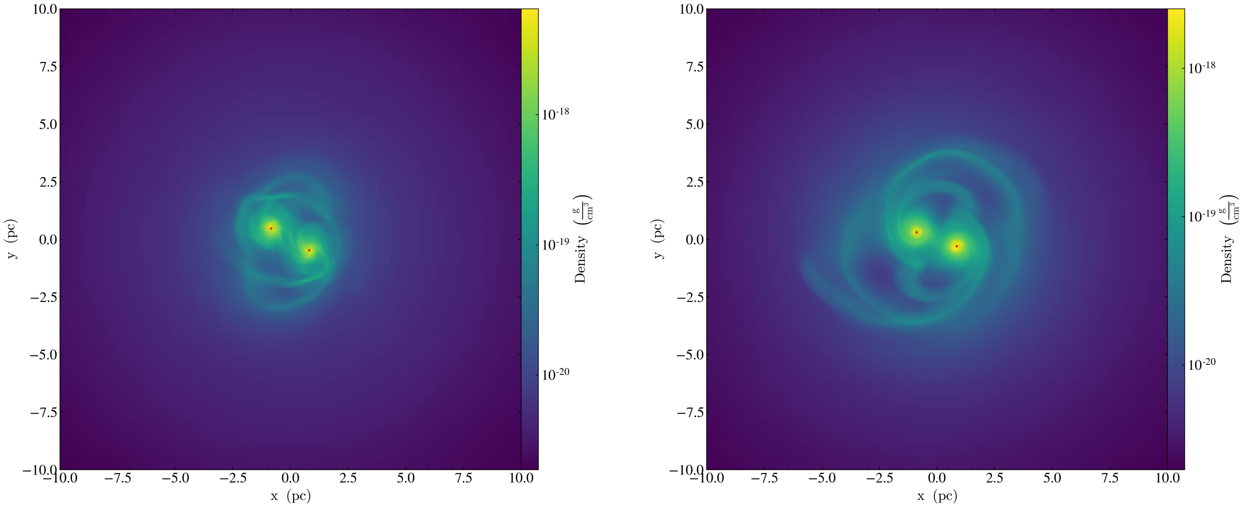

Figure 3.7: XY density slices for simulation GAP-a2
at times $t0.5t_{orb}$, $1.5t_{orb}$

We see there is a clear gap forming at times as soon as a couple of t_{orb} which for setup GAP-a3 corresponds to a timescale of $t_{orb} \approx 54.8$kyr and $t_{orb} \approx 29.8$kyr for GAP-a2. As expected, the gap formation is less violent for GAP-a2, but still the cavity is apparent, eg: let us see the YZ density projection of this at $t = 2t$

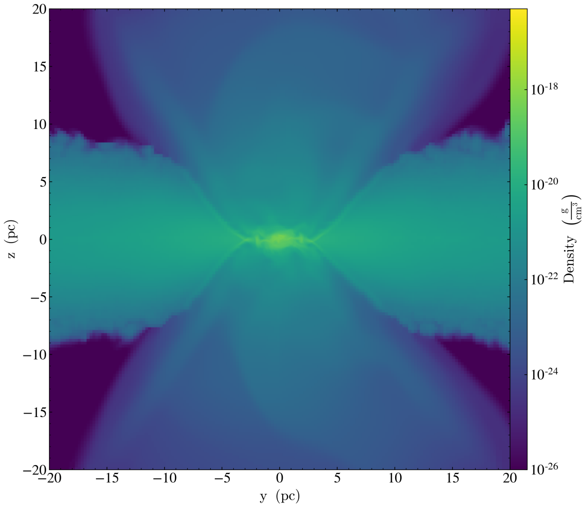

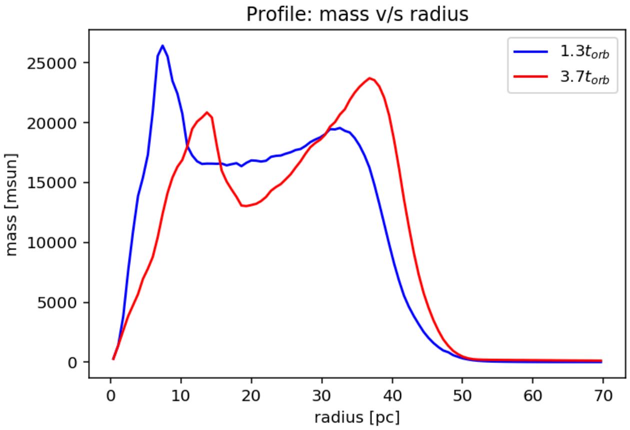

The profiles at different times show clear evidence of how mass is allocated out of the central regions of the disk. It also shows how matter will tend to pile up between the inner limit set by the excavated gap and the ring's outer boundary defined by the equilibrium of pressure against self-gravitation (and the external gravity from the stellar bulge)

A direct measure of agreement between the original runs done with GADGET is to measure the binary separation evolution, which where we see agreement in how there is now perceivable orbital decay (just as in VV18):

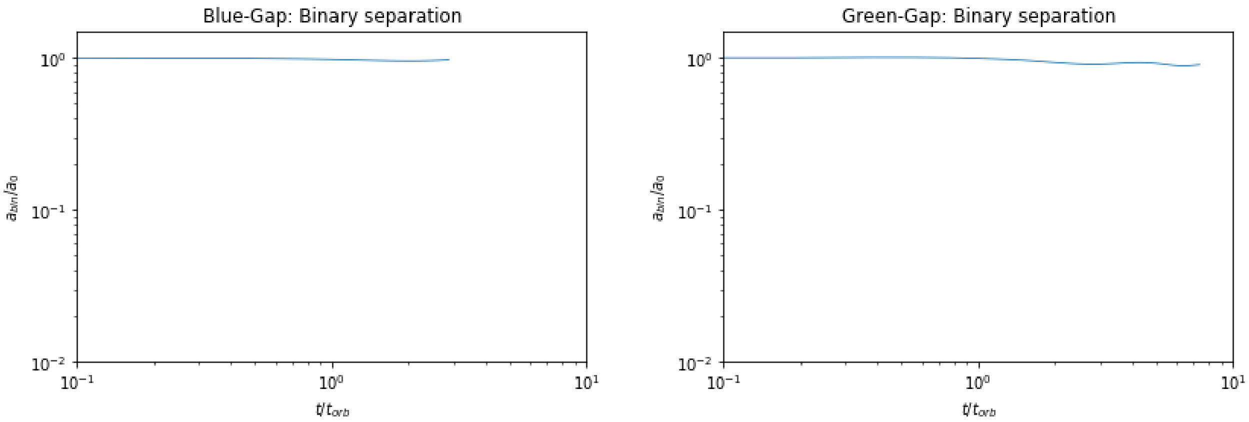

Figure 3.9: Binary separation of tidal opening setups without AGN feedback GAP-a3 (left) and GAP-a2 (right). Both show an evolution where the binary separation is maintained almost constant.

As mentioned, we see that the evolution of binary separation is almost flat in our timeframe, which is consistent for gap forming setups, as the timescale in which slow migration operates is $\frac{1}{a_{\text{bin}}}\frac{\mathrm{d}a_{\text{bin}}}{\mathrm{d}t} \sim 10^3 - 10^4\, t_{\text{orb}}$. It is not rare that we see how the setup that forms the gap more quickly

It is also of interest to measure the torque exchange the binary has with its gas environment through dynamical friction as a way to see the system coupled interaction. We recall equations 13-14 (we reiterate these equations here only to improve the readability of this document), where quoting the formulas from Escala et al., 2004, Escala et al., 2005 the gas coupling may be stated as:

$$T \approx 4\pi\rho r \left(\frac{GM_{BH}}{v_{BH}}\right)^2 \times f^{(\text{gas})}(\mathcal{M}) \tag{3.1}$$

Where $\mathcal{M} := v_{BH}/c_s$, and $f^{(\text{gas})}(\mathcal{M})$ is a dimensionless factor taken from Ostriker, 1999, which takes a different form depending in how the binary is moving in a supersonic/subsonic regime:

$$f^{(\text{gas})}(\mathcal{M}) = \begin{cases} \frac{1}{2\mathcal{M}^2}\ln\left(\frac{1+\mathcal{M}}{1-\mathcal{M}}\right) - \frac{1}{\mathcal{M}}\,, & \mathcal{M} < 1 \\ \frac{1}{2\mathcal{M}^2}\left[\ln\left(\frac{\mathcal{M}+1}{\mathcal{M}-1}\right) - 2\ln\left(\frac{r_{\text{max}}}{r_{\text{min}}}\right)\right]\,, & \mathcal{M} > 1 \end{cases} \tag{3.2}$$

Setting the value of the Coulomb logarithm to a best fit value of $\ln\left(\frac{r_{\text{max}}}{r_{\text{min}}}\right) = \begin{cases} 4.7\,, & \mathcal{M} \geq 0.8 \\ 1.5\,, & \mathcal{M} < 0.8 \end{cases}$ just as in Escala et al., 2004, we get from our simulations the following evolution of torque exertion (in code/arbitrary units):

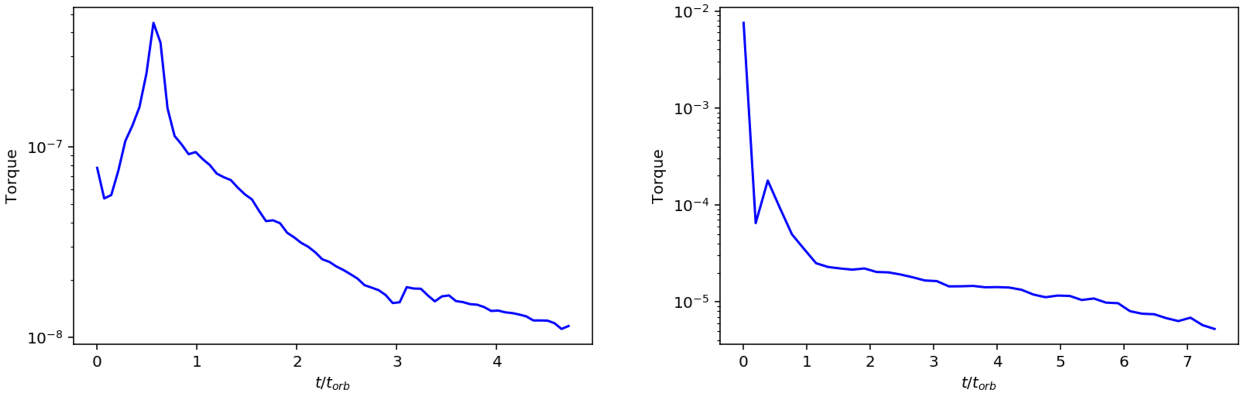

Figure 3.10: Torque evolution for case GAP-a3 (left) and GAP-a2 (right) respectively (code units)

In the graph a noticeable diminishing of the torque exchange is seen, which is consistent with gas being migrated away (and therefore immediately diminishing ρ in equation 3.1). Even though this is in code units, we can directly compare between the two disks, showing that the torque values in the first setup are $3-6$ orders of magnitude below those of the gap opening setup with a more massive disk. All this supports the resulting constant orbital separation we observe at 3.9.

A synthesis for comparison of results between the orbital evolution at 3.1 and the ones that been mentioned one-by-one in this section looks like this:

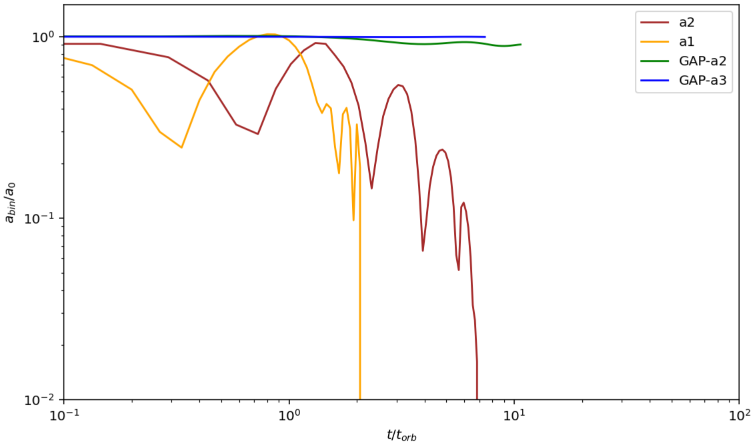

Figure 3.11: Compiled orbital evolutions for our different setup runs without AGN feedback. We see coalescence in a few $t_{\rm orb}$ units for fast migration simulations, and an almost constant orbital evolution for slow migration

Which we see, is in almost one-to-one concordance to the GADGET runs done without feedback, this consistency bodes well because it suggests that differences between findings in radiation-runs will be mostly induced by the AGN implementations, and as such we may isolate the limitations of the past findings.

3.2 Runs with AGN Feedback

3.2.1 No gap opening setups with radiation feedback and coupling

Along this section we will focus more in simulation a2-AGN, as this system in which no gap is predicted (nor observed, in the purely hydrodynamical runs), is the setup which we chose to run in most detail compared to the rest of our simulation suite, as working through the rationale of no-gap forming systems are in the regime that is predicted to be affected the most by the inclusion of feedback, by virtue of us basically adding a new disruptive factor in the disk which could potentially make it so the system cannot sustain gas reservoir needed to remove angular momentum and promote the binary's merger. Now, we choose to focus our analysis on a2-AGN over a1-AGN (take this as a soft statement: the analysis will **of course** include both setups, taking care to outline differences and similarities) not only due to the fact that the writing is clearer due to see how a-posteriori they share most of their evolving trends, but also it is of note that we want to see a maximization of what feedback 'may' do on our working context, and we already saw how in 3.1.1 the former is the setup in which the binary has a much bigger impact in its overall context.

We begin with a basic rundown of what is seen in terms of behaviour of the BHs and the gas. The simulations start out by carving out a 'feedback bubble' which occurs by a combination of two things: Accretion at the instant-initial simulation stages is quite high, and therefore the feedback's net luminosity is high, and secondly, as we begin with gas that is fully non-ionized, high frequency radiation couples easily to the gas thus transferring energy very efficiently.

Now, between our two setups, this radiation bubble behaves differently, as for our less massive setup a1-AGN, the bubble is not strong enough to perturb the medium in a disk-wide manner, and accretion is less inhibited, whilst for a2-AGN the bubble progressively expands up to a point where accretion starts becoming quite inhibited and at around $\sim 1 t_{\rm orb}$ (see the accretion graph at 3.13 the downturn is already quite apparent. Let us see how density maps look:

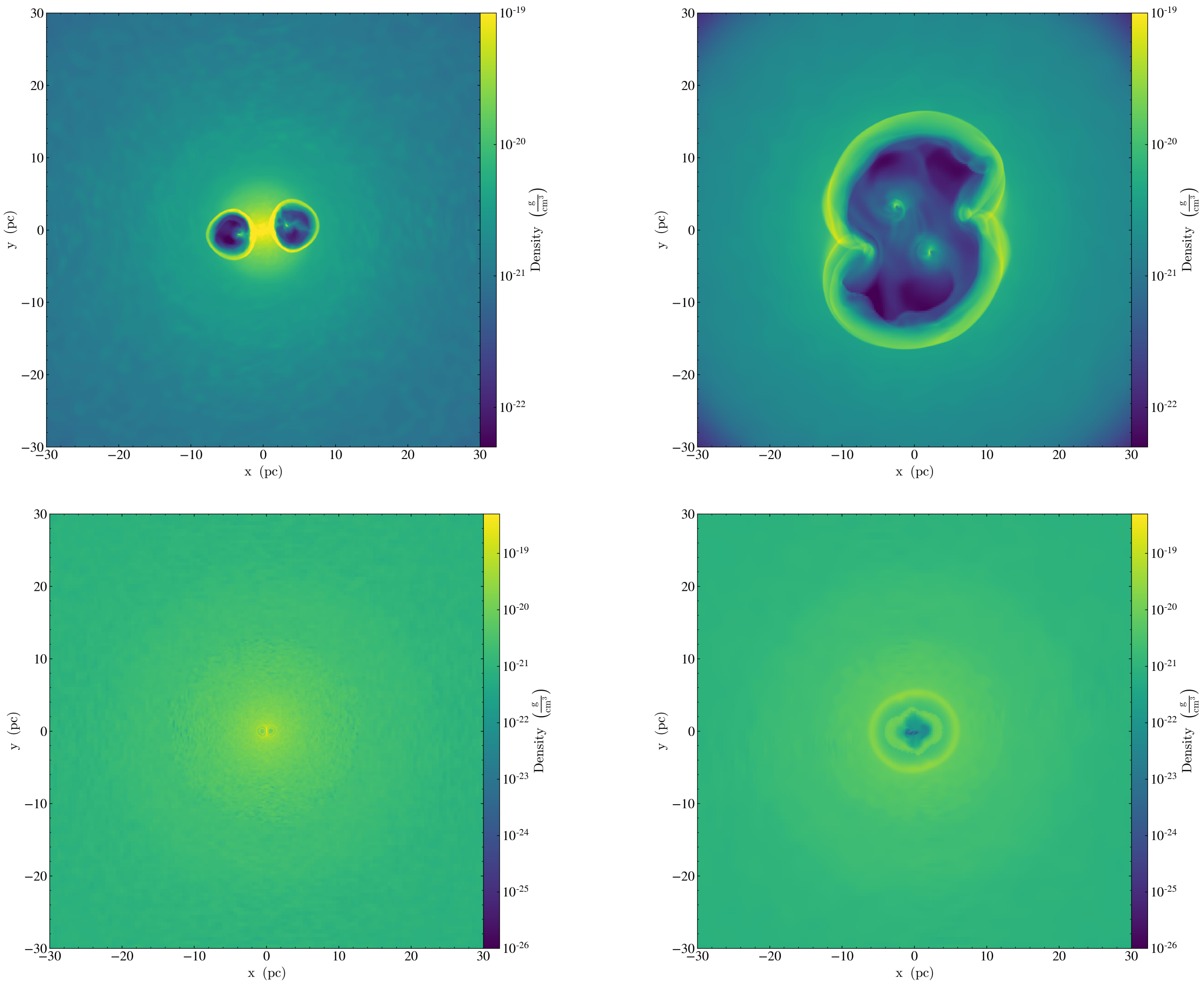

Figure 3.12: Density projection at times $t = 0.1t_{orb}$ and $1t_{orb}$ for a2-AGN (top panels) and a1-AGN (bottom panels)

We see in these maps an illustration of just how much difference the effects of AGN feedback may have, where the feedback bubble in a1-AGN is quite small even after a whole t_{orb} has turned, whilst in the more BH-massive setup, feedback is extremely disruptive towards its immediate environ. Let us now see the evolution of accretion in these two setups:

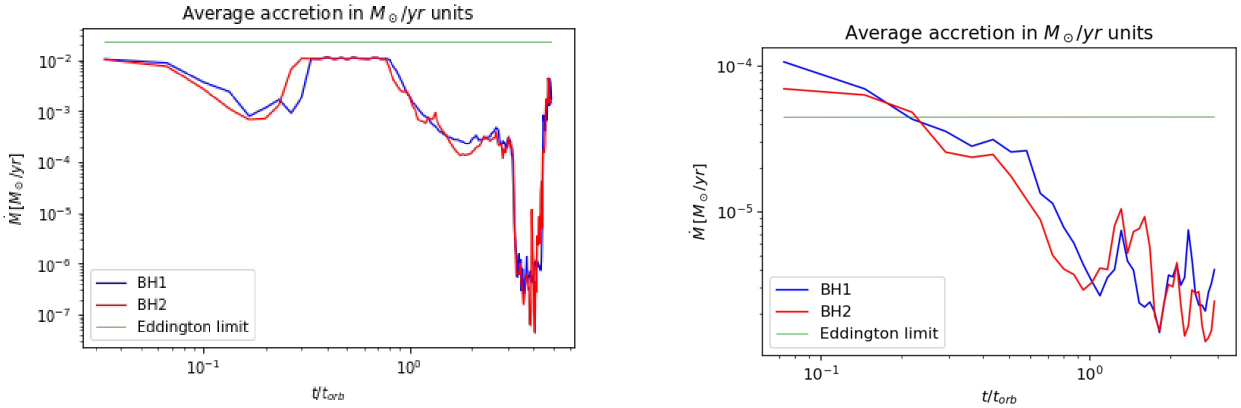

Figure 3.13: Accretion evolution for a2-AGN (left) and a1-AGN (right)

The question of why does the accretion not become immediately inhibited after the feedback bubble is formed for setup a2-AGN, instead showing an upturn at $\sim 0.2t_{\mathrm{orb}}$, can be explained by how, after each individual bubble forms, the expansion front does not follow the rotation of the binary, and eventually the BHs intercept the high density forefront of this feedback cavity, which then 'artificially' ups accretion. Other clear feedback bubbles are created on smaller scales during this simulation which usually correspond to accretion feedback being able to couple more efficiently to a medium that tends to both mix with the outer non-ionized gas from the disk and to smooth out due to diffusion (the changes of coupling efficiency due ionization is quite relevant and covered in 3.2.1.2). The eventual sharp reignition of feeding that occurs is due to the close passage of the BHs, which does not trigger a violently coupling feedback event as gas is much more ionized, and there are also enough low-density channels for radiation to be funneled (specially in the vertical direction).

3.2.1.1 Extended disk structure

If we were to see the overall mass extension of our CMB disks, for our less massive setup we would see no large scale changes, as the feedback bubble is small enough to remain contained onto the center of the extended disk, and it eventually starts refilling. At the same time, for a2-AGN we can look at the density maps at 3.14, and observe how the evolution seems to start roughly at the predicted 45pc radius that is specified in our initialization analytical model, followed by an epoch of contraction of the disk's radius that accompanies the out-of-equilibrium overall state of the system that is spurred by the feedback cavity and vertical outflows that stem from the nuclear regions nearby the BHs, and finally we see a 'repairing' phase of the disk, where the system begins stabilizing, once again at a disk extension comparable to that of the initial values:

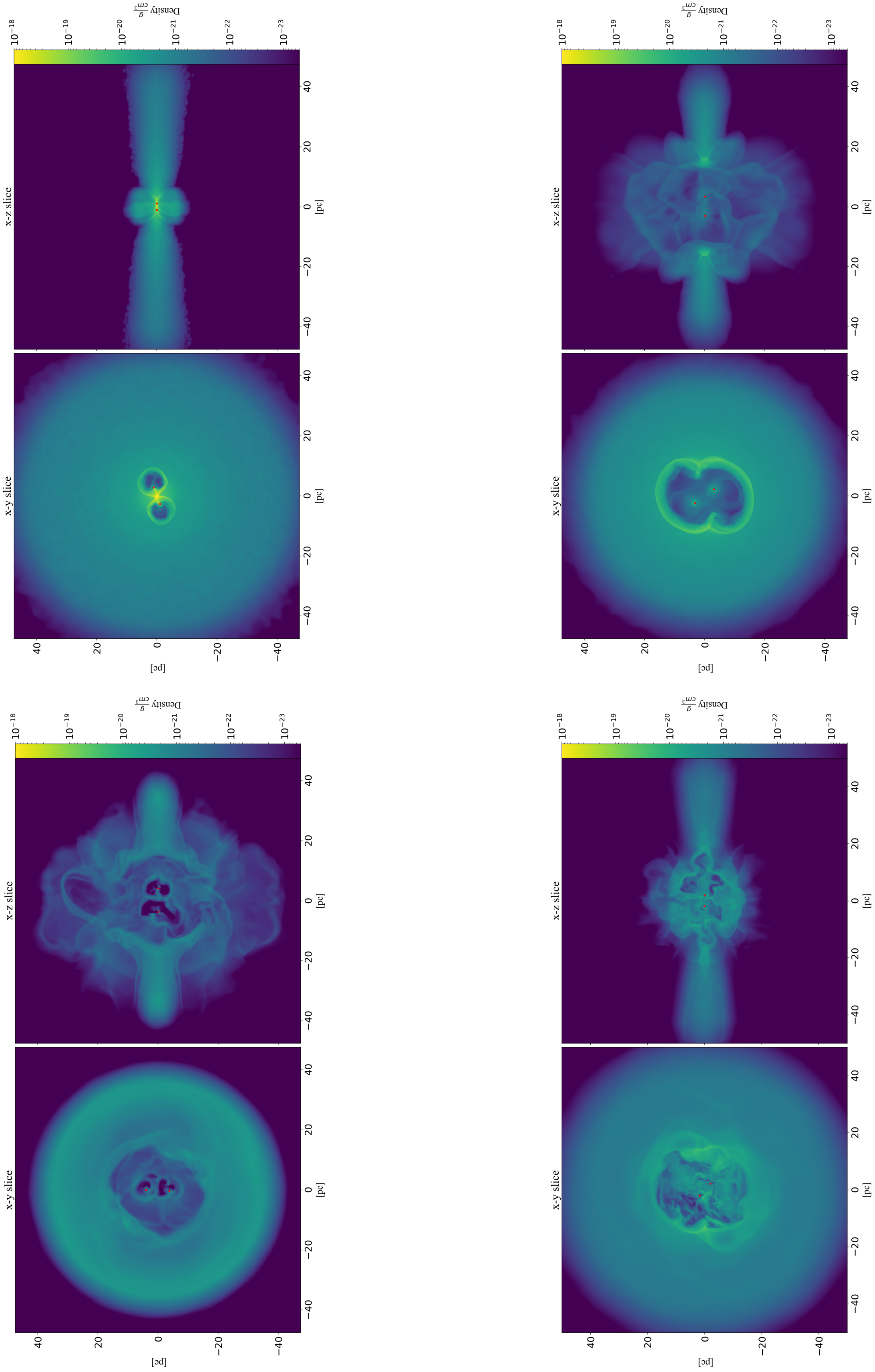

Figure 3.14: XY density slices from upper left to lower right at times $t = 0.2t_{orb}$, $0.75t_{orb}$, $1.8t_{orb}$, $2.4t_{orb}$

The rationale derived by looking at the disk's integrity evolution, is accompanied by looking at the behaviour of mass concentration with respect to the z-axis over time at 3.15. We can appreciate how mass is orderly packed at certain height intervals, then this mass concentration is expanded to much bigger heights due to the feedback, and finally the vertical structure becomes similar to the initial one but in a smoother more spread distribution.

This big spread of mass in the vertical axis is linked to the shortening of the outer disk radius, as it is due to the isotropical expulsion we see by the AGN 'cavity', which vertically propels big quantities of material that the disk. This low density inner region of the disk is refilled by viscous diffusion (which should be efficient, as predicted by the system initial conditions) with material that comes from disk's axis at the inner boundary of the cavity, and thus a momentary contraction of the disk occurs. This is later stabilized, as the vertically expelled material never reaches the system's escape velocity and as it falls back into the disk (this is a relevant issue at gap-forming systems with the inclusion of radiation, see **??**), the structure gradually restores itself back to an equilibrium akin to a more spread-out version of the initial conditions. This can only happen of course, if no big subsequent AGN induced bubbles form, which is what we observe, the reason for this is mentioned in the following section 3.2.1.2.

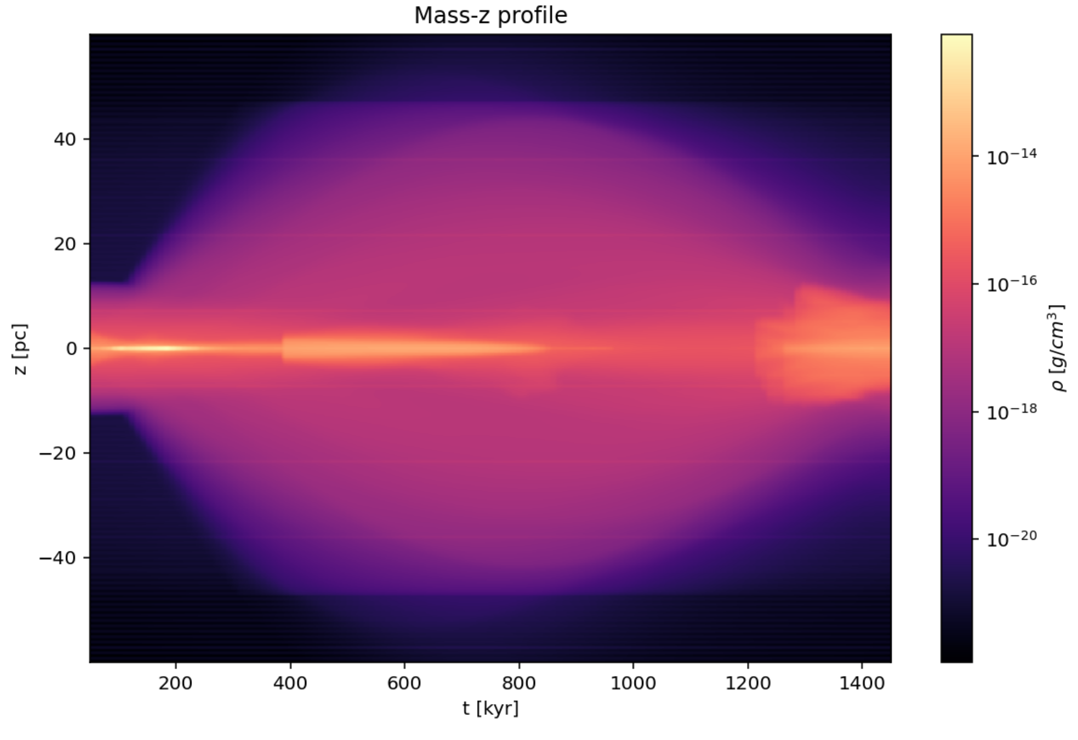

Figure 3.15: Evolution of the vertical concentration of mass throughout time. At the beginning, mass is vertically diffused on average, after which the disk vertical structure is gradually regained to approximate that of the original setup

3.2.1.2 Feedback and radiation-medium interactions and evolution

Now, as predicted by the title of this work, the behaviour of radiation in our simulations is central, as it is the main differentiator on how feedback is implemented. Not only AGNs are better represented by making a much more complete modelling of the actual direct mediator of interactions between gas and the feedback energy, but it also, in our implementation we can follow the loss of radiation-coupling efficiency by virtue of ionization, and we can also follow the details of energy propagation through photons (opposite to the direct heating recipes usually used in simulations that are only hydrodynamical in nature).

Firstly, we know by construction that the net radiated energy (bolometric luminosity) will always be proportional to radiation, but as our simulations not only deposit different fractions of luminosity in different photon bands due to a SMBH spectrum, but also have changing spectrums depending on the medium's state (see 2.3 and 5.2). At simulation a2-AGN the exact photon emission from our BHs is:

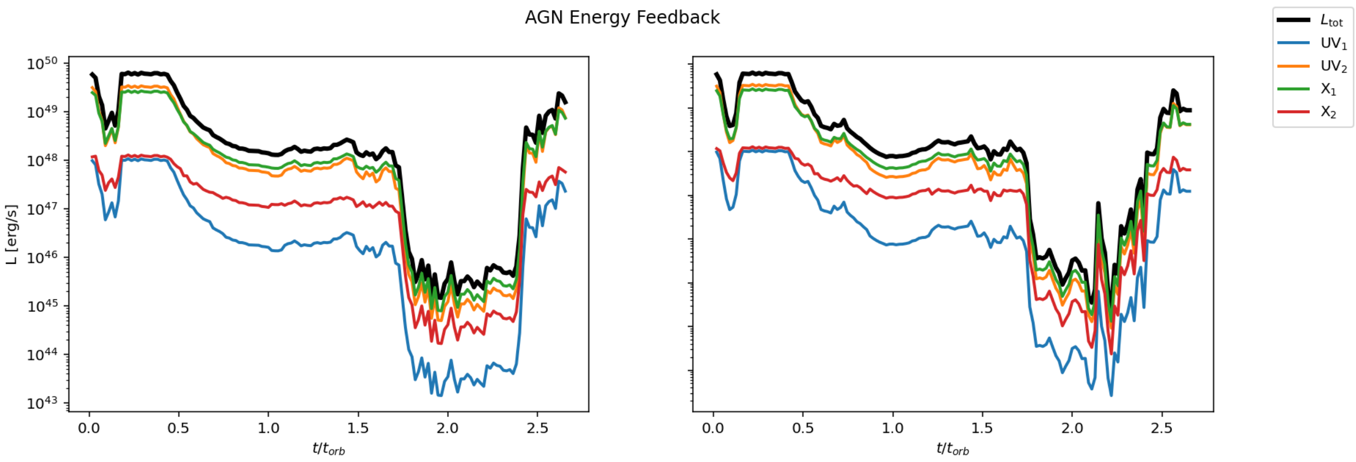

Figure 3.16: Net radiated energy and specific photon group radiated energy for a2-AGN

The first thing to look at with this graph, is to see that the absolute emitted luminosity does not exceed $L \sim 10^{43} \frac{\text{erg}}{\text{s}}$ with values staying usually closer to $L \sim 10^{42} \frac{\text{erg}}{\text{s}}$, which is close to expected values for BHs if $M_{\text{BH}} \leq 10^{6}$, as for instance the Eddington limit, which sets a maximum luminosity for the idealized case of spherical accretion and hydrogen medium sets a limit of $L_{\text{Edd}} = 1.25 \times 10^{38} \times M_{\text{BH}}/M_{\odot} \frac{\text{erg}}{\text{s}^{-1}}$. This graph also shows how in practice, by far, the most energy inducing photon bands are the high energy *UV* photons and the soft X-ray photons, with the latter edging out the former in most instances (except at the highest radiation levels). It is important to note though, that even though both are mostly comparable, UV rays couple more efficiently to gas (see its effective cross sections at 5.2) and thus if the emitted values are comparable for both bands, the UV band will always have a bigger impact on the system. Another thing to note here, is that even though IR band is not created from the sinks, it is very much present in the simulation, as it is the form that reprocessed radiation takes after being absorbed. We also note that this depositing of energy in photon bands is in general terms, consistent along all our other setups, as even though there are potentially, conditions that would have for example hard X-ray photons as most of the energy, these are quite extreme and not really feasible in our context (eg: $\log_{10}(\xi) = 0 \wedge \Gamma = 1.76$).

Now with the working hypothesis of, ionized gas is much less efficient at capturing photons and thus coupling to feedback, we can start delving more and better into how the behaviour and impact of the AGNs evolves in the simulation. Let us see how the ion numerical density maps change through time:

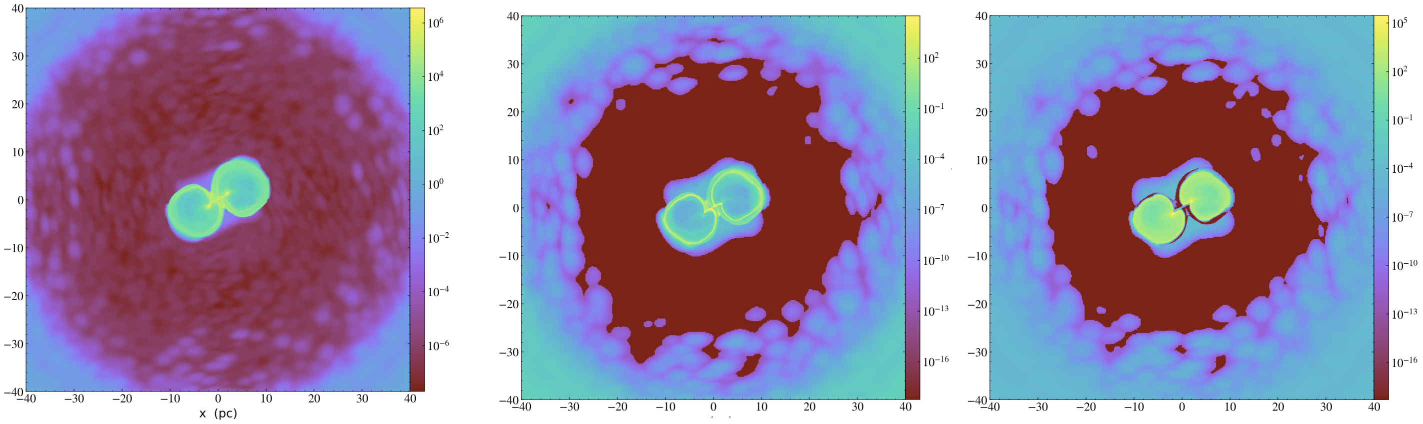

Figure 3.17: H_{II}, He_{II} and He_{III} number density at $t = 0.2t_{\rm orb}$

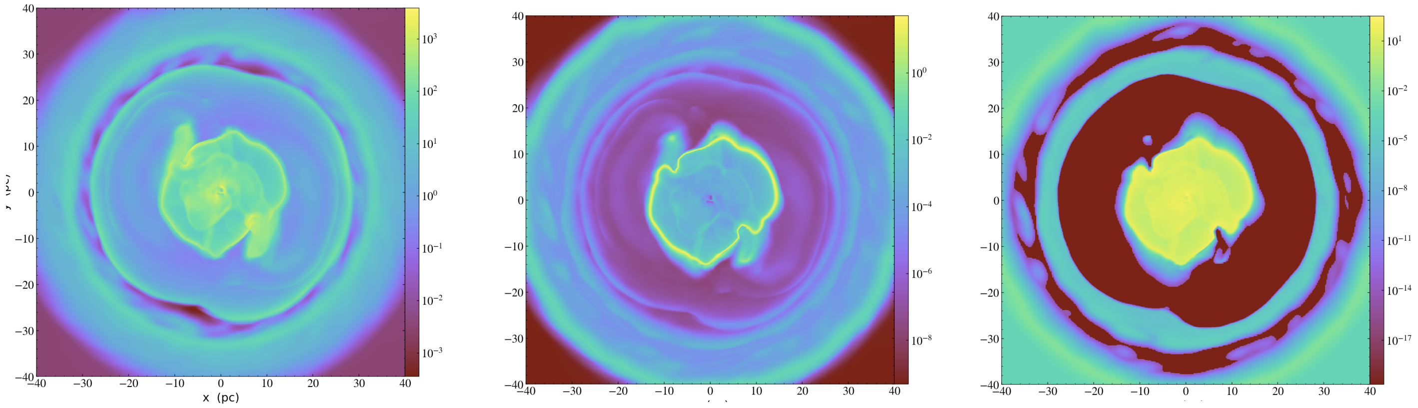

Figure 3.18: H_{II}, He_{II} and He_{III} number density at $t = 1.75t_{\rm orb}$

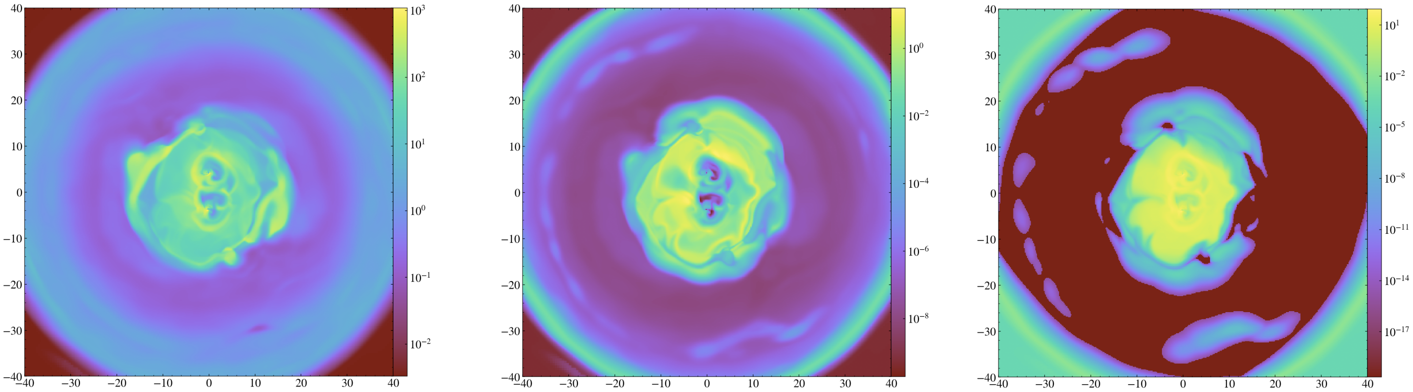

Figure 3.19: H_{II}, He_{II} and He_{III} number density at $t = 2.2t_{\rm orb}$

We see different things at play here, with the first being that evidently the ionization concentration is focused on the low density region excavated by feedback, which is intuitive given that this will be the region that has been most recently and most highly exposed to radiation. At the initial stages this is extremely evident, but as the simulation keeps evolving, we see that the ion density stays centralized but stops being a transpose of the density map, as ionized matter is now mixing with non-ionized material, whilst radiation now does not carve such large scale feedback bubbles as the one that appears at the beginning. Other secondary feature we can observe is how doubly ionized Helium exhibits this features in a more extreme manner, due to its existence stemming from either Helium interacting with the most energetic radiation bands or through the ionization of $\mathrm{He}_{\mathrm{II}}$ which also explains why we sometimes can see the doubly ionized density map to be a transpose of the single ionized Helium in certain evident regions (as this process depletes He_{I}). Indeed if we go a little beyond than 3.20, as far as $3t_{\mathrm{orb}}$ the centralization of ion concentration is now extremely prevalent, with a very high density contrast:

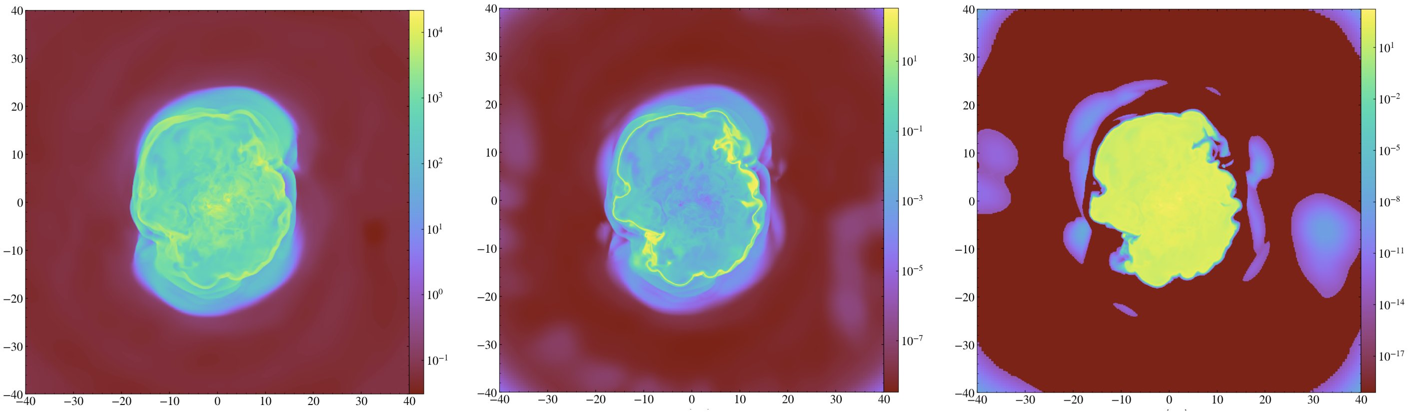

Figure 3.20: H_{II}, $\mathrm{He}_{\mathrm{II}}$ and $\mathrm{He}_{\mathrm{III}}$ number density at $t = 3t_{\mathrm{orb}}$

This Strömgren-like region, where ionization is contained is quite relevant, because it suggests that the disk is moving towards an equilibrium in which there is an inner highly ionized region where the effective cross section will be much lower and thus the mean free path will be much higher and the corresponding radiation force will be small, and where at the point where recombination is able to keep up with ionization, the outwards pressure will be much lower as the flux field is still proportional to $\sim r^{-2}$. Just to illustrate how relevant ionization states are in regard to coupling, let us start by seeing how the cross sections of our species look:

$$\sigma(\varepsilon) = \sigma_0 \left[(x-1)^2 + y_w^2\right] \frac{y^{0.5P-5.5}}{(1+\sqrt{y/y_a})^P} \cdot \delta_{\varepsilon \geq \varepsilon_{\mathrm{ion}}} \tag{3.3}$$

Where $x \equiv \frac{\varepsilon}{\varepsilon_0} - y_0,$, $y \equiv \sqrt{x^2 + y_1^2}$ and σ_0, ε_0, y_w, P, y_a, y_0, y_1 are fitting parameters. For already ionized gas the cross section becomes a Thompson-like cross section σ_T (opacity of the gas becomes uncorrelated to frequency of the incident radiation), and then the radiative acceleration becomes:

$$g_{\mathrm{rad}} = \frac{\sigma_T}{\mu_{\mathrm{e}}} \frac{L}{4\pi c r^2}$$

Where $\sigma_T \approx 6.7 \times 10^{-29}$ for ionized hydrogen, which would be around $10 - 8$ orders of magnitude lower than that of neutral hydrogen (of course this depends on the spectrum shape and frequency band, see 5.2).

Of course we can talk about the ramifications of how the ionization states should affect, but we are still not directly quantifying how radiation is affecting the disk, which is something we may understand by looking at the actual flowing and absorption properties of photons. This is easier said than done, because there are different things at play here than directly looking at density maps of photons (which is maybe a first step, but not enough), we also want to look at how absorption maps in correlation to the system, and how density couples to radiation absorption (and thus interacting energetically) with the gas. We will be mainly showcasing the properties of the UV_2 photons because as we explained before, it is the main energetic contributor, and also because it behaves in the same way than groups UV_1 and X_1 (this does not hold true for X_2 that penetrates gas much strongly, and IR which is not generated by feedback but through re-emission). Let us see how photons look:

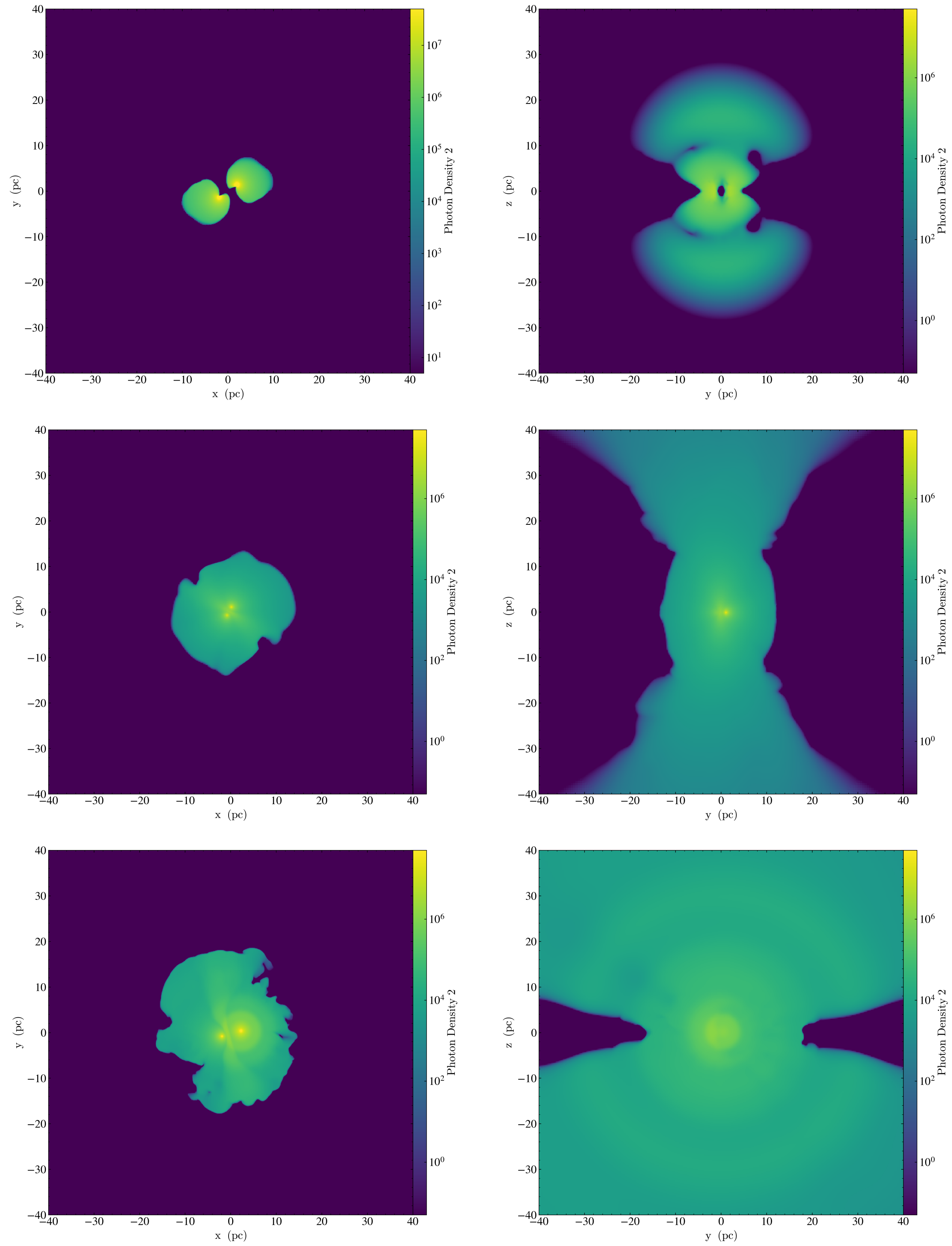

Figure 3.21: UV$_2$ photons for a2-AGN at $t = 0.2t_{\rm orb}$, $t = 1.5t_{\rm orb}$ and $t = 3t_{\rm orb}$

The first thing that is easy to appreciate is how photons have a very strong tendency to stream freely from the disk in the vertical axis. We also see how even though it is known that radiation usually prefers to transport through lower density regions, this is not majorly evidenced in the XY slices, as radiation maps tend to have a smoother gradient than density. This is mainly due to the already described evolution of the density/ion-density at the inner parts of the circumbinary ring, namely the fact that it initially has a low density that is induced by the blowback of feedback, and then as gas repopulates the center, it is highly ionized and thus of a very low opacity. We are not explicitly going to graph the differing two photons groups, but to reiterate the point we made before, if for instance we were to map out IR radiation, we would see a much larger encompassing and diffuse photon presence which softly follows the same behaviour of ionizing radiation, and if we were to map out hard X-rays, we would basically see no absorption from the gas at all.

A good way of seeing the actual interaction of photons with the gas, is to map the mean free path (MFP) of radiation. MFP codifies the expected value of the distance a random abritrary photon at $\vec{\mathbf{x}}$ would be able to traverse unimpeded given the information of the cross section and number density of said targets at $\vec{\mathbf{x}}$, ie:

$$l = \frac{1}{\sigma n}$$

As this value comes from the idea of an L sided rectangular slab of thickness $\mathrm{d}x$, the formula from which the MFP comes from is the probability of collision within $\mathrm{d}x$, $\mathcal{P}(\text{colliding within } \mathrm{d}x) = \frac{\text{Area}_{\text{targets}}}{\text{Area}_{\text{slab}}} = \frac{\sigma n L^2 \,\mathrm{d}x}{L^2} = n\sigma \,\mathrm{d}x$, where if we assume that the target areas of our different ion species are independent and cannot intersect, this means that we can actually do a direct ponderation, leaving $l = \frac{1}{\sum_{\mathrm{i}\in S} \sigma_{\mathrm{i}} n_{\mathrm{i}}}$. If we map out this field, with the information of the cross sections from the tables at 5.2 ionization states, we get:

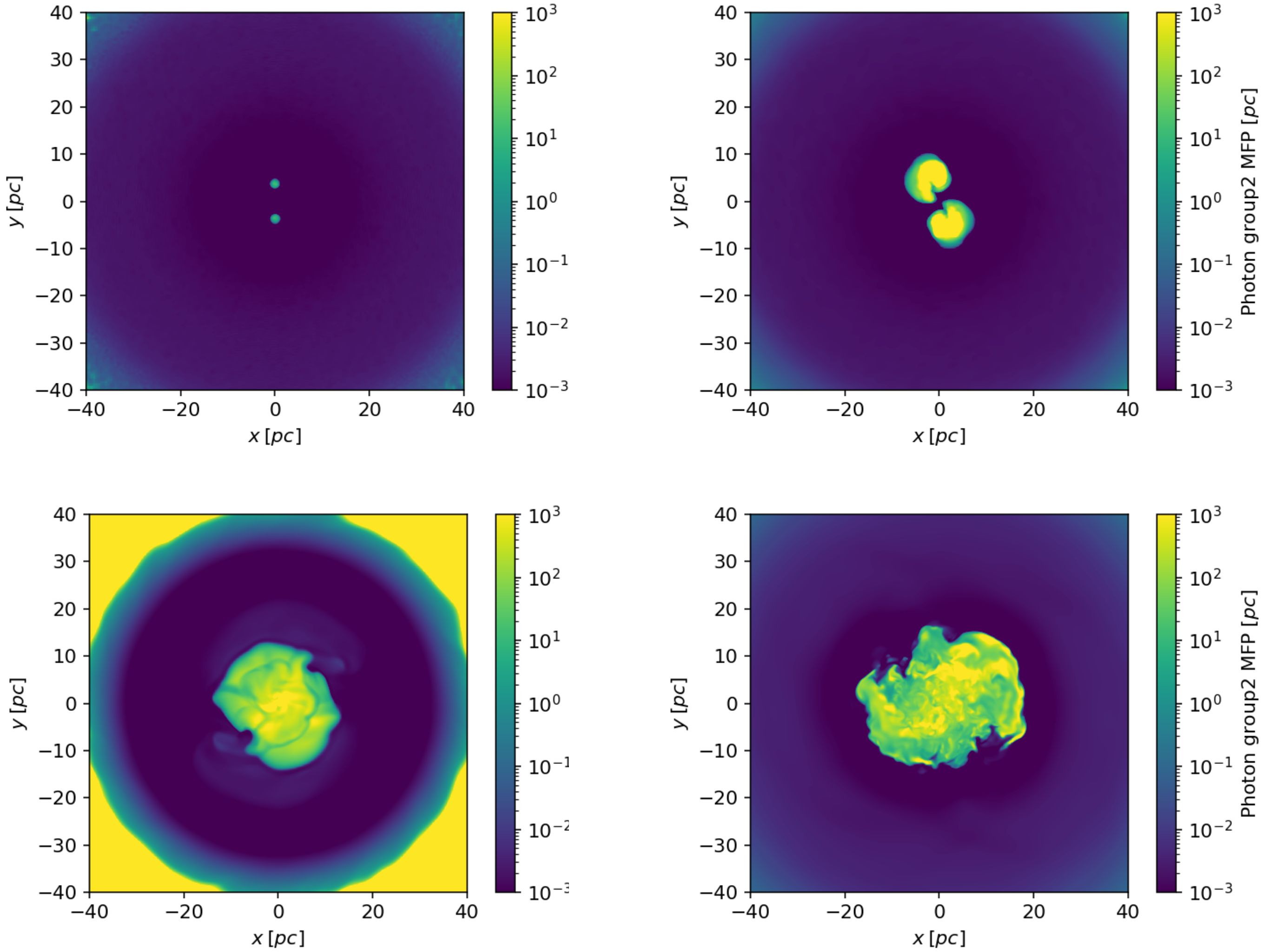

Figure 3.22: Mean free path of photons for a2-AGN at $t = 0.02t_{\mathrm{orb}}$, $t = 1.75t_{\mathrm{orb}}$ and $t = 3t_{\mathrm{orb}}$

What we are seeing here, is very telling, as we are seeing a map with an easy interpretation at all simulation times: Inner regions of the disk have MFPs that are $l > 100\,\mathrm{pc}$, which means that radiation will almost definitely penetrates onto the optically thick regions which are marked by sharp decreases to immediate values in the order of $l \sim 10^{-2}$ pc. These low opacity regions are clearly correlated initially to the low density excavated region and then with the repairing ionized central region we see in figures 3.17-3.20. Figure 3.22 finalizes the confirmation on how, feedback from the BHs will effectively move with a very high mean free path once ionized gas is funneled towards the center, which creates the configuration in which active capture of photons will only occur at a point in which the coupling is not strong enough as the radiative flux diminishes quadratically. This evolution towards a coherent, ionized center suggests how the system creates a configuration in which gas may be maintained nearby the binary, eventually moving closer back to the non-AGN version of the run.

The concept of an ionized central gas region and an ionizing radiation vertical cone in CMBs is consistent with literature (see eg: Krolik, 1999 or see figure 3.23 from Pogge, 1989 for reference)

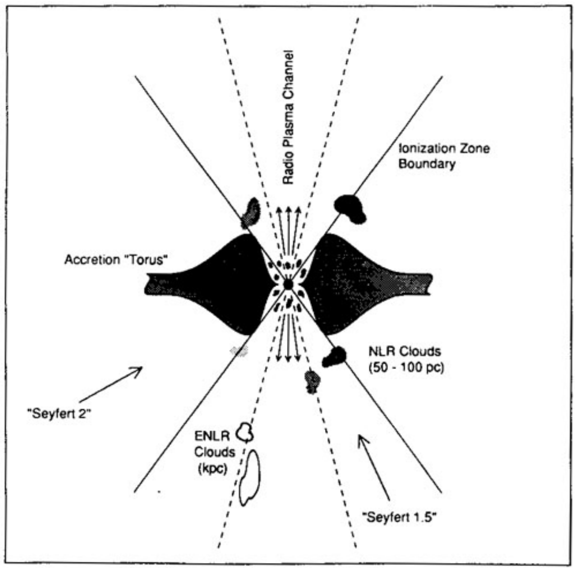

Figure 3.23: AGN schematic including photoionizing bi-cone

As a closing subsection remark, we reiterate that all the behaviour found here, is mimicked in different scales for a1-AGN. A low-density initial feedback cavity is initially carved out by radiation but it is much smaller, as is the ionized-gas region, which is expected due to the binary being much less massive in proportion to its environment. Since the disk is much less affected overall, a semblance of turning back to a stable disk appears to occur more quickly.

3.2.1.3 Evolution of binary separation

Now we remember that the final standard of impact and the overall objective of our work, is to measure the effects that including feedback has on the coalescence of our binary, and as such we proceed to look at the binary separation evolution

We see that as the initial orbit eccentricity is high, there is a clear demarcation of binary passes, but the peaks/valleys of separation do not clearly evolve, which indicates that there is no indication of a couple that would remove angular momentum of the binary. As mentioned, since we saw that disk structure seems to start regaining integrity, a gas reservoir should be nurtured on the short term to transition back towards fast migration. It is left as future work, to continue our runs until we can see an appreciable return to fast orbital decay.

3.2.2 Tidal gap opening setups with radiation feedback and coupling

It is easy to see our gap opening setups as 'less interesting' when adding feedback, as the systems already hydrodynamically push out the available gas they have, that would usually be able to remove angular momentum from the binary, and the addition of radiation should not really affect coalescence properties, as gas is now moving away from the disk's center through additional mechanisms. As in the no-gap cases, we will guide our overall analysis

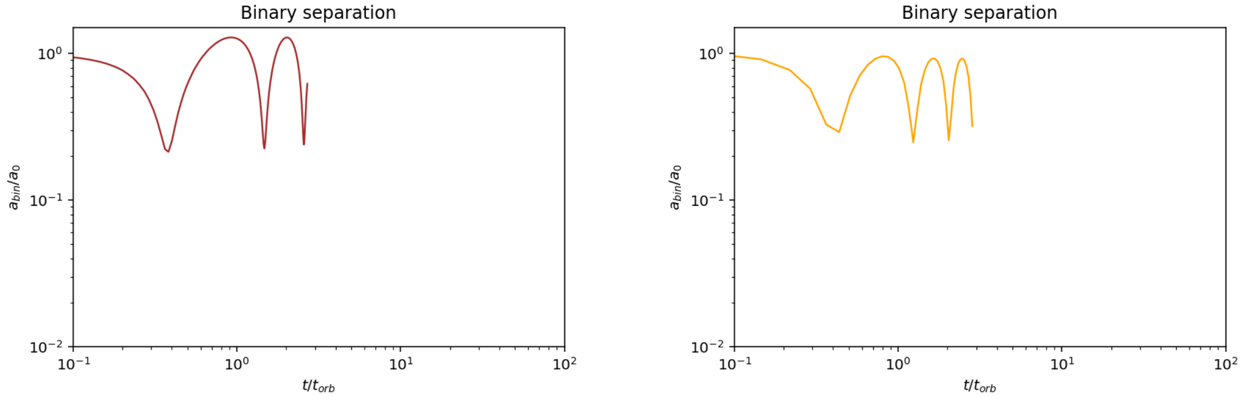

Figure 3.24: Orbital evolution for cases a2-AGN (left) and a1-AGN (right). Due to the initial orbit eccentricity we see a periodic fluctuation of orbital separation, but the decay is stalled

through focusing on one of the setups, namely we will be focusing mostly no GAP-a2-AGN over GAP-a3-AGN. It is to be noted though, the evolution of these two setups is somewhat less unified than the no-gap systems, both as the scope of this systems will be narrower and thus more focused and contextual, and because the mass fraction $M_{\rm disk}/M_{\rm bin}$ difference is very high between them (thus leaving space for more drastic changes between the two setups). It is also of notice, that as the system will dynamically tend to create a low density region surrounding the binary, accretion will be naturally suppressed, which will proportionally lead to bolometric luminosity (radiation emission) to have naturally suppressed values.

What we see happening on the course of these two setups is that indeed we see a gap forming, but the somewhat-orderly fashion in which this feature is formed on the hydrodynamical side of things, is not a given when including feedback. When tidal cavities form hydrodynamically, they do so by the removal of angular momentum of the binary's sorrounding material through the tidal perturbation it creates due to the propagaton of spiral-wave patterned wakes from that trail the BHs. In the context of the inclusion of feedback, one has to realize that the initial feedback radiation (which spreads isotropically from each BH in opposite to the spiral wake pattern that normally propagates away from the binary) that is incident onto the disk, will operate on a much faster timescale. This means that the slower hydrodynamical process in which the system will tend to form a tidal cavity has to work in tandem with the new, faster, cavity formation process, which may have different ramifications. Before going into this ramifications let us look at some XY slice density maps:

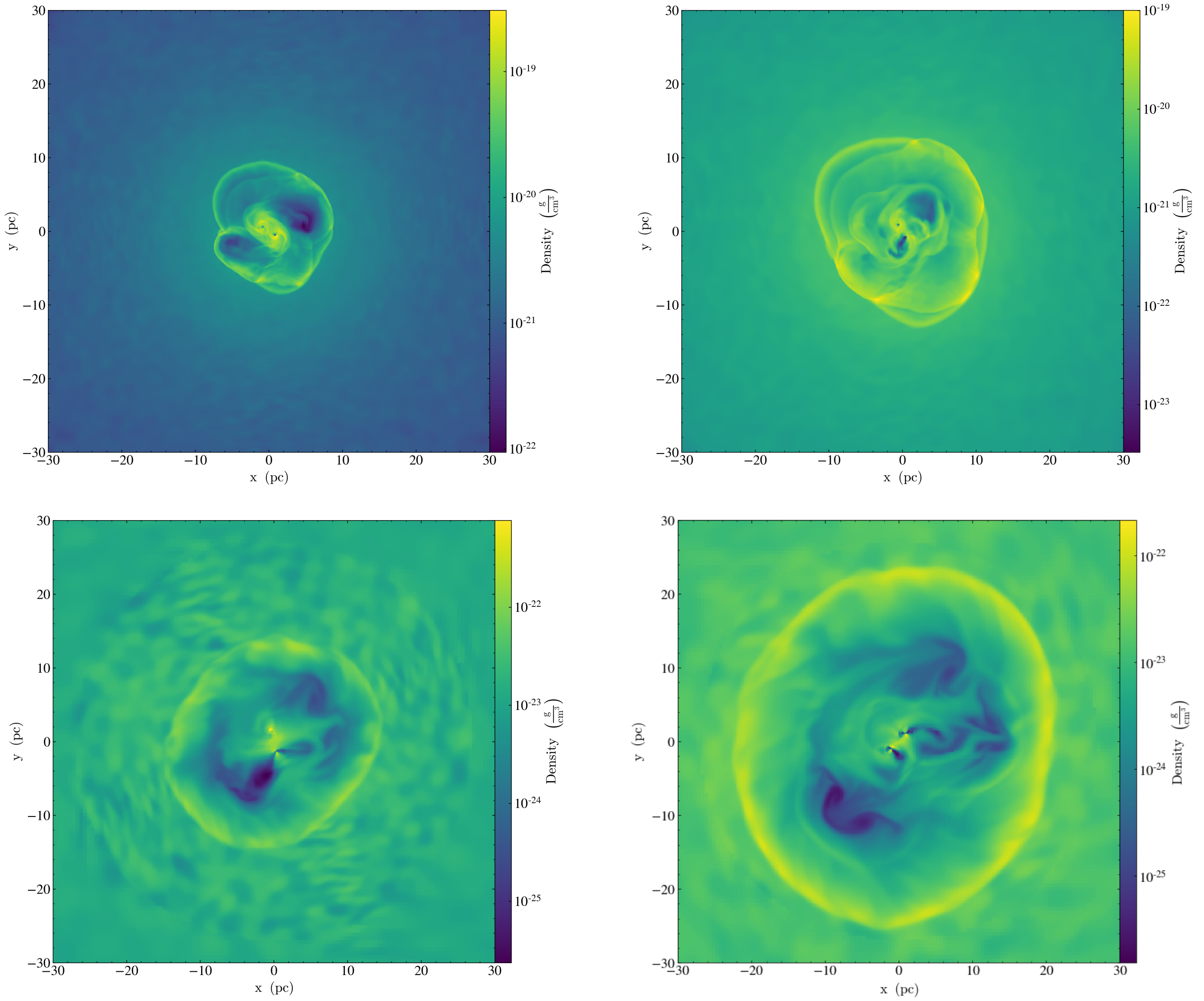

Figure 3.25: XY density slices for GAP-a2-AGN (upper) and GAP-a3-AGN (lower) at times $t = t_{\mathrm{orb}}$ and $t = 2t_{\mathrm{orb}}$

From this density slices we might notice a couple of things happening. system GAP-a3-AGN has a much more perturbed and clearly defined low density inner region compared to its non radiative counterpart at 3.6 at the same evolution time, and it has a farther reaching gas density front stemming from the initial feedback bubble than the GAP-a2-AGN setup, but still they both show a subdued feedback bubble when compared to the appreciable extended structural impact seen at 3.14. We also see, how we anticipated, how in the GAP-a2-AGN system, wakes are not as relevant at least initially (although a semblance of spiral wave propagation does start appearing as the system evolves).

At a cursory viewing of GAP-a2-AGN one might think that the tidal cavity formation is not necessarily strong, as the density contrast between the outer CMB and the excavated region is not notorious, but it is important to note that this is an artifact of mapping density as a slice (a projection in this case, also leads to misleading viewing). To elucidate this point, let us look at the lateral slice that would be the companion of GAP-a2-AGN at $t = 2t_{\mathrm{orb}}$ from 3.2.2:

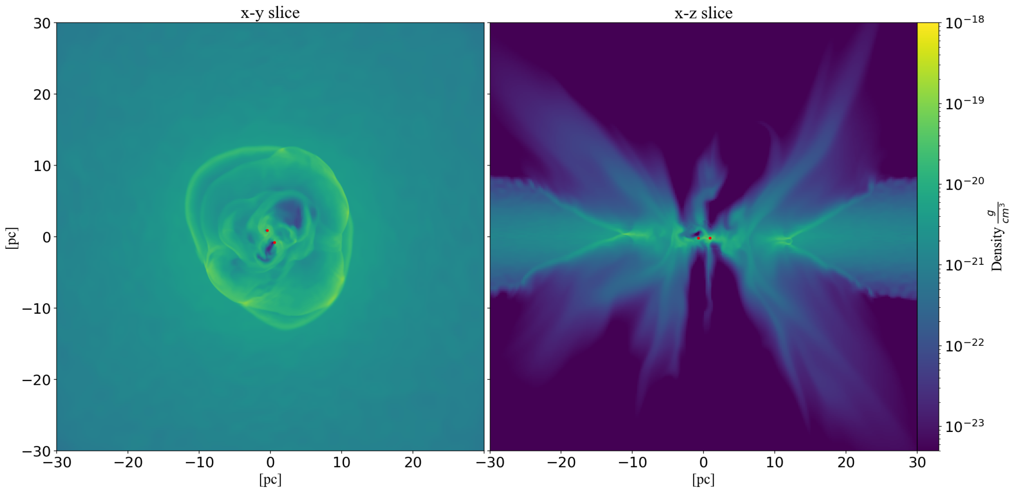

Figure 3.26: Density slices in different projected axis for GAP-a2-AGN at $t = 2t_{\rm orb}$

Here the central low density region is strongly evidenced, but now we can also observe a new feature, which is the outflowing gas that follows a conical flow akin to what the natural geometry to which radiation conforms in the XZ axis. There are several moving pieces here that have to be mentioned, and a good start is to look at the actual magnitude of emitted luminosity:

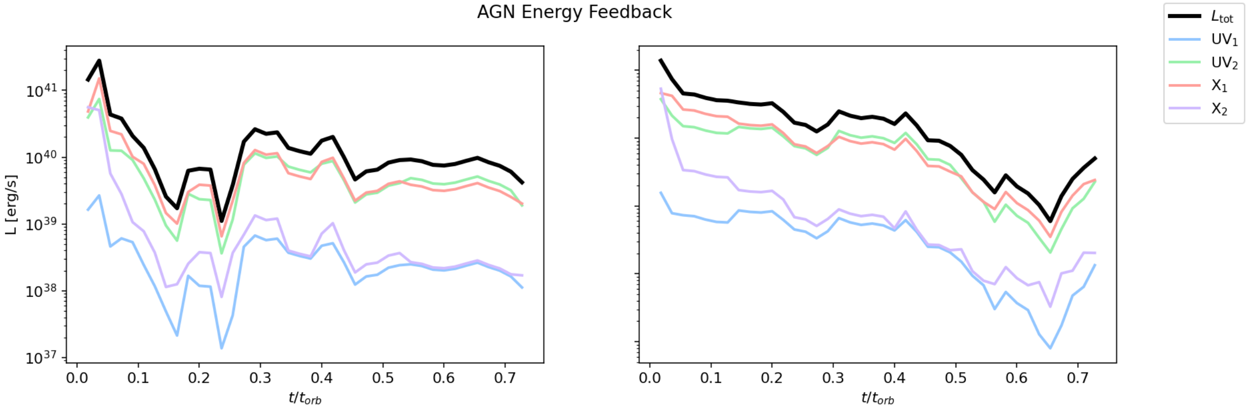

Figure 3.27: Net radiated energy and specific photon group radiated energy for GAP-a2-AGN

This shows how, the net amount of radiation is around $1 - 2$ orders of magnitude lower than what is seen at 3.16, which means that on a superficial level, the impact of feedback will be lower (as the disk has the same mass). This is directly correlated with the radiation bubble being much smaller than in non-gap forming systems. The feedback bubble being small does not mean that radiation does nothing, as gas is swept up from the disk by feedback.

3.2.2.1 Disk photoevaporation

This swept material is expelled from the gap's inner limit mostly as singly ionized gas, with a large fraction at speeds that exceed the escape velocity of the system. Some material is steadily expelled during all the simulation, as gas that is not strongly bound to the disk is not maintained as highly ionized at the the cavity's interface, both because there is mixing between ion species at the interface where viscosity is trying to refill the low density gradient and mostly because radiation is too spread out to ionize too deeply into the denser regions of the disk (see 3.28), and as such, couples efficiently to the highly energetic radiation.

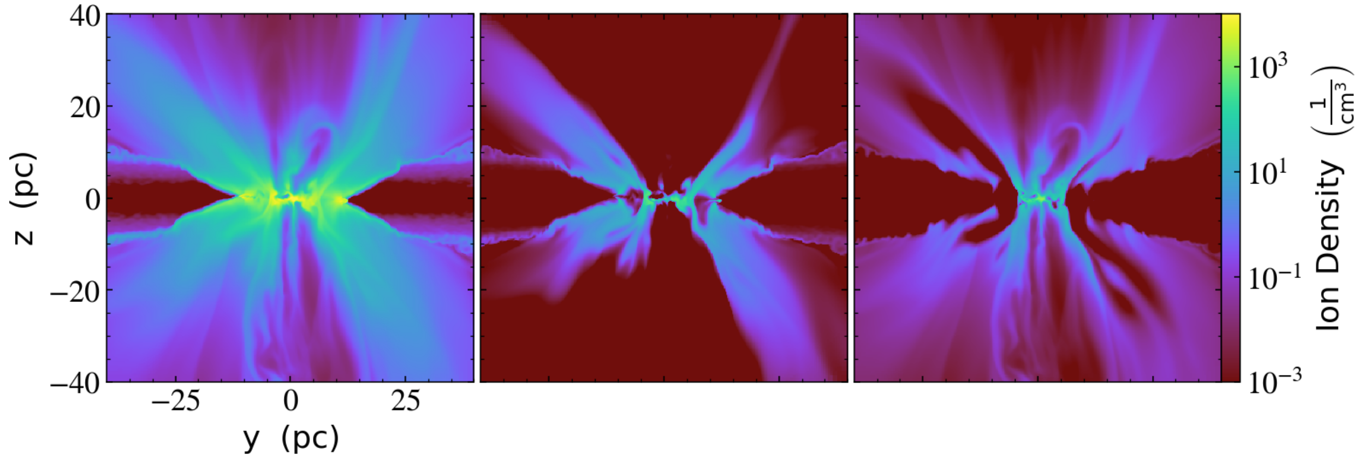

Figure 3.28: H_{II}, He_{II} and He_{III} ion number density XZ slice for GAP-a2-AGN at $t = 2t_{\mathrm{orb}}$

This process in the context of protoplanetary disk theory, is known as 'disk photoevaporation' (see eg Alexander et al., 2006) and has been widely studied in systems with highly ionizing radiation sources in their centers. The amount of ejected mass is not high enough to pose a structural risk to the system, and eventually will have to stabilize, as the low density region becomes bigger, accretion decreases (see fig 3.32, this by proxy will also decrease ionizing radiation) and the inner boundary of the gap becomes both more ionized and thinner. We have to keep this mind, for instance when comparing density profiles of this setups with their non-radiative counterparts, as we should not count material that is unbound from the disk when making this comparisons. First we approximate the escape velocity (as it has no analytic expression) by doing

$$v_{\mathrm{esc}}(R) = \sqrt{2GM(<R)/R}\,;\;\; M(<R) = M_{\mathrm{bin}} + M_{\mathrm{bulge}}(<R) + M_{\mathrm{disk}}(<R)$$

Where M_{bulge} comes from a Plummer profile $M_{\mathrm{bulge}}(<R) = M_0 \frac{R^3}{(R^2+a^2)^{3/2}}$, and M_{bin}, $M_{\mathrm{disk}}(<R)$ come empirically from the simulation. We then tag all gas that fulfills $v(\vec{r}) \cdot \hat{r} > v_{\mathrm{esc}}(r)$, as gas that is unbound and shall not be considered as part of the disk for density/mass profiling. Let us see how the density profiles for the times at 3.2.2 are when considering both bound and unbound material:

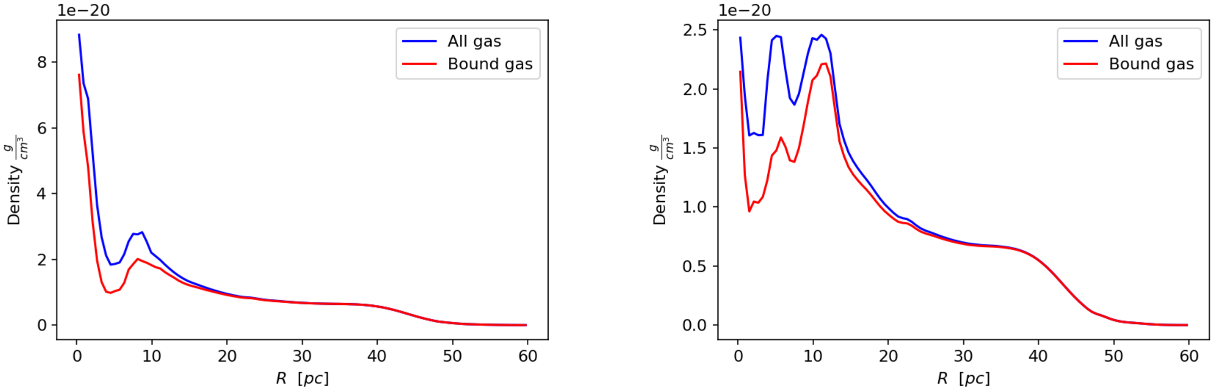

Figure 3.29: Density profiles when considering unbound material for GAP-a2-AGN at $t = t_{\mathrm{orb}}$ and $t = 2t_{\mathrm{orb}}$

If we were to see the same profile for the non-radiative system, also taking into account whether there is unbound material or not, we get at $t = t_{\mathrm{orb}}$:

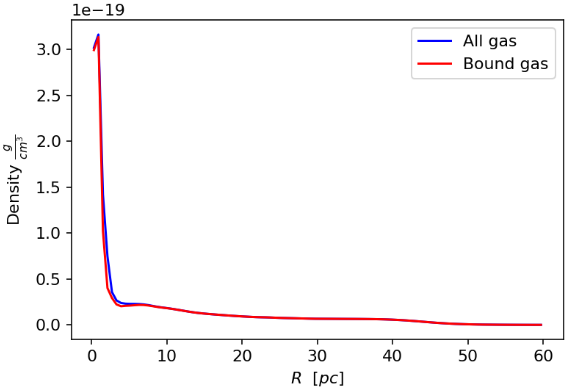

Figure 3.30: Density profile when considering unbound material for GAP-a2 at $t = t_{\mathrm{orb}}$

We see that indeed setups without radiation are not strongly affected by this elimination of mass, and we can also see how it may be misleading to effect comparisons on density profiles between radiation and no-radiation setups without taking into account photoevaporation, as they might look artificially similar.

This differences will inevitably mean that the posited idea put forward in VV18, that these setups have the same behaviour and almost the same structure that their counterpart in simulations without AGN feedback, does not hold for this implementation of feedback. In fact, if we were to measure the amount of net mass that is lost through time by the AGNs' influence, we see that it boils down to:

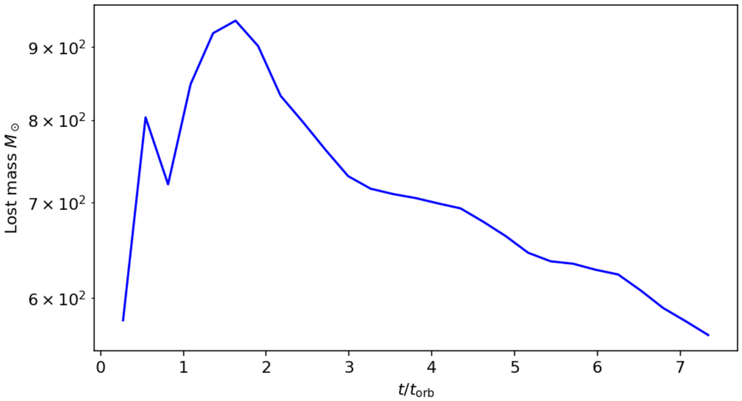

Figure 3.31: Net mass loss to photoevaporation in time

We see that the net amount of unbound material (at least on a 30pc height around the disk) is lowering with time, due mainly to the fact that of accretion -and therefore feedback- is lowered. This speaks about how at first approximation, disk evaporation in our setups is a self-regulated process, where as the disk thins out and the gap is markedly formed, accretion will slow down and evaporation will naturally slow down as well. This may also mean that the eventual pseudo-equilibrium state of this self-regulated disk, will have a bigger gap and thinner disk that we would see without the presence of feedback.

The accretion graphs for both gap-forming setups show steady decreases, specially for GAP-a3-AGN:

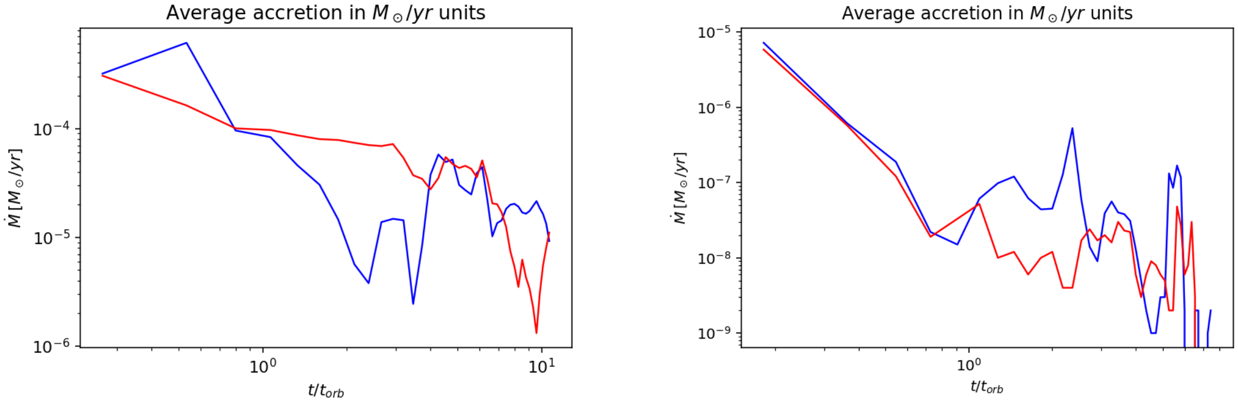

Figure 3.32: Density profiles when considering unbound material for GAP-a2-AGN at $t = t_{\mathrm{orb}}$ and $t = 2t_{\mathrm{orb}}$

What does still hold true in terms of similarities for both setups, is the behaviour of the orbital decay. As we had predicted, material is still being funneled away, and as such the gas budget for angular momentum removal is effectively decreased. This means that the root cause for slow migration stays, thus leaving us with the following binary separation graphs:

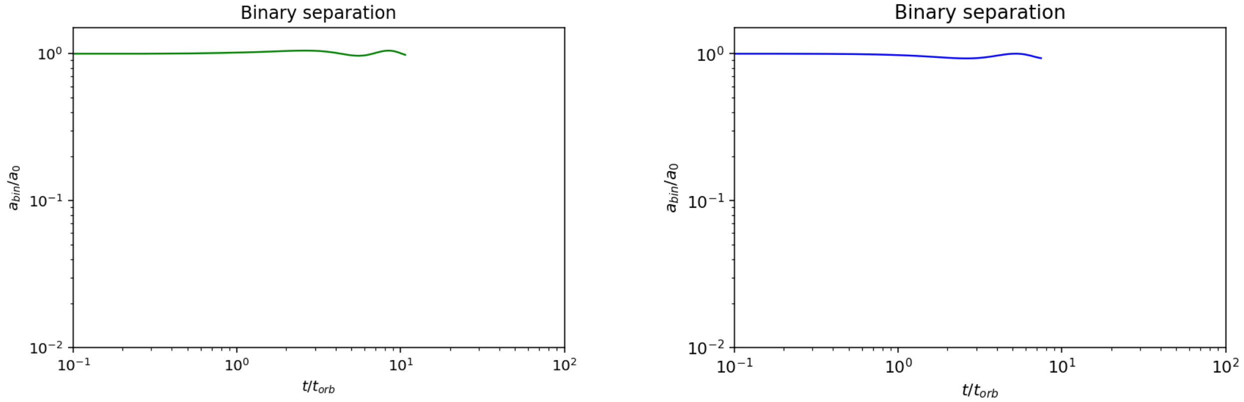

Figure 3.33: Orbital evolution for cases GAP-a2-AGN (left) and GAP-a3-AGN (right). As in the case without radiation, orbital separation becomes approximately flat

This confirms how indeed separations are hold almost at a constant value except for almost negligible perturbations that can be seen after some orbital times have passed. This finalizes our idea that, although the inclusion of AGN feedback is not something to ignore for tidal cavity forming setups in the overall picture, it will not be a facilitator for SMBH binary coalescence.

3.3 Overall Trend Similarities and Changes

3.3.1 Speed of Sound and rotational velocity

Let us begin by noticing the changes in sound speed throughout our simulations both with and without feedback, and the changes in rotational velocity:

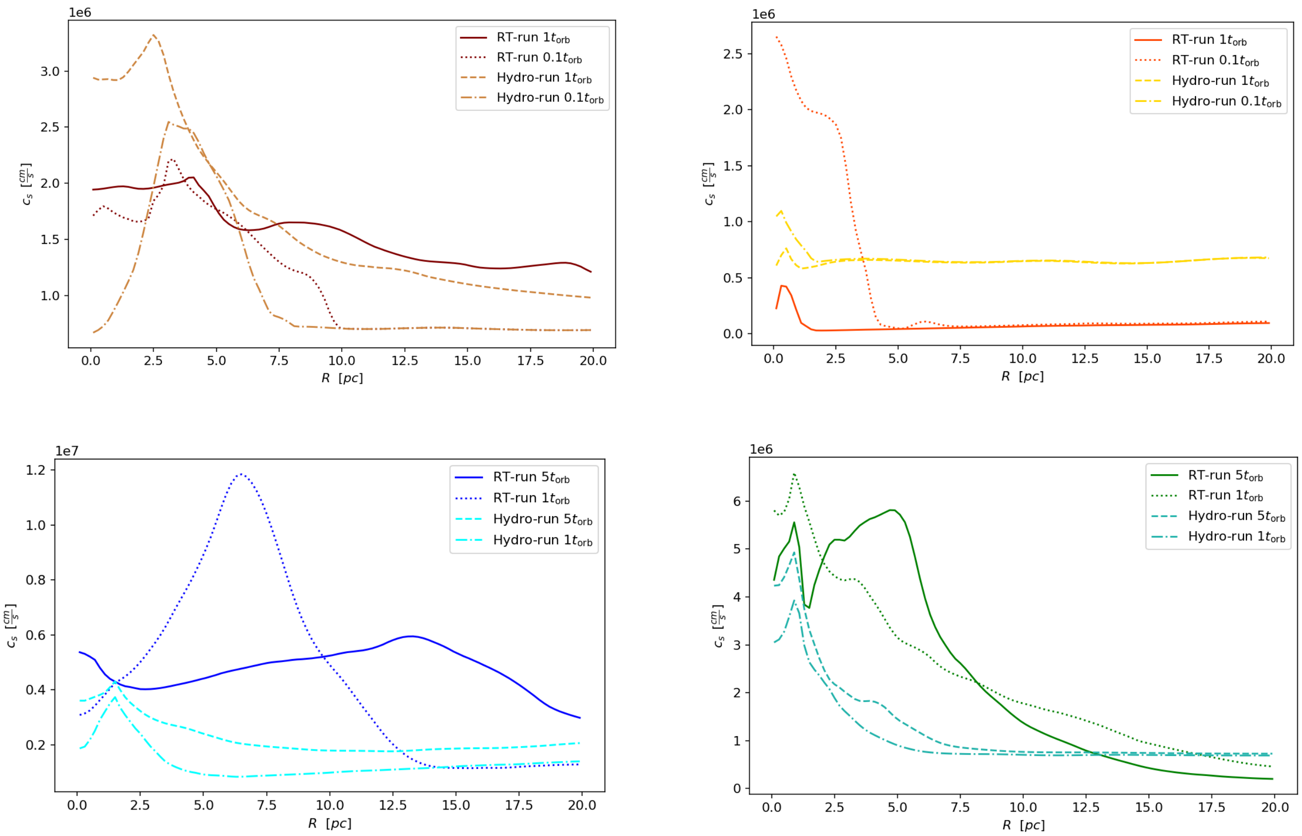

Figure 3.34: Sound velocity c_s radial profiles for all simulation setups. No-gap simulations were profiled at times $t = 0.1t_{\rm orb} \wedge 1t_{\rm orb}$ and gap simulations were profiled at times $t = 1t_{\rm orb} \wedge 5t_{\rm orb}$

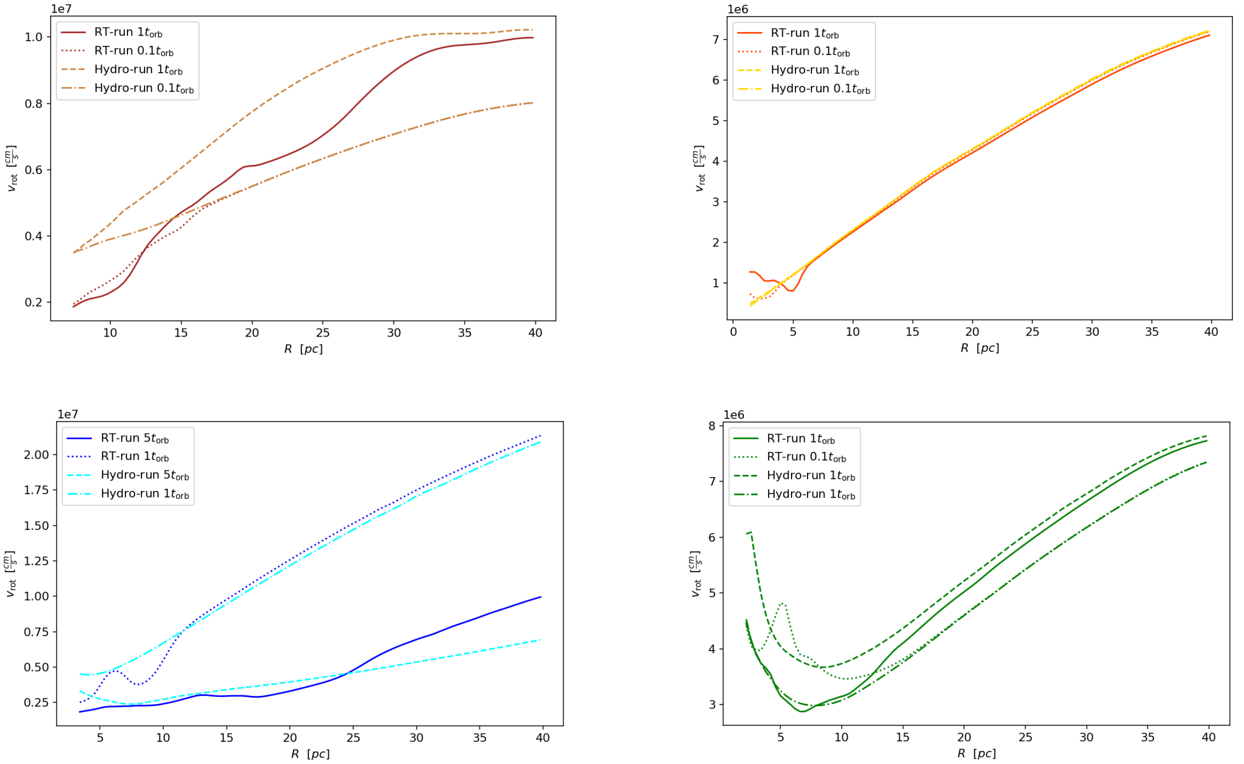

Figure 3.35: Rotational velocity v_{rot} radial profiles for all simulation setups. No-gap simulations were profiled at times $t = 0.1t_{\text{orb}} \wedge 1t_{\text{orb}}$ and gap simulations were profiled at times $t = 1t_{\text{orb}} \wedge 5t_{\text{orb}}$

The first thing of notice here, is that if we look at the plots in 3.36, independent of the setup, there are no major differences in rotational velocities between the radiative feedback and purely hydrodynamical setups except to some small degree at earlier times in the central disk areas, which is due because the initial feedback perturbs the overall velocity field. This point to the fact that the isotropic pressure from feedback that the SMBHs induce onto the disk, does not remove angular momentum from the disk at large scales. At the same time it is important to note that these profiles are all started from $a_{\text{bin}} + \max r_1^{\text{hill}}, r^{\{}\text{hill}_1\}$ on out, as rotational velocity is not well defined as a disk concept for the regions that surround the BHs inside their hill spheres (where material will tend to rotate around them).

In opposite, for sound speed we see a big spread between the behaviour of different setups, specially at the central regions, where this values may vary a lot with the presence of a feedback cavity, that may rapidly heat the environ near the binary.

This two quantities paint a picture on how feedback affect the kinematics/dynamics for different setups, kinematics that are inherently linked with the gravitational stability of the disk through Toomre's parameter (equation 3.3.1):

$$Q = \frac{c_s \kappa}{\pi \Sigma G}$$

If we plot the radial profiles to quantify the evolution of this parameter in the same way we constructed the already seen radial plots, we get the following:

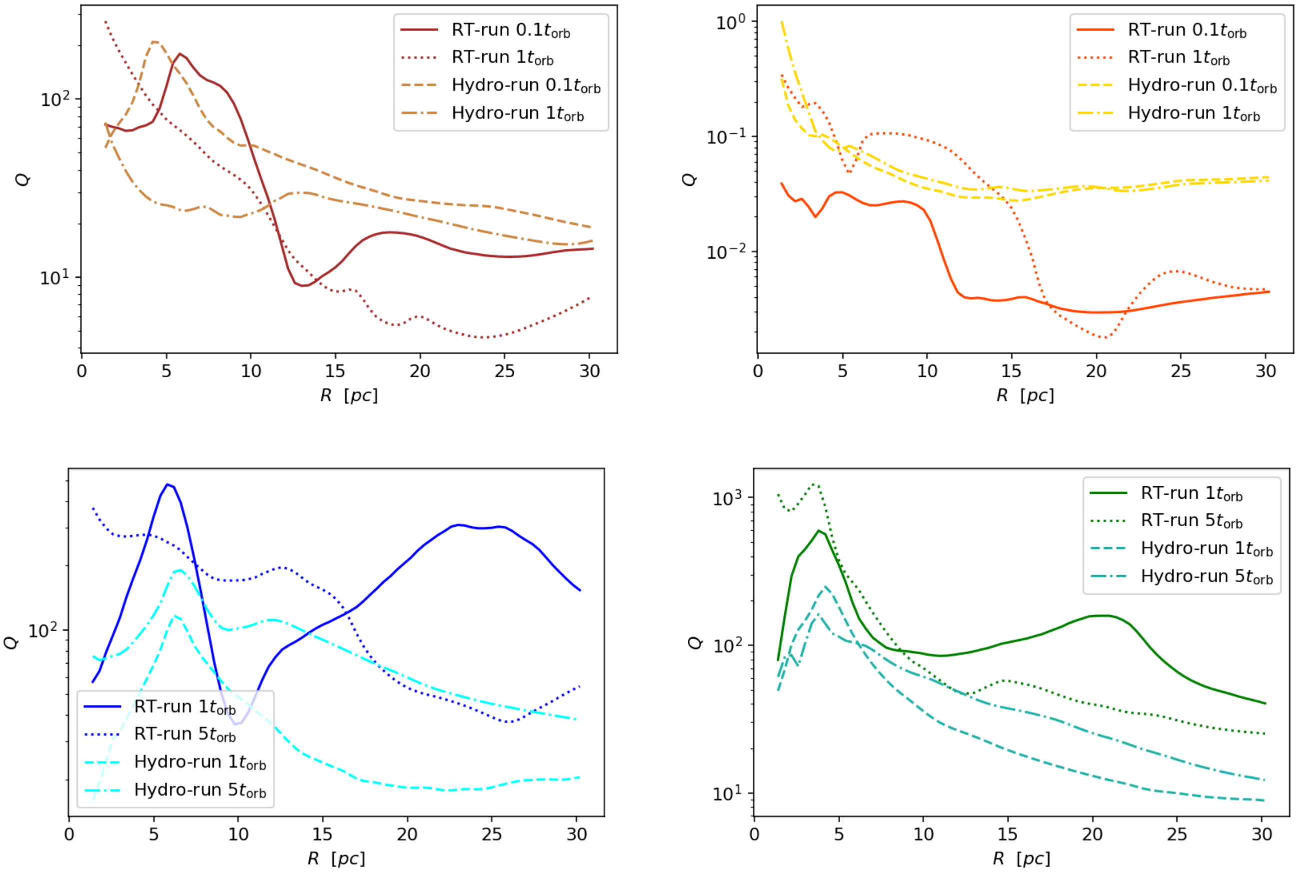

Figure 3.36: Toomre parameter Q radial profiles for all simulation setups. No-gap simulations were profiled at times $t = 0.1t_{\rm orb} \wedge 1t_{\rm orb}$ and gap simulations were profiled at times $t = 1t_{\rm orb} \wedge 5t_{\rm orb}$

We see here that non-gap forming setups generally lower their Q parameter specially on the outer radial regions. We see a somewhat opposite trend for gap-forming setups where the radiation runs exhibit a more erratic radial behaviour which stems from doing a vertical projection and integration for the acquiring of the quantities involved in the parameter's calculation, as we are inadvertently taking into consideration unbound material, which as explored in last section may introduce errors. It is also worth to remember what we mentioned for the profiling of rotational velocities, that the parameter is not well defined for the inner regions of the disk as gas does not have a well defined epicyclic frequency κ (the profiles above were made ignoring this point for the inner regions, where the epicylic frequency is just calculated using the simulation center as the reference for the rotational frame).

More important than the actual radial tendencies here, is the fact that the Toomre parameter is kept very high above the gravitational stability threshold. This is naively consistent with what we see, as no fragmentation is observed in any of our runs (as predicted by the selection of the setups), but there are additional considerations to be made as the derivation of the Toomre parameter is based only on dynamics and does not take into account the presence of radiative cooling/heating, thus at the moment only serving as a lower threshold type of criterion.

3.3.2 Disk stability and Heating/Cooling

Self-gravity may be important in the cool outer regions of accretion discs, where the combined effects of pressure and shear cannot stabilize the flow against gravitational instability. The local linear stability of self-gravitating discs is simple (Toomre, 1964) and it depends upon the accordingly named parameter 3.3.1, which as we mentioned, may not be enough to inform our analysis of disk stability.

The non-linear behaviour of stability is complex, as a self-gravitating disc can either fragment into bound objects, or attain a 'stable' self-gravitating state in which angular momentum transport results in accretion and energy dissipation. In the context of our simulations, a local description of thermal equilibrium implies that the stress, is inversely proportional to the time-scale on which the disc can radiate its thermal energy (Gammie, 2001). Due to this we employ a method similar to Gammie's parameter of

$$t_{\text{cool}} \cdot \Omega =: \beta > 3 \tag{3.4}$$

Where t_{cool} is the cooling time from 1.36. This criterion is still limited as it assumes that the heating/cooling processes of the disk are spurred by turbulence, and just as the Toomre parameter, it has been shown to be inadequate at predicting fragmentation in disks with radiative transfer (Tsukamoto et al., 2015). We retain the main idea of comparing the local heating rates to the cooling rates, where we will have the cooling time due to radiative losses, and heating due to photons and viscous diffusion. The viscous dissipation rate is given by $Q_v \mathrm{d}s \approx rH\tau_{r\phi} \cdot \mathrm{d}\Omega/\mathrm{d}r \approx (9/4)\Omega^2\nu\Sigma$. With this, we will finally look at the ratio

$$\Pi = \frac{t_{\text{cool}}}{t_{\text{heat}}} = \frac{\varepsilon}{\dot{\varepsilon}_-} \cdot \frac{\dot{\varepsilon}_+}{\varepsilon} = \frac{\dot{\varepsilon}_+}{\dot{\varepsilon}_-}$$

There are two immediate caveats when trying to deploy this criterion directly: The first is that we cannot apply it where Ω is not well defined (see 3.3.1), and the other problem lies in the fact that our viscous dissipation approximation depends on the disk possessing angular symmetry. What we do to cope with this last point, is to define regions in which assuming disk symmetry is valid, and only applying checking the criterion where this symmetry holds.

We could try to replicate the analysis on 2D by profiling values in (R, ϕ), and try to quantify viscous dissipation without symmetry-holding approximations by doing explicit calculations of a stress tensor $\tau_{r\phi}$, but in reality the non-symmetrical perturbations come from the direct influence of the SMBHB (through wakes, torques, resonances, etc.), and as such the analysis becomes too contextual when trying to analyze the disk that surrounds it. With this in hand, we separate the interval from where symmetry is a valid assumption in the disk, by analyzing its departure from it on a binned radius basis. The exposition to radiation should be symmetric enough in the long run, as the only important non-axisymmetric presence could come from the binary's self obscuration, but the sources are isotropic enough, the inner region is not dense enough (in the presence of gaps) and radiative transport is diffusive enough for this not to be a relevant issue when modelling β.

Like in the analysis of Galactic spiral structure (see eg: Binney and Tremaine, 2008 or Durbala et al., 2009 for a practical example), since the perturbation of the disk comes from a binary excitation, we can indirectly quantify its non symmetric component by measuring the density enhancement by trying to fit a Fourier series to the surface density at fixed R's, seeing how $\Sigma_R(\phi)$ behaves and how it relates to the strength of different Fourier modes. more explicitly we expand:

$$\Sigma(R,\phi) = A_0(R) + \sum_{m=1}^{\infty} A^c_m(R)\cos(m\phi) + A^s_m(R)\sin(m\phi) \tag{3.5}$$

In practice we define a fixed resolution buffer map for the integrated z density, partition said map in certain R bins, and we then do a least-squares non-linear fitting of the 3.5 expression truncated at a finite polynomial order of at least $5-10$ for a binned ϕ profile at the fixed radial interval. With this fitting we can test mode strength by observing the values

$$\zeta_m(R) = \frac{A_0(R)}{A_m(R)}\ ; \quad A_m(R) = \sqrt{(A^c_m(R))^2 + (A^s_m(R))^2} \tag{3.6}$$

Usually to ascertain that arm structure is present, a relative mode strength of at least $\zeta_m \geq 0.15$ is used. For our cylindrical radius threshold of analysis we require that no Fourier amplitude exceeds $\zeta_m = 0.05$. This means that if we are doing a fitting with a maximum number of M Fourier modes, we will consider a radius interval of analysis for 3.4 of $r \in I := [\hat{R}, R_{\text{disk}}]$, where $\hat{R} = \min\{\tilde{R} > 0 :\ \zeta_m(R) \leq 0.05,\ \forall m \in [M],\ \forall R \geq \tilde{R}\,\}$.

Let us consider for instance the no radiation run for the gap opening scenario GAP-a2 seen at $t = 8t_{orb}$ in 3.1.2. Visually there is a clear evidence of a strong two-armed density enhancement in the gap region, and since the binary has already completed several circular periods we may also expect smaller different order density enhancements. Indeed if we plot the evolution of the first mode amplitude for 6th-order fitting we get: Where we observe

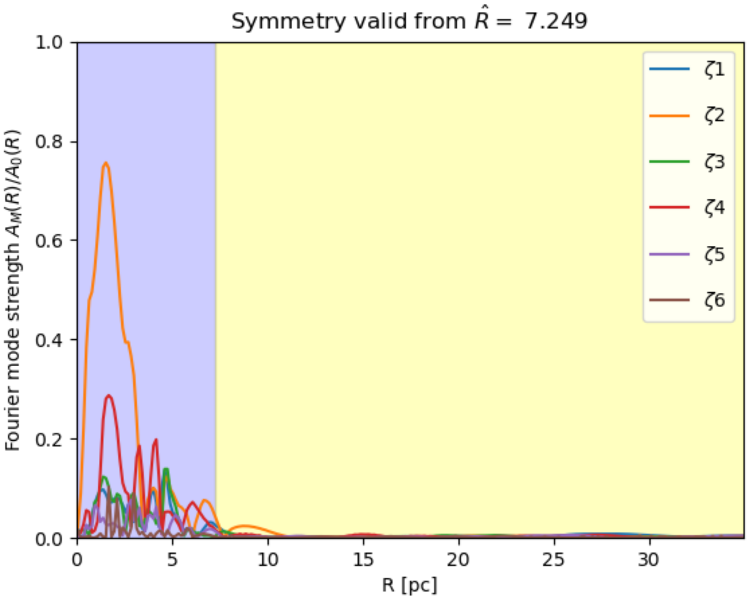

Figure 3.37: Radial profile of $\zeta_m(R)$ example: GAP-a2 at $t = 8t_{orb}$

that after $\hat{R}$ there is a clear delineation of lower oscillations in the ϕ variable, and where as expected the 2-fold perturbation is by far the most prominent due to the origin of it coming from the rotating SMBH-binary influence. We can see that ζ_1 is not an important contributor to the Fourier fitting, implying that there is not a strong lopsided perturbation of the density field. As expected, higher order terms are also minor contributors to the mode strength when modelling (but will be included when performing the actual analysis of viscosity, as to achieve as most consistency as possible).

With all this we have established the framework for a consistent mapping of fraction between cooling and heating processes. Before checking how the cooling/heating fraction behaves, let us first look at how cooling evolves on isolated terms. If we were to graph each cooling rate Λ [ergs/s] associated to the formulae from tables 1.1-1.2 (we separate the rates depending on the ion species they are associated, excluding Bremsstrahlung and Compton cooling), we get for simulation a2-AGN:

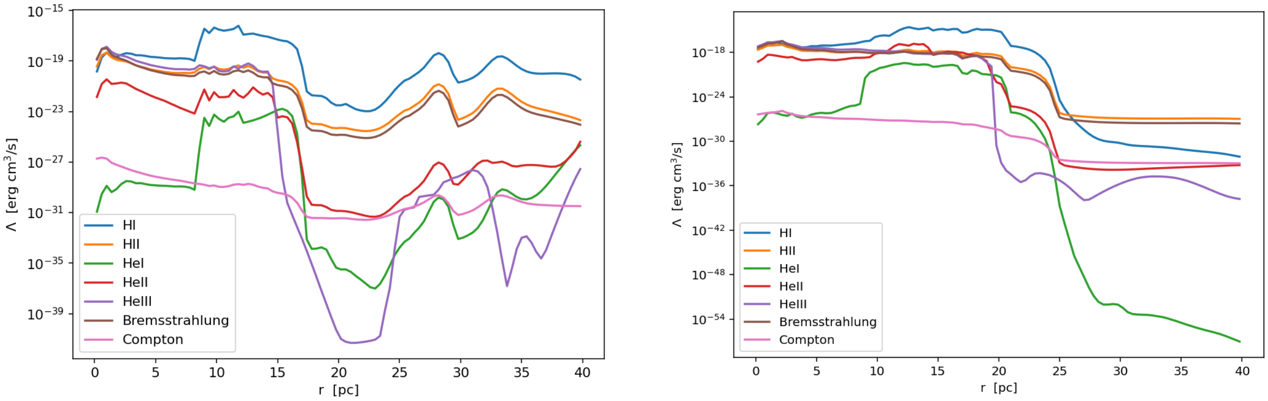

Figure 3.38: Cooling rate radial profiles with the separated contribution of different processes for simulation a2-AGN at times $0.2t_{\mathrm{orb}}$ and $1.5t_{\mathrm{orb}}$

At the same time if we plot the same cooling contributions for GAP-a2-AGN we get:

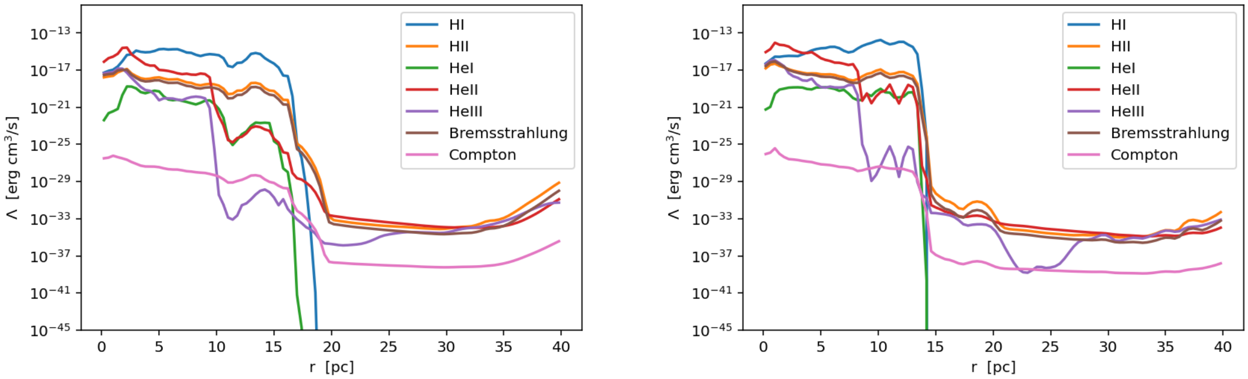

Figure 3.39: Cooling rate radial profiles with the separated contribution of different processes for simulation GAP-a2-AGN at times $1t_{\mathrm{orb}}$ and $8t_{\mathrm{orb}}$

With these graphs in hand we may observe first how there is a clear indication of how in terms of strength, processes that are associated with hydrogen (specially H_I) are the main contributors to radiative cooling, whereas it is clear that Compton cooling is consistently the least important mechanism (excepting instances where cooling ionized Helium mechanisms on the outer regions of the disk is extremely low). We also see in the non-gap system, how in the later stages ionization fraction pays a big role, as how between $5-10$pc where the 'Strömgren' area of ionization is located introduces not only overall changes to the rates, but also to the separation between mechanisms (non-ionized associated processes increase much more sharply than ionized associated processes). The final and probably most important takeaway, is how cooling as an overall net physical process slows down as time progresses, and at the same time becomes less centrally concentrated.

If we now move towards checking how cooling and heating balances out, let us see first how radial profiles for simulation a2-AGN look:

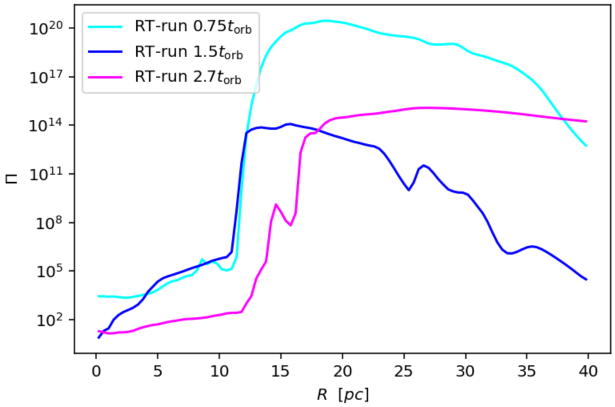

Figure 3.40: Different radial profiles for our Π parameter for simulation a2-AGN. For these profiles viscous heating was only considered above $\hat{R}$

We may also see the accompanying maps for the parameter for times $1.6t_{\rm orb}$ and $2.7t_{\rm orb}$:

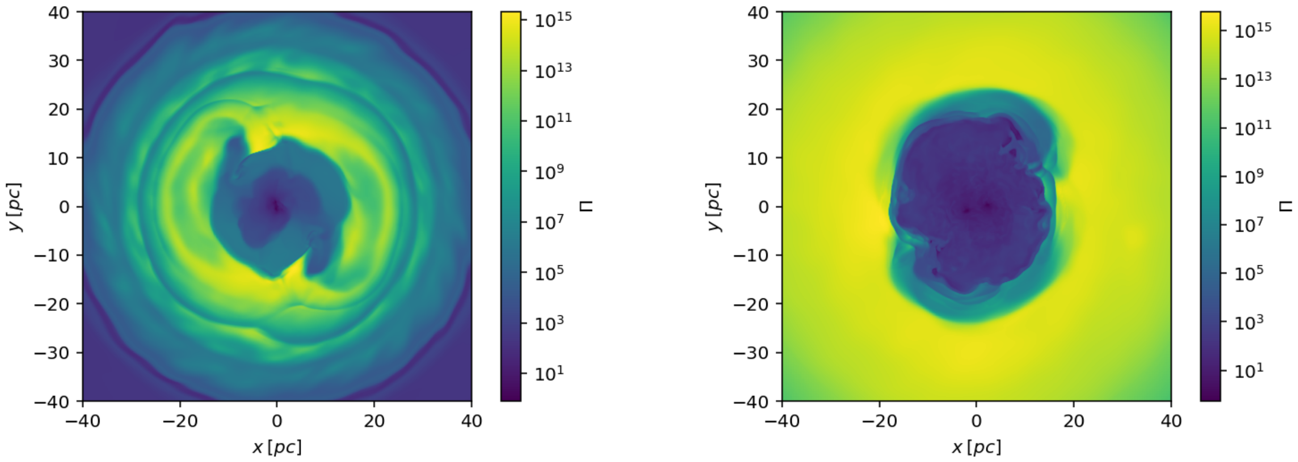

Figure 3.41: Π parameter projected XY maps for simulation a2-AGN at times $1.6t_{\text{orb}}$ and $2.7t_{\text{orb}}$

We first notice how our heating/cooling fraction is all around, above $\Pi > 1$, in some ways following the line set by our exploration of the Toomre parameter, which was comfortably over the stability threshold. We see that our ionized gas region where photons flow almost free, shows a sharp contrast to the non-ionized region in terms of Π, where the parameter reaches values in the range of $\Pi \in [1, 10]$:

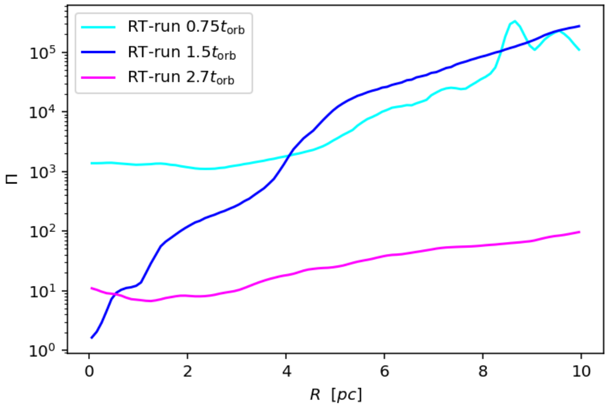

Figure 3.42: Different radial profiles for our Π parameter for simulation a2-AGN (same as figure 3.43 but zoomed at $R = 10$pc).

The fact here that this fraction nears unity at the inner regions is consistent with how radiation is not an efficient heating vehicle when it tries to couple with ionized material. It is still above the threshold, which makes sense, as no fragmentation occurs, and we see an overall lowering of the region's values as photoheating becomes less efficient and gas begins falling back towards the disk (at $t = 0.75t_{\text{orb}}$, gas at the nuclear disk regions is still in its AGN-blown state, and as such quite hot). As threshold values are kept above unity, and fragmentation does not occur we can only ascertain for the moment, that our criterion is consistent with this reality, but this still opens up and avenue for future work, where we could simulate setups that live near the fragmentation phase space interface and then test the consistency of using thermal energy balances to quantify the stability tendencies of a system, and potentially calibrate an actual stability threshold through .

Although we have already established how all the Π fraction maps will point to values comfortably above > 1, we still see very high value variances throughout simulation snapshots (with maximum/minimum Π value differences of up to $7 - 8$ orders of magnitude). It is easy to see from our criterion graphs, that most of the contrast is between central disk regions and outer disk regions, which could naively lead us to believe that these contrasts are aided on how viscous heating is only 'turned-on' in our estimations outside the symmetry radius $\hat{R}$. It is easy to dismiss this idea by just looking at figure 3.43, where we may that heating/cooling contrasts are much more prolonged than what the actual values that $\hat{R}$ take (which usually turn out to be $\sim$ 5pc). It is also of notice how, viscous dissipation is consistently at least 3 orders of magnitude lower than radiative heating for most our simulation cases. In reality the criterion follows photon concentrations more closely than anything, which explains the similarities in figure 3.43 between the initial states and the latter states, as heating will be inexorably linked to photon mean free path. We note that although viscous heating is indeed lower than radiative heating, it still enough to balance out cooling losses even at more initial states where radiation is not as prevalent as in more advanced points throughout our simulations. For instance, if we were to try to use Gammie's criterion directly (equation 3.4), using the cooling time as we calculated it, but making the assumption of turbulence-driven heating, we see the following result for a scaled parameter graph ($\beta/3$) at initial times for a2-AGN:

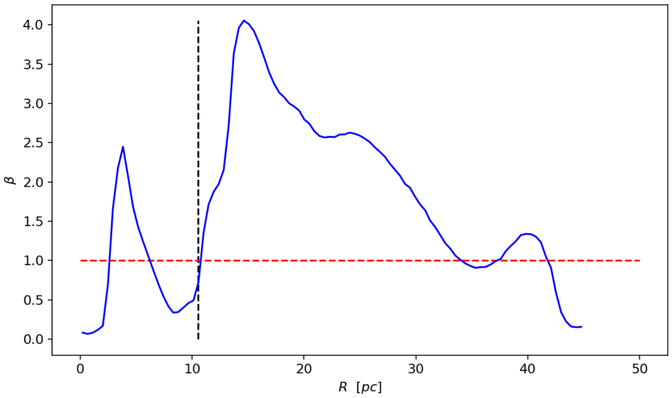

Figure 3.43: Gammie's scaled stability criterion $\beta/3$ for a2-AGN at 0.1torb. The vertical black-dotted line represents $\hat{R}$, and the horizonta red-dotted line represents Gammie's stability threshold.

Here we see that even simplifying and underestimating gas heating, this stability criterion does not break the fragmentation threshold, except at the edges of the disk at $\sim$ 45pc and at points where the symmetry is not well established and rotational velocity is not well defined (indeed, the threshold values line up almost perfectly with the point at which symmetry is reached). This means that our disk may even have its stability supported even by secondary heating mechanisms.

Chapter 4

Post-processed analysis of BH spin evolution

Understanding the evolution of BH angular momentum is critical for predicting and unveiling the spin configurations with which SMBH binaries enter their gravitational wave driven regime and become detectable by LISA/LIGO. BHs, their immediately surrounding accretion disk, and the circumbinary disk that hosts them, do not necessarily possess immediately aligned spins. This is to be expected, as the binary-disk assembly process up to the hardening stage, may strongly depend on interactions with randomly oriented stellar encounters. It is in this stage that gas accretion becomes a major player in spin orientations, where in the long-run angular momentum misalignment is expected to correct itself through a process known as the *Bardeen-Peterson effect* and is due to a combination of general relativistic frame dragging and viscous interactions (Bardeen and Petterson, 1975, Kumar and Pringle, 1985). In our case we could potentially observe variations in the typical alignment times due to the accretion flow being more chaotic, due to AGN feedback.

4.1 Model and postprocessing setup

Typical iterations of the Bardeen-Peterson effect involve modelling the evolution of a non-planar disk structure, with the presence of a warp that propagates non-linearly due to viscosity. The exchange of angular momentum between the disk and the BH is affected by the disk's geometry and how it deforms. A basic scheme of how this looks is illustrated at figure 4.1:

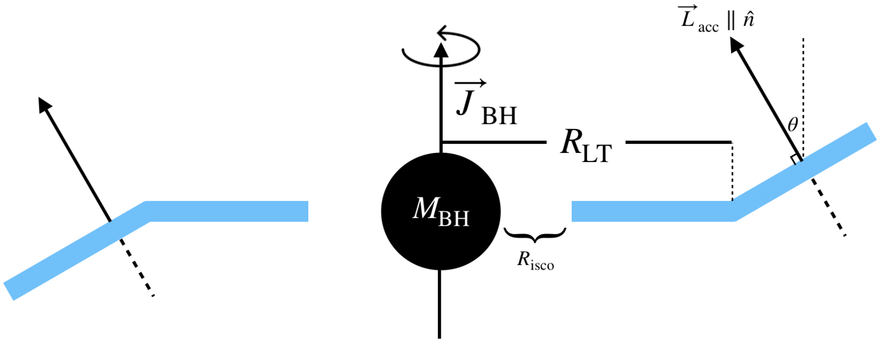

Figure 4.1: Scheme of how our Bardeen-Peterson setup woud look like

When this paradigm is adjusted to the presence of a binary, each BHs disk is perturbed in a way that pushes the warp characteristic radius, and speeds up the alignment process. The dynamics of this problem (when looking at one BH-inner disk system) are usually treated analytically by writing the mass and momentum conservation equations in an appropriate manner (see, eg: Papaloizou and Pringle, 1983, Ogilvie and Latter, 2013 or Gerosa et al., 2020), which take the following form:

$$\frac{\partial \Sigma}{\partial t} = \frac{3}{R}\frac{\partial}{\partial R}\left[R^{1/2}\frac{\partial}{\partial R}(\nu_1 \Sigma R^{1/2})\right] + \frac{1}{R}\frac{\partial}{\partial R}\left[\nu_2 \Sigma R^2 \left|\frac{\partial \hat{L}}{\partial R}\right|^2\right] \tag{4.1}$$

$$\frac{\partial L}{\partial t} = \frac{3}{R}\frac{\partial}{\partial R}\left[\frac{R^{1/2}}{\Sigma}\frac{\partial}{\partial R}(\nu_1 \Sigma R^{1/2}) L\right] + \frac{1}{R}\frac{\partial}{\partial R}\left[\left(\nu_2 \Sigma R^2 \left|\frac{\partial \hat{L}}{\partial R}\right|^2 - \frac{3}{2}\nu_1\right) L\right] + \frac{1}{R}\frac{\partial}{\partial R}\left(\frac{\nu_2 R L}{2}\frac{\partial \hat{L}}{\partial R}\right)$$
$$+ \frac{\partial}{\partial R}\left(\nu_3 R L \times \frac{\partial \hat{L}}{\partial R}\right) + \frac{2G}{c^2}\frac{J \times L}{R^3} + \frac{3 G M_* \Sigma R^2}{4 R_*^3}(\hat{L}\cdot\hat{L}_*)(\hat{L}\times\hat{L}_*) \tag{4.2}$$

Where L, L_* are the angular momentum of the disk and the angular momentum of the binary respectively, Σ is the surface density, $J = \frac{GM^2\chi}{c}\hat{J}$ is the BH spin, and the viscosities $\nu_{1,2,3}$ model the response of the disk to azimuthal and vertical stresses, and the the stress associated with precession. Now, this set of equations has certain approximations, which we selectively employ as subgrid tools for approximating the shape of the accretion flow and how it interacts with the BH.

In more concrete terms, our simulations store the value that angular momentum of the material that is accreted onto the sink cloud that represents the black holes. Once material is selected to be accreted to this sink though, it becomes material which we are not resolving, which occurs at orders of $1\times10^{-2} - 1\times10^{-3}$ pc, which is bigger than typical Lense-Thirring radii (warp characteristic radii) by $1-3$ orders of magnitude. This means that from the net angular momentum of the flow we have to employ a subgrid recipe to actually account for the BH spin and warped accretion disk interactions. What we do, is to first make the same assumptions done in Gerosa et al., 2020 by saying that the disks are Keplerian (angular momentum will be described by $L(R)=\Sigma(R)\sqrt{GM_{bh}R}$), and that this disks are in a steady state. If we assume that the disk is flattened at first, 4.1 yields:

$$3R^{1/2}\partial_R(\nu_1\Sigma(R)R^{1/2}) = 3R^{1/2}\partial_R\left[\nu_0\left(\frac{R}{R_0}\right)^{\beta}\alpha\Sigma(R)R^{1/2}\right] = \frac{\dot{M}}{2\pi}$$

$$\Rightarrow \nu_0\left(\frac{R}{R_0}\right)^{\beta}\alpha\Sigma(R)R^{1/2} = \frac{\dot{M}}{6\pi}\int R^{-1/2}\mathrm{dR} = \frac{\mathrm{R}^{1/2}\dot{\mathrm{M}}}{3\pi}+\mathrm{K}$$

$$\Rightarrow \Sigma(R) = \frac{R_0^{3/2}\dot{M}}{3\pi\nu_0\alpha}R^{-3/2}+\tilde{K}R^{-2} \tag{4.3}$$

But the integration constant may be found by using the magnitude of the accreted net angular momentum (which, as mentioned, we have from the simulation):

$$L = \int_{R_{\min}}^{R_{\max}}\Sigma(R)\sqrt{GM_{bh}R} = \underbrace{\frac{R_0^{3/2}\dot{M}\sqrt{GM}}{3\pi\nu_0\alpha}}_{:=C}\int_{R_{\min}}^{R_{\max}}\frac{\mathrm{dR}}{R}+\tilde{K}\sqrt{GM}\int_{R_{\min}}^{R_{\max}}R^{-3/2}\mathrm{dR}$$

$$= C\cdot[\ln(R_{\max})-\ln(R_{\min})]-2\tilde{K}\sqrt{GM}\cdot\left[R_{\max}^{-1/2}-R_{\min}^{-1/2}\right]$$

$$\Rightarrow \tilde{K} = \frac{L-C\cdot\ln(\frac{R_{\max}}{R_{\min}})}{-2\sqrt{GM}\cdot\left[R_{\max}^{-1/2}-R_{\min}^{-1/2}\right]}$$

Where we will use the ISCO radius as $R_{\min}$, and $R_{\max}$ is set over the constraint of the disk's mass being equal to the accreted mass, $\int_{R_{\min}}^{R_{\max}}\Sigma(R)\,\mathrm{dR}=\mathrm{M}_{\mathrm{acc}}$. If we integrate explicitly, we obtain this expression:

$$\int_{R_{\min}}^{R_{\max}}\Sigma(R)\,\mathrm{d}R = \int_{\mathrm{R}_{\min}}^{\mathrm{R}_{\max}}\left(\underbrace{\frac{R_0^{3/2}\dot{M}}{3\pi\nu_0\alpha}}_{:=\tilde{\mathrm{C}}}\mathrm{R}^{-3/2}+\tilde{\mathrm{K}}\mathrm{R}^{-2}\right)\mathrm{dR} = -2\tilde{\mathrm{C}}\sqrt{\mathrm{R}}\Big|_{\mathrm{R}_{\min}}^{\mathrm{R}_{\max}}-\tilde{\mathrm{K}}\mathrm{R}\Big|_{\mathrm{R}_{\min}}^{\mathrm{R}_{\max}} = \mathrm{M}_{\mathrm{acc}}$$

$$\Rightarrow \frac{2\tilde{C}}{\sqrt{R_{\max}}}+\frac{\tilde{K}}{R_{\max}} = -M_{\mathrm{acc}}\frac{2\tilde{C}}{\sqrt{R_{\min}}}+\frac{\tilde{K}}{R_{\min}} =: A$$

$$\Rightarrow \frac{2\tilde{C}R_{\max}+\tilde{K}\sqrt{R_{\max}}}{R_{\max}^{3/2}} = A \overset{u^2=:R}{\Rightarrow} 2\tilde{C}u^2+\tilde{K}u = Au^3 \Rightarrow u = \frac{2\tilde{C}+\sqrt{4\tilde{C}^2+4A\tilde{K}}}{A}$$

This closes out the necessary values for the profile density, where this $R_{\max}$ in practice is comparable to $\sim (0.7-1.5)R_{\rm d}$ where $R_{\rm d}$ is the characteristic disk radius used for accretion at 2.9. With this superficial density we now write $\rho(R,z)$, such that it has the vertical density of an isothermal disk, respecting $\int_{-\infty}^{\infty}\rho(R,z){\rm dz} = \Sigma({\rm R})$, which, using 4.3, will give us a disk density profile of the following shape

$$\rho(R,z) = \frac{\Sigma(R)}{\sqrt{2\pi H}}{\rm e}^{\frac{-z^2}{2H^2}} \tag{4.4}$$

In this derivation we glossed over a few definitions: We used from Gerosa et al., 2020, that $\nu_1 = \nu_0\left(\frac{R}{R_0}\right)^{\beta}\alpha$, where ν_0 and R_0 are constants. R_0 will from now on be treated as $R_0 = R_{LT}$, where R_{LT} is the Lense-Thirring radius, which is defined as

$$R_{LT} = \frac{4G^2M_{BH}^2\chi}{c^3\alpha\nu_0\zeta} \;\; ; \quad \zeta = \frac{2(1+7\alpha^2)}{\alpha^2(4+\alpha^2)} \tag{4.5}$$

With our viscosity-defining constant $\nu_0 = \left(\frac{H_{LT}}{R_{LT}}\right)\sqrt{GMR_{LT}}$. With all this set-up, parallel to the $xy-$axis, we create this artificial disks around the position of our BHs, and rotate them so $\hat{L}$ becomes the normal vector to the disk's rotation plane. So we generate the matrix composed by the orthogonal basis which defines $\mathbf{R}^3$ in a way that maps the original disk's normal vector ($\hat{k} = (0,0,1)$) onto the new normal vector. If we define:

$$\hat{w} = \hat{L} = \begin{bmatrix} l_1 \\ l_2 \\ l_3 \end{bmatrix}, \quad \vec{u} = \begin{bmatrix} -l_2 \\ l_1 \\ 0 \end{bmatrix}, \quad \vec{v} = \vec{w} \times \vec{u}$$

After normalizing $\hat{u} = \vec{u}/u$, $\hat{v} = \vec{v}/v$, we can use the rotation matrix so that we can relocate our disk in a way that it aligns with the accreted angular momentum by changing the vector field's position to:

$$\begin{bmatrix} x' \\ y' \\ z' \end{bmatrix} = \begin{bmatrix} \hat{u} & \hat{v} & \hat{w} \end{bmatrix} \begin{bmatrix} x \\ y \\ z \end{bmatrix}$$

This is all quite important as the interaction between the BH spin and the accretion disk angular momentum will be quantified by the integral of the Lense-Thirring term at 4.2, which we integrate along the disk profile:

$$\frac{{\rm d}\mathbf{J}}{{\rm d}t} = -\int_{R_{\min}}^{R_{\max}} \frac{2G}{c^2}\frac{\mathbf{J}\times L}{R^3}2\pi R{\rm d}R \tag{4.6}$$

We have to take into account that there is a timescale in which the warp occurs and the integration of the Lense-Thirring term is relevant, as the misaligned disk will stop being representative of the system as a subgrid recipe when trying to advance the BH spin at every snapshot. We cope with this by only advancing the spin by the minimum between the characteristic alignment and the snapshot time step:

$$\mathbf{J}^{\mathrm{i}} = \frac{\mathrm{d}\mathbf{J}^{\mathrm{\,i}}}{\mathrm{d}t} \cdot \Delta\tilde{t_{\mathrm{i}}} + \mathbf{J}^{\mathrm{i}-1} = \mathbf{J}^{\mathrm{i}-1} - \Delta\tilde{t_{\mathrm{i}}} \int_{R_{\min}}^{R_{\max}} \frac{2G}{c^2} \frac{\mathbf{J}^{\mathrm{i}-1} \times L}{R^3} 2\pi R \mathrm{d}R \ ; \quad \Delta\tilde{t_{\mathrm{i}}} = \min(\Delta t_{\mathrm{i}}, t_{\mathrm{i}}^{\mathrm{align}}) \quad (4.7)$$

Where the alignment time is given by:

$$t_{\mathrm{align}} = \frac{1}{\dot{M}} \sqrt{\frac{c}{G} M_{BH} \chi \frac{\alpha \nu_0}{\zeta}} \tag{4.8}$$

As our system is far from being at equilibrium, the accretion rate may vary in orders of magnitude, depending on how efficiently feedback is operating, whether a gap has formed in the disk, how close the BHs are passing each other, etc. This means that the alignment time also may vary by orders of magnitude at different times during the simulation, which is why it is pressing to have this variable time step for integrating the angular momentum. This of course, entails a loss of information, as the alignment time will be averaged out for every given snapshot (along with accretion), but it is still relevant as not to overshoot the amount of exchanged angular momentum, possibly by orders of magnitude, at a given snapshot. We see an example of Δt compared with t_{align} for one of our simulations:

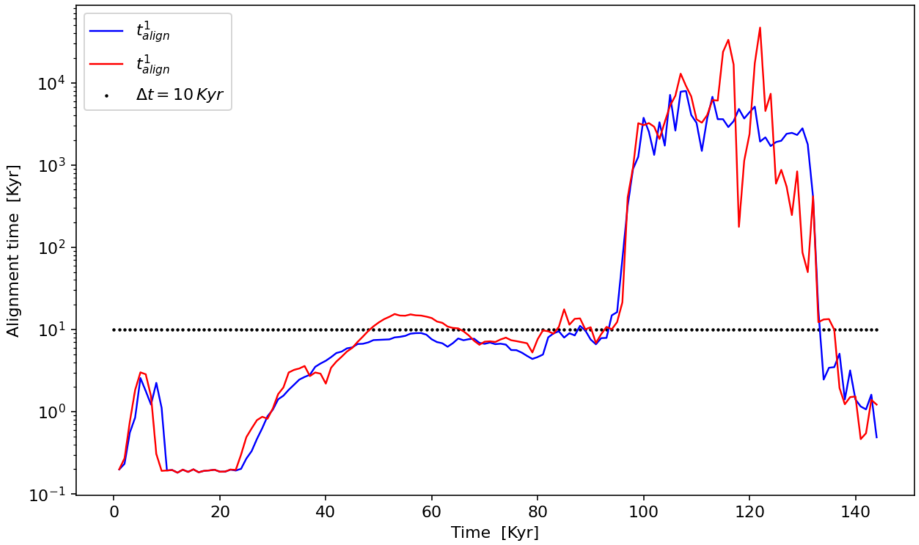

Figure 4.2: Evolution of t_{align} for a2-AGN

We see in this example, that indeed the alignment time follows somewhat consistently a profile that corresponds to a less pronounced inverse of accretion (see graph 3.13), and is below the simulation's time step of 10 Kyr, specially at the points where more angular momentum is added to the BH's spin, which means that the 'integration' of the LT term will be lessened at the points in which it would be stronger, thus 'flattening' the angular momentum exchange to a degree.

The only missing component at this point, are the initial values for the BH spin magnitude and directions, which we choose to be $\chi = 0.25$ of the maximum theoretical spin, and of an initial misalignment direction of $\theta = 30°$. Our spin parameter value is set as to be consistent with what we already used for our AGN spectrum generation at chapter 2, which was set looking at simulations from King et al., 2008. Our initial angle was not set with any particular rule beyond staying away of the critical obliquity angles defined at Gerosa et al., 2020, and thus chose 30° as it is a high enough initial angle to show the effects of existing misalignment between the BHs and the binary's plane and non-problematic in terms of analytical consistency. The variation of the initial misalignment angle and the effect it has on spin evolution will be left as future work.

4.2 Results: Spin and Alignment Evolution

We begin with a main component in our analysis, which is the accreted angular momentum, not only as it defines the orientation of the disks used for the Bardeen-Peterson, but also because we want to follow how the evolution of this accreted momentum evolves in correlation with how the BH spins evolve. For all the following figures, we are only going to use single BH graphs (as we saw that most of the behaviour seen in BH pairs is symmetrical in behaviour), we see first the accreted angular momentum for a2, a2-AGN, GAP-a2 and GAP-a2-AGN (we will use these two setups as representatives for no-gap and gap simulations, while taking care to mention relevant differences with our other two setups):

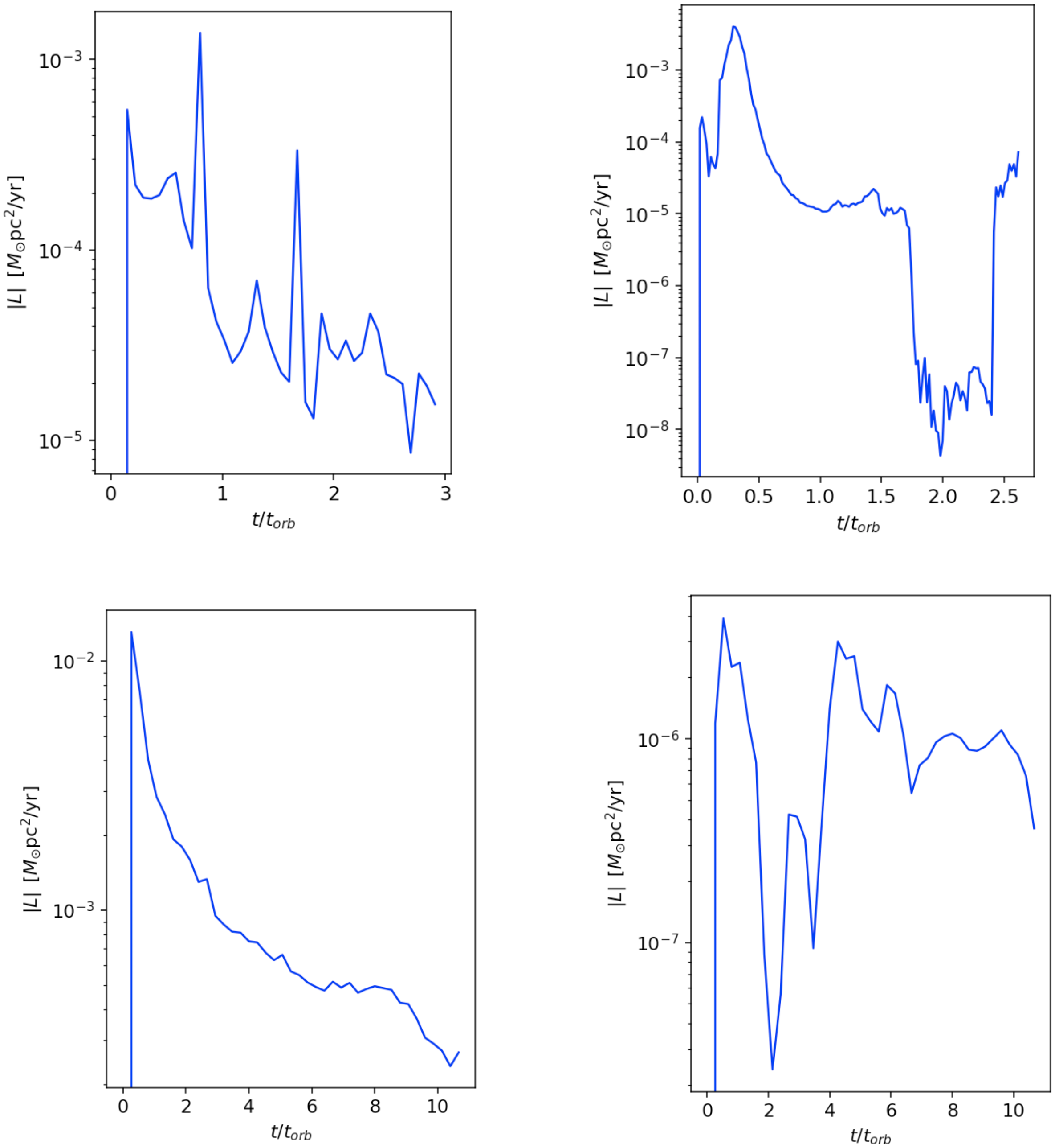

Figure 4.3: From left to right, angular momentum magnitude of accreted gas v/s time for: a2, a2-AGN, GAP-a2 and GAP-a2-AGN

The first, immediate takeaway from these graphs is that accreted angular momentum correlates to accreted mass but not perfectly. Overall trends of mass accretion are respected in angular momentum accretion but they manifest with differing impact: Take for instance a2-AGN's accretion graph 3.13 and we see how the two similar accretion peaks manifest with around one whole order of magnitude difference in angular momentum (and the second accretion peak, which has a somewhat even sustained shape, is much more 'peaked' in angular momentum).

We also may see how the net angular momentum magnitudes that are being accreted are generally lower overall in setups with AGN feedback, even when accretion rates are comparable. This property is more pronounced in setups that form gap, where the accreted angular momentum has a breach of two more orders of magnitude when compared to gas accretion.

Now when seeing these graphs, it is hard to have an actual idea of how much this accreted angular momentum actually affects and compares to the state of our BHs, not only because we are not taking into account how the efficiency of translating accreted angular momentum into spin is affected by BP, but because we are lacking the information on how the net aggregate directions of angular momentum look like (and thus how the aggregate net accreted angular momentum looks like). By starting out with our already mentioned $\xi = 0.25$ spin parameter and an initial misalignment of 30°, we can post-process taking into account the methods we have discussed and see the predicted spin magnitude evolution:

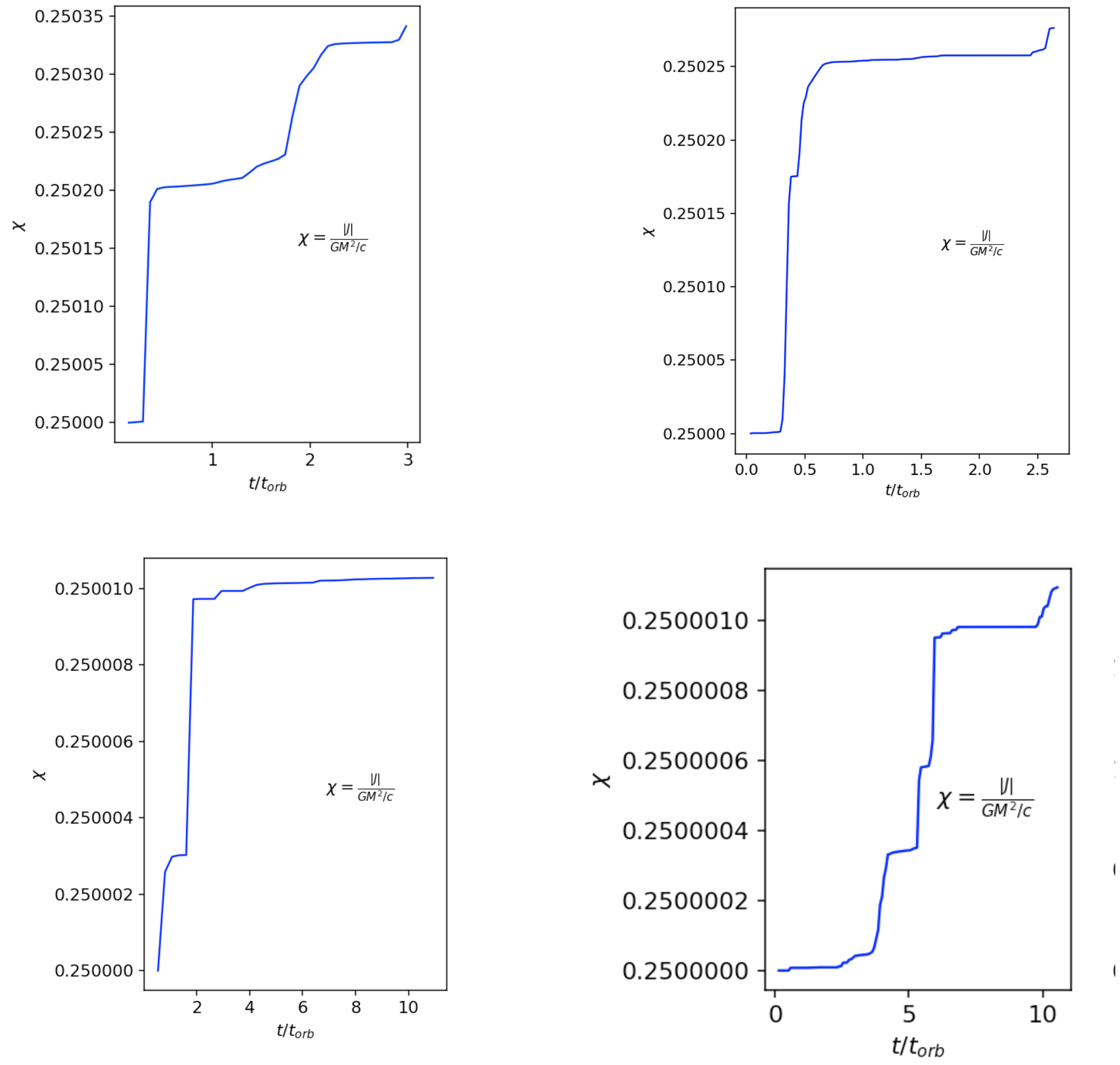

Figure 4.4: From left to right, BH spin J_{BH_1} for: a2, a2-AGN, GAP-a2 and GAP-a2-AGN

By all accounts the low percentage of effect we see in spin change is not surprising at all when considering that the accreted gas is low compared to overall BH mass, and as we saw, although imperfect, gas accretion is a proxy to angular momentum accretion, which will always be a good proxy on **actual** spin gain for our BHs (after processing BP effects and such). This is expected, if not over the expected amount of spin fluctuation when looking at relations such as the one from King et al., 2008:

$$\chi \simeq A \cdot M_8^{0.048}$$

Which although gives an order of magnitude reference of behaviour, should be taken as anecdotally at this point, since simulations in that paper operate at completely different timescales and resolutions as ours, where they take into account multiple BH encounters for galactic-scale simulations, and derive this averaged black hole spin parameter relation.

In the case of the setups in which no gaps are expected, we see that the systems show a sharp initial increase in BH spin, which in the presence of AGN feedback is effectively flattened, and without it is not. As already predicted we also see that spin increases more in cases where there is no suppression by feedback, but this is less pronounced when comparing the relative direct angular momentum accretion changes between feedback and no-feedback simulations.

It is important to remember that one of the, if not the most central property we want to inspect, is the evolution of spin alignment in the context of our binary disk. We then measure the angle between $\hat{J}_{\rm BH}$ and $\hat{L}_*$ by following the quantity

$$\theta_{\rm align} = \arccos\left(\frac{\langle J_{\rm BH}, L_*\rangle}{|J_{\rm BH}||L_*|}\right)$$

If we trace this quantity by evolving through 4.7, we see that the general trend is that of alignment for non-gap forming setups (this also holds true for our a1 and a1-AGN setups):

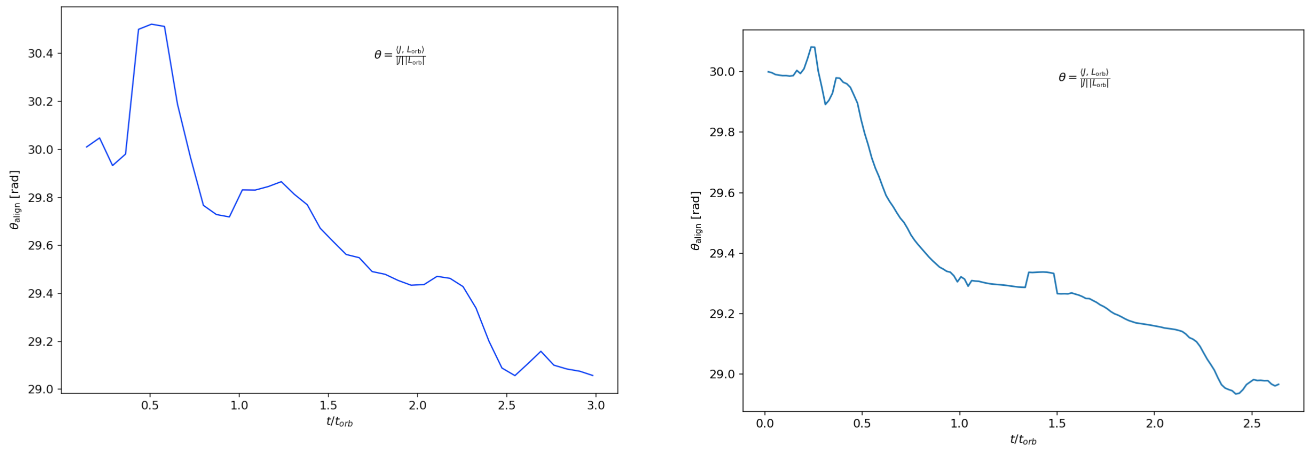

Figure 4.5: spin/orbit alignment $\theta_{\rm align}$ for a2, a2-AGN

This follows the trend of the aggregate accreted angular momentum alignment $\tilde{\theta}_{\text{align}} = \arccos\left(\frac{\langle L_{\text{acc}}, L_{*}\rangle}{|L_{\text{acc}}||L_{*}|}\right)$, for instance we can look at such a graph for a2-AGN:

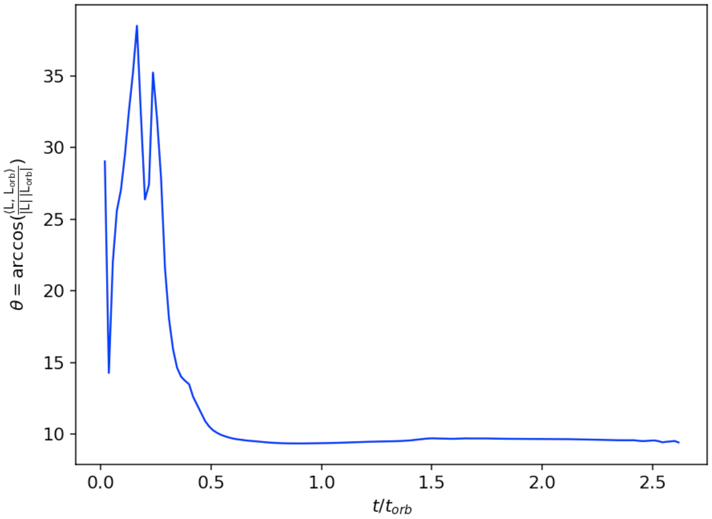

Figure 4.6: Evolution of the alignment angle between the accreted angular momentum and the orbital angular momentum for a2-AGN

Which although informative, it is somewhat hard to directly translate into how it relates with θ_{align} as the sink particles do not possess an initial spin value (outside our subgrid model), which means that we only have the 'trend' of alignment, but not the actual impact that direct accretion would have on the evolution of angular differences.

This does not hold in such a clear cut fashion for gap forming simulations, where the evolution does not follow an evidently decreasing angular separation, specifically for the feedback including setup:

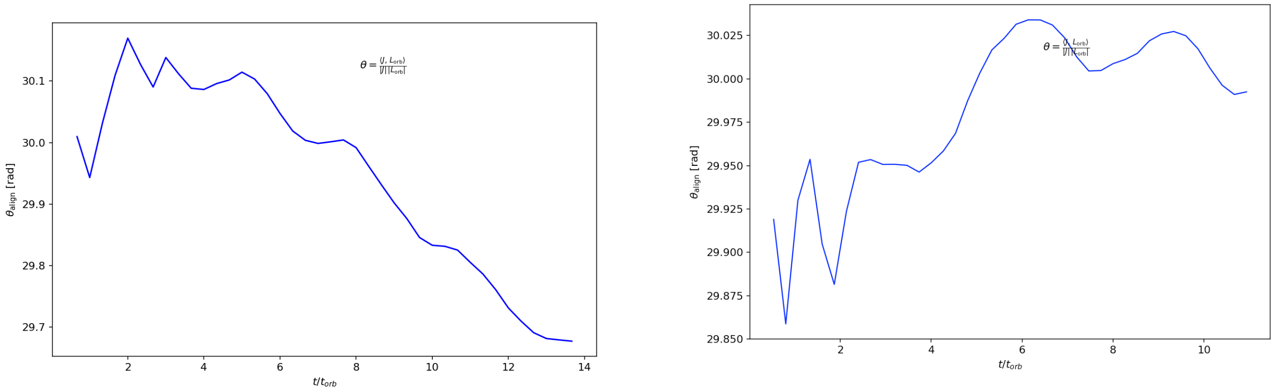

Figure 4.7: spin/orbit alignment θ_{align} for GAP-a2 and GAP-a2-AGN

We see here that the angular difference changes for the non-feedback setup follow the decreasing behaviour that we know to expect for non-gap setups, but in a minor scale, which is not surprising as accretion in general is lower. At the same time, for the gap forming setup that includes feedback, we see that the angular momentum of the SMBH is not aligning with the binary, although this can be taken as the angle staying almost constant, when looking at percent changes (and comparing with other setups).

At a first approximation we would be worried that the setup is not aligning BH spin with the orbital, because intuitively we would think that the BP paradigm aligns it by construction, but as already mentioned, the BP effect aligns the BH spin to the aggregate accreted angular momentum, which in the case of GAP-a2-AGN is not aligned with the binary's plane:

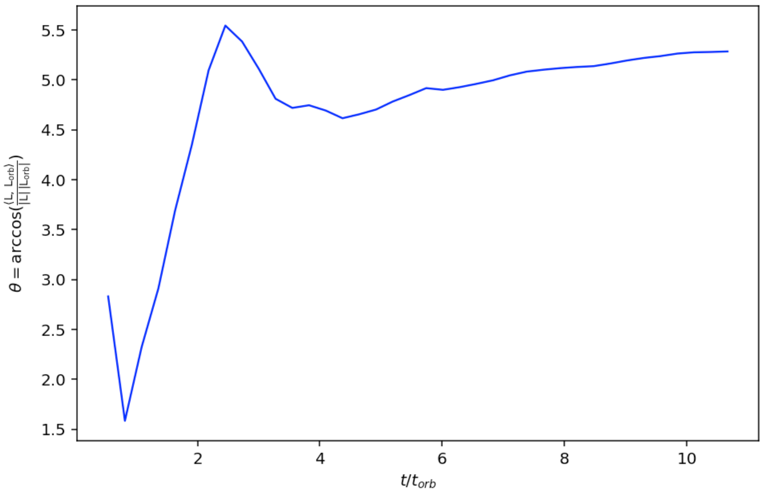

Figure 4.8: Evolution of the alignment angle between the accreted angular momentum and the orbital angular momentum for GAP-a2-AGN

Here we see that although the angular difference between the aggregate angular momentum and the orbital plane are small, the inherent alignment trend for accreted angular momentum is not as clear cut as in the non-gap forming setups, and thus the results we see with the BP postprocessing are still consistent.

It is of worthwhile mention that in all our setups the percent-wise changes of angular alignment are much bigger than the percent-wise spin parameter changes, even in gap-forming runs where we saw that alignment trends were not evident and angular difference stays more fixed than in no tidal cavity forming setups. This suggests that at least for our type of accretion flows and initial conditions, the variability of orbital-BH angular momentum alignment is potentially much higher than the variability of spin parameters. This idea of accretion flows having an 'easier time' of changing angular alignment values than BH spins, is still a premature conclusion, that has to be tested for different initial conditions of spin parameters and spin misalignment for our BP setups.

Chapter 5

Conclusions and Outlook

5.1 Discussion of our findings

In the work presented on this thesis we have studied using numerical simulations, the effects of AGN feedback on the context of gas rich SMBH binaries on their transition from the binary hardening stage towards the gravitational wave regime. We also centered some of the analysis on the impact that feedback has on how the accretion flow affects the evolution of the black hole spins and its alignment/misalignment with the overall orbital/CMD plane. For all this we ran simulations on the AMR-prescripted code RAMSES, with the inclusion of its RT module in order to couple radiation interactions with the present hydrodynamical+gravitational modelling. This radiation-hydrodinamical modelling allowed us to create a model for translating a flux prescription of accretion onto the SMBHs, to emitted luminosity in the form of photons that are deposited to the adaptive mesh through evolving emission spectrums. The photon interactions will take into account and solve self-consistently, physics involving radiative transfer, like the pressure generated by photoionization, electron-scattering or direct modelling of cooling/heating of ionization states of excitation, collisions and recombinations, in addition to Compton scattering.

Our simulation suite took the initial conditions from VV18, which were selected to be two disk+binary systems in which a tidal gap is expected to happen by hydrodynamical effects (let us call this, **group 1**) and two systems in which no gap is expected to form (**group 2**). We ran these two pairs of systems where slow and fast black hole migration is expected to occurs respectively, with and without AGN feedback and measured the impact of this phenomenon. The main findings of this exploration are:

- For runs without feedback, we saw an almost perfect correspondence of results with the runs made out of the same initial conditions with GADGET-3. As mentioned in VV18, these simulations work consistently with their expected results: Setups where tidal cavities form (which they do), show slow migration and no orbital decay is seen on their running time. On the other hand, where tidal gaps are not formed, migration occurs quite quickly, shrinking the binary separations over 2 orders of magnitude in less than $\sim 1 - 10$ orbital times.

- Separating our discussion between these two groups, we begin by going over the results involving specifically group 1 (fast migration setups). We already mentioned the evolution of binary orbit shrinkage without AGN feedback and how it consistently corresponds to their expected behaviour by construction. With the inclusion of feedback the analysis is less straightforward, but where pertaining gap formation setups, we did not see any relevant changes in their orbital evolution, as although the nature of the low-density region is affected, this region still effectively emerges and lowers the available gas reservoir that will be able to couple to the binary in a way that extracts angular momentum.

  The inclusion of feedback has different effects on the overall disk structure and dynamics in our simulations. For systems in group 1, as expected there is still formation of a low density central region around the binary, since the outwards-exerted pressure should not complicate gap formation, and although the cavity now forms more quickly it is now formed with less of a clear propagating spiral-wave pattern induced by the BH wakes. Disks in this regime also now show photoevaporation, where material from the inner edge of the tidal cavity is expelled at speeds above escape velocity due to ionizing radiation coupling very efficiently to gas that is not strongly bound. This mechanism is self-regulated, as its importance is mediated by accretion (and on the long term should be inhibited by some amount of slow ionization of the overall disk by radiation that incides edge-on, decreasing the coupling efficiency), but at least on our running time of the simulations, appreciable thinning of the disk is seen. Some mechanical feedback is seen in these setups, as accretion goes below the threshold which enables vertical jet formation, but is not a major feature as the volume of sustained ejected gas is not too high and is less than or comparable to the amounts of gas that is already being unbounded by radiation. This effect on disk structure impact is not observed VV18, who find that group 1 setups show no major structural changes from the inclusion of feedback.

  The tracing of evolution of photons and ionization states is crucial to understanding how feedback mediates its interactions with the gas. In group 1, photons radially flow quite freely through the low density cavity and flux reaches in a much lesser density onto the inner edge of said cavity, which means the ionization is not seen too deeply (also, as some fraction of the material is photoevaporated by incident ionizing radiation, it is mostly singly ionized). On the vertical axis radiation escapes quite freely, as per the disks natural geometry, creating an ionizing radiation cone structure that its known to appear on AGNs, which does not have much importance in the context of the disk+binary system, but may have overall ramifications for the galaxy it is in embedded in.

- For group 2, our fast migration setups where no gap is predicted to be excavated. Pertaining orbital evolution, the inclusion of feedback is on the short term potentially disruptive, but in the long term, after the ionization area is established around the binary, and the initial feedback blown bubbles are erased and the density gradient is 'repaired' back towards equilibrium, the gas may be maintained in order to promote BH coalescence (this is yet to be actually observed as simulation runs have to be continued). This means that although coalescence is indeed delayed, with the timescales in which the disks stabilize back, a fast migration regime should still be reached. This observations for group 2 are a direct result of how radiative feedback interacts on the long term with its immediate environ, which will mean that just as in our following points regarding the

feedback implementation, it shows different behaviour than the orbital evolution that is found when implementing a 'direct-heating' feedback recipe. One main implication of fast migration not being the end result in this branch of setups, is that we now do not need for additional mechanisms for BH coalescence (like the introduction of a third BH or big gas inflows from the outside of the CMD), making coalescence a more natural outcome in the hardening stages of binaries.
In these setups the effects on disk structure are on the short term quite pronounced (specially for the higher $M_{\rm bin}/M_{\rm disk}$ setup), as a feedback bubble created by the outwards radiation pressure is immediately produced. Now, this feedback bubble initially lowers the central region's density and suppresses accretion, but as time evolves, the energetic coupling efficiency between radiation and gas lowers, and as this occurs viscous diffusion will start bringing the disk back to an equilibrium in which fast migration may be fostered. This again is not what is observed in VV18, where they saw that group 2 setups become similar to tidal gap forming systems due to the AGN carving out a 'feedback-cavity' akin to a hydrodynamical (which we show, the system ends up filling out). We attribute both this differing result and the lack of photoevaporation to how direct heating implementations of AGN feedback do not take into account the coupling efficiency of radiation to gas in a consistent manner (eg: as mentioned in Prieto et al., 2021, order of magnitude differences may be seen in how luminosity translates into heating of gas depending on the context and resolution of different simulations), and how ionization states may effectively swing this coupling efficiency depending on the context.
It is in fact the case of group 2 simulations that mapping out photon behaviour is crucially bound to our understanding of how feedback interacts with our gas. After the initial feedback bubble is blown out, we can explain how feedback starts coupling less efficiently with gas as the disk's inner regions become quickly ionized and thus lose much of its opacity towards photons, effectively increasing the mean free path of radiation until it balances out with a decrease in radiation flux density. This eventually means that in group 2 systems the disk eventually forms an area akin to a strömgren sphere to which photons are radially confined and the ionization rate of neutral gas is counterbalanced by recombination rates.

- In terms of overall trends between all simulations, we saw different behaviours arise. In general we see that in regions where properly defined, rotational velocities do not differ too strongly between feedback runs and non-feedback runs (one could point at some value difference at certain points in specific setups, but at least trends, are clearly respected). Sound speeds on the other hand do show appreciable differences between non-feedback and feedback simulations for both groups, this differences are mainly seen on the central simulation regions where feedback strongly affects the thermal properties of the disk (at least initially), and tend to smooth out as one looks radially outwards. The biggest differences that we see are in gap forming setups between feedback/non-feedback runs, where we see somewhat-artificially perturbed radial profiles, as the evaporating material spreads radially, and this hot unbound material introduces an independently high component that will flatten and 'travel' through the evolution of time if we were to plot out more profiles at different times. We also saw very high (although quite variable) values for the Toomre stability parameter, that indicate that at least, at first approximation our disks will be stable against fragmentation. We do establish though, that this parameter does not take into account for its stability analysis, the presence of strong radiational influence, and thus only acts as a lower bound threshold for stability. We therefore defined a criterion that should test the gravitational stability trend of the medium by checking how cooling and heating processes balance out. By testing this, we saw results that are consistent with the lack of gas fragmentation, where heating processes always stay on top of cooling for our simulations.

- A main point of this work was the description of black hole spin magnitude and alignment evolution and how it links with the accretion flow before and after it becomes affected by the inclusion of feedback processes. We saw how raw accreted angular momentum directly correlates -albeit imperfectly- to mass accretion respecting overall proportionality, and setups with the inclusion of AGN feedback show a lowering of angular momentum accretion that is higher than the respective difference of accreted mass between their non-feedback counterparts. If we stop talking about direct accreted angular momentum, and put it into perspective with the postprocessed effects of the BP framework, we see that for typical starting spin parameter values of $\xi = 0.25$, the net gain of spin is quite low percentage-wise (which is consistent with order of magnitude estimations for simulations that correlate BH mass changes to spin changes), but we also see that the bridge between proportionality that existed in the proportion of mass v/s accreted angular momentum between feedback/non-feedback simulations is decreased.

  A point of discussion today in the findings of LIGO merger detections is the model constraints on how BH spins align (or potentially counter-align) with respect to the binary orbit angular momentum. Our postprocessing model assigns a constructed accretion disk with a normal plane aligned with the accreted angular momentum's direction at given snapshots and then tries to quantify the alignment the BH spin suffers by interacting with said artificial disk through the frame dragging effects that form part of the Bardeen-Peterson effect. We saw that systems in group 2 show clear alignment trends, where the angular difference between the orbital plane and the BH spin decreases in a remarkably similar fashion overall between non-feedback and feedback runs. On the other hand the alignment trends for gap forming setups (group 1) are not evident at all, a fact that does not come from the implementation of the BP processing tools, but from the actual simulations themselves, where cavity forming disks do not seem to have accretion flows that necessarily show alignment trends. When seeing the overall numbers, we saw that the impact of our accretion flows for typical initial conditions, is much stronger percent-wise in alignment trends than magnitude trends, which seems to suggest that alignment or counter-alignment variability is much higher overall than BH spin variability for our type of accretion flows.

5.2 Improvements and future work

There are several avenues for improvement in our results and for future research endeavours related to the work presented here. As for the improvements of this work there are different things that could be added here, we can start by the obvious almost-always improvable things such as resolution, photon grouping resolution (more photon bands), exploring more setups spanning the phase space that defines gap and non gap setups to get better informed statistics of behaviour, or even manually adding stars instead of a fixed gravitational field that emulates their presence. Most of these improvements are barred by computational resources or time resources and their cost benefits mostly put them outside the scope of this thesis.

Beyond this aforementioned overall upgrades to our simulations, there are three different things that should definitely be and could be improved in this work by the author's estimation: The first one, is running the group 2 setups with feedback for longer times, as to see the actual behaviour of our setup on longer timescales and see if we indeed reach a point of fast migration (and hopefully, coalescence at some point), this was not done purely because of time constraints and the point of this writing, this is being done (for reference, every snapshot in a2-AGN takes about $\sim$ 20hrs of computation time and amounts to 0.02 orbital times). The second accessible and notorious improvement that could be made, is to run our same simulation suite, but implementing a direct heating feedback model in order to make a self-contained comparison between methods, which should not be too hard, as these are already written in their simplest forms for the main RAMSES distribution (the only reference we have, is that after running one of our group 2 simulations with no heating recipe beyond translating accretion to an injection of heating by 0.1 proportionality, most of the CMD gas blew up immediately). The third improvement we could expand upon, is to include setups that go over the Toomre parameter's threshold and see how fragmented disks interact with feedback and radiation in practice.

Another, already mentioned possible refinement that this work may see, is in the context of our exploration of BH spin evolution, where we have the ambition to properly explore the phase space of initial spin parameters and misalignment angles $(\xi_0, \theta_0^{\rm align})$. This is necessary to draw correct conclusions and confirm whether the evolutionary trends we observed are concrete or are just artifacts of our implementation, specially the assertion on how the variability of alignment angles is much higher than the variability of spin parameters, given that alignment evolution should be quite dependant on the initial state of angular difference between the BHs and the orbital plane.

Beyond these improvements, there are some uses that could be seen for the radiative feedback implementation we have developed here for RAMSES. One possible avenue would be for instance, looking at common envelope setups in which the massive component of the pair is a BH, where radiative feedback has been investigated, but as per the author's knowledge, not with simulations that employ detailed radiation interaction from a dynamical BH spectrum. Other avenues of research include different contexts in which one would like to see a detailed BH emission spectrum interact with its environment, like in high resolution simulations of AGN evolution or TDEs.

Bibliography

R. Abbott, T. Abbott, S. Abraham, F. Acernese, K. Ackley, C. Adams, R. Adhikari, V. Adya, C. Affeldt, M. Agathos, and et al. Gw190521: A binary black hole merger with a total mass of 150 $M_{\odot}$. *Physical Review Letters*, 125(10), Sep 2020.

R. Alexander, C. Clarke, and J. Pringle. Photoevaporation of protoplanetary discs–ii. evolutionary models and observable properties. *Monthly Notices of the Royal Astronomical Society*, 369(1):229–239, 2006.

P. Amaro-Seoane, S. Aoudia, S. Babak, P. Binétruy, E. Berti, A. Bohé, C. Caprini, M. Colpi, N. J. Cornish, K. Danzmann, and et al. Low-frequency gravitational-wave science with elisa/ngo. *Classical and Quantum Gravity*, 29(12):124016, Jun 2012. ISSN 1361-6382.

K. A. Arnaud. XSPEC: The First Ten Years. In G. H. Jacoby and J. Barnes, editors, *Astronomical Data Analysis Software and Systems V*, volume 101 of *Astronomical Society of the Pacific Conference Series*, page 17, Jan. 1996.

J. M. Bardeen and J. A. Petterson. The lense-thirring effect and accretion disks around kerr black holes. *The Astrophysical Journal*, 195:L65, 1975.

J. E. Barnes and L. Hernquist. Transformations of Galaxies. II. Gasdynamics in Merging Disk Galaxies. , 471:115, Nov. 1996.

J. E. Barnes and L. E. Hernquist. Fueling Starburst Galaxies with Gas-rich Mergers. , 370: L65, Apr. 1991.

M. R. Bate, I. A. Bonnell, and N. M. Price. Modelling accretion in protobinary systems. , 277(2):362–376, Nov. 1995.

M. C. Begelman, R. D. Blandford, and M. J. Rees. Massive black hole binaries in active galactic nuclei. , 287(5780):307–309, Sept. 1980.

M. Berger and P. Colella. Local adaptive mesh refinement for shock hydrodynamics. *Journal of Computational Physics*, 82(1):64–84, May 1989.

M. Berger and J. Oliger. Adaptive mesh refinement for hyperbolic partial differential equations. *Journal of Computational Physics*, 53(3):484–512, Mar. 1984.

R. Bieri, Y. Dubois, J. Rosdahl, A. Wagner, J. Silk, and G. A. Mamon. Outflows driven by quasars in high-redshift galaxies with radiation hydrodynamics. *Monthly Notices of the*

Royal Astronomical Society, 464(2):1854–1873, 2017.

J. Binney and S. Tremaine. *Galactic Dynamics: Second Edition.* 2008.

J. H. Black. The physical state of primordial intergalactic clouds. , 197:553–563, Nov. 1981.

A. Bleuler and R. Teyssier. Towards a more realistic sink particle algorithm for the ramses code. *Monthly Notices of the Royal Astronomical Society*, 445(4):4015–4036, Nov 2014.

H. Bondi. On spherically symmetrical accretion. , 112:195, Jan. 1952.

H. Bondi and F. Hoyle. On the mechanism of accretion by stars. , 104:273, Jan. 1944.

G. L. Bryan, M. L. Norman, B. W. O'Shea, T. Abel, J. H. Wise, M. J. Turk, D. R. Reynolds, D. C. Collins, P. Wang, S. W. Skillman, and et al. Enzo: An adaptive mesh refinement code for astrophysics. *The Astrophysical Journal Supplement Series*, 211(2):19, Mar 2014.

R. Cen. A Hydrodynamic Approach to Cosmology: Methodology. , 78:341, Feb. 1992.

S. Chandrasekhar. Dynamical Friction. I. General Considerations: the Coefficient of Dynamical Friction. , 97:255, Mar. 1943.

D. Chapon, L. Mayer, and R. Teyssier. Hydrodynamics of galaxy mergers with supermassive black holes: is there a last parsec problem? *Monthly Notices of the Royal Astronomical Society*, 429(4):3114–3122, Jan 2013.

S. Cielo, R. Bieri, M. Volonteri, A. Y. Wagner, and Y. Dubois. Agn feedback compared: jets versus radiation. *Monthly Notices of the Royal Astronomical Society*, 477(1):1336–1355, 2018.

P. Colella. Multidimensional Upwind Methods for Hyperbolic Conservation Laws. *Journal of Computational Physics*, 87(1):171–200, Mar. 1990.

M. Colpi. Massive binary black holes in galactic nuclei and their path to coalescence. *Space Science Reviews*, 183(1-4):189–221, Jul 2014.

J. Cuadra, P. J. Armitage, R. D. Alexander, and M. C. Begelman. Massive black hole binary mergers within subparsec scale gas discs. *Monthly Notices of the Royal Astronomical Society*, 393(4):1423–1432, 02 2009. ISSN 0035-8711.

T. Dauser, J. Wilms, C. S. Reynolds, and L. W. Brenneman. Broad emission lines for a negatively spinning black hole. *Monthly Notices of the Royal Astronomical Society*, 409(4): 1534–1540, Sep 2010.

L. del Valle and A. Escala. Binary–disk interaction: Gap-opening criteria. *The Astrophysical Journal*, 761(1):31, 2012.

L. del Valle and A. Escala. Binary-disk interaction. ii. gap-opening criteria for unequal-mass binaries. *The Astrophysical Journal*, 780(1):84, Dec 2013.

L. del Valle and M. Volonteri. The effect of agn feedback on the migration time-scale of supermassive black holes binaries. *Monthly Notices of the Royal Astronomical Society*, 480 (1):439–450, Jul 2018.

M. Dotti, M. Colpi, F. Haardt, and L. Mayer. Supermassive black hole binaries in gaseous and stellar circumnuclear discs: orbital dynamics and gas accretion. *Monthly Notices of the Royal Astronomical Society*, 379(3):956–962, 2007.

A. Durbala, R. Buta, J. W. Sulentic, and L. Verdes-Montenegro. Fourier photometric analysis of isolated galaxies in the context of the amiga project. *Monthly Notices of the Royal Astronomical Society*, 397(4):1756–1775, Aug 2009.

A. Escala, R. Larson, P. Coppi, and D. Mardones. The role of gas in the merging of massive black holes in galactic nuclei. i. black hole merging in a spherical gas cloud. *The Astrophysical Journal*, 607, 10 2004.

A. Escala, R. Larson, P. Coppi, and D. Mardones. The role of gas in the merging of massive black holes in galactic nuclei. ii. black hole merging in a nuclear gas disk. *The Astrophysical Journal*, 630, 06 2005.

L. Ferrarese and D. Merritt. A Fundamental Relation between Supermassive Black Holes and Their Host Galaxies. , 539(1):L9–L12, Aug. 2000.

C. F. Gammie. Nonlinear Outcome of Gravitational Instability in Cooling, Gaseous Disks. , 553(1):174–183, May 2001.

J. Garcia and T. R. Kallman. X-ray reflected spectra from accretion disk models. i. constant density atmospheres. *The Astrophysical Journal*, 718(2):695, 2010.

J. García, T. Dauser, C. S. Reynolds, T. R. Kallman, J. E. McClintock, J. Wilms, and W. Eikmann. X-ray reflected spectra from accretion disk models. iii. a complete grid of ionized reflection calculations. *The Astrophysical Journal*, 768(2):146, Apr 2013.

D. Gerosa, G. Rosotti, and R. Barbieri. The bardeen–petterson effect in accreting supermassive black hole binaries: a systematic approach. *Monthly Notices of the Royal Astronomical Society*, 496(3):3060–3075, 2020.

R. A. Gingold and J. J. Monaghan. Smoothed particle hydrodynamics: theory and application to non-spherical stars. , 181:375–389, Nov. 1977.

N. Y. Gnedin and T. Abel. Multi-dimensional cosmological radiative transfer with a variable eddington tensor formalism. *New Astronomy*, 6(7):437–455, Oct 2001.

K. Gültekin, D. O. Richstone, K. Gebhardt, T. R. Lauer, S. Tremaine, M. C. Aller, R. Bender, A. Dressler, S. M. Faber, A. V. Filippenko, R. Green, L. C. Ho, J. Kormendy, J. Magorrian, J. Pinkney, and C. Siopis. The M-σ and M-L Relations in Galactic Bulges, and Determinations of Their Intrinsic Scatter. , 698(1):198–221, June 2009.

F. Haardt and L. Maraschi. X-ray spectra from two-phase accretion disks. *The Astrophysical*

Journal, 413:507–517, 1993.

Z. Haiman, A. A. Thoul, and A. Loeb. Cosmological Formation of Low-Mass Objects. , 464: 523, June 1996.

N. Häring and H.-W. Rix. On the black hole mass-bulge mass relation. *The Astrophysical Journal Letters*, 604(2):L89, 2004.

R. W. Hockney and J. W. Eastwood. *Computer Simulation Using Particles*. 1981.

P. F. Hopkins. A new class of accurate, mesh-free hydrodynamic simulation methods. *Monthly Notices of the Royal Astronomical Society*, 450(1):53–110, 2015.

L. Hui and N. Y. Gnedin. Equation of state of the photoionized intergalactic medium. , 292 (1):27–42, Nov. 1997.

I. T. Iliev, B. Ciardi, M. A. Alvarez, A. Maselli, A. Ferrara, N. Y. Gnedin, G. Mellema, T. Nakamoto, M. L. Norman, A. O. Razoumov, et al. Cosmological radiative transfer codes comparison project–i. the static density field tests. *Monthly Notices of the Royal Astronomical Society*, 371(3):1057–1086, 2006.

C. Jessop, M. Duncan, and W. Chau. Multigrid methods for n-body gravitational systems. *Journal of Computational Physics*, 115:339–351, 12 1994.

T. Kallman and M. Bautista. Photoionization and High-Density Gas. , 133(1):221–253, Mar. 2001.

N. Katz, D. H. Weinberg, and L. Hernquist. Cosmological Simulations with TreeSPH. , 105: 19, July 1996.

A. Khokhlov. Fully threaded tree algorithms for adaptive refinement fluid dynamics simulations. *Journal of Computational Physics*, 143(2):519 – 543, 1998.

A. King and K. Pounds. Powerful outflows and feedback from active galactic nuclei. *Annual Review of Astronomy and Astrophysics*, 53(1):115–154, Aug 2015.

A. King, J. Pringle, and J. Hofmann. The evolution of black hole mass and spin in active galactic nuclei. *Monthly Notices of the Royal Astronomical Society*, 385(3):1621–1627, 2008.

P. I. Kolykhalov and R. A. Syunyaev. The Outer Parts of the Accretion Disks around Supermassive Black Holes in Galaxy Nuclei and Quasars. *Soviet Astronomy Letters*, 6: 357–361, June 1980.

J. Kormendy and L. C. Ho. Coevolution (Or Not) of Supermassive Black Holes and Host Galaxies. , 51(1):511–653, Aug. 2013.

A. V. Kravtsov, A. A. Klypin, and A. M. Khokhlov. Adaptive Refinement Tree: A New High-Resolution N-Body Code for Cosmological Simulations. , 111(1):73–94, July 1997.

J. H. Krolik. *Active galactic nuclei: from the central black hole to the galactic environment*, volume 60. Princeton University Press, 1999.

M. R. Krumholz, C. F. McKee, and R. I. Klein. Embedding lagrangian sink particles in eulerian grids. *The Astrophysical Journal*, 611(1):399–412, Aug 2004.

S. Kumar and J. Pringle. Twisted accretion discs: The bardeen–petterson effect. *Monthly Notices of the Royal Astronomical Society*, 213(3):435–442, 1985.

C. D. Levermore. Relating Eddington factors to flux limiters. , 31(2):149–160, Feb. 1984.

C. Lu, J. Qiu, and R. Wang. A numerical study for the performance of the weno schemes based on different numerical fluxes for the shallow water equations. *Journal of Computational Mathematics*, 28(6):807–825, 2010.

L. B. Lucy. A numerical approach to the testing of the fission hypothesis. , 82:1013–1024, Dec. 1977.

A. Lupi, F. Haardt, and M. Dotti. Massive black hole and gas dynamics in galaxy nuclei mergers – i. numerical implementation. *Monthly Notices of the Royal Astronomical Society*, 446(2):1765–1774, Nov 2014.

S. Markoff, M. A. Nowak, and J. Wilms. Going with the flow: Can the base of jets subsume the role of compact accretion disk coronae? *The Astrophysical Journal*, 635(2):1203–1216, Dec 2005.

D. Merritt and M. Milosavljević. Massive black hole binary evolution. *Living Reviews in Relativity*, 8, 2005.

G. I. Ogilvie and H. N. Latter. Local and global dynamics of warped astrophysical discs. *Monthly Notices of the Royal Astronomical Society*, 433(3):2403–2419, 2013.

D. E. Osterbrock and G. J. Ferland. *Astrophysics Of Gas Nebulae and Active Galactic Nuclei.* University science books, 2006.

E. C. Ostriker. Dynamical friction in a gaseous medium. *The Astrophysical Journal*, 513(1): 252–258, Mar 1999.

J. P. Ostriker and S. Ikeuchi. Physical properties of the intergalactic medium and the Lyman-alpha absorbing clouds. , 268:L63–L68, May 1983.

J. C. B. Papaloizou and J. E. Pringle. The time-dependence of non-planar accretion discs. , 202:1181–1194, Mar. 1983.

V. Perret, F. Renaud, B. Epinat, P. Amram, F. Bournaud, T. Contini, R. Teyssier, and J. C. Lambert. Evolution of the mass, size, and star formation rate in high redshift merging galaxies. MIRAGE - A new sample of simulations with detailed stellar feedback. , 562:A1, Feb. 2014.

P. C. Peters. Gravitational radiation and the motion of two point masses. *Phys. Rev.*, 136: B1224–B1232, Nov 1964.

M. Petkova and V. Springel. A novel approach for accurate radiative transfer in cosmological hydrodynamic simulations. *Monthly Notices of the Royal Astronomical Society*, 415(4): 3731–3749, Jun 2011.

T. Plewa, T. Linde, V. G. Weirs, et al. Adaptive mesh refinement-theory and applications. 2005.

H. C. Plummer. On the problem of distribution in globular star clusters. 71:460–470, Mar. 1911.

R. W. Pogge. Ionized gas in the nuclear regions of nearby non-seyfert spiral galaxies. *The Astrophysical Journal Supplement Series*, 71:433–453, 1989.

K. Pounds, K. Nandra, G. Stewart, I. George, and A. Fabian. X-ray reflection from cold matter in the nuclei of active galaxies. *Nature*, 344(6262):132–133, 1990.

W. H. Press, S. A. Teukolsky, W. T. Vetterling, and B. P. Flannery. *Numerical recipes in C. The art of scientific computing.* 1992.

J. Prieto, A. Escala, G. Privon, and J. d'Etigny. Black hole fueling in galaxy mergers: A high-resolution analysis. *arXiv preprint arXiv:2101.09407*, 2021.

G. D. Quinlan. The dynamical evolution of massive black hole binaries i. hardening in a fixed stellar background. *New Astronomy*, 1(1):35–56, 1996.

D. Richstone, E. A. Ajhar, R. Bender, G. Bower, A. Dressler, S. M. Faber, A. V. Filippenko, K. Gebhardt, R. Green, L. C. Ho, J. Kormendy, T. R. Lauer, J. Magorrian, and S. Tremaine. Supermassive black holes and the evolution of galaxies. , 385(6701):A14, Oct. 1998.

J. Rosdahl and R. Teyssier. A scheme for radiation pressure and photon diffusion with the M1 closure in RAMSES-RT. , 449(4):4380–4403, June 2015.

J. Rosdahl, J. Blaizot, D. Aubert, T. Stranex, and R. Teyssier. RAMSES-RT: radiation hydrodynamics in the cosmological context. , 436(3):2188–2231, Dec. 2013.

R. Ross and A. Fabian. The effects of photoionization on x-ray reflection spectra in active galactic nuclei. *Monthly Notices of the Royal Astronomical Society*, 261(1):74–82, 1993.

R. R. Ross and A. C. Fabian. A comprehensive range of X-ray ionized-reflection models. , 358(1):211–216, Mar. 2005.

E. E. Salpeter. Accretion of Interstellar Matter by Massive Objects. , 140:796–800, Aug. 1964.

J. Saltzman. An Unsplit 3D Upwind Method for Hyperbolic Conservation Laws. *Journal of*

Computational Physics, 115(1):153–168, Nov. 1994.

D. B. Sanders and I. F. Mirabel. Luminous Infrared Galaxies. , 34:749, Jan. 1996.

S. Y. Sazonov, J. P. Ostriker, and R. A. Sunyaev. Quasars: the characteristic spectrum and the induced radiative heating. , 347(1):144–156, Jan. 2004.

N. I. Shakura and R. A. Sunyaev. Reprint of 1973A&A....24..337S. Black holes in binary systems. Observational appearance. , 500:33–51, June 1973.

A. Soltan. Masses of quasars. , 200:115–122, July 1982.

V. Springel. The cosmological simulation code gadget-2. *Monthly Notices of the Royal Astronomical Society*, 364(4):1105–1134, Dec 2005. ISSN 1365-2966.

V. Springel. Smoothed particle hydrodynamics in astrophysics. *Annual Review of Astronomy and Astrophysics*, 48:391–430, 2010.

T. Tang. Moving mesh methods for computational fluid dynamics. *Contemp. Math.*, 383, 01 2005.

C. B. Tarter, W. H. Tucker, and E. E. Salpeter. The interaction of x-ray sources with optically thin environments. *The Astrophysical Journal*, 156:943, 1969.

E. J. Tasker, R. Brunino, N. L. Mitchell, D. Michielsen, S. Hopton, F. R. Pearce, G. L. Bryan, and T. Theuns. A test suite for quantitative comparison of hydrodynamic codes in astrophysics. *Monthly Notices of the Royal Astronomical Society*, 390(3):1267–1281, 10 2008.

R. Teyssier. Cosmological hydrodynamics with adaptive mesh refinement. A new high resolution code called RAMSES. , 385:337–364, Apr. 2002.

R. Teyssier, B. Moore, D. Martizzi, Y. Dubois, and L. Mayer. Mass distribution in galaxy clusters: the role of active galactic nuclei feedback. *Monthly Notices of the Royal Astronomical Society*, 414(1):195–208, 2011.

R. J. Thacker, C. MacMackin, J. Wurster, and A. Hobbs. Agn feedback models: correlations with star formation and observational implications of time evolution. *Monthly Notices of the Royal Astronomical Society*, 443(2):1125–1141, 2014.

A. Toomre. On the gravitational stability of a disk of stars. , 139:1217–1238, May 1964.

E. Toro. *Godunov Methods: Theory and Applications.* 01 2001. ISBN 978-1-4613-5183-2.

E. Toro. The hllc riemann solver. *Shock Waves*, 29, 06 2019.

M. Trebitsch, M. Volonteri, Y. Dubois, and P. Madau. Escape of ionizing radiation from high-redshift dwarf galaxies: role of AGN feedback. , 478(4):5607–5625, Aug. 2018.

E. Treister, K. Schawinski, C. M. Urry, and B. D. Simmons. Major galaxy mergers only trigger the most luminous active galactic nuclei. *The Astrophysical Journal*, 758(2):L39, Oct 2012.

J. K. Truelove, R. I. Klein, C. F. McKee, I. Holliman, John H., L. H. Howell, and J. A. Greenough. The Jeans Condition: A New Constraint on Spatial Resolution in Simulations of Isothermal Self-gravitational Hydrodynamics. , 489(2):L179–L183, Nov. 1997.

Y. Tsukamoto, S. Z. Takahashi, M. N. Machida, and S.-i. Inutsuka. Effects of radiative transfer on the structure of self-gravitating discs, their fragmentation and the evolution of the fragments. *Monthly Notices of the Royal Astronomical Society*, 446(2):1175–1190, 2015.

Y. Ueda, M. Akiyama, G. Hasinger, T. Miyaji, and M. G. Watson. Toward the Standard Population Synthesis Model of the X-Ray Background: Evolution of X-Ray Luminosity and Absorption Functions of Active Galactic Nuclei Including Compton-thick Populations. , 786(2):104, May 2014.

D. A. Verner, G. J. Ferland, K. T. Korista, and D. G. Yakovlev. Atomic Data for Astrophysics. II. New Analytic FITS for Photoionization Cross Sections of Atoms and Ions. , 465:487, July 1996.

M. Volonteri. Formation of supermassive black holes. *The Astronomy and Astrophysics Review*, 18(3):279–315, Apr 2010.

M. Volonteri, P. R. Capelo, H. Netzer, J. Bellovary, M. Dotti, and F. Governato. Growing black holes and galaxies: black hole accretion versus star formation rate. *Monthly Notices of the Royal Astronomical Society*, 449(2):1470–1485, 2015.

R. Weinberger, V. Springel, and R. Pakmor. The arepo public code release. *arXiv preprint arXiv:1909.04667*, 2019.

S. D. M. White and C. S. Frenk. Galaxy Formation through Hierarchical Clustering. , 379: 52, Sept. 1991.

S. D. M. White and M. J. Rees. Core condensation in heavy halos: a two-stage theory for galaxy formation and clustering. , 183:341–358, May 1978.

J. H. Wise and T. Abel. ENZO+MORAY: radiation hydrodynamics adaptive mesh refinement simulations with adaptive ray tracing. , 414(4):3458–3491, July 2011.

S. E. Woosley. Pulsational Pair-instability Supernovae. , 836(2):244, Feb. 2017.

Q.-X. Yang, F.-G. Xie, F. Yuan, A. A. Zdziarski, M. Gierliński, L. C. Ho, and Z. Yu. Correlation between the photon index and x-ray luminosity of black hole x-ray binaries and active galactic nuclei: observations and interpretation. *Monthly Notices of the Royal Astronomical Society*, 447(2):1692–1704, 2015.

Q. Yu. Evolution of massive binary black holes. *Monthly Notices of the Royal Astronomical Society*, 331(4):935–958, Apr 2002.

F. Yuan and R. Narayan. Hot accretion flows around black holes. *Annual Review of Astronomy and Astrophysics*, 52(1):529–588, Aug 2014.

Y. B. Zel'dovich and I. D. Novikov. The Hypothesis of Cores Retarded during Expansion and the Hot Cosmological Model. , 10:602, Feb. 1967.

Annex A: $\xi - \Gamma$ grid of spectra

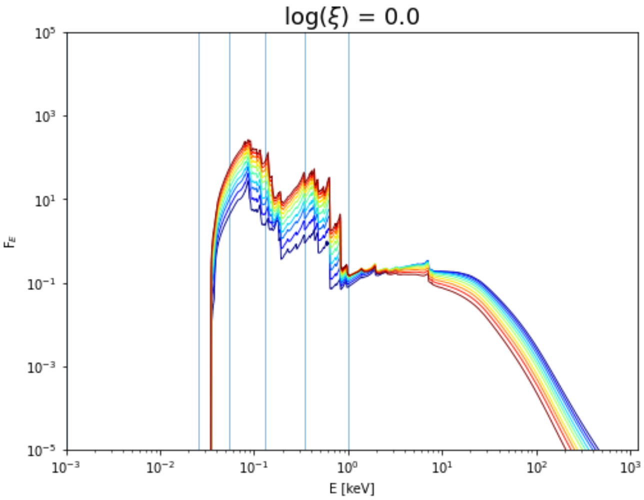
log(ξ) = 0.0

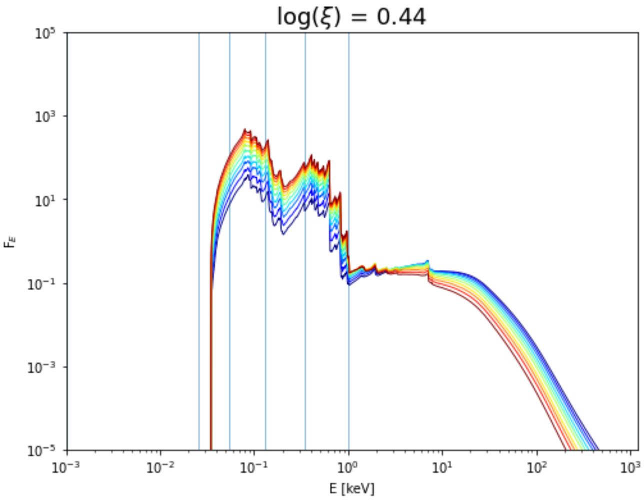
log(ξ) = 0.44

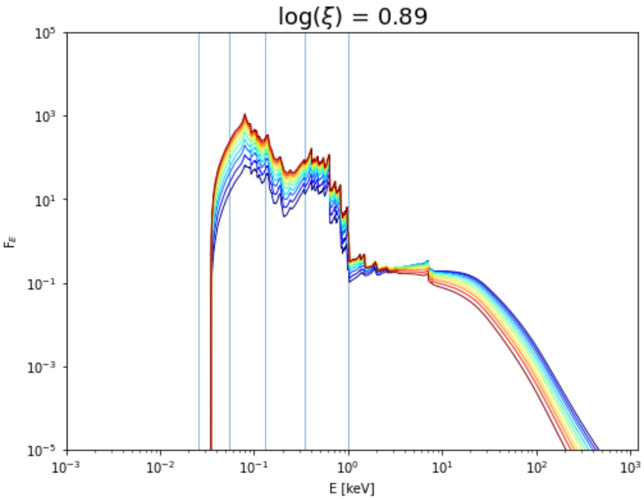
log(ξ) = 0.89

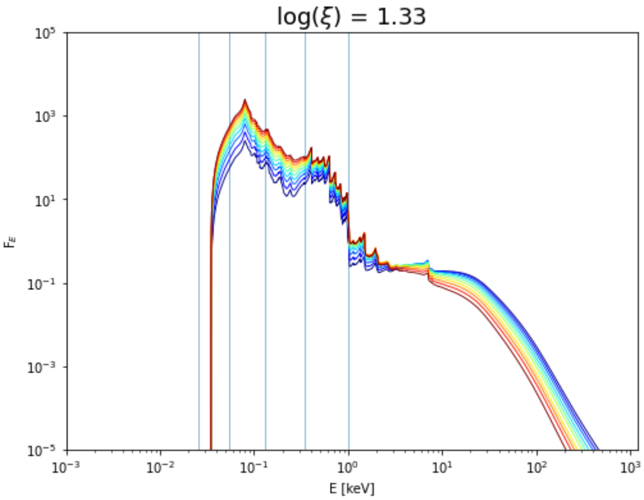
log(ξ) = 1.33

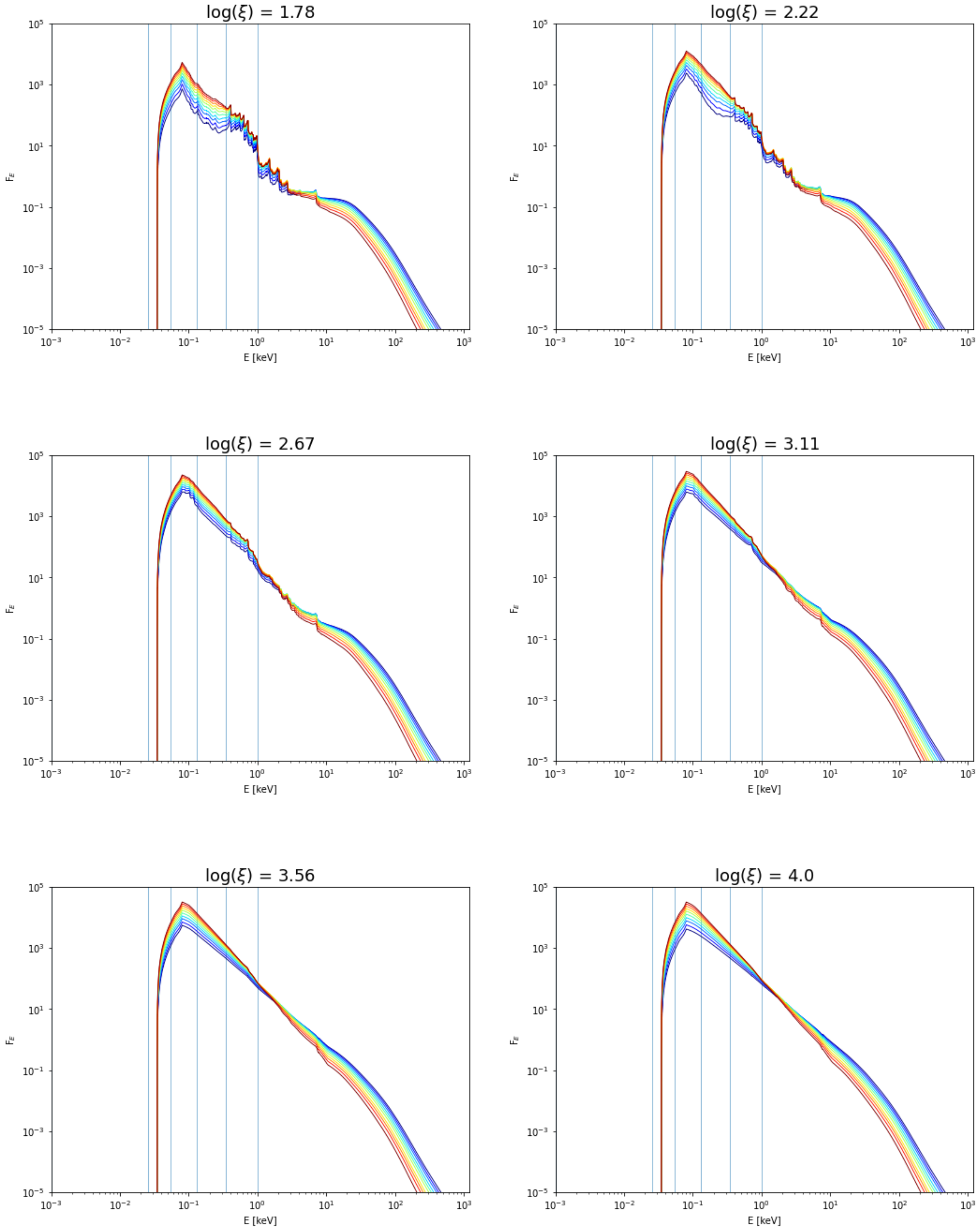
log(ξ) = 1.78

log(ξ) = 2.22

log(ξ) = 2.67

log(ξ) = 3.11

log(ξ) = 3.56

log(ξ) = 4.0

Figure 5: Spectrum grid graphs

$\log_{10}(\xi)$	Γ	UV_1 fraction	$\sigma_{\mathrm{H_I}}$	$\sigma_{\mathrm{He_I}}$	$\sigma_{\mathrm{He_{II}}}$
0.0	1.76	0.4%	1.8×10^{-19}	2.2×10^{-18}	0
0.44	1.76	0.5%	1.8×10^{-19}	2.2×10^{-18}	0
0.89	1.76	0.6%	1.8×10^{-19}	2.2×10^{-18}	0
1.33	1.76	1.3%	1.9×10^{-19}	2.2×10^{-18}	0
1.78	1.76	2.3%	1.9×10^{-19}	2.2×10^{-18}	0
2.22	1.76	2.3%	1.8×10^{-19}	2.2×10^{-18}	0
2.67	1.76	1.7%	1.8×10^{-19}	2.2×10^{-18}	0
3.11	1.76	1.4%	1.8×10^{-19}	2.2×10^{-18}	0
3.56	1.76	1.2%	1.8×10^{-19}	2.2×10^{-18}	0
4.0	1.76	1.0%	1.8×10^{-19}	2.2×10^{-18}	0
0.0	1.83	0.6%	1.8×10^{-19}	2.2×10^{-18}	0
0.44	1.83	0.6%	1.8×10^{-19}	2.2×10^{-18}	0
0.89	1.83	0.8%	1.8×10^{-19}	2.2×10^{-18}	0
1.33	1.83	1.7%	1.9×10^{-19}	2.2×10^{-18}	0
1.78	1.83	2.4%	1.8×10^{-19}	2.2×10^{-18}	0
2.22	1.83	2.3%	1.8×10^{-19}	2.2×10^{-18}	0
2.67	1.83	1.7%	1.8×10^{-19}	2.2×10^{-18}	0
3.11	1.83	1.4%	1.8×10^{-19}	2.2×10^{-18}	0
3.56	1.83	1.2%	1.8×10^{-19}	2.2×10^{-18}	0
4.0	1.83	1.1%	1.8×10^{-19}	2.2×10^{-18}	0
0.0	1.91	0.8%	1.8×10^{-19}	2.2×10^{-18}	0
0.44	1.91	0.8%	1.8×10^{-19}	2.2×10^{-18}	0
0.89	1.91	1.0%	1.8×10^{-19}	2.2×10^{-18}	0
1.33	1.91	2.0%	1.9×10^{-19}	2.2×10^{-18}	0
1.78	1.91	2.5%	1.8×10^{-19}	2.2×10^{-18}	0
2.22	1.91	2.2%	1.8×10^{-19}	2.2×10^{-18}	0
2.67	1.91	1.7%	1.8×10^{-19}	2.2×10^{-18}	0
3.11	1.91	1.5%	1.8×10^{-19}	2.2×10^{-18}	0
3.56	1.91	1.3%	1.8×10^{-19}	2.2×10^{-18}	0
4.0	1.91	1.2%	1.8×10^{-19}	2.2×10^{-18}	0
0.0	1.98	1.0%	1.8×10^{-19}	2.2×10^{-18}	0
0.44	1.98	0.8%	1.8×10^{-19}	2.2×10^{-18}	0
0.89	1.98	1.1%	1.8×10^{-19}	2.2×10^{-18}	0
1.33	1.98	2.2%	1.9×10^{-19}	2.2×10^{-18}	0
1.78	1.98	2.6%	1.8×10^{-19}	2.2×10^{-18}	0
2.22	1.98	2.2%	1.8×10^{-19}	2.2×10^{-18}	0
2.67	1.98	1.7%	1.8×10^{-19}	2.2×10^{-18}	0
3.11	1.98	1.5%	1.8×10^{-19}	2.2×10^{-18}	0
3.56	1.98	1.3%	1.8×10^{-19}	2.2×10^{-18}	0
4.0	1.98	1.2%	1.8×10^{-19}	2.2×10^{-18}	0
0.0	2.05	1.1%	1.8×10^{-19}	2.2×10^{-18}	0
0.44	2.05	1.0%	1.8×10^{-19}	2.2×10^{-18}	0
0.89	2.05	1.4%	1.8×10^{-19}	2.2×10^{-18}	0
1.33	2.05	2.4%	1.9×10^{-19}	2.2×10^{-18}	0
1.78	2.05	2.6%	1.8×10^{-19}	2.2×10^{-18}	0
2.22	2.05	2.1%	1.8×10^{-19}	2.2×10^{-18}	0

2.67	2.05	1.7%	1.8×10^{-19}	2.2×10^{-18}	0
3.11	2.05	1.5%	1.8×10^{-19}	2.2×10^{-18}	0
3.56	2.05	1.4%	1.8×10^{-19}	2.2×10^{-18}	0
4.0	2.05	1.3%	1.8×10^{-19}	2.2×10^{-18}	0
0.0	2.12	1.2%	1.8×10^{-19}	2.2×10^{-18}	0
0.44	2.12	1.1%	1.8×10^{-19}	2.2×10^{-18}	0
0.89	2.12	1.6%	1.9×10^{-19}	2.2×10^{-18}	0
1.33	2.12	2.6%	1.9×10^{-19}	2.2×10^{-18}	0
1.78	2.12	2.7%	1.8×10^{-19}	2.2×10^{-18}	0
2.22	2.12	2.0%	1.8×10^{-19}	2.2×10^{-18}	0
2.67	2.12	1.7%	1.8×10^{-19}	2.2×10^{-18}	0
3.11	2.12	1.6%	1.8×10^{-19}	2.2×10^{-18}	0
3.56	2.12	1.5%	1.8×10^{-19}	2.2×10^{-18}	0
4.0	2.12	1.4%	1.8×10^{-19}	2.2×10^{-18}	0
0.0	2.19	1.3%	1.8×10^{-19}	2.2×10^{-18}	0
0.44	2.19	1.1%	1.8×10^{-19}	2.2×10^{-18}	0
0.89	2.19	1.8%	1.9×10^{-19}	2.2×10^{-18}	0
1.33	2.19	2.7%	1.9×10^{-19}	2.2×10^{-18}	0
1.78	2.19	2.7%	1.8×10^{-19}	2.2×10^{-18}	0
2.22	2.19	2.0%	1.8×10^{-19}	2.2×10^{-18}	0
2.67	2.19	1.7%	1.8×10^{-19}	2.2×10^{-18}	0
3.11	2.19	1.6%	1.8×10^{-19}	2.2×10^{-18}	0
3.56	2.19	1.5%	1.8×10^{-19}	2.2×10^{-18}	0
4.0	2.19	1.5%	1.8×10^{-19}	2.2×10^{-18}	0
0.0	2.26	1.4%	1.8×10^{-19}	2.2×10^{-18}	0
0.44	2.26	1.2%	1.8×10^{-19}	2.2×10^{-18}	0
0.89	2.26	1.9%	1.9×10^{-19}	2.2×10^{-18}	0
1.33	2.26	2.8%	1.9×10^{-19}	2.2×10^{-18}	0
1.78	2.26	2.7%	1.8×10^{-19}	2.2×10^{-18}	0
2.22	2.26	2.0%	1.8×10^{-19}	2.2×10^{-18}	0
2.67	2.26	1.7%	1.8×10^{-19}	2.2×10^{-18}	0
3.11	2.26	1.7%	1.8×10^{-19}	2.2×10^{-18}	0
3.56	2.26	1.6%	1.8×10^{-19}	2.2×10^{-18}	0
4.0	2.26	1.5%	1.8×10^{-19}	2.2×10^{-18}	0
0.0	2.33	1.4%	1.8×10^{-19}	2.2×10^{-18}	0
0.44	2.33	1.3%	1.8×10^{-19}	2.2×10^{-18}	0
0.89	2.33	2.0%	1.9×10^{-19}	2.2×10^{-18}	0
1.33	2.33	2.9%	1.9×10^{-19}	2.2×10^{-18}	0
1.78	2.33	2.8%	1.8×10^{-19}	2.2×10^{-18}	0
2.22	2.33	2.0%	1.8×10^{-19}	2.2×10^{-18}	0
2.67	2.33	1.8%	1.8×10^{-19}	2.2×10^{-18}	0
3.11	2.33	1.7%	1.8×10^{-19}	2.2×10^{-18}	0
3.56	2.33	1.7%	1.8×10^{-19}	2.2×10^{-18}	0
4.0	2.33	1.6%	1.8×10^{-19}	2.2×10^{-18}	0
0.0	2.4	1.5%	1.8×10^{-19}	2.2×10^{-18}	0
0.44	2.4	1.4%	1.8×10^{-19}	2.2×10^{-18}	0
0.89	2.4	2.1%	1.9×10^{-19}	2.2×10^{-18}	0
1.33	2.4	2.9%	1.9×10^{-19}	2.2×10^{-18}	0
1.78	2.4	2.8%	1.8×10^{-19}	2.2×10^{-18}	0
2.22	2.4	2.0%	1.8×10^{-19}	2.2×10^{-18}	0

2.67	2.4	1.8%	1.8×10^{-19}	2.2×10^{-18}	0
3.11	2.4	1.7%	1.8×10^{-19}	2.2×10^{-18}	0
3.56	2.4	1.7%	1.8×10^{-19}	2.2×10^{-18}	0
4.0	2.4	1.7%	1.8×10^{-19}	2.2×10^{-18}	0

Table 1: UV1 group spectrum grid information

$\log_{10}(\xi)$	Γ	UV_2 fraction	σ_{H_I}	σ_{He_I}	$\sigma_{He_{II}}$
0.0	1.76	8.3%	4.3×10^{-20}	7.4×10^{-19}	6.1×10^{-19}
0.44	1.76	13.3%	3.9×10^{-20}	6.8×10^{-19}	5.5×10^{-19}
0.89	1.76	16.9%	3.7×10^{-20}	6.5×10^{-19}	5.3×10^{-19}
1.33	1.76	26.6%	4.2×10^{-20}	7.2×10^{-19}	5.9×10^{-19}
1.78	1.76	40.0%	4.4×10^{-20}	7.5×10^{-19}	6.2×10^{-19}
2.22	1.76	54.6%	4.0×10^{-20}	6.9×10^{-19}	5.7×10^{-19}
2.67	1.76	58.0%	3.6×10^{-20}	6.4×10^{-19}	5.2×10^{-19}
3.11	1.76	47.2%	3.6×10^{-20}	6.3×10^{-19}	5.1×10^{-19}
3.56	1.76	40.2%	3.6×10^{-20}	6.3×10^{-19}	5.1×10^{-19}
4.0	1.76	33.9%	3.5×10^{-20}	6.2×10^{-19}	5.0×10^{-19}
0.0	1.83	12.6%	4.3×10^{-20}	7.3×10^{-19}	6.0×10^{-19}
0.44	1.83	17.4%	3.9×10^{-20}	6.7×10^{-19}	5.5×10^{-19}
0.89	1.83	20.8%	3.8×10^{-20}	6.6×10^{-19}	5.4×10^{-19}
1.33	1.83	31.2%	4.3×10^{-20}	7.3×10^{-19}	6.0×10^{-19}
1.78	1.83	43.4%	4.4×10^{-20}	7.5×10^{-19}	6.1×10^{-19}
2.22	1.83	55.3%	4.0×10^{-20}	6.9×10^{-19}	5.6×10^{-19}
2.67	1.83	57.3%	3.6×10^{-20}	6.4×10^{-19}	5.2×10^{-19}
3.11	1.83	48.1%	3.6×10^{-20}	6.3×10^{-19}	5.1×10^{-19}
3.56	1.83	41.9%	3.6×10^{-20}	6.3×10^{-19}	5.1×10^{-19}
4.0	1.83	36.6%	3.5×10^{-20}	6.2×10^{-19}	5.0×10^{-19}
0.0	1.91	17.9%	4.2×10^{-20}	7.1×10^{-19}	5.8×10^{-19}
0.44	1.91	21.3%	3.8×10^{-20}	6.6×10^{-19}	5.4×10^{-19}
0.89	1.91	24.6%	3.9×10^{-20}	6.8×10^{-19}	5.5×10^{-19}
1.33	1.91	35.9%	4.4×10^{-20}	7.4×10^{-19}	6.1×10^{-19}
1.78	1.91	46.5%	4.4×10^{-20}	7.4×10^{-19}	6.1×10^{-19}
2.22	1.91	55.5%	3.9×10^{-20}	6.8×10^{-19}	5.6×10^{-19}
2.67	1.91	56.6%	3.6×10^{-20}	6.4×10^{-19}	5.2×10^{-19}
3.11	1.91	49.3%	3.6×10^{-20}	6.3×10^{-19}	5.1×10^{-19}
3.56	1.91	43.9%	3.6×10^{-20}	6.3×10^{-19}	5.1×10^{-19}
4.0	1.91	39.5%	3.5×10^{-20}	6.2×10^{-19}	5.0×10^{-19}
0.0	1.98	22.1%	4.1×10^{-20}	7.1×10^{-19}	5.8×10^{-19}
0.44	1.98	23.7%	3.8×10^{-20}	6.6×10^{-19}	5.4×10^{-19}
0.89	1.98	26.9%	4.0×10^{-20}	6.8×10^{-19}	5.6×10^{-19}
1.33	1.98	38.8%	4.4×10^{-20}	7.5×10^{-19}	6.2×10^{-19}
1.78	1.98	48.3%	4.3×10^{-20}	7.4×10^{-19}	6.1×10^{-19}
2.22	1.98	55.5%	3.9×10^{-20}	6.8×10^{-19}	5.5×10^{-19}
2.67	1.98	56.1%	3.6×10^{-20}	6.4×10^{-19}	5.2×10^{-19}
3.11	1.98	50.0%	3.6×10^{-20}	6.3×10^{-19}	5.1×10^{-19}
3.56	1.98	45.2%	3.6×10^{-20}	6.3×10^{-19}	5.1×10^{-19}

4.0	1.98	41.5%	3.6×10^{-20}	6.2×10^{-19}	5.1×10^{-19}
0.0	2.05	27.1%	4.0×10^{-20}	6.9×10^{-19}	5.7×10^{-19}
0.44	2.05	26.7%	3.8×10^{-20}	6.6×10^{-19}	5.4×10^{-19}
0.89	2.05	30.1%	4.1×10^{-20}	7.0×10^{-19}	5.7×10^{-19}
1.33	2.05	41.4%	4.4×10^{-20}	7.5×10^{-19}	6.2×10^{-19}
1.78	2.05	50.1%	4.3×10^{-20}	7.3×10^{-19}	6.0×10^{-19}
2.22	2.05	55.5%	3.9×10^{-20}	6.7×10^{-19}	5.5×10^{-19}
2.67	2.05	56.0%	3.6×10^{-20}	6.4×10^{-19}	5.2×10^{-19}
3.11	2.05	51.2%	3.6×10^{-20}	6.3×10^{-19}	5.1×10^{-19}
3.56	2.05	47.2%	3.6×10^{-20}	6.3×10^{-19}	5.1×10^{-19}
4.0	2.05	44.2%	3.6×10^{-20}	6.3×10^{-19}	5.1×10^{-19}
0.0	2.12	31.1%	4.0×10^{-20}	6.8×10^{-19}	5.6×10^{-19}
0.44	2.12	29.0%	3.8×10^{-20}	6.6×10^{-19}	5.4×10^{-19}
0.89	2.12	32.9%	4.1×10^{-20}	7.1×10^{-19}	5.8×10^{-19}
1.33	2.12	43.6%	4.4×10^{-20}	7.5×10^{-19}	6.2×10^{-19}
1.78	2.12	51.6%	4.3×10^{-20}	7.3×10^{-19}	6.0×10^{-19}
2.22	2.12	55.4%	3.8×10^{-20}	6.6×10^{-19}	5.4×10^{-19}
2.67	2.12	55.9%	3.6×10^{-20}	6.4×10^{-19}	5.2×10^{-19}
3.11	2.12	52.4%	3.6×10^{-20}	6.3×10^{-19}	5.1×10^{-19}
3.56	2.12	49.0%	3.6×10^{-20}	6.3×10^{-19}	5.1×10^{-19}
4.0	2.12	46.5%	3.6×10^{-20}	6.3×10^{-19}	5.1×10^{-19}
0.0	2.19	33.9%	3.9×10^{-20}	6.8×10^{-19}	5.6×10^{-19}
0.44	2.19	30.6%	3.8×10^{-20}	6.6×10^{-19}	5.4×10^{-19}
0.89	2.19	35.0%	4.2×10^{-20}	7.2×10^{-19}	5.9×10^{-19}
1.33	2.19	45.2%	4.4×10^{-20}	7.5×10^{-19}	6.2×10^{-19}
1.78	2.19	52.6%	4.3×10^{-20}	7.3×10^{-19}	6.0×10^{-19}
2.22	2.19	55.4%	3.8×10^{-20}	6.6×10^{-19}	5.4×10^{-19}
2.67	2.19	55.9%	3.6×10^{-20}	6.4×10^{-19}	5.2×10^{-19}
3.11	2.19	53.2%	3.6×10^{-20}	6.3×10^{-19}	5.1×10^{-19}
3.56	2.19	50.4%	3.6×10^{-20}	6.3×10^{-19}	5.1×10^{-19}
4.0	2.19	48.3%	3.6×10^{-20}	6.3×10^{-19}	5.1×10^{-19}
0.0	2.26	36.7%	3.9×10^{-20}	6.7×10^{-19}	5.5×10^{-19}
0.44	2.26	32.7%	3.9×10^{-20}	6.7×10^{-19}	5.4×10^{-19}
0.89	2.26	36.9%	4.2×10^{-20}	7.2×10^{-19}	5.9×10^{-19}
1.33	2.26	47.0%	4.4×10^{-20}	7.5×10^{-19}	6.2×10^{-19}
1.78	2.26	54.2%	4.2×10^{-20}	7.2×10^{-19}	6.0×10^{-19}
2.22	2.26	55.9%	3.8×10^{-20}	6.6×10^{-19}	5.4×10^{-19}
2.67	2.26	56.4%	3.7×10^{-20}	6.4×10^{-19}	5.2×10^{-19}
3.11	2.26	54.5%	3.6×10^{-20}	6.3×10^{-19}	5.2×10^{-19}
3.56	2.26	52.2%	3.6×10^{-20}	6.3×10^{-19}	5.1×10^{-19}
4.0	2.26	50.5%	3.6×10^{-20}	6.3×10^{-19}	5.1×10^{-19}
0.0	2.33	38.7%	3.9×10^{-20}	6.7×10^{-19}	5.5×10^{-19}
0.44	2.33	34.5%	3.9×10^{-20}	6.7×10^{-19}	5.5×10^{-19}
0.89	2.33	38.5%	4.2×10^{-20}	7.2×10^{-19}	5.9×10^{-19}
1.33	2.33	48.5%	4.4×10^{-20}	7.5×10^{-19}	6.2×10^{-19}
1.78	2.33	55.6%	4.2×10^{-20}	7.2×10^{-19}	5.9×10^{-19}
2.22	2.33	56.5%	3.8×10^{-20}	6.6×10^{-19}	5.3×10^{-19}
2.67	2.33	56.9%	3.7×10^{-20}	6.4×10^{-19}	5.2×10^{-19}
3.11	2.33	55.6%	3.6×10^{-20}	6.4×10^{-19}	5.2×10^{-19}
3.56	2.33	53.8%	3.6×10^{-20}	6.4×10^{-19}	5.2×10^{-19}

4.0	2.33	52.4%	3.6×10^{-20}	6.3×10^{-19}	5.2×10^{-19}
0.0	2.4	40.3%	3.9×10^{-20}	6.7×10^{-19}	5.4×10^{-19}
0.44	2.4	35.9%	3.9×10^{-20}	6.7×10^{-19}	5.5×10^{-19}
0.89	2.4	39.9%	4.3×10^{-20}	7.2×10^{-19}	6.0×10^{-19}
1.33	2.4	49.8%	4.4×10^{-20}	7.5×10^{-19}	6.2×10^{-19}
1.78	2.4	56.7%	4.2×10^{-20}	7.2×10^{-19}	5.9×10^{-19}
2.22	2.4	57.0%	3.8×10^{-20}	6.5×10^{-19}	5.3×10^{-19}
2.67	2.4	57.4%	3.7×10^{-20}	6.4×10^{-19}	5.2×10^{-19}
3.11	2.4	56.5%	3.6×10^{-20}	6.4×10^{-19}	5.2×10^{-19}
3.56	2.4	55.0%	3.6×10^{-20}	6.4×10^{-19}	5.2×10^{-19}
4.0	2.4	53.9%	3.6×10^{-20}	6.4×10^{-19}	5.2×10^{-19}

Table 2: UV2 group spectrum grid information

$\log_{10}(\xi)$	Γ	Soft X-ray fraction	$\sigma_{\mathrm{H_I}}$	$\sigma_{\mathrm{He_I}}$	$\sigma_{\mathrm{He_{II}}}$
0.0	1.76	7.6%	2.6×10^{-21}	6.1×10^{-20}	4.4×10^{-20}
0.44	1.76	27.3%	1.9×10^{-21}	4.6×10^{-20}	3.3×10^{-20}
0.89	1.76	47.1%	2.0×10^{-21}	4.8×10^{-20}	3.5×10^{-20}
1.33	1.76	52.0%	2.2×10^{-21}	5.1×10^{-20}	3.7×10^{-20}
1.78	1.76	44.7%	2.4×10^{-21}	5.8×10^{-20}	4.2×10^{-20}
2.22	1.76	36.5%	3.1×10^{-21}	7.4×10^{-20}	5.3×10^{-20}
2.67	1.76	36.9%	3.6×10^{-21}	8.5×10^{-20}	6.1×10^{-20}
3.11	1.76	46.0%	3.4×10^{-21}	8.0×10^{-20}	5.8×10^{-20}
3.56	1.76	50.5%	3.3×10^{-21}	7.7×10^{-20}	5.6×10^{-20}
4.0	1.76	53.8%	3.1×10^{-21}	7.4×10^{-20}	5.3×10^{-20}
0.0	1.83	12.9%	2.4×10^{-21}	5.6×10^{-20}	4.0×10^{-20}
0.44	1.83	36.4%	2.0×10^{-21}	4.8×10^{-20}	3.4×10^{-20}
0.89	1.83	52.7%	2.1×10^{-21}	5.0×10^{-20}	3.6×10^{-20}
1.33	1.83	52.2%	2.3×10^{-21}	5.3×10^{-20}	3.8×10^{-20}
1.78	1.83	44.3%	2.5×10^{-21}	6.0×10^{-20}	4.3×10^{-20}
2.22	1.83	37.4%	3.2×10^{-21}	7.6×10^{-20}	5.5×10^{-20}
2.67	1.83	37.9%	3.6×10^{-21}	8.5×10^{-20}	6.1×10^{-20}
3.11	1.83	45.7%	3.4×10^{-21}	8.1×10^{-20}	5.9×10^{-20}
3.56	1.83	49.9%	3.3×10^{-21}	7.9×10^{-20}	5.7×10^{-20}
4.0	1.83	52.9%	3.2×10^{-21}	7.6×10^{-20}	5.5×10^{-20}
0.0	1.91	20.1%	2.2×10^{-21}	5.2×10^{-20}	3.8×10^{-20}
0.44	1.91	44.9%	2.1×10^{-21}	4.9×10^{-20}	3.6×10^{-20}
0.89	1.91	56.4%	2.2×10^{-21}	5.2×10^{-20}	3.7×10^{-20}
1.33	1.91	51.2%	2.3×10^{-21}	5.5×10^{-20}	4.0×10^{-20}
1.78	1.91	43.6%	2.7×10^{-21}	6.3×10^{-20}	4.5×10^{-20}
2.22	1.91	38.5%	3.3×10^{-21}	7.7×10^{-20}	5.6×10^{-20}
2.67	1.91	39.0%	3.6×10^{-21}	8.5×10^{-20}	6.1×10^{-20}
3.11	1.91	45.2%	3.5×10^{-21}	8.2×10^{-20}	5.9×10^{-20}
3.56	1.91	49.1%	3.4×10^{-21}	8.0×10^{-20}	5.8×10^{-20}
4.0	1.91	51.6%	3.3×10^{-21}	7.8×10^{-20}	5.6×10^{-20}
0.0	1.98	25.9%	2.2×10^{-21}	5.1×10^{-20}	3.7×10^{-20}
0.44	1.98	50.4%	2.1×10^{-21}	5.0×10^{-20}	3.6×10^{-20}

0.89	1.98	58.6%	2.2×10^{-21}	5.3×10^{-20}	3.8×10^{-20}
1.33	1.98	50.5%	2.4×10^{-21}	5.6×10^{-20}	4.1×10^{-20}
1.78	1.98	43.2%	2.7×10^{-21}	6.4×10^{-20}	4.6×10^{-20}
2.22	1.98	39.1%	3.3×10^{-21}	7.8×10^{-20}	5.6×10^{-20}
2.67	1.98	39.8%	3.6×10^{-21}	8.5×10^{-20}	6.1×10^{-20}
3.11	1.98	44.9%	3.5×10^{-21}	8.3×10^{-20}	6.0×10^{-20}
3.56	1.98	48.5%	3.4×10^{-21}	8.1×10^{-20}	5.9×10^{-20}
4.0	1.98	50.8%	3.4×10^{-21}	7.9×10^{-20}	5.7×10^{-20}
0.0	2.05	33.3%	2.2×10^{-21}	5.2×10^{-20}	3.8×10^{-20}
0.44	2.05	54.3%	2.2×10^{-21}	5.3×10^{-20}	3.8×10^{-20}
0.89	2.05	58.6%	2.3×10^{-21}	5.4×10^{-20}	3.9×10^{-20}
1.33	2.05	49.6%	2.5×10^{-21}	5.9×10^{-20}	4.3×10^{-20}
1.78	2.05	42.6%	2.8×10^{-21}	6.7×10^{-20}	4.8×10^{-20}
2.22	2.05	39.9%	3.4×10^{-21}	8.1×10^{-20}	5.8×10^{-20}
2.67	2.05	40.3%	3.6×10^{-21}	8.6×10^{-20}	6.2×10^{-20}
3.11	2.05	44.3%	3.6×10^{-21}	8.4×10^{-20}	6.1×10^{-20}
3.56	2.05	47.3%	3.5×10^{-21}	8.3×10^{-20}	6.0×10^{-20}
4.0	2.05	49.2%	3.4×10^{-21}	8.1×10^{-20}	5.9×10^{-20}
0.0	2.12	39.3%	2.3×10^{-21}	5.3×10^{-20}	3.9×10^{-20}
0.44	2.12	56.8%	2.3×10^{-21}	5.4×10^{-20}	3.9×10^{-20}
0.89	2.12	58.0%	2.4×10^{-21}	5.6×10^{-20}	4.0×10^{-20}
1.33	2.12	48.8%	2.6×10^{-21}	6.2×10^{-20}	4.5×10^{-20}
1.78	2.12	42.2%	2.9×10^{-21}	6.8×10^{-20}	4.9×10^{-20}
2.22	2.12	40.5%	3.5×10^{-21}	8.3×10^{-20}	6.0×10^{-20}
2.67	2.12	40.6%	3.7×10^{-21}	8.7×10^{-20}	6.2×10^{-20}
3.11	2.12	43.6%	3.6×10^{-21}	8.5×10^{-20}	6.2×10^{-20}
3.56	2.12	46.1%	3.6×10^{-21}	8.4×10^{-20}	6.1×10^{-20}
4.0	2.12	47.7%	3.5×10^{-21}	8.3×10^{-20}	6.0×10^{-20}
0.0	2.19	43.6%	2.3×10^{-21}	5.4×10^{-20}	3.9×10^{-20}
0.44	2.19	58.6%	2.4×10^{-21}	5.5×10^{-20}	4.0×10^{-20}
0.89	2.19	57.6%	2.4×10^{-21}	5.7×10^{-20}	4.1×10^{-20}
1.33	2.19	48.1%	2.7×10^{-21}	6.4×10^{-20}	4.6×10^{-20}
1.78	2.19	41.8%	3.0×10^{-21}	7.0×10^{-20}	5.0×10^{-20}
2.22	2.19	41.0%	3.6×10^{-21}	8.4×10^{-20}	6.1×10^{-20}
2.67	2.19	40.9%	3.7×10^{-21}	8.7×10^{-20}	6.3×10^{-20}
3.11	2.19	43.1%	3.7×10^{-21}	8.6×10^{-20}	6.2×10^{-20}
3.56	2.19	45.2%	3.6×10^{-21}	8.5×10^{-20}	6.1×10^{-20}
4.0	2.19	46.6%	3.6×10^{-21}	8.4×10^{-20}	6.1×10^{-20}
0.0	2.26	46.5%	2.4×10^{-21}	5.6×10^{-20}	4.1×10^{-20}
0.44	2.26	58.8%	2.4×10^{-21}	5.7×10^{-20}	4.1×10^{-20}
0.89	2.26	56.8%	2.5×10^{-21}	5.9×10^{-20}	4.3×10^{-20}
1.33	2.26	47.0%	2.8×10^{-21}	6.6×10^{-20}	4.8×10^{-20}
1.78	2.26	40.8%	3.1×10^{-21}	7.2×10^{-20}	5.2×10^{-20}
2.22	2.26	40.7%	3.7×10^{-21}	8.6×10^{-20}	6.2×10^{-20}
2.67	2.26	40.6%	3.7×10^{-21}	8.8×10^{-20}	6.4×10^{-20}
3.11	2.26	42.1%	3.7×10^{-21}	8.7×10^{-20}	6.3×10^{-20}
3.56	2.26	43.8%	3.7×10^{-21}	8.7×10^{-20}	6.2×10^{-20}
4.0	2.26	45.0%	3.6×10^{-21}	8.6×10^{-20}	6.2×10^{-20}
0.0	2.33	48.6%	2.5×10^{-21}	5.8×10^{-20}	4.2×10^{-20}
0.44	2.33	58.7%	2.5×10^{-21}	5.9×10^{-20}	4.2×10^{-20}

0.89	2.33	56.0%	2.6×10^{-21}	6.1×10^{-20}	4.4×10^{-20}
1.33	2.33	46.1%	2.9×10^{-21}	6.8×10^{-20}	4.9×10^{-20}
1.78	2.33	39.8%	3.1×10^{-21}	7.4×10^{-20}	5.4×10^{-20}
2.22	2.33	40.4%	3.7×10^{-21}	8.8×10^{-20}	6.3×10^{-20}
2.67	2.33	40.3%	3.8×10^{-21}	8.9×10^{-20}	6.4×10^{-20}
3.11	2.33	41.3%	3.8×10^{-21}	8.9×10^{-20}	6.4×10^{-20}
3.56	2.33	42.7%	3.7×10^{-21}	8.8×10^{-20}	6.3×10^{-20}
4.0	2.33	43.6%	3.7×10^{-21}	8.7×10^{-20}	6.3×10^{-20}
0.0	2.4	50.1%	2.6×10^{-21}	6.0×10^{-20}	4.3×10^{-20}
0.44	2.4	58.6%	2.6×10^{-21}	6.0×10^{-20}	4.3×10^{-20}
0.89	2.4	55.3%	2.7×10^{-21}	6.3×10^{-20}	4.6×10^{-20}
1.33	2.4	45.2%	3.0×10^{-21}	7.0×10^{-20}	5.0×10^{-20}
1.78	2.4	39.1%	3.2×10^{-21}	7.6×10^{-20}	5.5×10^{-20}
2.22	2.4	40.1%	3.8×10^{-21}	8.9×10^{-20}	6.4×10^{-20}
2.67	2.4	40.0%	3.8×10^{-21}	9.0×10^{-20}	6.5×10^{-20}
3.11	2.4	40.6%	3.8×10^{-21}	9.0×10^{-20}	6.5×10^{-20}
3.56	2.4	41.7%	3.8×10^{-21}	8.9×10^{-20}	6.4×10^{-20}
4.0	2.4	42.4%	3.8×10^{-21}	8.8×10^{-20}	6.4×10^{-20}

Table 3: Soft X-ray group spectrum grid information

$\log_{10}(\xi)$	Γ	Hard X-ray fraction	$\sigma_{\mathrm{H_I}}$	$\sigma_{\mathrm{He_I}}$	$\sigma_{\mathrm{He_{II}}}$
0.0	1.76	83.6%	6.4×10^{-25}	1.9×10^{-23}	1.6×10^{-23}
0.44	1.76	58.9%	6.6×10^{-25}	2.0×10^{-23}	1.6×10^{-23}
0.89	1.76	35.4%	7.6×10^{-25}	2.3×10^{-23}	1.9×10^{-23}
1.33	1.76	20.1%	1.4×10^{-24}	4.2×10^{-23}	3.4×10^{-23}
1.78	1.76	13.1%	2.6×10^{-24}	7.8×10^{-23}	6.4×10^{-23}
2.22	1.76	6.5%	3.6×10^{-24}	1.1×10^{-22}	8.8×10^{-23}
2.67	1.76	3.4%	4.2×10^{-24}	1.2×10^{-22}	1.0×10^{-22}
3.11	1.76	5.4%	4.1×10^{-24}	1.2×10^{-22}	9.9×10^{-23}
3.56	1.76	8.1%	4.1×10^{-24}	1.2×10^{-22}	9.9×10^{-23}
4.0	1.76	11.4%	4.1×10^{-24}	1.2×10^{-22}	9.9×10^{-23}
0.0	1.83	73.9%	7.1×10^{-25}	2.1×10^{-23}	1.7×10^{-23}
0.44	1.83	45.5%	7.4×10^{-25}	2.2×10^{-23}	1.8×10^{-23}
0.89	1.83	25.7%	9.0×10^{-25}	2.7×10^{-23}	2.2×10^{-23}
1.33	1.83	14.9%	1.7×10^{-24}	5.1×10^{-23}	4.2×10^{-23}
1.78	1.83	9.8%	2.9×10^{-24}	8.7×10^{-23}	7.1×10^{-23}
2.22	1.83	5.0%	3.8×10^{-24}	1.1×10^{-22}	9.2×10^{-23}
2.67	1.83	3.0%	4.3×10^{-24}	1.3×10^{-22}	1.0×10^{-22}
3.11	1.83	4.8%	4.2×10^{-24}	1.2×10^{-22}	1.0×10^{-22}
3.56	1.83	6.9%	4.2×10^{-24}	1.2×10^{-22}	1.0×10^{-22}
4.0	1.83	9.4%	4.2×10^{-24}	1.2×10^{-22}	1.0×10^{-22}
0.0	1.91	61.2%	7.8×10^{-25}	2.3×10^{-23}	1.9×10^{-23}
0.44	1.91	33.0%	8.4×10^{-25}	2.5×10^{-23}	2.1×10^{-23}
0.89	1.91	18.0%	1.1×10^{-24}	3.2×10^{-23}	2.7×10^{-23}
1.33	1.91	10.9%	2.1×10^{-24}	6.2×10^{-23}	5.1×10^{-23}
1.78	1.91	7.4%	3.2×10^{-24}	9.5×10^{-23}	7.8×10^{-23}

2.22	1.91	3.9%	3.9×10^{-24}	1.2×10^{-22}	9.5×10^{-23}
2.67	1.91	2.6%	4.4×10^{-24}	1.3×10^{-22}	1.1×10^{-22}
3.11	1.91	4.0%	4.3×10^{-24}	1.3×10^{-22}	1.0×10^{-22}
3.56	1.91	5.8%	4.3×10^{-24}	1.3×10^{-22}	1.0×10^{-22}
4.0	1.91	7.7%	4.3×10^{-24}	1.3×10^{-22}	1.0×10^{-22}
0.0	1.98	51.0%	8.6×10^{-25}	2.6×10^{-23}	2.1×10^{-23}
0.44	1.98	25.1%	9.3×10^{-25}	2.8×10^{-23}	2.3×10^{-23}
0.89	1.98	13.4%	1.3×10^{-24}	3.8×10^{-23}	3.1×10^{-23}
1.33	1.98	8.4%	2.4×10^{-24}	7.1×10^{-23}	5.8×10^{-23}
1.78	1.98	5.9%	3.4×10^{-24}	1.0×10^{-22}	8.3×10^{-23}
2.22	1.98	3.2%	4.1×10^{-24}	1.2×10^{-22}	9.8×10^{-23}
2.67	1.98	2.4%	4.5×10^{-24}	1.3×10^{-22}	1.1×10^{-22}
3.11	1.98	3.5%	4.4×10^{-24}	1.3×10^{-22}	1.1×10^{-22}
3.56	1.98	5.0%	4.3×10^{-24}	1.3×10^{-22}	1.1×10^{-22}
4.0	1.98	6.5%	4.4×10^{-24}	1.3×10^{-22}	1.1×10^{-22}
0.0	2.05	38.5%	9.4×10^{-25}	2.8×10^{-23}	2.3×10^{-23}
0.44	2.05	18.1%	1.0×10^{-24}	3.1×10^{-23}	2.5×10^{-23}
0.89	2.05	9.9%	1.5×10^{-24}	4.4×10^{-23}	3.6×10^{-23}
1.33	2.05	6.5%	2.6×10^{-24}	7.9×10^{-23}	6.4×10^{-23}
1.78	2.05	4.6%	3.6×10^{-24}	1.1×10^{-22}	8.6×10^{-23}
2.22	2.05	2.5%	4.2×10^{-24}	1.2×10^{-22}	1.0×10^{-22}
2.67	2.05	2.0%	4.6×10^{-24}	1.4×10^{-22}	1.1×10^{-22}
3.11	2.05	3.0%	4.5×10^{-24}	1.3×10^{-22}	1.1×10^{-22}
3.56	2.05	4.1%	4.4×10^{-24}	1.3×10^{-22}	1.1×10^{-22}
4.0	2.05	5.3%	4.4×10^{-24}	1.3×10^{-22}	1.1×10^{-22}
0.0	2.12	28.3%	1.0×10^{-24}	3.1×10^{-23}	2.5×10^{-23}
0.44	2.12	13.1%	1.2×10^{-24}	3.4×10^{-23}	2.8×10^{-23}
0.89	2.12	7.4%	1.7×10^{-24}	5.0×10^{-23}	4.1×10^{-23}
1.33	2.12	5.1%	2.9×10^{-24}	8.5×10^{-23}	7.0×10^{-23}
1.78	2.12	3.6%	3.7×10^{-24}	1.1×10^{-22}	9.0×10^{-23}
2.22	2.12	2.0%	4.3×10^{-24}	1.3×10^{-22}	1.0×10^{-22}
2.67	2.12	1.7%	4.7×10^{-24}	1.4×10^{-22}	1.1×10^{-22}
3.11	2.12	2.5%	4.7×10^{-24}	1.4×10^{-22}	1.1×10^{-22}
3.56	2.12	3.4%	4.5×10^{-24}	1.3×10^{-22}	1.1×10^{-22}
4.0	2.12	4.3%	4.5×10^{-24}	1.3×10^{-22}	1.1×10^{-22}
0.0	2.19	21.1%	1.1×10^{-24}	3.3×10^{-23}	2.8×10^{-23}
0.44	2.19	9.6%	1.3×10^{-24}	3.8×10^{-23}	3.1×10^{-23}
0.89	2.19	5.6%	1.9×10^{-24}	5.7×10^{-23}	4.7×10^{-23}
1.33	2.19	4.0%	3.1×10^{-24}	9.2×10^{-23}	7.5×10^{-23}
1.78	2.19	2.9%	3.8×10^{-24}	1.1×10^{-22}	9.3×10^{-23}
2.22	2.19	1.7%	4.4×10^{-24}	1.3×10^{-22}	1.1×10^{-22}
2.67	2.19	1.5%	4.8×10^{-24}	1.4×10^{-22}	1.2×10^{-22}
3.11	2.19	2.1%	4.8×10^{-24}	1.4×10^{-22}	1.2×10^{-22}
3.56	2.19	2.9%	4.6×10^{-24}	1.4×10^{-22}	1.1×10^{-22}
4.0	2.19	3.6%	4.6×10^{-24}	1.4×10^{-22}	1.1×10^{-22}
0.0	2.26	15.5%	1.2×10^{-24}	3.6×10^{-23}	3.0×10^{-23}
0.44	2.26	7.3%	1.4×10^{-24}	4.1×10^{-23}	3.4×10^{-23}
0.89	2.26	4.4%	2.1×10^{-24}	6.2×10^{-23}	5.1×10^{-23}
1.33	2.26	3.2%	3.2×10^{-24}	9.6×10^{-23}	7.9×10^{-23}
1.78	2.26	2.3%	3.9×10^{-24}	1.2×10^{-22}	9.5×10^{-23}

2.22	2.26	1.4%	4.4×10^{-24}	1.3×10^{-22}	1.1×10^{-22}
2.67	2.26	1.2%	4.8×10^{-24}	1.4×10^{-22}	1.2×10^{-22}
3.11	2.26	1.7%	4.9×10^{-24}	1.4×10^{-22}	1.2×10^{-22}
3.56	2.26	2.4%	4.7×10^{-24}	1.4×10^{-22}	1.1×10^{-22}
4.0	2.26	3.0%	4.7×10^{-24}	1.4×10^{-22}	1.1×10^{-22}
0.0	2.33	11.3%	1.3×10^{-24}	3.9×10^{-23}	3.2×10^{-23}
0.44	2.33	5.5%	1.5×10^{-24}	4.5×10^{-23}	3.7×10^{-23}
0.89	2.33	3.5%	2.3×10^{-24}	6.8×10^{-23}	5.5×10^{-23}
1.33	2.33	2.6%	3.4×10^{-24}	1.0×10^{-22}	8.2×10^{-23}
1.78	2.33	1.8%	4.0×10^{-24}	1.2×10^{-22}	9.8×10^{-23}
2.22	2.33	1.1%	4.5×10^{-24}	1.3×10^{-22}	1.1×10^{-22}
2.67	2.33	1.0%	4.9×10^{-24}	1.5×10^{-22}	1.2×10^{-22}
3.11	2.33	1.4%	5.0×10^{-24}	1.5×10^{-22}	1.2×10^{-22}
3.56	2.33	1.9%	4.8×10^{-24}	1.4×10^{-22}	1.2×10^{-22}
4.0	2.33	2.4%	4.8×10^{-24}	1.4×10^{-22}	1.2×10^{-22}
0.0	2.4	8.2%	1.4×10^{-24}	4.2×10^{-23}	3.5×10^{-23}
0.44	2.4	4.1%	1.7×10^{-24}	4.9×10^{-23}	4.1×10^{-23}
0.89	2.4	2.7%	2.5×10^{-24}	7.4×10^{-23}	6.0×10^{-23}
1.33	2.4	2.0%	3.5×10^{-24}	1.0×10^{-22}	8.6×10^{-23}
1.78	2.4	1.4%	4.1×10^{-24}	1.2×10^{-22}	1.0×10^{-22}
2.22	2.4	0.9%	4.6×10^{-24}	1.4×10^{-22}	1.1×10^{-22}
2.67	2.4	0.8%	5.0×10^{-24}	1.5×10^{-22}	1.2×10^{-22}
3.11	2.4	1.1%	5.1×10^{-24}	1.5×10^{-22}	1.2×10^{-22}
3.56	2.4	1.6%	4.9×10^{-24}	1.5×10^{-22}	1.2×10^{-22}
4.0	2.4	2.0%	4.9×10^{-24}	1.4×10^{-22}	1.2×10^{-22}

Table 4: Hard X-ray group spectrum grid information

Annex B: Custom code for analysis

Throughout our work, we wrote many different routines for interacting between the raw outputs of our simulations and the display of fields of interest and such. We reference here only **some** of our main original routines, specifically the techniques and codes that are not too context specific or too long-winded. For instance, we will not make explicit, the code for generating the disk models used for the Bardeen-Peterson effect post processing as the code is too long and non-modular, nor will we make explicit the code for spectrum generation as it is mostly some ingenious uses of the relxill module. This codes may be given by the author on request.

Let us start by seeing how the actual scripts are run on our accessed high performance computing resources:

NLHPC running scripts

Throughout this work, we ran all of our relevant simulations on the high performance computational resources of the 'Laboratorio Nacional de Computación de Alto Rendimiento' (NLHPC). We specifically ran most of our simulations on the Guacolda CPU partition. The general template of our jobscripts obey usual SLURM nomenclature .sh scripts, such a template for our case would look like:

```
#!/bin/bash
#SBATCH --job-name=job_ex_tesis_j
#SBATCH --partition=general
#SBATCH -n 132
#SBATCH --mem-per-cpu=4363
#SBATCH --ntasks-per-node=44
#SBATCH --output=dice_new.out
#SBATCH --error=dice_new.err
#SBATCH -D /home/jetigny/path/to/data_output

module purge
ml intel/2018.04

srun  --partition=general /home/jetigny/path/to/compilation/script/ramses_comp
/home/jetigny/path/to/simulation/parameters/setup.nml > /home/jetigny/path/to/simulation/logs/job.log
```

Python object for SMBH pairs

We begin by mentioning the only piece of python code that does not make use of the `.yt` library (although it does still use the numpy, matplotlib and scipy suites), which is the isolated binary analysis package, which deals only with the information from the sink particles, this information may be handled directly as it comes codified in simple .csv files instead of raw fortran output files. We wrote a package that handles the binary's properties (the isolated SMBH pair), through python's object-oriented programming. This code may be accessed and used from `https://github.com/detigny/misc-ramses/blob/master/SMBH.py`, or by asking the author directly (you may download it in your working directory and load it as a regular import).

The routines of this objects allows for three main functionalities: Looking at the 'spatial' evolution of BHs, the 'angular' evolution and the 'feeding' evolution. By calling different methods in our class, we can immediately graph things like accretion (which may be switched to be scaled by Eddington units), binary separation, accreted angular momentum, $L_{acc} - L_{bin}$ alignment, etc.

Accessing and handling fields directly in equipartitioned grids

As the AMR paradigm gives information in unstructured grids. This is a problem for consistently mapping the evolution of fields in the form $f(x, y, z, t)$. For this we use three main routines from `.yt` to create different 'fixed resolution buffers' (FRB), which are just arrays that specify data emulating an equispaced grid of customizable resolution. This three routines generate projected fields in 2D, a slice of a field in 2D, and a generalized 3D equispaced data grid of a field inside a region of simulation space. This three routines obey the following scripts:

- For a projection over axis='paxis' FRB of a field:

```
    ytproj = ds.proj(field , paxis)
    frb = ytproj.to_frb(width,resolution)
```

- For a slice FRB, if we instantiate the yt.load as ds, the following code creates a slice centered at cn:

```
    ytxyz = yt.SlicePlot(ds,paxis,field ,width,center=cn)
    frb = ytxyz.data_source.to_frb(width, resolution)
```

- The code for the general 3D field array, is just as simple:

```
    slab = ds.arbitrary_grid(leftco,rightco, dims=res)
    frb = slab['density'].in_units('g/cm**3').value
```

This is specially important for handling non trivial quantities that are not on the default (derived) fields that can be handled direclty by `.yt`. One example would be the Toomre parameter: If we were to map $Q(x, y)$, we need to at least combine the integrated density field (to get surface density $\Sigma(x, y)$), the projected sound velocity field c_s and the angular velocity $\Omega(x, y)$, which is also a field that is not listed by the software (which means we need to map the tangential velocity and get $v_t \times r$).

Cooling/Heating calculation over the grid

We showcase the code employed for the calculation of the thermal timescale over the simulation grid:

The first block of code is that of cooling by primordial gas methods, which include recombination processes, collisional cooling, excitation cooling and Compton cooling. In the code we separated the cooling functions that group processes by each ion/particle species involved.

```

def lmbda(species,T):
    if species == 'HI':
        return 315614/T
    elif species == 'HeI':
        return 570670/T
    elif species == 'HeII':
        return 1263030/T
    else:
        return 'No info for such species'

def factor(T):
    return 1/(1+np.sqrt(T/10**5))

def cool_ne_nHI(T,ne,nHI):
    f1 = 1.27e-21*np.sqrt(T)*np.exp(-1.58e5/T)
    f2 = 7.5e-19*np.exp(-1.18e5/T)
    return factor(T)*(f1+f2)*ne*nHI

def cool_ne_nHeI(T,ne,nHeI):
    return 9.38e-22*factor(T)*np.exp(-2.85e5/T)*ne*nHeI

def cool_ne_nHeII(T,ne,nHeII):
    kb = sp.constants.Boltzmann*1e7
    f1 = 4.95e-22*factor(T)*np.exp(-6.32e5/T)
    f2 = 5.54e-17*factor(T)*np.exp(-4.74e5/T)*T**(-0.397)
    f3 = kb*T*3e-14*lmbda('HeI')**0.654
    f4 = 1.24e-13*(T**-1.5)*np.exp(-4.7e5/T)*(1+0.3*np.exp(-9.4e4/T))
    return (f1+f2+f3+f4)*ne*nHeII

def cool_ne_nHII(T,ne,nHII):
    l = (lmbda('HI')**1.965)/((1+(lmbda('HI')/0.541)**0.502)**2.697)
    return 1.778e-29*T*l*ne*nHII

def cool_ne_nHeIII(T,ne,nHeIII):
    l = (lmbda('HeII')**1.965)/((1+(lmbda('HeII')/0.541)**0.502)**2.697)
    return 8*1.778e-29*T*l*ne*nHeIII

def brems(T,ne,nHII,nHeII,nHeIII):
    theta = 1.42e-27*np.sqrt(T)
    return theta*ne*(nHII + nHeII + 4*nHeIII)

def compton(T,ne):
    return 1.017e-37*(2.727**4)*(T-2.727)*ne
```

This is of course, then followed by the photoheating block that depends on ionization:

```
def ph_heat_HI(N,nHI,sigE_HI,sigN_HI,eps1,epsi):

    if np.size(sigN_HI) != np.size(sigE_HI):
        return 'Something is wrong with the cross sections'
    M = np.size(sigN_HI)
    obj = 0

    for i in range(M):
        obj = obj + N[i]*(epsi[i]*sigE_HI[i] - eps1*sigN_HI)

    return nHI*obj

def ph_heat_HeI(N,nHeI,sigE_HeI,sigN_HeI,eps2,epsi):

    if np.size(sigN_HeI) != np.size(sigE_HeI):
        return 'Something is wrong with the cross sections'
    M = np.size(sigN_HeI)
    obj = 0

    for i in range(M):
        obj = obj + N[i]*(epsi[i]*sigE_HeI[i] - eps2*sigN_HeI)

    return nHeI*obj

def ph_heat_HeII(N,nHeII,sigE_HeII,sigN_HeII,eps3,epsi):

    if np.size(sigN_HeII) != np.size(sigE_HeII):
        return 'Something is wrong with the cross sections'
    M = np.size(sigN_HeII)
    obj = 0

    for i in range(M):
        obj = obj + N[i]*(epsi[i]*sigE_HeII[i] - eps3*sigN_HeII)

    return nHeII*obj

def final_ph_heat(N,cr,nHI,nHeI,nHeII,sigE_HI,sigE_HeI,sigE_HeII,sigN_HI,
                  sigN_HeI,sigN_HeII,epsj,epsi):

    f1 = ph_heat_HI(N,nHI,sigE_HI,sigN_HI,epsj[0],epsi)
    f2 = ph_heat_HeI(N,nHeI,sigE_HeI,sigN_HeI,epsj[1],epsi)
    f3 = ph_heat_HeII(N,nHeII,sigE_HeII,sigN_HeII,epsj[2],epsi)

    return cr*(f1+f2+f3)
```

With this we can calculate the net heating/cooling rate by subtracting all the cooling contributions to the heating rate, and then we may determine the thermal timescale. It is of notice that this code uses the abundancies of ion species/electrons and their corresponding cross sections, which means that the thermal timescale is only calculable with this method, if the output is that of an -RT simulation.

For the purely hydrodynamical+gravitational simulations, the methods differ: We have to estimate the photoionization rates, and solve a system of equations recursively for the ion species abundancies. We did this by solving the six-variable system of equations using a fixed point method that employs Anderson mixing, and by assuming that the photionization flux is $\propto \dot{M}$ at a fixed rate. We will not add this code here in honor of space, but it may be asked from the author of this work.